Development of Novel Physical Methods to Enhance Contrast and Sensitivity in Magnetic Resonance Imaging

by

Elizabeth Rose Jenista

Department of Chemistry
Duke University

Date:_____
Approved:

_____
Warren S. Warren, Supervisor

_____
Barbara Ramsay Shaw

_____
Eric Toone

_____
Leonard Spicer

Dissertation submitted in partial fulfillment of
the requirements for the degree of Doctor of Philosophy in the Department of
Chemistry in the Graduate School
of Duke University

2010

ABSTRACT

Development of Novel Physical Methods to Enhance Contrast and Sensitivity in Magnetic Resonance Imaging

by

Elizabeth R. Jenista

Department of Chemistry
Duke University

Date:_____
Approved:

_____
Warren S. Warren, Supervisor

_____
Barbara Ramsay Shaw

_____
Eric Toone

_____
Leonard Spicer

An abstract of a dissertation submitted in partial fulfillment of the requirements for the degree of Doctor of Philosophy in the Department of Chemistry in the Graduate School of Duke University
2010

Copyright by
Elizabeth Rose Jenista
2010

Abstract

The purpose of this thesis is to report technological developments in contrast mechanisms for MRI. The search for new forms of contrast is on-going, with the hope that new contrast mechanisms and new contrast agents will provide new and unique insight into various molecular processes and disease states. In this dissertation, we will describe new contrast mechanisms developed by manipulating the inherent physics of the system, as well as the development of exogenous contrast agents. More specifically, we will describe the application of iMQCs (intermolecular multiple quantum coherences) to thermometry and structural imaging, and the unique information provided from these studies. We will also describe methods for migrating iMQC-based pulse sequences from a Bruker research console onto a clinical GE console, thus enabling the application of iMQCs to humans. We will describe the development of hyperpolarized contrast agents which have the potential to provide an unprecedented level of molecular contrast to MRI and the development of techniques to enhance the lifetime of these hyperpolarized contrast agents. Finally, we will discuss a new type of T_2-weighted imaging which significantly improves the refocusing of CPMG-type sequences.

Contents

Abstract iv

List of Tables x

List of Figures xi

List of Abbreviations xix

Acknowledgements xxi

Chapter 1 Introduction to Magnetic Resonance 1

1.1 Classical Description of Magnetic Resonance 1

1.2 Quantum Mechanical Description of Magnetic Resonance 6

1.2.1 The Hamiltonian 8

1.2.2 The Density Matrix 14

1.2.3 Product Operator Theory 17

1.3 Phase Cycling 18

Chapter 2 - Introduction to Intermolecular Multiple Quantum Coherences 24

2.1 The Theory of iMQCs 24

2.1.1 The High Temperature Approximation 26

2.1.2 Dipolar Couplings 27

2.2 Standard iMQC Experiment 31

2.2.1 Description of the CRAZED sequence 33

Chapter 3 - Hyperpolarization using Dynamic Nuclear Polarization 36

3.1 Dynamic Nuclear Polarization 39

3.1.1 Solid Effect 40

3.1.2 Thermal Mixing 42
3.2 NMR and MRI using hyperpolarized compounds 46
3.3 Technical Description of the Hypersense Instrument 47
3.3.1 Technical Specifications of the Hypersense 47
3.3.2 Sample Formulation 48
3.3.3 Hypersense Operation 49
3.3.4 Calibration and Polarization Monitoring 51
3.3.3 Common Hypersense Problems 52
3.3.3.1. Ice in the helium reservoir 52
3.3.3.2. Contamination of the VTI 52
3.3.3.3. Contamination of the Capillary Tube 54
3.3.3.4. Slipping Needle Valve Motor 55
3.3.3.5. VTI Level Miscalibration 55
3.3.3.6. Lost Cups 57
Chapter 4 - Temperature Imaging using iMQCs 58
4.1 iMQC temperature detection 63
4.2 Modifications to the HOMOGENIZED Sequence for Temperature Imaging 65
4.2 Single acquisition HOT imaging 69
4.4 Product Operator Description of the HOT sequence 76
4.4.1. Two Window HOT 76
4.4.2. Four window HOT 78
4.5 Data Processing 81

4.5.1 One – window HOT 81

4.5.2 Two – window HOT 82

4.6. Results and Discussion 83

4.6.1 Spectroscopy Results 83

4.6.2 Results from single window HOT imaging experiments 86

4.6.3 Results from two window HOT imaging experiments 90

4.6.4. Conclusion 94

Chapter 5 GE Programming 96

5.1 Basics of GE programming 96

5.2 Writing the pulse sequence 97

5.2.1 Inserting gradients 97

5.2.2 Wait times 100

5.2.3 RF pulses 101

5.2.4 External Waveforms 102

5.2.5 Phase Cycling 105

5.2.6 Adding buttons, changing default values, allowed values and CVs 107

5.3 Compiling 108

5.4 Troubleshooting Code 111

5.5 Analyzing Data 111

5.5.1 Acquiring Incremented Data 112

5.5.2 Special Considerations at CIVM 112

5.6 Demonstrations of iMQCs on the GE scanner 114

Chapter 6 – ^{1}H – ^{13}C Intermolecular Multiple Quantum Coherences 119

6.1 Properties of Proton – Carbon iMQCs 121

6.1.1 The CRAZED sequence with heteronuclear iMQCs 121

6.1.2 Characteristics of the Heteronuclear iMQC signal from the CRAZED experiment 125

6.2 Reducing Inhomogeneity in the Hyperpolarized Carbon Linewidth using Heteronuclear iMQCs 130

6.2. Demonstration of Inhomogeneity Compensated Heteronuclear iMQCs 132

Chapter 7 - ^{13}C – ^{13}C iMQCs 137

7.1 Generation and Detection of carbon- carbon iMQCs 138

7.2 Experimental Demonstration of ^{13}C-^{13}C iMQCs 141

Conclusion 144

Chapter 8 – Long lived singlet states 147

8.1 What is a singlet state? 150

8.2 Previous demonstrations of singlet states 154

8.3 Molecular system for storage of populations in the singlet state 157

8.4 Selection and characterization of a molecular system for use with the singlet state. 161

8.5 Demonstration of the existence of singlet states in a thermal sample 163

8.6 Hyperpolarized population storage with the singlet state 165

Chapter 9 - Calculation of Singlet Character and Relaxation 168

9.1 Calculating the overlap of the singlet state and actual eigenstates of the system 169

9.2 Calculating the time-dependent behavior of the singlet state 171

Chapter 10 - Improved T2 weighted imaging using unequally spaced pulses.....180

10.1 Refocusing Static Field Inhomogeneities 181

10.2 Toggling Frame Hamiltonian 182

10.2 Refocusing Time Varying Inhomogeneities 185

10.3 Comparing UDD and CPMG.....187

10.4 Experimental Demonstration of the UDD sequence 189

Chapter 11 - Future directions for signal enhancement 195

11.1 Temperature Detection with iMQCs in Adipose Tissue.....195

11.1.1 iMQC signal enhancement with ZEBRA 196

11.2 Future work with the singlet state 198

11.2.1 – Singlet delivery systems 199

11.2.2 – Singlets with para-hydrogen 199

11.3 – Conclusion.....200

Bibliography 202

Biography.....216

List of Tables

Table 1 – Example of a phase cycling table selecting for p = 2. Note that the phase is always modulo 360, so the final column (coherence shift) is technically 0, 180, 360, 540, but it is written 0, 180, 0, 180. 21

Table 2 - Phase cycling table for the same pulse sequence, but calculating the effect of this phase cycle on zero quantum (p = 0) and single quantum (p = 1) coherences. 22

Table 3 – Phase cycling scheme for the 2-window HOT sequence. 74

Table 4- Detailed view of the phase cycling for two-window HOT. 75

Table 5 - Comparison of predicted iMQC signal for protons, thermally polarized carbon and hyperpolarized carbon. 140

Table 6 - Comparison of the hydrate-diacetyl exchange rates. The top row gives the hydration rate (i.e. diacetyl to hydrate), the middle row gives the dehydration rate (hydrate to diacetyl) and the bottom row gives the rate of exchange of the hydrate groups between the two labeled carbon sites on the molecule. Table courtesy of Y. Morris Chen. 163

Table 7 - Comparison of the SNR from the UDD, anti-UDD and CPMG sequences. Free water and tissue ROIs were selected as shown in figure 2. Note that at the longer echo times with 16 pulses, the CPMG sequence refocuses the free water very well, while the UDD sequence has significantly improved SNR in the tissue ROI. In addition, the anti-UDD sequence significantly underperforms both the UDD and CPMG sequence in the tissue ROI for the 16 pulse sequence with TE=80ms. 191

List of Figures

Figure 1-1: Vector diagram of a spin echo. The 90°-x pulse takes the magnetization vector from +z to +y. While in the plane, the spins dephase during TE/2 due to T2 relaxation. The 180°y pulse reverses the dephasing, causing a refocusing after TE/2. 5

Figure 2-1 A. The CRAZED pulse sequence. The top sequence is the classic sequence, but it suffers from T_2^* weighting. The insertion of a refocusing pulse (below) reduces the effect of T_2^* relaxation. B. Energy level diagram showing the DQC and ZQC transitions for a 2 spin system. C. Pictoral description of the effect of the gradients and dipolar coupling. The gradients break the isotropy of the magnetic field, and reintroduce dipolar couplings. The dipolar couplings convert the unobservable 2-spin coherences into observable 1-spin coherences. 31

Figure 3-1 - Comparison of signal intensity of ^{1}H water (left), thermally polarized ^{13}C urea (middle) and hyperpolarized ^{13}C urea (right). The proton image was acquired using a FLASH sequence in less than 1 minute, while the thermally polarized carbon image required 14 hours of averaging in order to acquire enough signal to make an image. The hyperpolarized carbon image series (right) has sufficient signal to allow acquisition in 2s using a FLASH sequence. Note that the slice for the hyperpolarized image was acquired using a different slice orientation than the proton and thermally polarized carbon images. 38

Figure 3-2 - Description of the solid effect. A – polarization at the sum of the electron and nuclear Larmor frequencies, resulting in an overpopulation of the upper energy level (spin down). B – polarization at the difference frequency of the nuclear and electron Larmor frequencies resulting in a polarization of the lower energy level (spin up). 42

Figure 3-3 - Description of thermal mixing using spin temperature. Polarization proceeds via off-resonance irradiation near the electron Larmor frequency which cools the electron dipolar bath. The cooling of the electron dipolar bath causes the nuclear Zeeman bath to cool as well, transferring the polarization of the electron spins to the nuclear system. 44

Figure 3-4 - Thermal mixing energy level diagram. Microwave irradiation drives transitions to the middle energy levels and electron relaxation returns the populations to the lowest two energy levels. Through mixing of the degenerate energy levels the nuclear populations slowly polarize. 46

Figure 3-5 - Hypersense diagram. The Hypersense is based on a standard 3.35 T vertical bore magnet. Instead of the usual core for the NMR probe, the Hypersense has been altered to contain a polarizing chamber which receives helium from the helium can of the magnet, and a sample holder in which the sample is placed and irradiated by microwaves at 1.4 K. Once polarized, the dissolution stick drops into the sample holder and removes the sample from the helium bath and rapidly dissolves the sample from the Hypersense User's Manual). 50

Figure 3-6 - Microwave sweep of pyruvate..... 51

Figure 4-1: Top: Standard 2D iZQC spectrum of a 75% water- 25% acetone sample. Bottom left: Projection along F2 (direct, SQC dimension). Bottom right: Projection along F1 (indirect, iZQC dimension). In this spectrum, the bulk of the signal is coming from the temperature insensitive same spin iZQC signal (such as that from water-water or fat-fat iZQCs). If the standard iZQC sequence was used to image temperature, the bulk of the signal in that image would be temperature insensitive signal, thus contaminating the temperature sensitivity of the image..... 68

Figure 4-2: Single acquisition HOT pulse sequence. This sequence is a modified version of the CRAZED pulse sequence. The frequency selective 180° pulse converts iZQCs to iDQCs and the subsequent gradients filter out all signals except the desired mixed – spin iMQCs. 69

Figure 4-3- Two-window HOT sequence. This sequence acquires two images simultaneously, one which was iDQC during t_1, the other from signal that was iZQC during t_1. The signals in each acquisition window have different amounts of evolution, allowing for a temperature map to be created in a single application of the pulse sequence. In addition, the extra gradients provide a more robust coherence filter, further preventing contamination from unwanted coherence pathways. 72

Figure 4-4- Four window HOT sequence. The addition of two 180° pulses after the acquisition of the temperature sensitive iMQC images (acquisition windows 1 and 2) allow for the detection of chemically selective, spin-density images. 78

Figure 4-5 - The frequency of the iZQC crosspeak between water and fat shifts linearly with temperature in a water-fat phantom. A graph of the frequencies detected using the HOT sequence is shown in figure 7. The graph below the spectra is a plot of the absolute value of the iZQC frequency versus temperature. The error bars were determined by the resolution in the indirect dimension. All spectra were taken with TE=15 ms, TR=4 s, 8 averages, 512 x 256 matrix, spectral width (direct dimension) = 12626.26 Hz, spectral width (indirect dimension) 3200 Hz, correlation distance = 0.06406 mm. 84

Figure 4-6- Spectra of an obese mouse post mortem demonstrate that the sequence cleanly isolates the water-fat coherence. Spectra on the left are the first (top) and second (bottom) acquisition windows. On the right are traces along F2 (blue) and F1 (black) showing narrower lines in the iZQC dimension. Scan parameters: mGT= 11 G/cm*1ms, nGT=-17 G/cm*1ms, correlation distance = 0.198 mm, TE = 40 ms, t_1 = 2.5 ms, τ = 3 ms, and TR = 4.5 s. 86

Figure 4-7- Top Right: Spin echo image of cream sample, axial slice. Arrows mark the position of the three fiber optic temperature probes, and the plot below shows the temperature recorded at each point. Top left: Temperature map of the heated sample showing the distribution of iZQC frequencies at the different temperatures. Bottom left: Graph of temperature vs. iZQC frequency. Three data points come from this experiment and the additional three data points come from single temperature measurements reported in [104]. The temperature images were acquired using a RARE acquisition, RARE factor = 4, 28 averages, 76 repetitions, 32 x 32 matrix, TE = 7.54 ms, TR = 1783 ms, t_1 = 1.87 ms, FOV = 4 cm, correlation distance = 0.093474 mm, spectral width of indirect dimension = 5000 Hz. 88

Figure 4-8 - The sensitivity of the iMQC temperature imaging sequence is demonstrated by looking at the heating effects of RF pulses. In the top left image, the temperature map was generated using single line acquisitions. The same experiment was done again, but this time using a RARE acquisition (top right image). The figures on the bottom are confidence intervals for each of the images on the top. The application of 8 additional pulses elevates the sample temperature by about 1 ºC, which is detected by the iMQC temperature map. Scan parameters for the RARE=8 experiment: 16 averages, 50 repetitions, TE = 8 ms, TR = 2 s, t_1 = 1.87 ms, correlation distance = 0.06406 mm, FOV = 4cm, 32 x 32 matrix. For the single line acquisition, the scan parameters were: 16 averages, 40 repetitions, 32 x 8 matrix, TE = 15 ms, TR = 2 s, t_1 = 1.87 ms, correlation distance = 0.06406 mm. Figure courtesy of Dr. R.T. Branca. 90

Figure 4-9 - iZQC temperature maps for the heating of porcine adipose tissue acquired every 2 minutes using the two acquisition pulse sequence. Increasingly hot water was pushed through a tube running through the center of the tissue. The sample was imaged every two minutes using the two window HOT sequence. Each individual image is numbered to indicate the order of the time course of the images. In these experiments, we initially acquired ten images typically spanning 10 ms of τ evolution. Once these scans verified iZQC evolution, the initial temperature map was made by fitting the phases of images 2 and 7 of the series. Subsequent dynamic thermometry was performed by repeatedly running the scan at the τ equivalent to image 7, and phase changes in each window were related to temperature changes. Temperature near the core was seen to increase from 14°C to 36°C as monitored by a temperature probe. FOV

= 4 cm TE = 40 ms; TR = 2 s; mGT = 1 ms*8.4 G/cm; nGT = 1 ms*-21 G/cm; correlation distance = 0.0945 mm, t_1 = 3 ms; τ = 10.66 ms. Figure from[124] 91

Figure 4-10 - Four window HOT on a tube of water and acetone next to a tube of water. Scan was done at 8.45 T, 64 x 64 matrix size, FOV = 4 cm, 4 averages, TE/2 = 100 ms. Correlation gradient m = 23 G/cm, correlation gradient n = 36.8 G/cm, t_1 = 4.1 ms, correlation distance = 0.0863 mm, τ = 12.5 ms, slice thickness = 2 cm. In figure 10A and B, we detect only the larger tube with a mixture of water and acetone. In C we detect both tubes, since they both contain water. In D, we detect only the larger tube, since it is the only one with acetone. Figure 10E shows a standard spin echo of this sample. All the images are on independent intensity scales. The SNR of A (water + acetone tube) is 488, B (water + acetone tube) is 251, C (water + acetone tube) is 418 and (water only tube) is 595 and D (water + acetone tube) is 33. 93

Figure 5-1 - Comparison of signal phase in a spin echo experiment. A sample of cream was imaged on both the 2T and 7T scanner using a spin echo sequence. The echo time was incremented between images, and the phase of two representative pixels is presented above. On the 2T scanner, the phase change between images is exactly as predicted, while the phase change on the 7T is unpredictable and changes greatly between scans. Images were taken with an increment size of 240 us between images. . 113

Figure 5-2 - Comparison of the frequency selection of a standard sinc pulse on the 2 T and 1.5 T scanners. The frequency selection of the clinical 1.5 T scanner is much cleaner than that of the 2T scanner, allowing for improved frequency selection. 114

Figure 5-3 - Confirmation of iDQC signal on the GE scanner. Images were of a 50 ml tube of water taken at 7T. TE=60ms, tau = 6.2 ms, correlation distance = 64 μm, 20 mm slice, FOV = 10 cm x 10 cm, matrix = 256 x 128. 115

Figure 5-4 - iDQC image of a human brain. TE=20 ms, correlation distance = 140 μm along z, 2 cm slice, tau = 1ms, matrix = 256 x 128. 116

Figure 5-5 - 2D spectrum of cream using the HOT pulse sequence (acquisition of window 1). The 2D spectroscopy experiment on cream confirms that the main signal detected comes from the mixed spin iZQC crosspeak. This experiment was done with 4 averages, TE/2 =30 ms, TR = 1s, offset = 200 Hz, receiver bandwidth = 15.8 kHz, indirect detection bandwidth = 1000 Hz, 32 reps. 117

Figure 5-6 Demonstration of the HOT sequence on a cream phantom (milk jug filled with cream) on the clinical 1.5 T scanner. The signal intensity is still fairly low, limiting the quality of the temperature detection with this method. Matrix = 256 x 16, TE/2=30 ms,

TR=1s, FOV= 30 cm^2, no slice selection. Image was taken with the HOT sequence acquiring the first window only. 117

Figure 6-1 - Pulse sequence for the detection of heteronuclear iMQCs. This sequence is very similar to the CRAZED sequence, except for the gradient ratios and timings. Note that the gradients act upon both spin types. 122

Figure 6-2 - Comparison of the calculated signal for a heteronuclear and homonuclear iMQC experiments. By using heteronuclear iMQCs, significantly more signal is detected than in the case of thermal carbon homonuclear iMQCs. Note that in order to graph all three signals on the same graph, the signal from the thermal proton-carbon experiment was enlarged by 625 and the thermal carbon-carbon signal was enlarged 8,333 times. 127

Figure 6-3 - The effect of changing the dipolar demagnetizing time for the indirectly detected spin. Only the signal intensity is affected by this change, not the position of the largest signals. 128

Figure 6-4 - Comparison of the calculated iMQC signal for heteronuclear iMQC experiments as the dipolar demagnetizing time of the directly detected spin is changed. The signal is much more sensitive to changes in the concentration of the directly detected spin than changes in the indirectly detected spin. 129

Figure 6-5 – Pulse sequence used to detect heteronuclear iMQCs with minimal contributions from inhomogeneities. The pulse sequence uses the same tricks as the HOT sequence – by converting the coherences from DQCs to ZQCs and carefully choosing the timings, the system can evolve with inhomogeneity compensation..... 130

Figure 6-6 - 2D 1H - 13C iMQC spectrum (proton detection) of 13C enriched urea in water. The crosspeak occurs at (100 Hz, -425 Hz), the expected frequency for the inhomogeneity compensated heteronuclear iMQC pulse sequence. NA = 64, NR = 64, water offset = +100 Hz, carbon offset = -400, direct spectral width = 2003.2 Hz, indirect spectral width = 2222.2 Hz. 132

Figure 6-7 - Comparison of the directly detected carbon linewidth with the indirectly detected iMQC carbon linewidth. The iMQC detection allows for narrower lines because of the inhomogeneity compensation. 133

Figure 6-8 - Experimental demonstration of hyperpolarized heteronuclear iMQCs. The signal on the right comes from a hyperpolarized pyruvate sample, while the signal on the right is the same sample, thermally polarized. The hyperpolarization of the sample allows for significantly more heteronuclear iMQC signal, and the iMQC pulse sequence

can be used to detect this hyperpolarized signal without broadening from inhomogeneities. 134

Figure 6-9 - Comparison of the echo timing for the iDQC only sequence (bottom) and the iDQC to iZQC to iDQC pulse sequence (top). For these experiments, τ = 28 ms, τ' = 27.6 ms, and τ'' = 10.1 ms. The difference in echo spacing is 37.6 ms, as predicted. 135

Figure 7-1 - The multi-CRAZED sequence takes advantage of differences in the echo timing to separate the different echoes at full intensity. The +DQC, -DQC and ZQC (+2, -2 and 0 quantum coherences, respectively) have contrast from sub-voxel variations in the magnetization density or resonance frequency. The +SQC and –SQC (+1 and -1 quantum coherences, respectively) signals have conventional contrast..... 139

Figure 7-2 - Multi-CRAZED FID of hyperpolarized urea compared to the multi-CRAZED FID of water (top corner). It is important to note that this is not one long FID, but a series of consecutive FIDs separated by a gradient pulse. 142

Figure 7-3 - Comparison of the calculated signal (from eq. 1) for a ZQC (top) experiment with an SQC (bottom) experiment for water (T_2 = 2s), and two hyperpolarized carbon samples with T_2s of 300ms and 36 ms with the following parameters: $\Delta\omega = 0$, τ=7ms, $\phi_1 = \phi_2 = \phi_3 = 0$, M_0 (hyperpolarized carbon) = 2.5, M_0 (water) = 1, $\theta_1 = \pi/2$, $\theta_2 = 3\pi/4$, τ_d=298 ms (hyperpolarized carbon), τ_d=185 ms (water) and Δ_s=1..... 143

Figure 8-1 - Energy levels for an A_2 system. In this system there are three accessible energy levels (triplet) and one disconnected energy level (singlet). Transitions between the singlet and triplet levels are forbidden, and populations in the singlet state have a much longer relaxation rate than populations in the triplet energy levels. 151

Figure 8-2 – Energy level diagram for the singlet experiment. The sample is hyperpolarized in the AX form, which allows the transfer of hyperpolarized populations into the $|\alpha\beta>$ or $|\beta\alpha>$ energy levels. The sample is converted to an A_2 system where the hyperpolarized population is trapped. The populations in the triple energy levels equilibrate, but the population in the singlet state is trapped. By converting the system back to an AX system, the populations are released, allowing for a resurgence of hyperpolarized signal at a later time..... 159

Figure 8-3 – FIDs of the hydrate signal. Left – a single line of the hydrate doublet was inverted, and then some time was allowed to pass, followed by a 45° pulse to probe the magnetization. Right – the magnetization preparation sequence was applied to hyperpolarized samples. The signal at 1/2J is initially present after the preparation of the perturbed state. This signal goes away as the sample converts from the AX hydrate form

to the A_2 diacetyl storing the singlet state. At a later time, when the diacetyl has converted back to hydrate the signal reappears. 165

Figure 8-4 - Experimental demonstration of the storage of hyperpolarized species in the singlet state. Hyperpolarized diacetyl was inserted into the magnet and the magnetization preparation sequence was used to overpopulate the middle energy levels. Acetone was then injected forcing the system away from the AX configuration to the A_2 system (first point on the graph). The signal in the triplet energy levels decays, and then water is injected, causing the system to convert back to an AX system and releasing the stored populations and causing a resurgence of signal at a later time. 166

Figure 9-1 - Calculated behavior of diacetyl singlet state. The oscillations of the transition rate are determined by the scalar couplings in the molecule as well as the chemical shift differences between the spins. For this calculation the following parameters were used: Chemical shift (in ppm): spin 1 (C) = 198, spin 2 (C) = 198, spin 3-8 (H) = 2. J couplings (Hz): J12=50, J12=50, J13=6.4, J14=6.4, J15=6.4, J16=-1.1, J17=-1.1, J18=-1.1, J23=-1.1, J24=-1.1, J25=-1.1, J26=6.4, J27=6.4, J28=6.4. Magnetic field is 7T. 173

Figure 9-2 Transition rate of the hydrate of diacetyl. The average transition rate for the hydrate is 1 which indicates that the singlet state is not a stationary state in this molecule and populations in the singlet state are free to move to other states. For this calculation the following parameters were used: Chemical shift (in ppm): Spin 1 (C) = 210, spin 2 (C) = 95 ppm, spin 3-5 (H) =4, spin 6-8 (H) = 3. J coupling (Hz): J12=50, J12=50, J13=6.4, J14=6.4, J15=6.4, J16=-1.1, J17=-1.1, J18=-1.1, J23=-1.1, J24=-1.1, J25=-1.1, J26=6.4, J27=6.4, J28=6.4 All other J couplings set to zero. Magnetic field is 7T. 174

Figure 9-3 - Calculation of the transition rate from the singlet state for L-DOPA at 1.5T and 7T. The parameters for the calculations are: Chemical shift (ppm): spin 1 = 145.08, spin 2 = 144.4, spin 3 = 6.62e-6, spin 4 = 6.49, spin 5= 6.67, spin 6=2.58, spin 7=2.59, and spin 8=3.31. J coupling (Hz): J12=50; J13=0; J14=0; J15=0; J16=0; J17=0; J18=0; J23=0; J24=0; J25=0J26=0;J27=0; J28=0; J34=8; J35=.3; J36=.1; J37=.1;J38=0; J45=1; J46=.5; J47=.5; J48=.1; J56=.5; J57=.5; J58=.1; J67=11; J68=1; J78=1;..... 175

Figure 9-4 - Comparison of the experimental spectra and calculated spectra for acetone and diacetyl. A. Experimental carbon (proton coupled) spectrum of singly labeled diacetyl. B. Proton-coupled carbon spectrum of acetone. C. Proton-coupled spectrum of doubly labeled diacetyl. D. Simulated spectrum of a 8 spin molecule with the C-C coupling set to zero. E. Same simulated spectrum, but with a large C-C coupling. F. Simulation of the diacetyl molecule, doubly labeled. 178

Figure 10-1 - UDD, CPMG and Anti-UDD 16 pulse sequences. The CPMG sequence is characterized by even spacings between the 180° pulses, while the UDD sequence has unequal spacings. The anti-UDD sequence is designed to create a valid echo (the delays add up to create an echo in the absence of time varying fluctuations), and uses the same timings as the UDD sequence, but the timings are not arranged in the same way as prescribed by the UDD formula. 184

Figure 10-2 - Graph of the power spectrum of UDD, CPMG and Spin echo pulses sequences vs. frequency. Total echo time is 50 ms, CPMG and UDD sequences use 4 pulses. From this plot it is obvious that the UDD and CPMG sequences create a strong filtering function for a wider range of frequencies than the spin echo pulse sequence. Figure courtesy of Yesu Feng. 188

Figure 10-3 – Top: Spin echo image of the slice used for the UDD and CPMG images. The arrows point to the location of free water created by cellular degradation during the freezing/thawing processes. The red box indicated the region used for the comparison of the signal presented in table 1. Bottom: Comparison of the UDD, CPMG and anti-UDD pulse sequences on a thawed mouse. The subtraction images show that the UDD sequence provides enhanced refocusing in the bulk tissue, while the CPMG sequence does a better job of refocusing signal from the water deposits. Pulses were 1.27 ms hermite, 256 x 256 matrix, 8 mm axial slice, 8 cm FOV, crusher gradients flanking the refocusing pulses. 190

Figure 10-4 - Comparison of T_2 and the effectiveness of UDD and CPMG. The T_2 map was generated by fitting the decay of a series of spin echo images with the TE varying from 10 ms to 160 ms. The difference map on the right was generated by taking the difference between a UDD and CPMG (8 pulse) images with a TE of 80 ms. 192

Figure 10-5 - In vivo demonstration of the UDD sequence compared to the CPMG and spin echo pulse sequences. The UDD sequence provides enhanced refocusing in the bulk tissue, while the CPMG and spin echo sequences refocus signal from necrotic areas of the tumor. All of the bright regions in the image are tumor tissue. Slice is a 2 mm, axial slice, .5 ms hermite pulses, 2s TR, 3 cm FOV, 120 ms TE. 193

Figure 11-1 - The ZEBRA pulse sequence. The 180 pulses and gradient create a binary modulation of the magnetization, resulting in enhanced iMQC SNR. Figure from [155]. 197

Figure 11-2 - Demonstration of the application of iMQCs with the UDD pulse sequence. Both the UDD and CPMG pulse sequences increase the iMQC signal compared to a spin-echo of the same duration. Figure courtesy of A. Stokes. 198

List of Abbreviations

iMQC – Intermolecular multiple quantum coherence

iDQC – Intermolecular double quantum coherence

iZQC – Intermolecular zero quantum coherence

HOT – Homogenized with off-resonance transfer (thermometry pulse sequence)

$\mathbf{B_0}$ – main magnetic field

$\omega_{\mathbf{0}}$ - nuclear Larmor frequency

T_1 – Longitudinal relaxation rate

T_2 - Transverse relaxation rate

TE – Echo time

CRAZED – COSY Revamped by Asymmetric Z-Gradient Echo Detection (basic iMQC pulse sequence)

FLASH – Fast Low Angle Shot (gradient echo pulse sequence)

SAR – Specific Absorption Rate (RF power absorbed per unit of mass, given in units of W/kg)

ω_0 - Larmor frequency

σ - Chemical shift

ρ - Density matrix

γ - Gyromagnetic ratio (for protons, this is 42.8 MHz/T or 2.68×10^8 rad/s/Tesla)

k – Boltzmann constant (1.38×10^{-23} m^2 kg s^{-2} K^{-1})

$\hbar$ - Planck's constant divided by 2π (6.626×10^{-34} J*s)

ρ_0 - Spin density

Acknowledgements

This thesis would not have been possible without the support and assistance of a large number of people. I would like to thank all the members of the Warren Group including Thomas Matthews, Rachael Reese, Ashley Stokes, Yesu Feng and Y. Morris Chen. I would like to especially thank Gigi Galiana for helping me at the very beginning of my thesis – for all the hours of patient teaching and guidance that she provided. I would also like to thank Rosa Tamara Branca for all the support and guidance she has provided. I would like to thank the Center for In Vivo Microscopy (CIVM) for letting me into their research family. I would especially like to thank Gary Cofer for his constant assistance with every aspect of my work, especially for his help building my first coil and for all he taught me about GE programming. I would also like to thank Bastiaan Driehyus for his invaluable advice and Al Johnson and Larry Hedlund for their support.

I particularly would like to thank my research advisor, Warren S. Warren for all the support, instruction and guidance he has provided me during the course of my thesis. I am very grateful to have been able to be a member of the lab and to have had access to such a wide variety of exciting and novel projects to work on. I would like to thank my parents, Tim and Louise Specht for encouraging my interest in science and supporting me throughout my studies. Finally, I would like to thank one of the most important people who helped me achieve my thesis, my husband, Mike. Without his

support and assistance (with everything mathematical), I would have never achieved as much as I have.

Chapter 1 **Introduction to Magnetic Resonance**

The focus of this dissertation is to provide a description of new developments in contrast enhancement for magnetic resonance. It is easiest to understand how these new techniques lead to novel contrast if we can easily switch between a classical and quantum mechanical description of magnetic resonance. Thus, the first chapter will provide a description of magnetic resonance from both the classical and quantum mechanical perspectives. In addition, a description of hyperpolarization will be provided so that the advances in hyperpolarized contrast agents can be better understood.

1.1 Classical Description of Magnetic Resonance

Nuclear spin may is the basis for all magnetic resonance research. The concept of spin is challenging and abstract, and it is mainly a convention developed describe experimental evidence. Spin is a form of angular momentum that is not produced by a rotation of the particle, but rather is an intrinsic property of the particle itself. Spin behaves as expected from a classical description of a rotating object and fits the quantum mechanical descriptions of angular momentum. The total angular momentum of a particle with spin takes values of the form $[I(I+1)]^{1/2}$, with $2I+1$ possible sublevels. The spin quantum

number, I, depends on the nature of the particle – for fermions, this value is half integer; for bosons, this number is an integer. The applications described here deal with systems that are spin-½ , thus, the focus of this introduction will be solely on the spin ½ situations.

Nuclear magnetic resonance (and magnetic resonance imaging) are based on the interaction of a nuclear spin with an external magnetic field, referred to as B_0. This interaction causes the spin to feel a torque, forcing it to precess around the magnetic field (B_0). The size of the torque experienced by the spin depends both on the characteristics of the spin as well as the size of the magnetic field, therefore, the rate at which the spin precesses also depends on the magnetic field as well as the characteristics of the nucleus. Taking into account all these factors, the frequency of the precession (ω_0) is given by the Larmor equation:

$$\omega_0 = \gamma * (1 - \sigma)\, B_0 \tag{1}$$

where γ is the gyromagnetic ratio (2.68 x 10^8 rad/s/Tesla for ^{1}H), a characteristic of the nucleus, and σ is the shielding constant due to any electrons orbiting the nucleus.

For spin – ½ nuclei, there are two stationary states, one aligned with the magnetic field and one anti-aligned with the magnetic field. The magnetic moment can assume any orientation, but unless it is in one of these two states, it

precesses. The difference in energy between those two states is the Larmor frequency ($\hbar\omega_0$). At room temperature this number is very small compared to kT, and there is only a slight excess of spins aligned with the magnetic field (in the lower energy level) compared to those aligned against the field (in the higher energy level) for nuclei with a positive gyromagnetic ratio. The slight excess of spins aligned in one direction yields a net magnetic moment, which is the signal detected in an NMR experiment. The excess of spins in the lower energy level is quite small (often approximately 1 ppm), yet because there are 10^{23} spins in a mole of water, the net magnetization is not negligible. Rather than consider a single spin, Bloch [1] showed that it was possible to consider the ensemble of spins. More precisely, the net magnetization for an ensemble of spin – ½ nuclei is:

$$M_0 = \frac{\rho_0 \gamma^2 \hbar^2 B_0}{4kT} \tag{2}$$

The spin density is ρ_0, k is the Boltzmann constant, 1.380 x 10^{-23} J·K^{-1}, $\hbar$ is Planck's constant divided by 2π, 1.054 x 10^{-34} J·s, and T is the temperature in Kelvin. By taking the vector sum over all spins, the behavior of the spins in a magnetic field can be described by the Bloch equations [1].

$$\frac{dM_x}{dt} = \gamma \left(M_y B_0 + M_z B_1 \sin(\omega t) \right) - \frac{M_x}{T_2} \tag{3}$$

$$\frac{dM_y}{dt} = \gamma\left(-M_x B_0 + M_z B_1 \sin(\omega t)\right) - \frac{M_y}{T_2} \tag{4}$$

$$\frac{dM_z}{dt} = \gamma\left(M_x B_1 \sin(\omega t) + M_y B_1 \cos(\omega t)\right) - \frac{M_z - M_0}{T_1} \tag{5}$$

M_x, M_y and M_z are the x, y and z components, respectively, of the macroscopic magnetization of a sample placed in a magnetic field B_0. B_1 is the applied magnetic field created by an RF pulse, and T_1 and T_2 are the longitudinal and transverse relaxation times, respectively. The longitudinal relaxation time indicates the time it takes for M_z to be restored to its equilibrium value of M_0. T_1 relaxation is the result of non-radiative interactions between the spin system and the lattice (which connects the spin system and the external world). Relative to other types of spectroscopy, T_1 is fairly slow (usually on the order of seconds), reflecting the weak interactions between the spins and their environment. T_2 relaxation comes from the spin-spin interactions, which cause the Larmor frequency of the spins to change and dephasing the magnetization. In the absence of broadening effects (such as those from magnetic field imperfections), the spin-spin interactions determine the width of the peak, where the peak shape is Lorentzian (due to the Fourier transform of an exponential decay).

Many experiments can be explained correctly using a vector diagram representation, where the behavior of the system under different conditions can

be drawn and understood simply. For example, a spin echo experiment is outlined in Figure 1-1:.

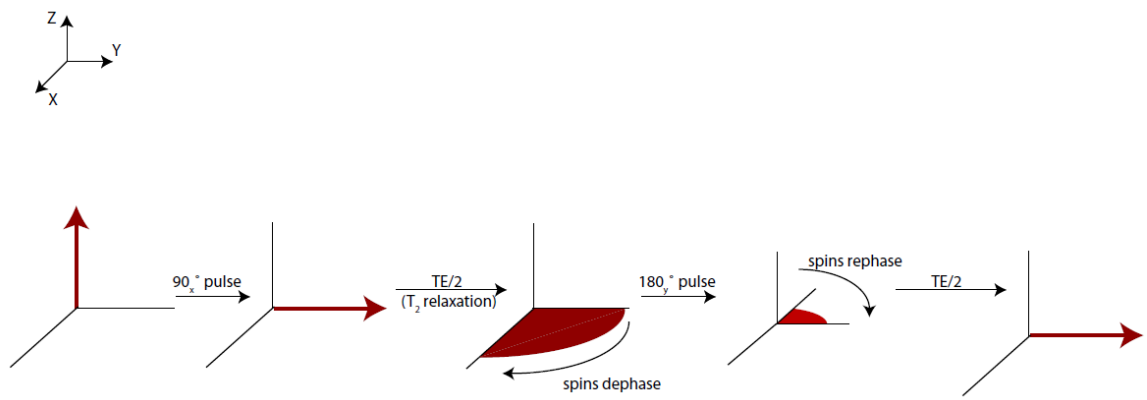

Figure 1-1: Vector diagram of a spin echo. The 90°-x pulse takes the magnetization vector from +z to +y. While in the plane, the spins dephase during TE/2 due to T2 relaxation. The 180°y pulse reverses the dephasing, causing a refocusing after TE/2.

In this sequence, the net magnetization is initially oriented along the net magnetic field (the z-direction). A 90_{-x}° RF pulse is applied to the sample, which rotates the magnetization vector into the xy plane. The magnetization is allowed to precess, where the vector rotates around the net magnetic field at the Larmor frequency and becomes dephased due to T_2. The time that the spins are allowed to freely precess is referred to as the echo time, TE. TE is usually defined as the time between the 90° pulse and the center of the echo. After a time TE/2, 180° RF

pulse is applied, which reverses the evolution and causes refocusing of the signal TE/2 later.[2]

A large number of experiments and magnetic resonance phenomena can be clearly understood using similar descriptions and the Bloch equations [2-4]. However, other phenomena (such as intermolecular multiple quantum coherences, iMQCs, or the behavior of coupled spins) are more thoroughly and clearly understood using a quantum mechanical description of the system.

1.2 Quantum Mechanical Description of Magnetic Resonance

To better understand more complicated phenomena, such as the interactions of coupled spins or multiple quantum experiments, a switch to the quantum mechanical description is necessary. As described before, a spin-½ nucleus has two possible orientations when placed in a magnetic field. In quantum mechanics, we refer to these stationary states as "eigenstates", which are the possible energy states for the spins; in magnetic resonance, these eigenstates (for nuclei with positive γ) are described as $|\alpha\rangle$ (aligned with the magnetic field, lower energy level) and $|\beta\rangle$ (aligned against the magnetic field, higher energy level)[2-4]. While these are the eigenstates of the system, an important distinction must be made. In general, the spins do not reside in one or

the other of the two states, but rather, they may reside in any coherent superposition of the two energy states. Moreover, we often want to consider what happens if the system is perturbed in such a way that populations get temporarily knocked out of an eigenstate. While $|\alpha\rangle$ and $|\beta\rangle$ are eigenstates of this system, they are, by no means, the only available states for the system. Their role as an eigenstate means only that a system in one of those states stays in that state as long as the Hamiltonian does not change. Any state that can be written as a linear combination of eigenstates is an allowed state.

Using this information, the state of the system at any time can be given by the sum of the $|\alpha\rangle$ and $|\beta\rangle$ eigenstates. These states form an orthonormal basis, such that every possible state of the system can be written as a combination of these states. For example, in a system of isolated spin-½ nuclei, the following wavefunction can be written:

$$\Psi(t) = c_\alpha(t)|\alpha\rangle + c_\beta(t)|\beta\rangle \tag{6}$$

where the coefficients, c_α and c_β, are related to the populations in each state. Although these coefficients are often complex numbers, we are observing the eigenvalues of Hermitian matrices, which are always real-valued. Rather, the complex notation is used because there are two components of the magnetization

that are 90° out of phase with each other, and it is convenient to represent these vectors using the complex notation.

As mentioned in the previous section, the observable signal in magnetic resonance comes from the ensemble of spins, and not from one isolated spin. The Hamiltonian describes all interactions of the entire system, and the wavefunction contains all positions, velocities, interactions and spin states of every nuclei and electron in the sample. While the Hamiltonian and wavefunction are the most complete descriptions of the system, they are not solvable in most realistic situations. Instead, it is commonly assumed that the electrical and magnetic influences of the rapidly moving electrons are blurred to the extent that only their average contribution can be seen, and thus, the Hamiltonian can be reduced to simply the nuclear spin Hamiltonian.

1.2.1 The Hamiltonian

Free Precession

The Hamiltonian is the operator that describes the energy of the system. This operator is especially important because the eigenvalues and eigenfunctions of the Hamiltonian are the energy levels of the system. The transitions between these energy levels are what we detect in a NMR or MRI experiment. The Hamiltonian is more powerful than just defining the energy levels of the system;

the Hamiltonian also affects the evolution of the system with time. Through manipulations of the Hamiltonian, the evolution of the system can be controlled in such a way to obtain interesting contrast and spectroscopic results that lie at the heart of NMR and MRI.

The first step in understanding the Hamiltonian is to consider all the different components that affect a standard experiment. The first component is the free evolution (denoted H_{free}) of the spin system in the presence of only the main magnetic field, B_0.

$$H_{free} = \gamma\,(1-\sigma)\,B_0\mathbf{I}_z \tag{7}$$

where γ is the gyromagnetic ratio and σ is the chemical shift, which can also be expressed as ω_0 shown in (1). Since $|\alpha\rangle$ and $|\beta\rangle$ are eigenfunctions of $\mathbf{I}_z$, they are also eigenfunctions of any operator proportional to $\mathbf{I}_z$, including H_{free}.

$$H_{free}|\alpha\rangle = \omega_0\mathbf{I}_z|\alpha\rangle = \frac{1}{2}\omega_0|\alpha\rangle \tag{8}$$

$$H_{free}|\beta\rangle = \omega_0\mathbf{I}_z|\beta\rangle = -\frac{1}{2}\omega_0|\beta\rangle \tag{9}$$

Thus, $|\alpha\rangle$ and $|\beta\rangle$ are eigenfunctions of H_{free} with eigenvalues of $+\frac{1}{2}\omega_0$ and $-\frac{1}{2}\omega_0$, respectively. The transition between $|\alpha\rangle$ and $|\beta\rangle$ is the energy difference between the levels and is equal to ω_0.

If there is more than one type of spin in the system, the Hamiltonian is more complicated. The free precession term, H_{free}, can be modified to include the contribution of the different *n* spins.

$$H_{free} = \gamma_1 B_0 (1 - \sigma_1) \mathbf{I}_{z1} + \gamma_2 B_0 (1 - \sigma_2) \mathbf{I}_{z2} + ...\gamma_n B_0 (1 - \sigma_n) \mathbf{I}_{zn} \tag{10}$$

If we consider a system with 2 spin types, the free evolution Hamiltonian is

$$H_{free} = \gamma_1 B_0 (1 - \sigma_1) \mathbf{I}_{z1} + \gamma_2 B_0 (1 - \sigma_2) \mathbf{I}_{z2} \tag{11}$$

In this case, there are four possible configurations, since each spin has two different states, $|\alpha\rangle$ and $|\beta\rangle$. The four possible eigenstates are $|\alpha\alpha\rangle$, $|\alpha\beta\rangle$, $|\beta\alpha\rangle$ and $|\beta\beta\rangle$. Note that the order of the states indicates which spin is in the $|\alpha\rangle$ or $|\beta\rangle$ state. In other words, the state $|\alpha\beta\rangle$ is where spin 1 is in the $|\alpha\rangle$ state and spin 2 is in the $|\beta\rangle$ state. Since the Hamiltonian for the multispin system is a sum of the terms, the action of the Hamiltonian on the eigenstates of the system is a product of the action of the system on each individual state:

$$H_{free}|\alpha\beta\rangle = (\omega_{0,1}\mathbf{I}_{z1} + \omega_{0,2}\mathbf{I}_{z2}) |\alpha\beta\rangle = \frac{1}{2}\omega_{0,1}|\alpha\beta\rangle - \frac{1}{2}\omega_{0,2}|\alpha\beta\rangle = \left(\frac{1}{2}\omega_{0,1} - \frac{1}{2}\omega_{0,2}\right) |\alpha\beta\rangle \tag{12}$$

Scalar Coupling

In addition to the main magnetic field, each spin experiences a much smaller magnetic field that is created by the nearby spins. There are two

coupling regimes – weak coupling and strong coupling. Weakly coupled spin pairs are when the difference in chemical shift is much larger than the coupling constant of the spin pair. Strongly coupled spin pairs occur when the chemical shift frequency difference is similar in magnitude to the coupling constant.

The coupling between nearby spins is usually referred to as J coupling and adds an additional perturbation to the Hamiltonian:

$$H_{coupled} = 2\pi J_{ij}(\mathbf{I}_i \bullet \mathbf{I}_j) \tag{13}$$

J_{ij} is the proportionality constant of the coupling (also referred to as the spin-spin coupling constant or J-value). With J coupling included, the Hamiltonian becomes

$$H = \omega_{0,1}\mathbf{I}_{z1} + \omega_{0,2}\mathbf{I}_{z2} + 2\pi J_{12}(\mathbf{I}_1 \bullet \mathbf{I}_2) \tag{14}$$

The J coupling term of the Hamiltonian contains the coupled spin pair:

$$\mathbf{I}_1 \bullet \mathbf{I}_2 = \mathbf{I}_{x1}\mathbf{I}_{x2} + \mathbf{I}_{y1}\mathbf{I}_{y2} + \mathbf{I}_{z1}\mathbf{I}_{z2} \tag{15}$$

The $\mathbf{I}_{x1}\mathbf{I}_{x2} + \mathbf{I}_{y1}\mathbf{I}_{y2}$ term creates the off-diagonal parts of the Hamiltonian, while the term $\mathbf{I}_{z1}\mathbf{I}_{z2}$ contributes to the diagonal part of the Hamiltonian. In the case of a weakly coupled system, the secular approximation is often used, and the off-diagonal terms $\mathbf{I}_{x1}\mathbf{I}_{x2} + \mathbf{I}_{y1}\mathbf{I}_{y2}$ are thus discarded. The reason this is advantageous will become clear in the next few paragraphs. To calculate the effect of an RF pulse or the action of the Hamiltonian on the system, we write the pulse as a

rotation of the initial state by the Hamiltonian or RF pulse. For example, for a 2 spin system, the evolution of the magnetization along the x direction (in the absence of RF pulses or gradients) is given by

$$e^{iHt}\mathbf{I}_x e^{-iHt} \tag{16}$$

If the Hamiltonian (H) is made up of many different components, such as the chemical shift evolution and J coupling terms, the Hamiltonian can be broken up, and the effects of pulses, etc., can be calculated for each component of the Hamiltonian separately. For example, one might want to break up a Hamiltonian, H=A+B, and calculate the effect of this Hamiltonian as follows:

$$e^{i(A+B)t}\mathbf{I}_x e^{-i(A+B)t} = e^{iBt}e^{iAt}\mathbf{I}_x e^{-iAt}e^{-iBt} \tag{17}$$

However, it should be noted that this is only true if A and B commute. The sum of exponentials can be broken up as follows:

$$e^{A+B} = e^{A}e^{B}e^{[A,B]} \tag{18}$$

If A is chemical shift evolution of inequivalent spins and B is J coupling, then A and B do not commute, and thus, the exponential cannot be broken up as shown above.

The effect of the secular approximation is that all non-$\mathbf{I}_z$ terms of the Hamiltonian are ignored. In terms of the matrix representation, this is because the diagonal terms are exactly the $\mathbf{I}_z$terms, and all of the $\mathbf{I}_x$ and $\mathbf{I}_y$ terms are off-

diagonal. In the secular approximation, the diagonal terms dominate when the chemical shift difference is much greater than the J coupling constant (in other words, in the weak coupling limit). Under this condition, everything but the $\mathbf{I}_z$terms can be dropped, and all of the remaining terms commute. Thus, the Hamiltonian exponential can be broken into the product of each individual $\mathbf{I}_z$ -term and evaluated individually. Outside the weak coupling limit, the full expression for J coupling is necessary. Using the secular approximation for the J coupling, the product states ($|\alpha\alpha\rangle, |\alpha\beta\rangle, |\beta\alpha\rangle$ and $|\beta\beta\rangle$) are now eigenstates of the system (i.e., the Hamiltonian is diagonal in this basis). Without the secular approximation, these states are not perfect eigenstates of the system.

Assuming we are in the weakly coupled regime, the action of the Hamiltonian on these states is as follows:

$$\begin{aligned}
H|\alpha\alpha\rangle &= \omega_{0,1}\mathbf{I}_{z1} + \omega_{0,2}\mathbf{I}_{z2} + 2\pi J_{12}\mathbf{I}_{z1}\mathbf{I}_{z2}|\alpha\alpha\rangle \\
&= \left(\frac{1}{2}\omega_{0,1} + \frac{1}{2}\omega_{0,2} + \pi J_{12}\right)|\alpha\alpha\rangle \\
H|\alpha\beta\rangle &= \omega_{0,1}\mathbf{I}_{z1} + \omega_{0,2}\mathbf{I}_{z2} + 2\pi J_{12}\mathbf{I}_{z1}\mathbf{I}_{z2}|\alpha\beta\rangle \\
&= \left(\frac{1}{2}\omega_{0,1} - \frac{1}{2}\omega_{0,2} + \pi J_{12}\right)|\alpha\beta\rangle \\
H|\beta\alpha\rangle &= \omega_{0,1}\mathbf{I}_{z1} + \omega_{0,2}\mathbf{I}_{z2} + 2\pi J_{12}\mathbf{I}_{z1}\mathbf{I}_{z2}|\beta\alpha\rangle \\
&= \left(-\frac{1}{2}\omega_{0,1} + \frac{1}{2}\omega_{0,2} + \pi J_{12}\right)|\alpha\beta\rangle \\
H|\beta\beta\rangle &= \omega_{0,1}\mathbf{I}_{z1} + \omega_{0,2}\mathbf{I}_{z2} + 2\pi J_{12}\mathbf{I}_{z1}\mathbf{I}_{z2}|\beta\beta\rangle \\
&= -\left(\frac{1}{2}\omega_{0,1} + \frac{1}{2}\omega_{0,2} - \pi J_{12}\right)|\beta\beta\rangle
\end{aligned} \tag{19}$$

1.2.2 The Density Matrix

These properties are useful for calculating NMR spectra, but to understand the behavior of the ensemble, it would be necessary to sum over all the spins in the system, thus making for a difficult calculation. An alternative approach is to use the density matrix theory, which can be further extended into the product operator theory. These formalisms allow us to understand the behavior of the system as a whole and predict the outcome of an NMR experiment.

If we consider an ensemble of magnetically equivalent spins, such as a tube of water, the behavior of each proton spin is very similar to what has previously been described. To a good approximation, the spins are isolated from the other 10^{23} spins in the sample, and each spin behaves like an isolated spin[4]. Once this ensemble is placed in a magnetic field, some proportion (given by the Boltzmann distribution) of the spins will assume the $|\alpha\rangle$state, and others will take the slightly higher energy $|\beta\rangle$ state (for I=1/2). The net magnetization of the system is a sum of all of the tiny contributions from each spin, but the actual exact calculation of the net magnetization (by considering the contributions from every individual spin) is impractical because of the size of the ensemble.

Instead, we can use the density operator formalism, which describes the quantum state of the ensemble without considering each individual spin state. For non-interacting spin-1/2 nuclei, the wavefunctions $|\alpha\rangle$ and $|\beta\rangle$ form a suitable basis. The density matrix for a system of non-interacting spins (*I*= ½) is

$$\rho = \begin{pmatrix} \rho_{\alpha\alpha} & \rho_{\alpha\beta} \\ \rho_{\beta\alpha} & \rho_{\beta\beta} \end{pmatrix} \tag{20}$$

The diagonal elements, $\rho_{\alpha\alpha}$ and $\rho_{\beta\beta}$, are the populations in the $|\alpha\rangle$ and $|\beta\rangle$states, and the off-diagonal elements, $\rho_{\alpha\beta}$ and $\rho_{\beta\alpha}$, are the coherences between $|\alpha\rangle$ and $|\beta\rangle$. The coherences are complex numbers that indicate the transverse magnetization of the system. Since coherences are complex numbers, they have both a phase and amplitude, which indicates the size and direction of the coherence.

At thermal equilibrium, the populations of the energy states obey the Boltzmann distribution:

$$\rho_{eq} = \frac{e^{\frac{H}{kT}}}{Tr\left\{e^{\frac{H}{kT}}\right\}} = \frac{e^{\sum_i \frac{-\hbar\omega_0}{kt}\mathbf{I}_{zi}}}{Tr\left\{e^{\sum_i \frac{-\hbar\omega_0}{kt}\mathbf{I}_{zi}}\right\}} = \frac{\prod_i e^{\frac{-\hbar\omega_0}{kt}\mathbf{I}_{zi}}}{Tr\left\{\prod_i e^{\frac{-\hbar\omega_0}{kt}\mathbf{I}_{zi}}\right\}} \tag{21}$$

The Boltzmann distribution forces the lower energy levels (assuming γ is positive) to be more populated than the higher energy levels, and this population imbalance depends on both temperature and magnetic field.

To make this expression clearer and more easily manipulated, the exponentials can be expanded, as sums of hyperbolic functions or a Taylor series. The expansion using hyperbolic functions is of the form:

$$\begin{aligned}\rho_{eq} &= \frac{\prod_i \left\{\cosh\left(\frac{\hbar\omega_0}{2kT}\right) E - 2\sinh\left(\frac{-\hbar\omega_0}{2kT}\right) \mathbf{I}_{zi}\right\}}{Tr\left\{\prod_i \left\{\cosh\left(\frac{\hbar\omega_0}{2kT}\right) E - 2\sinh\left(\frac{-\hbar\omega_0}{2kT}\right) \mathbf{I}_{zi}\right\}\right\}} \\ &= \frac{\prod_i \left\{\cosh\left(\frac{-\hbar\omega_0}{2kT}\right) E - 2\sinh\left(\frac{-\hbar\omega_0}{2kT}\right) \mathbf{I}_{zi}\right\}}{2^N \cosh^N\left(\frac{-\hbar\omega_0}{2kT}\right)} \\ &= 2^{-N} \prod_i \left\{E - 2\tanh\left(\frac{-\hbar\omega_0}{2kT}\right) \mathbf{I}_{zi}\right\} \qquad (22)\end{aligned}$$

Since $\tanh\left(\frac{\hbar\omega_0}{kT}\right) \approx \left(\frac{\hbar\omega_0}{kT}\right)$ at room temperature, the density matrix expansion is similar to the normalized Taylor expansion of the exponential (where E is the identity matrix) :

$$\rho_{eq} = 2^{-N}\left\{\mathbf{E} + \left(\frac{-\hbar\omega_0}{2kT}\right)\sum_i^N \mathbf{I}_{zi} + \left(\frac{-\hbar\omega_0}{2kT}\right)^2 \sum_{i,j}^{N^2} \mathbf{I}_{zi}\mathbf{I}_{zj} + \left(\frac{-\hbar\omega_0}{2kT}\right)^3 \sum_{i,j,k}^{N^3} \mathbf{I}_{zi}\mathbf{I}_{zj}\mathbf{I}_{zk} + \ldots\right\}$$

(23)

The equilibrium density matrix is the starting place for many calculations. Since $\frac{\hbar\omega_0}{2kT}$ is a very small number (10^{-4}) at room temperature, coefficients of $\left(\frac{\hbar\omega_0}{2kT}\right)^2$ and $\left(\frac{\hbar\omega_0}{2kT}\right)^3$ might be expected to render the later terms negligible. The assumption (formally called the high temperature approximation) is that the later terms in

the density matrix are negligible, and can be disregarded. Under this assumption, the equilibrium density matrix is:

$$\rho_{eq} = 2^{-N}\left(\mathbf{E} + \left(\frac{-\hbar\omega_0}{2kT}\right)\sum_i^N \mathbf{I}_{zi}\right) \tag{24}$$

1.2.3 Product Operator Theory

In quantum mechanics, operators represent observables such as energy, mass or angular momentum. At any given time, the state of a system (given by the density matrix) can be written as a sum of the x, y and z components of angular momentum ($\mathbf{I}_x, \mathbf{I}_y$ and $\mathbf{I}_z$). These values are analogous to the x, y and z components of the magnetization vector (M_x, M_y, M_z). The outcome of a magnetic resonance pulse sequence can be calculated by starting with the equilibrium density matrix (which is often truncated at the linear, $\mathbf{I}_z$ term – this approximation is called the high temperature approximation as mentioned above) and working through the different elements of the pulse sequence.

The time dependent density matrix, $\rho(t)$, at time t is found by starting from the initial density matrix, $\rho(0)$, and calculating the effects of the pulse sequence on this initial density matrix:

$$\rho(t) = e^{iHt}\rho(0)e^{-iHt} \tag{25}$$

where H is the Hamiltonian describing the perturbations to the system. For a simple pulse sequence (for example, a x-pulse (of length t_p and amplitude ω_1), followed by an evolution time, τ) of a simple sample (one spin ½), the density matrix at time t is given by:

$$\rho(t) = e^{i\omega_0\tau\mathbf{I}_z} e^{i\omega_1 t_p \mathbf{I}_x} \mathbf{I}_z e^{-i\omega_1 t_p \mathbf{I}_x} e^{-i\omega_0\tau\mathbf{I}_z} \tag{26}$$

As the pulse sequence (and the sample) gets more complex, the expression for the time dependent density matrix gets longer and more complex. A shorthand has been developed which describes the same effects but is easier to handle.

In this shorthand, called the product operator formalism, an arrow (with the appropriate Hamiltonian written over it) connects the old and new density operators. For example, the effect of the same x- pulse is written:

$$\mathbf{I}_z \xrightarrow{\omega_1 t_p \mathbf{I}_x} \cos(\omega_1 t_p)\,\mathbf{I}_z + \sin(\omega_1 t_p)\,\mathbf{I}_y \tag{27}$$

This shorthand will be used extensively in later chapters to describe the effects of new pulse sequences and how novel contrast can be obtained using the inherent physics of the system.

1.3 Phase Cycling

Phase cycling is a method for coherence selection in which the phases of the pulses in the pulse sequence and the phase of the receiver are changed to select a desired coherence order. Coherence order (represented by the letter, p) can take on any integer

value (e.g. +2, +1, 0, -1, -2…), and represents the phase shift that a particular coherence experiences when undergoing a z-axis rotation[5]. A coherence of order p experiences the following phase shift under the influence of a z- rotation:

$$e^{i\phi \mathbf{I}_z}\rho_p e^{i\phi \mathbf{I}_z} = e^{-i*p*\phi}\rho_p \tag{28}$$

If this was a zero quantum coherence (p = 0), the coherence would experience no phase shift, if it were a double quantum coherence (p = 2), the coherence would experience a phase shift of 2ϕ.

A phase cycle is a series of averages in which the phases of the pulses and receiver are designed such that only the desired coherence order survives, while undesired coherence orders are suppressed. Phase shifting the RF pulses in a sequence is done by phase shifting the output from the frequency synthesizer used to create the pulse. An example of a phase shifted RF pulse is a 90_x pulse, which takes z-magnetization and rotates it to the –y axis. Or, in product operator notation, it takes $\mathbf{I}_z$ to $\mathbf{I}_{-y}$.

The concept of receiver phase is more complicated. The detected signal is an oscillating RF field at or near the Larmor frequency. The electronics of the spectrometer downshift the signal in order to digitize it. This is done by subtracting a reference (or carrier) frequency from the observed signal. Often, the reference frequency is the same as the transmitter frequency. This creates a signal

of the form $\cos(\Omega t)$, where $\Omega = \omega_{ref} - \omega_0$. Since $\cos(-\omega) = \cos(\omega)$ this means that the spectrometer cannot differentiate between positive and negative offsets relative to the reference frequency. To solve this problem, the signal can be detected on two perpendicular axes, and the projection along one axis is proportional to $\cos(\Omega t)$ and $\sin(\Omega t)$ along the other axis, creating a total detected signal proportional to:

$$\cos(\Omega t) + i\sin(\Omega t) = e^{i\Omega t} \tag{29}$$

It is assumed that at t = 0, the magnetization is aligned along a chosen axis. By shifting the phase of the reference frequency by ϕ, the final detected component is proportional to $e^{i\Omega t}e^{-i\phi}$.

Controlling the phase of a sequence can be done by applying different combinations of gradients and pulses, and by changing the phase shift of the receiver. The total phase shift of the detected signal is given by multiplying the phase shift created by the sequence and by the phase shift of the receiver:

$$e^{i\Omega t}e^{\phi_{sig}}e^{-i\phi_{rx}} \tag{30}$$

Where ϕ_{sig} is the phase shift created by the pulse sequence and ϕ_{rx} is the phase shift of the receiver. Thus the final signal is the difference in the phase introduced by the pulse sequence and the phase of the receiver[3].

To design a phase cycling sequence, first identify the desired coherence pathway. Then, write down the number of averages used and the pulses which are cycled. The phase shift introduced by the pulses is the phase of the pulse multiplied by the coherence order. The receiver phase is matched to the net phase shift, causing the signal to constructively add. An example of a phase cycling table for a sequence with one pulse, selecting for a coherence order of p = 2 (double quantum coherence) is given in table 1.

Table 1 – Example of a phase cycling table selecting for p = 2. Note that the phase is always modulo 360, so the final column (coherence shift) is technically 0, 180, 360, 540, but it is written 0, 180, 0, 180.

Step number	Pulse Phase	Coherence shift
1	0	0
2	90	180
3	180	0
4	270	180

In order to select for this coherence, the receiver cycles between 0 and 180°. An additional shorthand often used is to represent the phases by 0, 1, 2, 3 instead of writing them in degrees, where each change in integer represents a 90° phase shift.

This same phase cycling scheme does not select for coherences of different orders, such as single quantum (p = 1) or zero quantum (p = 0). This phase cycling applied to these two coherences is given in Table 2.

Table 2 - Phase cycling table for the same pulse sequence, but calculating the effect of this phase cycle on zero quantum (p = 0) and single quantum (p = 1) coherences.

Step Number	Pulse Phase	Coherence Shift (p = 0)	Coherence Shift (p = 1)
1	0	0	0
2	1	0	1
3	2	0	2
4	3	0	3

This table demonstrates that through phase cycling, undesired coherences are not selected, allowing for detection of only the desired coherence order. For more complicated pulse sequences, additional phase cycling can be added which can select for a desired coherence pathway.

The next chapter will introduce the concept of intermolecular multiple quantum coherences (iMQCs). Chapter 3 will cover the basics of dynamic nuclear polarization and the Hypersense technology. Chapter 4 will cover applications of iMQCs to temperature imaging in fatty tissue. Chapter 5 will discuss the translation of the temperature imaging pulse sequences from a

Bruker research console to a clinical console for the application of temperature imaging in humans. Chapter 6 will provide a discussion of iMQCs between two carbons, and Chapter 7 will discuss iMQCs between a carbon and a proton. Chapter 8 discusses the extension of hyperpolarized lifetimes through storage of populations in a protected eigenstate (singlet state) and Chapter 9 will provide details on the simulations and calculations of the properties of the singlet state. Chapter 10 will describe a new type of multiple spin echo pulse sequence which reduces the effects of dephasing, creating new contrast and longer T_2 for tissue. The final chapter of the thesis will discuss future directions for signal enhancement using the techniques described in this thesis.

Chapter 2 - **Introduction to Intermolecular Multiple Quantum Coherences**

Intermolecular multiple quantum coherences (iMQCs) are a type of magnetic resonance signal that comes from the simultaneous transition of two spins on separate molecules [6-22]. The distance between the two molecules is tunable, but in common applications is about 100 μm. The two most common types of iMQCs are intermolecular zero quantum coherences (iZQCs) and intermolecular double quantum coherences (iDQCs). This chapter describes the physics that create iMQCs and defines the unique properties of these coherences. First, we will discuss the assumptions made in magnetic resonance theory that ruled that iMQCs were undetectable and the experimental conditions under which these assumptions break down. Then we will discuss the effects of iMQCs and their applications in both imaging and spectroscopy.

2.1 The Theory of iMQCs

In the early 1990s, the underlying framework of magnetic resonance was challenged by a series of simple pulse sequences that provided unusual and unexpected results [23]. The prevailing wisdom at that time was that the theory of magnetic resonance was so well understood that if a result disagreed with the

theoretical predictions, then the experiment, not the theory, was at fault. In the experiments, two 90° pulses and a gradient were applied to very simple samples (such as water, or chloroform and benzene), and these experiments resulted in signal appearing where the theory predicted no signal should exist. Even stranger, that signal had many unique characteristics which led some researchers [9, 22] to question the underlying theory.

Two explanations (both correct) were put forward to describe the unexpected effects of this signal (which we now know as iMQCs). The first was a classical description of the effect and used the framework of a "dipolar demagnetizing field" [9] to describe the unusual signal. The second description used a quantum mechanical framework to describe the effects [19, 24]. While both explanations are correct, the quantum mechanical one provides the most predictive power and will be the description provided in this dissertation. Two reviews of iMQCs also go in depth about the quantum mechanical description and experimental effects of iMQCs [10, 15].

Two (usually valid) assumptions that are often made in magnetic resonance are challenged when considering iMQCs. The first assumption involves the definition of the density matrix of the system, while the second involves the effect of the dipolar interaction between spins. For the majority of

experiments, these assumptions are valid, and the predicted result is the same as the experimental result. However, when a gradient pulse is introduced or the sample geometry is far from spherical, these assumptions have to be revisited (as in the case of iMQCs).

2.1.1 The High Temperature Approximation

To understand the first assumption that was revisited with the discovery of iMQCs, we must recall the definition of the equilibrium density matrix (ρ_{eq}). At thermal equilibrium, the populations of the energy states obey the Boltzmann distribution, as given by the equilibrium density matrix. The exact expression for the density matrix of *N* identical spins under a Zeeman Hamiltonian is given in equation (21). From chapter 1, this expression can be made clearer and more easily manipulated by expanding the exponentials as sums of hyperbolic functions. At room temperature, the density matrix expansion is similar to the normalized Taylor expansion of the exponential (22):

$$\rho_{eq} = 2^{-N}\left\{\mathbf{E} + \left(\frac{-\hbar\omega_0}{2kT}\right)\sum_{i}^{N}\mathbf{I}_{zi} + \left(\frac{-\hbar\omega_0}{2kT}\right)^2\sum_{i,j}^{N^2}\mathbf{I}_{zi}\mathbf{I}_{zj} + \left(\frac{-\hbar\omega_0}{2kT}\right)^3\sum_{i,j,k}^{N^3}\mathbf{I}_{zi}\mathbf{I}_{zj}\mathbf{I}_{zk} + ...\right\}$$

(31)

Since $\frac{\hbar\omega_0}{2kT}$ is a very small number (10^{-4}) at room temperature, coefficients of $\left(\frac{\hbar\omega_0}{2kT}\right)^2$ and $\left(\frac{\hbar\omega_0}{2kT}\right)^3$ might be expected to render the later terms negligible. However, the third and higher order terms grow exponentially with the number of spins, N. It is from these higher-order terms in the density matrix that iMQCs derive their signal.

2.1.2 Dipolar Couplings

Each spin in a sample in an NMR experiment can be thought of as a tiny bar magnet (or dipole). This tiny bar magnet creates a small field that interacts with the fields created by the other spins in the sample. For a dipole in the field of another dipole, the shift in the energy gap between the energy levels can be approximated:

$$D_{ij} = \frac{\mu_0 \gamma_i \gamma_j \hbar}{16\pi r_{ij}^3} \left(1 - 3\cos^2\theta_{ij}\right) \left(3\mathbf{I}_{z1}\mathbf{I}_{z2} - \mathbf{I}_1 \bullet \mathbf{I}_2\right)$$

$$D_{ij} = \left(-188.7\frac{rad}{s}\right) \left(\frac{1 - 3\cos^2\theta_{ij}}{r^3}\right) \left(3\mathbf{I}_{z1}\mathbf{I}_{z2} - \mathbf{I}_1 \bullet \mathbf{I}_2\right) \tag{32}$$

where θ is the angle between the vector connecting the two spins and the main magnetic field, and r is the distance separating the spins in nm. The shift in the energy gap between the energy levels created by the interactions of the dipolar fields is approximately 1 kHz, and if we expand our thinking to the interactions of all the spins in the sample with each other, then the magnitude and direction

of this shift will vary dramatically across the sample. This creates very broad lines and is the precise situation found in solid-state NMR.

Yet, in liquids the lines are very narrow and sharp (in a well shimmed NMR, linewidths can be below 1 Hz). This is a fortunate situation because it enables us to detect small changes in resonance frequency due to perturbations from J coupling and chemical shift differences. The sharp lines in NMR can be explained by analyzing three different cases.

1) Short range diffusion: Short range dipolar couplings average to zero over the timescale of a magnetic resonance experiment. Considering two spins separated by a short distance (e.g., 0.2 nm), the interaction between these two spins is not constant over the course of a NMR experiment due to the diffusion of the spins. The diffusion is sufficient to cause the orientation of the interaction between the spins to sample a spherical geometry, causing the net effect of the dipolar action to average to zero[15].
2) Long range diffusion: Long range dipolar couplings average to zero because of magnetic isotropy. Considering two spins separated in a sample over a long distance (relative to the distance they would diffuse), we can see that the interaction between those spins stays constant, and this individual dipolar coupling cannot be ignored. Because of the spherical symmetry of the sample, however, there is an identical coupling of the opposite sign that causes the average dipolar coupling over the sample to be zero.
3) Tumbling: The effects of dipolar couplings on connected spins (i.e., spins on the same molecule that are connected by chemical bonds) are significant, but the dipolar effects sum to zero because of tumbling. Spins on the same molecule do not diffuse around each other, but the molecule as a whole tumbles, and the internuclear vector changes direction with the

tumbling. During the course of a standard NMR experiment, the molecule tumbles thousands of times causing the direction of the internuclear vector to assume almost every possible orientation and causing $(1-3\cos^2(\theta))$ to average to zero.

The only situations in which dipolar couplings need to be considered are ones in which the magnetic isotropy of the system is broken (such as when gradient pulses are applied) or when the symmetry of the sample is no longer spherical. In most cases where the sample is not spherical, the effects of dipolar couplings are masked by larger effects and can be ignored. In an iMQC experiment, the dipolar field is broken by the application of a gradient pulse, causing the effects of the dipolar couplings to be reintroduced.

The signal in iMQC experiments generally arises from the two-spin terms (or higher-order terms if the magnetization is sufficiently large), which are rotated by RF pulses. To become observable, some rotated version of these operators (such as $\mathbf{I}_1^+\mathbf{I}_{2z}$) must be converted into one-spin operators, and this is possible because of the dipolar couplings. To understand how the dipolar coupling transforms the latter terms in the equilibrium density matrix into observable signals, consider the expression for the dipolar Hamiltonian. The dipolar Hamiltonian is given by:

$$H_d = \frac{\mu_0}{4\pi} \sum_{i,j} \frac{\gamma_i \gamma_j \hbar}{r_{ij}^3} \left(\mathbf{I}_i \mathbf{I}_j - 3 \frac{(\mathbf{I}_i \bullet \mathbf{r}_{ij})(\mathbf{I}_j \bullet \mathbf{r}_{ij})}{r_{ij}^2} \right) \tag{33}$$

where γ_i and γ_j are the gyromagnetic ratios of the respective nuclei. If this equation is rewritten in polar coordinates, and the nonsecular terms are removed because they vanish due to the Zeeman interaction, the remaining dipolar Hamiltonian is

$$\begin{aligned} H_d &= \frac{\mu_0}{4\pi} \sum_{i=0}^{N} \sum_{j=0}^{N} \frac{\gamma_i \gamma_j \hbar}{4 r_{ij}^3} \left(1 - 3\cos^2\theta_{ij}\right) \left(3\mathbf{I}_{iz}\mathbf{I}_{jz} - \mathbf{I}_i \bullet \mathbf{I}_j\right) \\ &= \sum_{i=0}^{N} \sum_{j=0}^{N} D_{ij} \left(1 - 3\cos^2\theta_{ij}\right) \left(3\mathbf{I}_{iz}\mathbf{I}_{jz} - \mathbf{I}_i \bullet \mathbf{I}_j\right) \\ D_{ij} &= \frac{\mu_0}{4\pi} \frac{\gamma_i \gamma_j \hbar}{4\pi r_{ij}^3} \left(1 - 3\cos^2\theta_{ij}\right) \end{aligned} \tag{34}$$

where θ_{ij} is the angle between the internuclear vector and the main magnetic field. We have also defined the dipolar coupling constant, D_{ij}. The only part of the dipolar Hamiltonian that matters here is the longitudinal part, so evolution under the dipolar Hamiltonian converts unobservable two-spin magnetization into observable signal:

$$\begin{aligned} \mathbf{I}_{iz}\mathbf{I}_j^+ &\xrightarrow{D_{ij}\mathbf{I}_{iz}\mathbf{I}_{jz}} \mathbf{I}_{iz}\mathbf{I}_j^+ \cos D_{ij}t + i\mathbf{I}_j^+ \sin D_{ij}t \\ \mathbf{I}_{iz}\mathbf{I}_j^- &\xrightarrow{D_{ij}\mathbf{I}_{iz}\mathbf{I}_{jz}} \mathbf{I}_{iz}\mathbf{I}_j^- \cos D_{ij}t - i\mathbf{I}_j^- \sin D_{ij}t \end{aligned} \tag{35}$$

2.2 Standard iMQC Experiment

The basic iMQC experiment is known as the CRAZED (COSY Revamped by Asymmetric Z-Gradient Echo Detection) [23] sequence. The CRAZED pulse sequence is shown in Figure 2-1a.

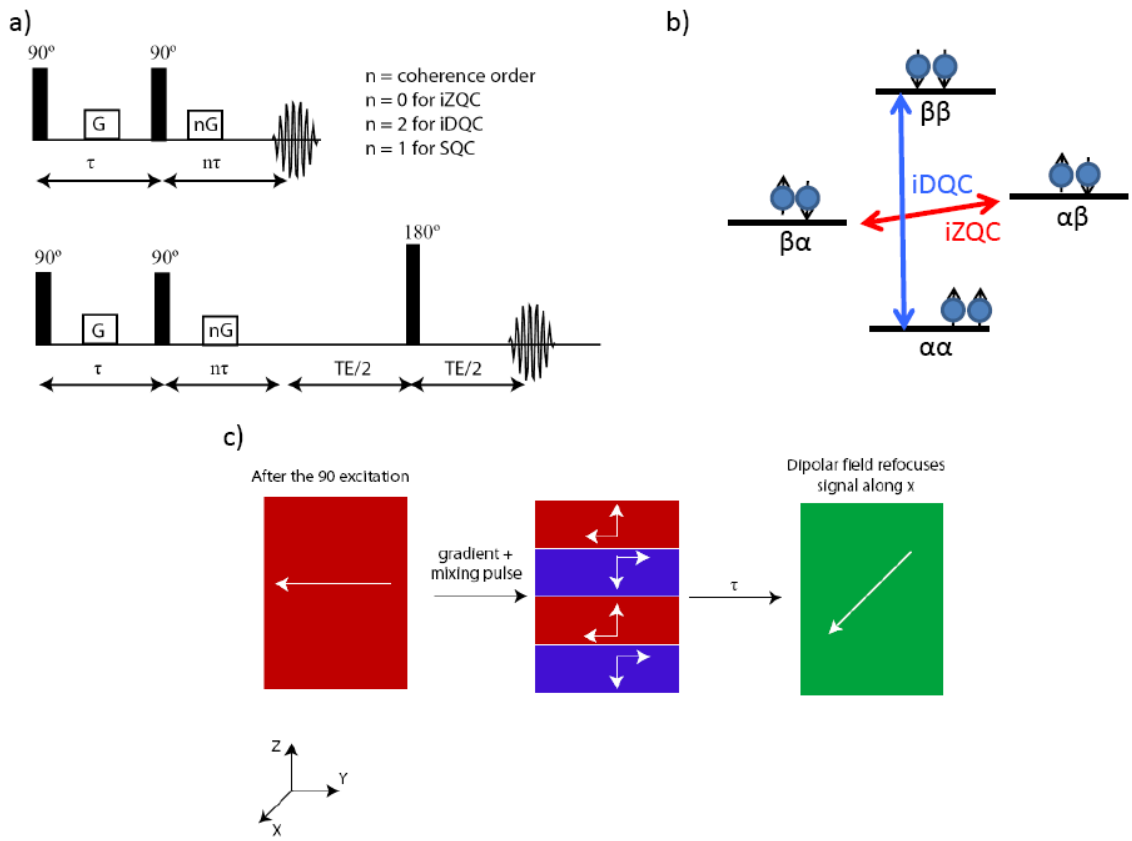

Figure 2-1 A. The CRAZED pulse sequence. The top sequence is the classic sequence, but it suffers from T_2^* weighting. The insertion of a refocusing pulse (below) reduces the effect of T_2^* relaxation. B. Energy level diagram showing the DQC and ZQC transitions for a 2 spin system. C. Pictoral description of the effect of the gradients and dipolar coupling. The gradients break the isotropy of the magnetic field, and reintroduce dipolar couplings. The dipolar couplings convert the unobservable 2-spin coherences into observable 1-spin coherences.

Let us assume that we have two coupled spins 1 and 2. The CRAZED experiment starts with a 90° pulse, which creates both the standard $\mathbf{I}_{x1}$ and $\mathbf{I}_{x2}$ terms (referred to as single quantum coherences, or SQCs), as well as the multiple quantum coherences such as $\mathbf{I}_1^+\mathbf{I}_2^+$ (DQCs) and $\mathbf{I}_1^+\mathbf{I}_2^-$ (ZQCs). These terms evolve for time τ and acquire a phase shift characteristic of the coherence.

$$\begin{aligned}
\mathbf{I}_1^+\mathbf{I}_2^+ &\xrightarrow{\tau} \mathbf{I}_1^+\mathbf{I}_2^+ e^{-i(\omega_1+\omega_2)\tau}(DQC) \\
\mathbf{I}_1^+\mathbf{I}_2^- &\xrightarrow{\tau} \mathbf{I}_1^+\mathbf{I}_2^- e^{-i(\omega_1-\omega_2)\tau}(ZQC) \\
\mathbf{I}_1^+ &\xrightarrow{\tau} \mathbf{I}_1^+ e^{-i(\omega_1)\tau}(SQC) \\
\mathbf{I}_2^+ &\xrightarrow{\tau} \mathbf{I}_2^+ e^{-i(\omega_2)\tau}(SQC)
\end{aligned} \tag{36}$$

The DQC terms evolve at the sum of the resonance frequencies, while the ZQCs evolve at the difference of the resonance frequencies. Then, the first gradient (area *GT*) is applied. This gradient works in two ways. First, it serves as a coherence selection gradient, since each coherence experiences a different effective gradient. Second, it disrupts the magnetic isotropy of the sample, causing the dipolar field to not average to zero.

$$\begin{aligned}
\mathbf{I}_1^+\mathbf{I}_2^+ e^{-i(\omega_1+\omega_2)\tau} &\xrightarrow{Gt} \mathbf{I}_1^+\mathbf{I}_2^+ e^{-i((\omega_1+\omega_2)\tau+2\gamma Gt)}(DQC) \\
\mathbf{I}_1^+\mathbf{I}_2^- e^{-i(\omega_1-\omega_2)\tau} &\xrightarrow{Gt} \mathbf{I}_1^+\mathbf{I}_2^- e^{-i((\omega_1-\omega_2)\tau+0\gamma Gt)}(ZQC) \\
\mathbf{I}_1^+ e^{-i(\omega_1)\tau} &\xrightarrow{Gt} \mathbf{I}_1^+ e^{-i((\omega_1)\tau+\gamma Gt)}(SQC) \\
\mathbf{I}_2^+ e^{-i(\omega_2)\tau} &\xrightarrow{Gt} \mathbf{I}_2^+ e^{-i((\omega_2)\tau-\gamma Gt)}(SQC)
\end{aligned} \tag{37}$$

The effect of the dipolar couplings will be considered after the mixing pulse and the gradients. The 90° mixing pulse rotates some of the dephased magnetization

along the z-axis, creating 2-spin, single quantum terms such as $\mathbf{I}_{z1}\mathbf{I}_2^+$. Subsequently, the dipolar couplings can convert these terms into observable single quantum magnetization such as $\mathbf{I}_2^+$.

$$\begin{aligned}
\mathbf{I}_2^+ e^{-i((\omega_1+\omega_2)\tau+2\gamma Gt)} &\xrightarrow{\pi/2} \mathbf{I}_{z1}\mathbf{I}_2^+ e^{-i((\omega_1+\omega_2)\tau+2\gamma Gt)} + \mathbf{I}_1^+\mathbf{I}_{z2} e^{-i((\omega_1+\omega_2)\tau+2\gamma Gt)} (DQC) \\
\mathbf{I}_1^+\mathbf{I}_2^- e^{-i((\omega_1-\omega_2)\tau+0\gamma Gt)} &\xrightarrow{Gt} \mathbf{I}_{z1}\mathbf{I}_2^- e^{-i(\omega_1-\omega_2)\tau} + \mathbf{I}_1^+\mathbf{I}_{z2} e^{-i(\omega_1-\omega_2)\tau} (ZQC) \\
\mathbf{I}_1^+ e^{-i((\omega_1)\tau+\gamma Gt)} &\xrightarrow{Gt} \mathbf{I}_1^- e^{-i((\omega_1)\tau+\gamma Gt)} (SQC) \\
\mathbf{I}_2^- e^{-i((\omega_2)\tau+\gamma Gt)} &\xrightarrow{Gt} \mathbf{I}_2^+ e^{-i((\omega_2)\tau-\gamma Gt)} (SQC)
\end{aligned} \tag{38}$$

The following gradient and τ evolution time rephase the coherences depending on the coherence order. To select the +2 quantum coherence (DQC), the second gradient is of area $+2GT$ and the second time is 2τ. To select a 0-quantum coherence (ZQC), there is no second gradient or refocusing time. Finally, choosing a gradient of $1GT$ and a timing of τ would simply select the SQC signal.

2.2.1 Description of the CRAZED sequence

Double quantum and zero quantum coherences can be visualized by drawing the energy level diagram for a 2-spin system (figure 1b). Double quantum coherences correspond to simultaneous transitions of both spins in the same direction (a flip-flip transition or up-up to down-down). The net change in angular momentum is 2 (instead of 1 for a standard transition). A zero quantum coherence is the simultaneous transition of two spins in opposite directions (a

flip-flop transition, or up-down to down-up). The net change in angular momentum is 0.

The energy (or frequency) for any transition is given by the difference in the energy levels; thus, the frequency for a double quantum transition is the energy difference between the upper energy level and the lower energy level (E_4-E_1). The energy of the uppermost level is given by $E_4 = - ½ \omega_1 - ½ \omega_2$, and the lower energy level is $E_1 = ½ \omega_1 + ½ \omega_2$. The energy of the transition therefore comes at the sum of the two frequencies. Since a zero quantum transition is a transition between energy levels E_2 and E_3, the energy of that transition is $E_2 - E_3 = \omega_1 - \omega_2$.

The effect of the gradients is slightly more complex because it acts on the system in two ways. First, it works as a coherence selection gradient. When the gradient is applied to the system, it creates a distribution of resonance frequencies depending on spatial position. This changes the effective magnetic field at different locations and causes the energy levels to shift depending on the spatial position of the spins. Since a double quantum transition occurs when both spins flip in the same direction, the effect of the gradient is doubled because it contributes to the resonance frequency once for each spin. For a zero quantum coherence, the spins flip in opposite directions and the effect of the gradient is canceled.

In addition, the gradient breaks the magnetic isotropy of the sample. When combined with the mixing pulse, the gradient introduces the dipolar field to the sample and converts the unobservable multiple quantum terms into observable single quantum terms. A more visual explanation of how this works is given in Figure 2-1c. After the application of the 90° pulse, all the magnetization is pointed along one direction in the transverse plane. The gradient is applied, which winds the magnetization into a helix along the direction of the gradient. The second pulse tips some of that magnetization back along the z-axis. Depending on the phase of the magnetization vector before the second pulse, the z-component of the magnetization will be pointed either along +z or –z. The z-magnetization created by this second pulse exerts a force on the remaining magnetization in the transverse plane, causing it to refocus. The time required for the magnetization to refocus depends on the size of the magnetization that was tipped along the z axis, and this time is referred to as the "dipolar demagnetizing time". The concept of refocusing created by the gradient and the pulse provides a qualitative description of the behavior of the dipolar field and how it transforms the multiple quantum signal to observable signal.

Chapter 3 - **Hyperpolarization using Dynamic Nuclear Polarization**

In recent years, hyperpolarized carbon (and more broadly over the last 20 years, hyperpolarization techniques in general) has received significant attention and excitement in the magnetic resonance community.[25-58] Hyperpolarization is a general term that describes a system in which the distribution of populations is disturbed to create an excess of populations in one level, thus boosting the net magnetization of the system.

Magnetic resonance is inherently an insensitive technique, and in general, magnetic resonance imaging is limited to systems with a large bulk magnetization, such as that of water in tissue. Imaging of other nuclei is possible, but challenging. These shortcomings are the result of both the gyromagnetic ratio and natural abundance of the other nuclei. More specifically, protons have a relatively high gyromagnetic ratio (ca. 267.513 rad/s*T) compared to other nuclei. The gyromagnetic ratio controls the difference in the energy levels of the system, and the larger the energy difference, the larger the polarization because of the Boltzmann distribution. The polarization of a sample can be defined as the difference in populations between energy levels[59]:

$$P = \frac{N\uparrow - N\downarrow}{N\uparrow + N\downarrow} \tag{39}$$

The populations in each energy level are determined by the energy difference between the energy levels and are given by the Boltzmann distribution:

$$\frac{N\uparrow}{N\downarrow} = e^{-\Delta E/kT} \tag{40}$$

ΔE is the energy difference between the two states, k is the Boltzmann constant and T is the temperature in Kelvin. The magnitude of the observable magnetization is:

$$M_0 = \frac{1}{2} N_s \gamma \hbar P \tag{41}$$

With N_s equal to the number of spins in the sample. At thermal equilibrium, in the presence of an external magnetic field, B_0, the polarization is given by:

$$P = \tanh\left(\frac{\gamma \hbar B_0}{2kT}\right) \tag{42}$$

Since other nuclei such as carbon, nitrogen or phosphorus have smaller gyromagnetic ratios, they have smaller energy level differences and thus smaller net polarizations. While spectroscopic applications of nuclei other than proton using NMR are possible, imaging of the other nuclei (especially in vivo) is nearly impossible. An illustrative

example is given in Figure 3-1.

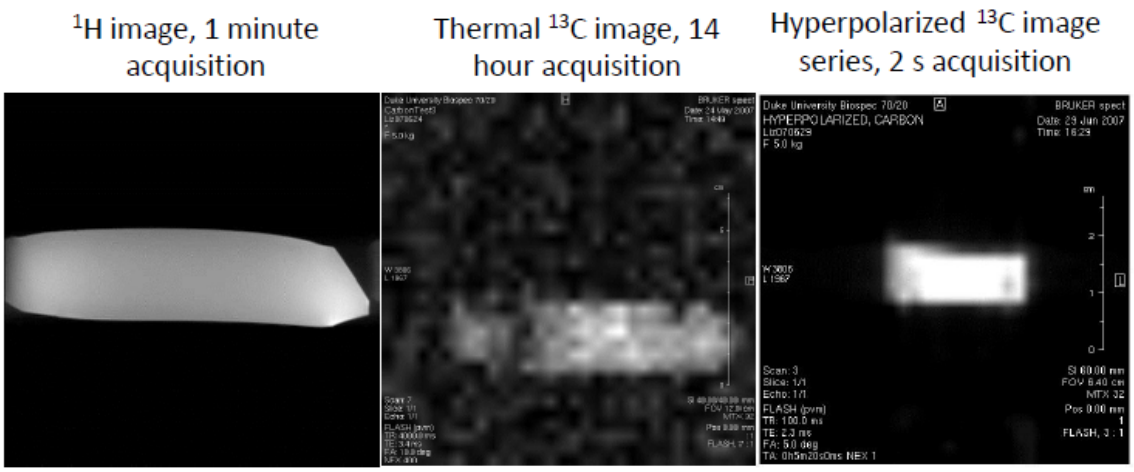

Figure 3-1 - Comparison of signal intensity of ^{1}H water (left), thermally polarized ^{13}C urea (middle) and hyperpolarized ^{13}C urea (right). The proton image was acquired using a FLASH sequence in less than 1 minute, while the thermally polarized carbon image required 14 hours of averaging in order to acquire enough signal to make an image. The hyperpolarized carbon image series (right) has sufficient signal to allow acquisition in 2s using a FLASH sequence. Note that the slice for the hyperpolarized image was acquired using a different slice orientation than the proton and thermally polarized carbon images.

In the carbon image in the middle, we have stacked the deck in our favor: the sample is a concentrated, ^{13}C labeled sample of urea. Since the natural abundance of ^{13}C is 1%, we have significantly increased our signal by labeling 98% of the carbons. Yet, under these conditions, it still took 14 hours to get an image, and the quality of the image is very low. Imaging smaller concentrations of non-proton nuclei, such as those in vivo, is nearly impossible.

The imaging of non-proton nuclei for different applications, such as mapping ventilation/perfusion in the lungs using Xe or He[60] , metabolic imaging with ^{13}C[25, 34,

36, 39, 50, 55], pH measurements[53], and enzyme flux measurements[47, 52], is only possible using hyperpolarized nuclei. There are several techniques for achieving hyperpolarization, including optical pumping for noble gases[59], para-hydrogen induced polarization[61], and dynamic nuclear polarization[62]. All work presented here was done using dynamic nuclear polarization.

Dynamic nuclear polarization (DNP) is a technique that has been well studied in the physics community since 1958[63]. Until recently, it was limited to systems such as coal, for use in high energy physics, and to study micro-ordering in the μK temperature regime[64]. Technical advances in the engineering of magnets and microwave sources have transformed DNP into a practical method for the creation of hyperpolarized samples[62].

3.1 Dynamic Nuclear Polarization

Dynamic nuclear polarization (DNP) has emerged as one of the most general methods for nuclear hyperpolarization, and the sample requirements with DNP are straightforward. The sample must have a source of free electrons (usually provided by a radical), a NMR active nucleus to be polarized and a glassy solvent system. The sample is cooled to between 1.2 K and 90 K (depending on the system; in our case, the sample is at 1.4K) and irradiated with microwaves that transfer the polarization from the electrons to the nucleus. A super-heated solvent system rapidly dissolves the frozen sample and ejects it from the system, thus allowing it to be used in the spectrometer.

The mechanism by which DNP proceeds depends on the type of system. There are two main mechanisms – the solid effect and thermal mixing (or cross effect). The dominant mechanism depends on the relative size of the ESR (electron spin resonance) linewidth and the nuclear Larmor frequency. If the ESR linewidth is greater than or equal to the NMR frequency and is homogeneously broadened, thermal mixing is the dominant mechanism. If the ESR linewidth is smaller than the NMR frequency, the solid effect is the dominant mechanism[63].

3.1.1 Solid Effect

The solid effect (Figure 3-2a) proceeds by a "forbidden" two-spin process, similar to that of a zero quantum or double quantum transition. Dipolar couplings mix the eigenstates of the system making these transitions allowed, and allowing for polarization to proceed via the solid effect. Assume a standard sample of nuclear spins, I, and electron spins, S. At low temperature (1.4 K), it is fair to assume that the electron spins are polarized with the magnetic field because they have a short relaxation rate and a large energy difference (GHz) compared to the nuclear spins. The nuclear spins are evenly distributed – approximately 50% are aligned with the magnetic field, and 50% are aligned against the field. Microwave energy at a particular frequency is applied, and depending on the frequency of the microwaves, the nuclear spins can either align with or against the magnetic field. If the microwaves are at a frequency $\omega_S + \omega_I$ (i.e., the sum of the electron Larmor frequency (ω_S) and the nuclear resonance frequency (ω_I)), then a

flip-flip transition is induced. In the case where the nuclei and the electron have the same orientation, this energy is absorbed, and both spins are flipped against the magnetic field. The electron then relaxes, and the coupled spin pair is left with the nuclear spin down and the electron spin up. If the spin pair starts with the nuclear spin down and electron spin up, none of the microwave energy is absorbed, and no transition occurs. In this case, all the nuclear spins become oriented against the magnetic field.

The reverse situation can also be considered. Assume we start with the nuclear spin pointed against the magnetic field and an electron spin polarized with the magnetic field, and we apply microwave energy at the difference frequency ($\omega_S - \omega_I$). This frequency will induce a flip-flop transition in which the nuclear spin will flip up and the electron spin will flip down. The electron recovers quickly leaving the final state of the spin pair as both spin up. If the pair starts out as both spins pointed up, none of the microwave energy is absorbed, and no transitions occur. Both of these processes are outlined in Figure 3-2b.

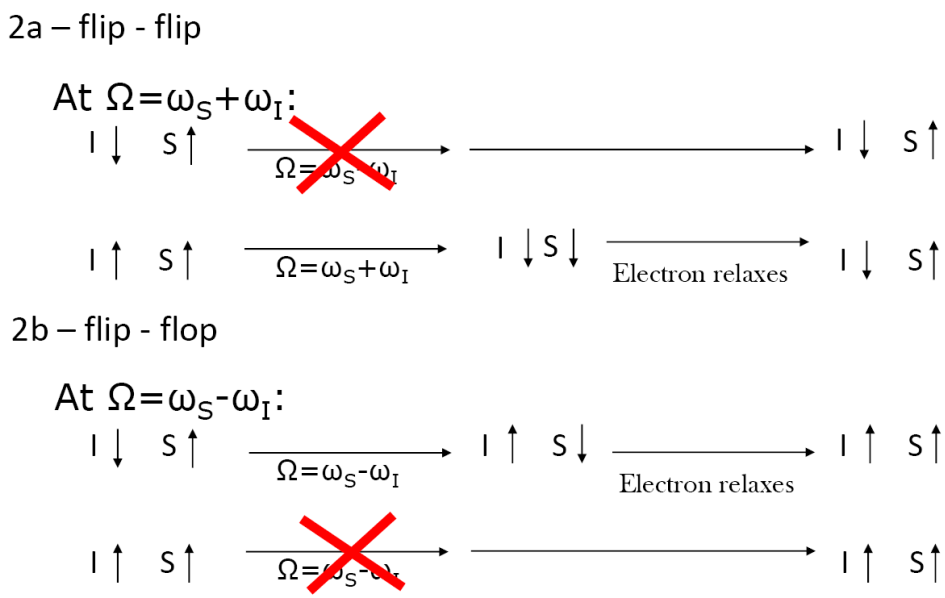

Figure 3-2 - Description of the solid effect. A – polarization at the sum of the electron and nuclear Larmor frequencies, resulting in an overpopulation of the upper energy level (spin down). B – polarization at the difference frequency of the nuclear and electron Larmor frequencies resulting in a polarization of the lower energy level (spin up).

3.1.2 Thermal Mixing

Spin temperature is a convenient concept for describing the mechanism of dynamic nuclear polarization. The basic concept of spin temperature is that a complex system of many interacting spins evolves toward a state of equilibrium that can be described by a temperature. In other words, the equilibrium density matrix can be re-written to include a temperature term:

$$\rho_{eq} = \frac{-\beta H}{tr\{e^{-\beta H}\}} \tag{43}$$

where H is the Hamiltonian of the system, $\beta = 1/kT_s$, and T_s is the spin temperature of the system. One advantage of this notation is that it can be used even when the Hamiltonian of the system is so complicated that it is impossible to calculate all the energy levels of the system (e.g., when the energy spectrum is quasi-continuous, such as in a solid at zero or low field where the spin-spin terms of the Hamiltonian dominate). To continue the description of the spin system using thermal terms, T_1 relaxation is an equalization of the spin temperature T_s and the lattice temperature T_L. If T_s is positive, then there are more populations in the lower energy levels, while if T_s is negative, there are more populations in the higher energy levels. Equivalently, an increase in $|\beta|$ is a decrease in $|T_s|$, which is the same as a reduction in entropy and can be described as "cooling" the system.

Thermal mixing can be explained by adopting a formalism that describes the electron-nucleus system as three connected baths representing the three different types of energy levels in the system. There is the electron Zeeman bath, the electron dipolar bath and the nuclear Zeeman bath, each of which is described by a separate spin temperature (Figure 3-3 from ref[64]).

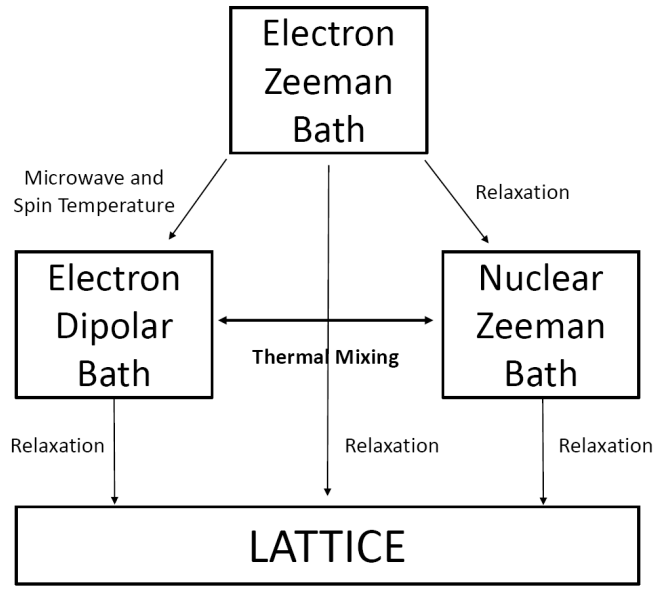

Figure 3-3 - Description of thermal mixing using spin temperature. Polarization proceeds via off-resonance irradiation near the electron Larmor frequency which cools the electron dipolar bath. The cooling of the electron dipolar bath causes the nuclear Zeeman bath to cool as well, transferring the polarization of the electron spins to the nuclear system.

Off-resonance irradiation near the electron Larmor frequency creates a polarization gradient in the EPR (electron paramagnetic resonance) line. This is equivalent to cooling the electron dipolar bath by pumping energy-conserving two-spin dipole-dipole transitions such as$\mathbf{I}^{+}\mathbf{I}^{-} \rightarrow \mathbf{I}^{-}\mathbf{I}^{+}$. Thermal contact between the electron dipolar bath and the nuclear Zeeman bath cools the nuclear bath by a three-spin electron-electron-nucleus transition. This drives the high polarization of the electron spins to the nuclear system, thus creating nuclear polarization.

The same process can be described using a three–spin energy level diagram (Figure 3-4). The thermal mixing phenomenon is often described as a three spin electron-electron-nucleus process. Assume you have two electron spins that are separated in frequency by the nuclear Larmor frequency. In this case, polarization occurs by a simple flip-flop-flip transition. Assume (as we did for solid mixing) that we have our nuclear spins 50% aligned with and 50% against the magnetic field. Assume the electron spins are polarized. Almost all the spins in the sample occupy the first two energy levels in figure 4. Because of the constraint that $\omega_{1e} - \omega_{2e} = \omega_n$, the middle energy levels are degenerate. If we apply microwave energy at the resonance frequency of electron 2, we pump transitions from $|\alpha\alpha\beta>$ to the middle energy level $|\alpha\beta\beta>$ (shown by the red arrow). The energy levels shown in the diagram are not perfect eigenstates of the system, and there is some mixing of the levels. Therefore, the transition being pumped by the microwave energy puts populations in both of the degenerate energy levels. Through the spin-lattice relaxation of the electrons (which is relatively fast), the populations in those levels decay down, as shown with the blue arrows. Decay from the $|\alpha\beta\beta>$ level goes to the initial level that was pumped $|\alpha\alpha\beta>$, and no net polarization is achieved. However, since the degenerate levels mix, some of the population is in the $|\alpha\beta\alpha>$ level, which decays to the $|\alpha\alpha\alpha>$ level, thus adding to the population there. As time progresses, the $|\alpha\alpha\beta>$ level is depleted, and population starts to gather in the $|\alpha\alpha\alpha>$ level, thus polarizing the nuclear spin system.

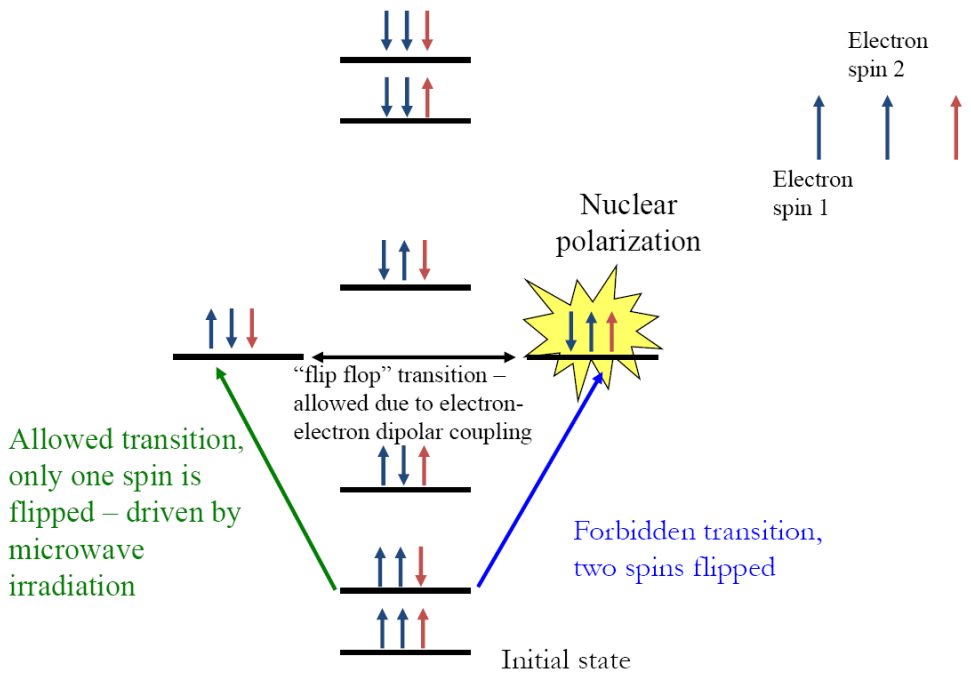

Figure 3-4 - Thermal mixing energy level diagram. Microwave irradiation drives transitions to the middle energy levels and electron relaxation returns the populations to the lowest two energy levels. Through mixing of the degenerate energy levels the nuclear populations slowly polarize.

3.2 NMR and MRI using hyperpolarized compounds

Any hyperpolarization technique creates a non-equilibrium distribution of populations that behaves differently than standard magnetization. First, since the population distribution is a non-equilibrium distribution, the system tries to return to equilibrium via T_1 relaxation. In a non-polarized sample, the initial magnetization is determined by the Boltzmann equilibrium constant and the population distribution is fixed. In hyperpolarized samples, the populations are attempting to return to the Boltzmann distribution and thus, the hyperpolarized signal decays with time at a rate of

$1/T_1$. This puts a constraint on any hyperpolarized experiment – the experiment must be completed before the signal decays (~5*T_1). In chapter 8, a technique will be described to store the hyperpolarized signal for longer than T_1. The second major consideration for a hyperpolarized experiments is the application of RF pulses, particularly concerning the flip angle applied. Since the hyperpolarized magnetization is non-equilibrium, after a 90° pulse, the signal will recover to thermal equilibrium as defined by the Boltzmann distribution, not to the high polarization achieved after DNP polarization. Thus, great care must be taken to ration the hyperpolarized magnetization to provide enough signal for the entire image (or dataset) acquisition. Third, if the hyperpolarized signal goes through a zero field in the magnetic field (most likely during transfer from the polarizer to the magnet), the polarization gets scrambled and lost. Thus, the path of the sample when it leaves the polarizer and enters the magnet must be carefully considered.

3.3 Technical Description of the Hypersense Instrument

The Hypersense is commercially available from Oxford Instruments and can provide DNP polarization. The Hypersense is a highly complex instrument, which requires routine checks and attention to detail.

3.3.1 Technical Specifications of the Hypersense

The Hypersense is built on a modified 3.35 T vertical bore Oxford magnet. It has a 94 GHz, 100 mW controllable power microwave source. Inside the bore of the magnet is a cryogenic chamber (VTI, variable temperature insert) that contains the sample

during the polarization process and is maintained at a temperature of 1.4K using a mixture of vacuum cooling and a liquid helium bath. The instrument control system is a PLC system controlled by the TwinCAT PLC control software.

3.3.2 Sample Formulation

To use the Hypersense, a sample is made from a labeled compound, a free radical and a glassing agent. The formulation of the sample is important and can drastically affect the amount of polarization achieved. One of the important characteristics is that the molecule of interest (i.e., the one to be polarized) and the radical have to be combined into a solution that forms a glass at low temperatures. The glass is important because it allows the radical to assume multiple orientations in the sample (thus providing a broad distribution of resonances on the ESR spectrum and allowing for thermal mixing) and because it allows the free electron on the radical to maintain contact with the nuclear spins. Since thermal mixing requires connection of the dipolar fields of the electrons and the nuclei, a good distribution of electrons and nuclei in the sample is crucial. One of the best molecules for polarization is pyruvic acid because the OX63 radical is soluble in the acid and it forms a glass without the need for any additional solvents.

The easiest way is discern whether the sample is forming a glassy solid is to make a mixture of the molecule with the solvent and then freeze beads of the mixture in liquid nitrogen. If the beads look transparent, then you likely have a good glass. If it

looks cloudy (not to be mistaken with frost on the surface), then it likely crystallizes and will not form a good glass. An example of an excellent glassy solvent system is a mixture of equal parts water and DMSO.

3.3.3 Hypersense Operation

To polarize the sample using DNP, the sample must be cooled to a temperature of 1.4 K. This is accomplished by placing the sample in a liquid helium bath under vacuum. The sample is then irradiated with microwaves of a particular frequency. A schematic of the inside of the Hypersense is shown below in Figure 3-5.

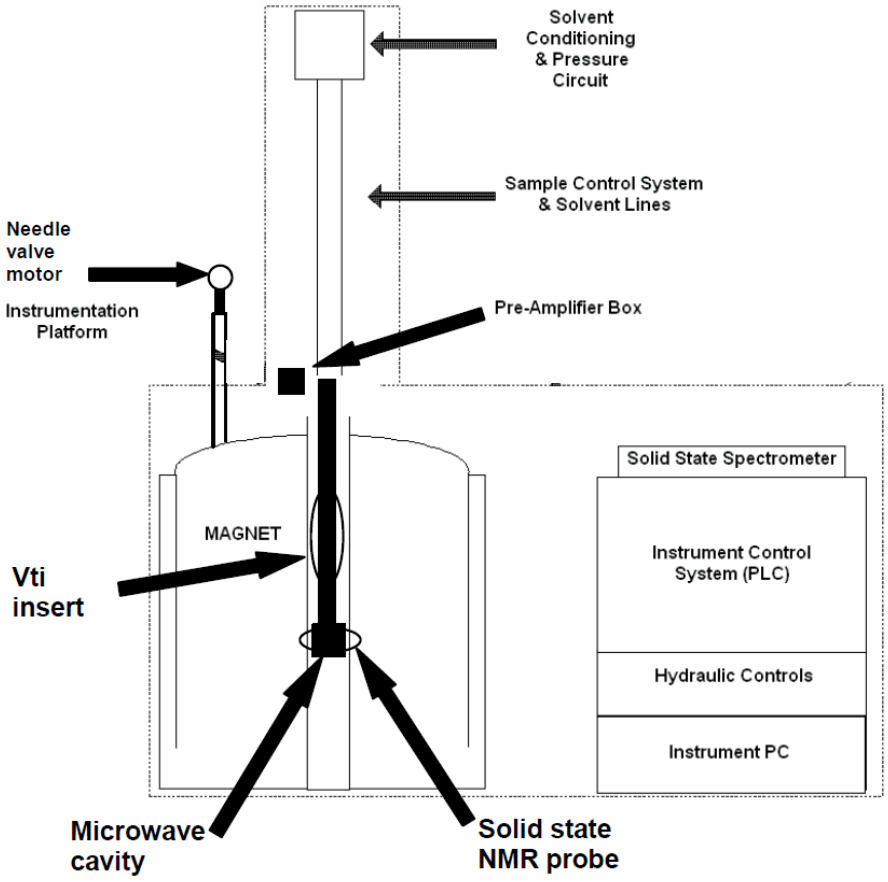

Figure 3-5 - Hypersense diagram. The Hypersense is based on a standard 3.35 T vertical bore magnet. Instead of the usual core for the NMR probe, the Hypersense has been altered to contain a polarizing chamber which receives helium from the helium can of the magnet, and a sample holder in which the sample is placed and irradiated by microwaves at 1.4 K. Once polarized, the dissolution stick drops into the sample holder and removes the sample from the helium bath and rapidly dissolves the sample from the Hypersense User's Manual).

The sample is placed in a sample cup, which is attached to the end of a sample insertion rod and is placed on the sample holder. The sample holder then lowers the sample into the helium bath.

The sample is positioned in the center of the magnet where it is irradiated by the microwave source at 1.4K. While the sample is polarizing, the polarization build-up is monitored using a series of low flip angle pulses, and the temperature is maintained at 1.4 K. The maintenance of the helium bath under vacuum is a challenge, and the Hypersense constantly balances the flow of helium into the sample chamber and the vacuum. The helium in the sample chamber comes from the helium can of the magnet.

The probe installed on the Hypersense is designed only to detect the signal from ^{13}C, although the system is capable of polarizing a wide range of nuclear spin types. Experience has shown that it is possible to detect the solid state polarization while polarizing other nuclei (such as ^{15}N), but this signal is weak. In this case, the signal detected is most likely that coming from the polarization of the natural abundance ^{13}C. To polarize nuclei other than ^{13}C, a reasonable estimate for the change in microwave

frequency is required; alternatively, special probes can be purchased from Oxford Instruments.

3.3.4 Calibration and Polarization Monitoring

During polarization it is possible to monitor the polarization buildup using the NMR coil located in the VTI as described above. Polarization rates and levels depend on the sample formulation. Some samples, such as neat pyruvic acid, form a glass on their own without any additional solvents. The buildup times for pyruvic acid usually range around 45 minutes to 1.5 hours. Efficient polarization also requires that the frequency of the microwave source be tuned to the specific compound being polarized. This calibration is done by slowly sweeping the microwave frequency to find the frequency that corresponds to the maximum buildup. An example of a microwave sweep curve is provided in Figure 3-6.

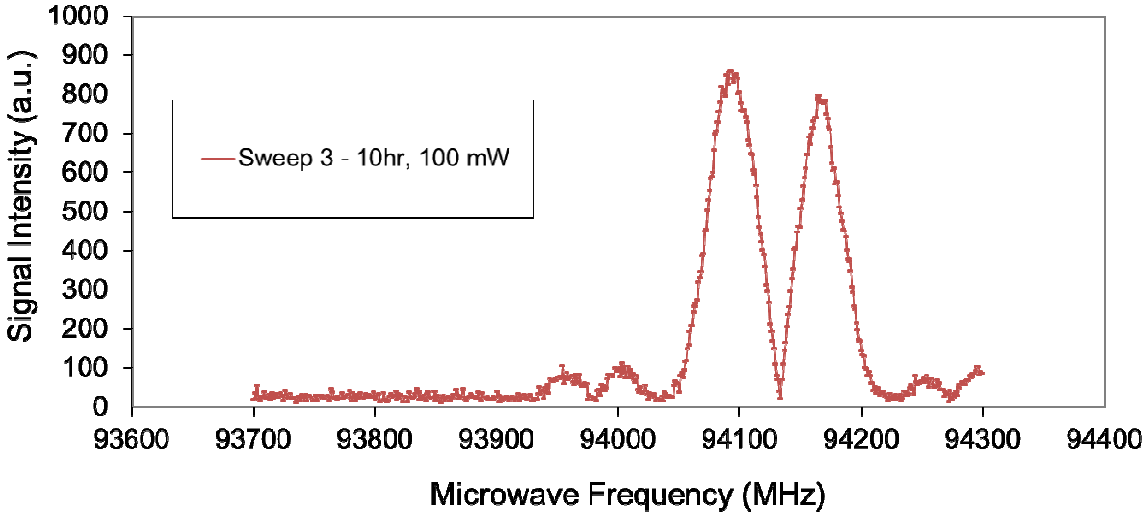

Figure 3-6 - Microwave sweep of pyruvate.

3.3.3 Common Hypersense Problems

3.3.3.1. Ice in the helium reservoir

The sample chamber is filled from the helium reservoir via a small capillary tube with a needle valve. This flow from the helium reservoir to the sample chamber presents some unique problems for the Hypersense. First, the vacuum that maintains the temperature inside the sample chamber also causes a vacuum in the helium reservoir. As a result, it is vitally important that all fittings to the outside environment are completely airtight, and the O-rings that make the seal need to be checked regularly. Any cracks or irregularities mean that the O-ring is no longer creating a good seal, which allows air to get in and create ice. The only way to clear ice from the helium reservoir is to warm the entire system to room temperature (which requires de-energizing the magnet) and pump and flush the system with pure helium gas.

3.3.3.2. Contamination of the VTI

To get the sample into the polarizing chamber where it is cooled to 1.4 K, the sample cup holding the sample is attached to the end of a specially designed stick, and is inserted into the Hypersense. It is important that the insertion process proceeds quickly because the polarizing chamber (or the VTI, variable temperature insert) is open to the environment during this process (and thus is taking in contamination). Any sample that is spilled will immediately freeze and create even more contamination. Contamination of the VTI is a concern for several reasons. As the contamination builds in the VTI, the

vacuum pump becomes less effective at reducing the pressure in the VTI, and thus, the temperature achieved during polarization increases. At a certain point (in our experience, around 1.52 K), the polarization efficiency diminishes significantly, and the system must be cleaned.

There is an automated routine, called a bakeout, for cleaning the system. The automated procedure heats the VTI to 300 K under vacuum and then flushes the system with UHP (ultra high purity) helium gas to wash out any contamination. The combination of the relatively high temperature (300 K) and low pressure (~0 mbar) causes any standard contamination to boil off. This pump-flush procedure is repeated many times over the course of 3 h. Occasionally, one bakeout is not sufficient to clean the system, especially if something has been spilled (or in very serious cases, if a dissolution occurred without a cup in the sample chamber, causing solvent to be sprayed into the VTI). In this case, repeating the bakeout several times (e.g., re-starting the bakeout every 3 hours for 24 hours) will clean the system effectively. Because the bakeout procedure involves heating the VTI (which is close to the magnet), helium will boil off at a much faster rate. It is important to note the amount of helium in the reservoir before starting the bakeout, and bakeouts should only be performed when there is adequate helium. In our system, there is usually a loss of 6% helium over the course of a 3 hour bakeout.

3.3.3.3. Contamination of the Capillary Tube

Occasionally, the contamination can move to the small capillary tube that feeds the liquid helium from the helium reservoir to the VTI. If this happens the throughput of helium into the VTI (i.e., the rate at which the helium fills the VTI) is reduced and may become nonexistent. An early symptom of contamination in the capillary tube is reduced pressure during the filling period. When the Hypersense begins filling the VTI, the needle valve opens to 100%, as does the butterfly valve (to provide a vacuum on the system). For the first few minutes, only gas comes through the capillary because the VTI is too warm for liquid helium. At this point, if the capillary is unblocked, the pressure should be > 50 mbar. As the VTI cools, liquid begins to flow, and once the liquid starts to flow, the pressure will drop to 30-50 mbar. At this point, the liquid helium gauge on the VTI will begin to register the liquid. If there is a block in the capillary tube, these numbers will drop significantly.

Often the contamination of the capillary tube can be cleared by heating the VTI and the needle valve (both have small heaters that can be controlled by the software) while under vacuum. It is important to watch the temperature on both heaters, and they should be turned off before they get above 300 K. The heating combined with the vacuum can clear the block after several hours.

3.3.3.4. Slipping Needle Valve Motor

Occasionally, the motor that drives the needle valve slips and does not properly open or close the needle valve. If the system is having no throughput from the helium can to the VTI, a slipping needle valve motor is the most common cause and can be easily identified. When the needle valve is set to open or close, watch it closely and see if the motor is actually turning the needle valve (which is controlled by the silver metal post, upon which the motor is mounted). If the needle valve is not opening, there are two hex screws on the sides of the gray foam attachment between the motor and the post that can be tightened.

3.3.3.5. VTI Level Miscalibration

The level sensor in the VTI measures the amount of liquid helium present in the VTI. This is important because the sample must be covered by liquid helium to cool properly, and an overfull VTI can result in large pressure spikes when the sample is inserted or removed (causing the system alarm to trip). Occasionally, contamination can get into the VTI level sensor, causing it to misread the volume of liquid or even short out. In the former case, an easy way to tell if this is happening is to watch the level in the VTI as it begins to fill. The level meter only switches on when the temperature gets below 4 K, and once it switches on, it may read an unlikely number. For example, if the system has been idle for a week (so there is no chance there is liquid still in the chamber) and is then put into cool-down (causing the filling procedure to begin), if the level

sensor switches on and reads 20% (or a negative number, such as -15%), it is clearly miscalibrated.

First, the system must be baked out to remove any contamination that might be causing a miscalibration. To calibrate the level meter, all the helium in the VTI must be baked off. The level check script in ScopeView should then be started. The system should be put into cool-down to start the VTI filling, which can be watched via the curve collected in ScopeView. At first, there will be an adjustment in the level of the line as the system cools. As it starts to fill, the line will gently slope up. The new zero point is the flat part of the line right before it begins to slope up. At this point, the cool-down can be stopped and the settings adjusted for the level meter on the HMI Hypersense software. The 0% and 100% marks are linearly related; therefore, a change in the zero point by +0.02 V will result in a change by +0.02 V for the 100% mark.

If the level meter is shorting out, this will also be obvious. In this case, when the system goes into cool-down and switches on the level meter, the level meter will send a "very full" message to the computer, causing it to trip the alarm. The system can be baked out several times to remove the contamination. If that does not resolve the problem, then one of the wires connected to the level meter must be broken, and the whole VTI insert needs to be removed by one of the Oxford service engineers.

3.3.3.6. Lost Cups

Cups can be lost in the instrument for several reasons, but if cups start to go missing, the only way to recover them is by removing the VTI, which should be done only by the Oxford service engineers.

There is an easy way to tell is a cup is missing. If you start the polarization and get no signal, then either the sample is bad or the cup is not in the polarization chamber. In this case, do not run a dissolution because if the cup has gone missing, the dissolution will simply spray solvent into the VTI. Instead, the cup can be retrieved (click 'abort' on the software). If no cup is retrieved, then it is lost, and you should contact Oxford Instruments.

DNP is a versatile technique that can allow for the polarization of a large variety of molecules. While the instrumentation for creating the polarization can be delicate, if treated with care, it can work robustly and allow for a wide range of hyperpolarized experiments.

Chapter 4 - **Temperature Imaging using iMQCs**

Non-invasive temperature measurements are useful for a variety of applications in medicine, chemistry and materials science. In particular, recent developments in hyperthermia, an adjunctive cancer therapy which treats tumors through focused RF or ultrasound heating, has created significant interest in developing methods for doing magnetic resonance temperature imaging. Numerous studies have shown that combining hyperthermic therapy with radiotherapy can result in a wide variety of benefits including increased tumor response and increased survival rates [65-67]. These studies use hyperthermic therapy in different ways to combat cancer. One method involves ablation (directly killing the cancerous cells) of the cancerous tissue through the application of focused ultrasound[67] as an alternative to lumpectomy. Alternative approaches use gentler heating (temperatures <41˚C) to supplement radiotherapy[68], chemotherapy and surgery[69]. In addition, more novel applications of hyperthermia are being applied to cause heat induced gene therapy[70], or to control drug delivery using thermally sensitive liposomes[71]. However, hyperthermic therapy requires the accurate delivery of a prescribed temperature dose for a sustained time (usually 40°C-45°C over 30-90 minutes) and monitoring the heating is challenging[72, 73]. Extensive, invasive thermometry (usually done via multiple thermocouples) can be used, and several studies have invasively monitored temperature during treatment and the outcome of the treatment is directly tied to the temperature achieved [74-80]. Still,

invasive thermometry has significant limitations, and particularly in the case of deep-seated tumors is not practical for routine use.

MRI can monitor temperature non-invasively and without the use of ionizing radiation [81-90]. Current temperature imaging methods detect changes in T_1, diffusion, magnetic resonance spectroscopy, or the chemical shift of water (proton resonance frequency or PRF). All these methods provide temperature information, but are complicated since the temperature information can be hidden under larger changes in susceptibility and magnetic field inhomogeneities. The most commonly used temperature-sensitive MR parameter is the change in the chemical shift of water with temperature. The resonance frequency of a particular spin is defined as[91]:

$$\omega = (1 - \sigma(t))\,\gamma B_0 \tag{44}$$

The chemical shift determined by the local electronic environment is σ, γ is the gyromagnetic ratio (42.8 MHz/T for protons) and B_0 is the main magnetic field. Heating changes the hydrogen bonding network of the water protons and shifts the observed magnetic resonance frequency by 0.01ppm/°C. This effect is often referred to as the PRF (proton resonance frequency) shift, but it is important to realize that non-water protons are not shifted by the same amount, as discussed below. The temperature sensitivity of MRI was first observed by Hindman in 1966 [92] and was later adapted to temperature imaging by Ishiara [83] and De Poorter [81, 82].

In order to measure temperature using shifts in the PRF, a series of images are acquired with a fixed echo time. Since MR image phase is a linear function of the frequency (for a fixed echo time), the changes in temperature appear as changes in the phase of the images. First, an image is acquired at a baseline temperature, and then at some elevated temperature the change in phase between the images is extracted, allowing temperature information to be found for each pixel in the image.

For lean tissues such as muscle, the temperature dependence of the water chemical shift is well known and fairly constant across tissue types [93]. The magnetic susceptibility, or magnetic flux density, can also change with temperature [94], adding an additional complication to the PRF methods. The local magnetic field can be approximated as [82, 94-96]:

$$B_{local} \cong \left(1 - \frac{2\chi}{3} - \sigma(t)\right) B_{mac} \tag{45}$$

B_{local} is the local magnetic field experienced by the nucleus, χ is the temperature dependent susceptibility constant of the material and $\sigma(T)$ is the chemical shift (which depends on the chemical environment). B_{mac} is the macroscopic magnetization and is a function of the main magnetic field (B_0), the susceptibility distribution and sample geometry. If we include susceptibility into the calculations of temperature change, then the resonance frequency of the water protons is not only dependent on the changes in the chemical shift (σ) of the protons, but also from changes to the susceptibility of the tissue. For the temperature ranges used in hyperthermic treatment, both σ and χ can be

treated as linear. The temperature dependence of χ depends on the tissue type and is 0.0026 ppm/°C for pure water, 0.0019 ppm/°C for muscle and 0.0094 ppm/ °C in fat [82, 97]. In tissues dominated by the water molecules (as opposed to fat molecules) the change in chemical shift dominates (at 0.01 ppm/°C), and the errors from changes in susceptibility only create 10% variations in the temperature detection [98].

In tissues with a high fat content, such as the breast, application of PRF methods is not immediately straightforward. First, the chemical shift of fat is nearly constant over the range of temperatures used in hyperthermic treatment (0.00018 ppm/°C)[99]. Thus, in tissues with large fat content, fat suppression methods are almost always used. An additional complication comes from changes in susceptibility with temperature. The changes in susceptibility for the water signal is negligible (as discussed above), but the change in susceptibility of fat is much larger, 0.0094 ppm/°C. Thus, even with fat suppression methods, the changes in the susceptibility of fat are significant relative to the change in chemical shift, especially in tissues which are high in fat content.

An additional wrinkle in the PRF method is caused by magnetic field drift. The maximum specification for a commercial MRI system is a magnetic field drift of 0.1 ppm/hour (approximately 6.4 Hz/hour at 1.5T), and most instruments have a drift which is smaller, closer to 3 Hz/hour [100]. Since hyperthermic therapies often last 60 to 90 minutes, this means that there could be enough drift to create up to 10°C of error in the

temperature measurement. Methods for correcting for drift have been developed [81, 100-103] and most involve the use of an external phantom as a reference for drift.

A temperature imaging technique using intermolecular multiple quantum coherences (iMQCs) has been developed to address the issues associated with temperature imaging in high fat tissues. The iMQC based technique (called HOT [104]) is designed for use in tissues with high fat content and is insensitive to errors due to changes in susceptibility of both water and fat, as well as magnetic field drift and magnetic field inhomogeneities. In addition, HOT also provides absolute temperature measurements instead of relative temperature measurements (as obtained from PRF methods).

In this chapter, we describe in detail how the iMQC signal can be used to measure temperature and which modifications need to be made to the standard iZQC pulse sequence in order to obtain an accurate temperature map on an absolute temperature scale. We demonstrate the iMQC temperature imaging method on several phantoms in different temperature situations (uniform temperature distribution as well as a phantom with a temperature gradient) and show that the iMQCs provide a very clean temperature measurement in all cases.

4.1 iMQC temperature detection

In order to understand how iMQCs can image temperature, it is necessary to start by understanding what iMQCs are and how they can be manipulated to generate a temperature image. The fundamentals of iMQCs are described in chapter 2.

A well-defined and sharp difference between the two components is critical for precise temperature imaging. In our temperature imaging sequence we are interested in cleanly detecting the changes to the water proton frequency with temperature. The proton frequency is well known to change frequency at a rate of 0.01ppm/ºC (or 3 Hz/ºC at 7T). In vivo, lineshapes are broad and variable since the topography of the local magnetic field changes dramatically with motion, heating, drift and susceptibility gradients. These effects overshadow the much smaller frequency shift due to temperature changes. Fat does not change resonance frequency with temperature (over a biologically relevant range), and can be used as a reference frequency. Since the fat protons are a correlation distance from the water proton of interest, they are in an identical environment, and experience the same macroscopic effects as the water proton. Since iZQCs evolve at the difference frequency between the two spins, it is possible to get a signal that is insensitive to the local magnetic field variations, but is sensitive to temperature changes.

It is intuitively clear that iZQCs retain chemical shift information while removing inhomogeneous broadening. Less obviously, +2-quantum iDQC (intermolecular double quantum coherence) evolution during one period (at the sum of the two different resonance frequencies) can combine with -1-quantum evolution during a later period to also give a signal that is free of inhomogeneous broadening. This works because the -1-quantum evolution is at only one of the two resonance frequencies, not the average. For example, the signal from a +2 quantum CRAZED sequence starts as $\mathbf{I}^{+}\mathbf{S}^{+}$, which acquires an evolution of $(\omega_I t_1 + \omega_S t_1)$ and also acquires inhomogeneous broadening of $(\Delta\omega_I t_1 + \Delta\omega_S t_1)$. After the mixing pulse, the coherence is either $\mathbf{I}^{-}\mathbf{S}_z$ or $\mathbf{I}_z\mathbf{S}^{-}$ and evolves for $2t_1$. The spin that is in the plane (either $\mathbf{I}^{-}$ or$\mathbf{S}^{-}$) evolves at $-2\omega_I t_1$ or $-2\omega_S t_1$. If that spin sees the same inhomogeneous broadening (i.e., $\Delta\omega_I = \Delta\omega_S$) during the $2t_1$ period as both the spins did during the t_1 period, then all the inhomogeneous broadening gets reversed (i.e., $\Delta\omega_I t_1 + \Delta\omega_S t_1 = 2\Delta\omega_s$ or $\Delta\omega_I t_1 + \Delta\omega_S t_1 = 2\Delta\omega_I$). In other words, the ability to refocus inhomogeneous broadening is more closely tied to the ability to couple spins that experience the same local field than the particular order of the coherence.

The temperature imaging pulse sequence used in our experiments uses both iZQCs and iDQCs to detect temperature. iZQCs have extraordinarily sharp lines, even in very inhomogeneous fields [14]. Unfortunately, iZQC experiments (known as the HOMOGENIZED sequence [18] or the iZQC – CRAZED sequence) are often

contaminated by a large amount of SQCs (one-spin, single quantum coherences – conventional magnetization), and it can be hard to extract the narrow iZQC peaks from the broad SQC peaks. On the other hand, iDQC experiments (such as those detected in the CRAZED sequence [22, 24, 105]) cleanly select the desired iDQC signal and have minimal contamination from SQCs. We use a sequence which has the narrow lineshape of an iZQC and the robust filtering of an iDQC. We do this by converting iZQCs into iDQCs and vice versa, allowing the system to evolve as both types of coherence and thus preserving the desired properties of each type of coherence.

4.2 Modifications to the HOMOGENIZED Sequence for Temperature Imaging

In the standard iMQC pulse sequences, the major contribution to the signal is given by the same spin (in the case of fatty tissue, water-water and fat-fat) iMQC transitions, which are insensitive to temperature changes. The mixed spin, water-fat iZQC transition frequency changes linearly with temperature and can be used to create a temperature map. The detection of the temperature-sensitive, mixed spin iZQC signal can be challenging, since the temperature-insensitive same spin iZQCs dominate. This can be easily seen by inspection of the standard signal for a two component iZQC CRAZED experiment, $(\pi/2)_x$-t_1-{gradient pulse}-θ_x-t_2-acquire, as shown in Figure 4-1 [106]. In a sample containing two chemical species I and S, ignoring diffusion, relaxation,

and inhomogeneous broadening, the signal arising from the I-I (same spin) iZQCs is given by [106]:

$$M^{I^+} = i\cos\theta M_0^I e^{i\omega t_2} \times J_1\left(-\sin\theta\frac{t_2}{\tau_{dI}}\right) J_0\left(-sin\theta\frac{2t_2}{3\tau_{dS}}\right) \tag{46}$$

Here ω_I is the chemical shift of spin I, and τ_{dI} and τ_{dS} are the dipolar demagnetizing times of spin I and S, respectively ($\tau_{dI} = \frac{1}{\gamma_I \mu_0 M_0^I}, \tau_{dS} = \frac{1}{\gamma_S \mu_0 M_0^S}$), where M_0^I and M_0^S are the equilibrium magnetizations of spins I and S). Note that there is no dependence of M^{I^+} on t_1, since this "homomolecular" zero-quantum coherence has no evolution during the first time period. In contrast, the signal arising from I-S (mixed spin) iZQCs of the form I^+S^- is given by [106]:

$$M^{I^+} = iM_0^I e^{i\omega_I t_2} e^{i(\omega_I - \omega_S)t_1} \times \left\{\cos\theta J_0\left(-\sin\theta\frac{t_2}{\tau_{dI}}\right) - \frac{(1-\cos\theta)\,\tau_{dI}}{t_2\sin\theta} J_1\left(-\sin\theta\frac{t_2}{\tau_{dI}}\right)\right\}$$
$$\times J_1\left(-\sin\theta\frac{2t_2}{3\tau_{dS}}\right) \tag{47}$$

If I and S are water and fat, respectively, the frequency of this "heteromolecular" peak in the indirectly detected dimension is $\omega_I - \omega_S$. Since ω_I has a linear dependence on temperature (since it is the water spins) while ω_S does not, the difference between these frequencies has a linear dependence on absolute temperature.

The effects of inhomogeneous broadening and relaxation on the CRAZED and related sequences have been extensively discussed elsewhere [6, 13, 107, 108]. The most

important practical limit for an iZQC temperature imaging sequence is the one where $T_2^* << T_{2I}, T_{2S} << \tau_{dS}, \tau_{dI}, T_{1,I}, T_{1,S}$. In that limit, the sequence in Figure 4-1 is severely compromised, as the iZQC signal is zero at t_2=0 and its linear growth with time is impeded by inhomogeneous broadening. A more practical sequence includes an echo pulse with TE≈T_2 (Figure 1b). In this case, at the peak of the echo, the components of detected I magnetization that evolved during t_1 as homomolecular (eq. 3) or heteromolecular signals (eq. 4, 5) are [106]:

$$M^{I^+} = i\cos\theta e^{-\frac{2t_1}{T_{2,I}}} M_0^I \times J_1\left(-\sin\theta\frac{TE}{\tau_{dI}}e^{-\frac{TE}{T_{2I}}}\right) J_0\left(-\sin\theta\frac{2TE}{3\tau_{dS}}\right) \tag{48}$$

$$M^{I^+} = iM_0^I e^{i(\Delta\omega_I-\Delta\omega_S)t_1} e^{-\frac{t_1}{T_{2I}}} e^{-\frac{t_1}{T_{2S}}} \times$$
$$\left\{\cos\theta J_0\left(-\sin\theta\frac{TE}{\tau_{dI}}\right) - \frac{(1-\cos\theta)\tau_{dI}}{TE\sin\theta} J_1\left(-\sin\theta\frac{TE}{\tau_{dI}}\right)\right\} J_1\left(-\sin\theta\frac{2TE}{3\tau_{dS}}\right) \tag{49}$$

$$M^{I^+} = iM_0^I e^{i(\Delta\omega_S-\Delta\omega_I)t_1} e^{-\frac{t_1}{T_{2I}}} e^{-\frac{t_1}{T_{2S}}} \times$$
$$\left\{\cos\theta J_0\left(-\sin\theta\frac{TE}{\tau_{dI}}\right) - \frac{(1-\cos\theta)\tau_{dI}}{TE\sin\theta} J_1\left(-\sin\theta\frac{TE}{\tau_{dI}}\right)\right\} J_1\left(-\sin\theta\frac{2TE}{3\tau_{dS}}\right) \tag{50}$$

Equations **(49)** and **(50)** show the heteromolecular peak for I^+S^- and I^-S^+, respectively. The heteromolecular peak is significantly smaller than the homomolecular peak in the common case where $M_o^S << M_o^I$ (Figure 1 shows an example).

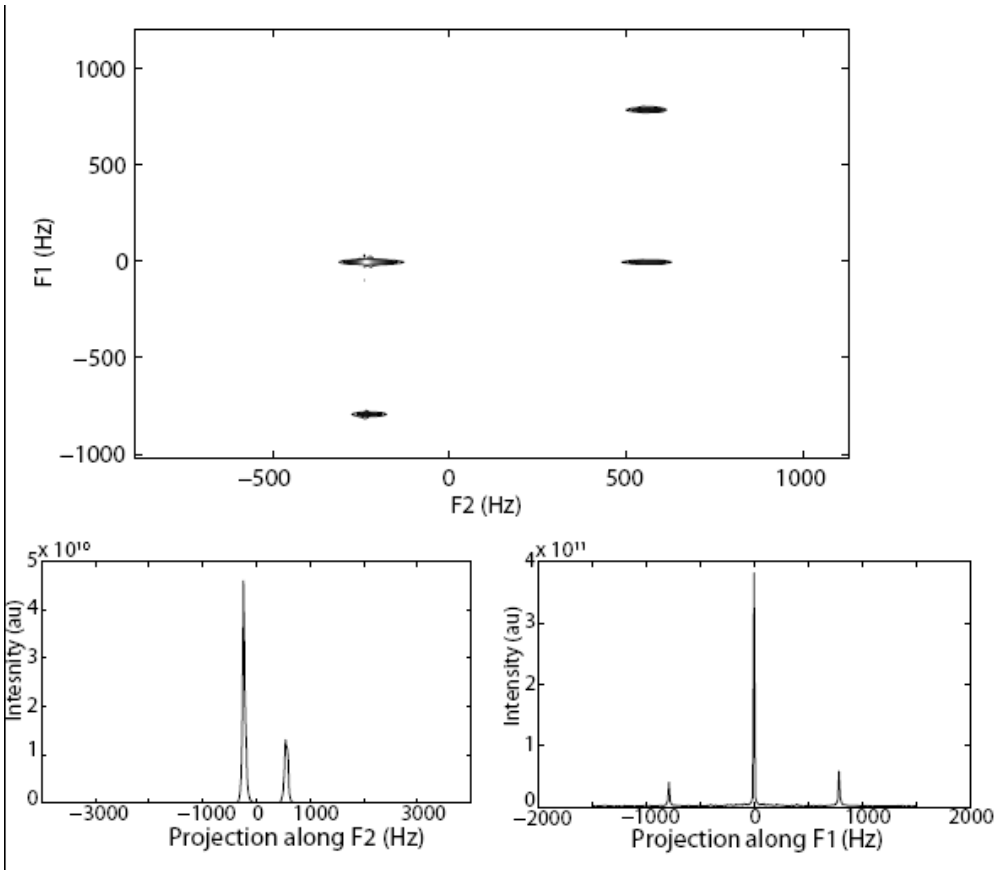

Figure 4-1: Top: Standard 2D iZQC spectrum of a 75% water- 25% acetone sample. Bottom left: Projection along F2 (direct, SQC dimension). Bottom right: Projection along F1 (indirect, iZQC dimension). In this spectrum, the bulk of the signal is coming from the temperature insensitive same spin iZQC signal (such as that from water-water or fat-fat iZQCs). If the standard iZQC sequence was used to image temperature, the bulk of the signal in that image would be temperature insensitive signal, thus contaminating the temperature sensitivity of the image.

The majority of the signal comes from the strong solvent signal, which in an imaging application would dominate the signal of the image. Further complicating matters, unlike other iMQC sequences, the iZQC sequence lacks a gradient filter that can remove SQC contamination generated by the mixing pulse.

4.2 Single acquisition HOT imaging

In order to accurately image temperature, it is crucial to create a filter that can cleanly remove contamination from same spin iZQCs, as well as from conventional magnetization. The basic pulse sequence used to image temperature is shown in Figure 4-2

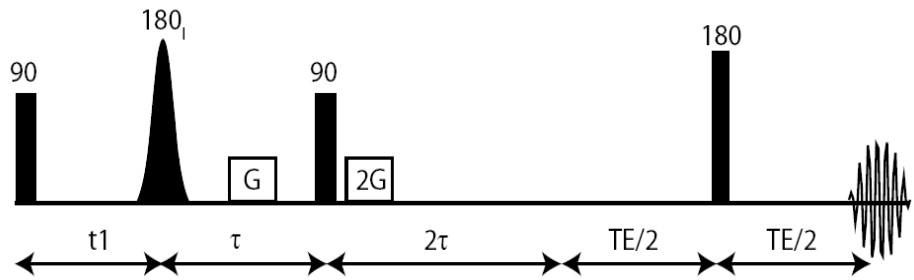

Figure 4-2: Single acquisition HOT pulse sequence. This sequence is a modified version of the CRAZED pulse sequence. The frequency selective 180° pulse converts iZQCs to iDQCs and the subsequent gradients filter out all signals except the desired mixed – spin iMQCs.

The frequency selective inversion pulse inverts only one chemical species, causing the mixed spin iZQC to convert to mixed spin iDQCs and vice versa [1;9;16] [109]:

$$\begin{aligned} \mathbf{I}^{+}\mathbf{S}^{+} &\xrightarrow{\pi_I} \mathbf{I}^{-}\mathbf{S}^{+} \\ \mathbf{I}^{-}\mathbf{S}^{+} &\xrightarrow{\pi_I} \mathbf{I}^{+}\mathbf{S}^{+} \end{aligned} \tag{51}$$

This pulse has no net effect on same spin iMQCs:

$$\begin{aligned} \mathbf{I}^{+}\mathbf{I}^{+} &\xrightarrow{\pi_I} \mathbf{I}^{-}\mathbf{I}^{-} \\ \mathbf{I}^{-}\mathbf{I}^{+} &\xrightarrow{\pi_I} \mathbf{I}^{+}\mathbf{I}^{+} \end{aligned} \tag{52}$$

Applying a double quantum filter of [τ,GTz-θ_{mix}-2τ,2GTz] dephases all coherences except those which existed as iDQCs during τ and were transferred into iSQCs (e.g., $\mathbf{I}^{+}\mathbf{S}_{z}$) by the mixing pulse [10, 15]. Since the unbalanced gradients flank the mixing pulse, they also efficiently dephase the SQCs created before or after the mixing pulse (Figure 2-1A), reducing the large static SQC component of the signal. In addition, this extra twist in the coherence pathway creates different routes for the iMQCs between equivalent and unequal spin pairs, so that standard methods can now be used to isolate the desired water-fat iZQCs. For example, of the signals preserved by the double quantum filter, only water-fat iZQCs are unaffected by the phase cycling of the first excitation pulse. Similarly, the phase of the selective inversion pulse has different effects on same-spin versus mixed-spin coherences, with a $\pi/2$ shift reversing the water-fat coherences, but leaving the water-water coherences unaffected.

With the selective inversion pulse, the phase reversal is more formally a change in coherence order. Since this modified HOMOGENIZED sequence only transfers coherences between water and off-resonance spins into observable signal, we refer to it as **H**OMOGENIZED with **O**ff-resonance **T**ransfer, or the HOT sequence.

2.3 Two-Window HOT

The previously described sequence can cleanly image a single temperature-sensitive coherence. It and all of the other iMQC sequences developed to remove

inhomogeneous broadening [110-113] are inherently two-dimensional sequences. There is a good reason why there are no clinical applications of such sequences: the sequence often requires several hours to acquire an image, and such sequences are highly susceptible to instabilities such as motion. Several methods have been used to speed up the sequence, including EPI acquisitions [114, 115] and RARE acquisitions [116, 117]. The EPI acquisitions impose geometric distortions as well as a T_2^* decay (inhomogeneous broadening, causing the signal to rapidly decay) on the signal, making it an unacceptable method for accelerating the acquisition. The RARE based sequences work well, but for clinical applications, the sequence quickly approaches SAR limitations for large RARE factors.

The primary reason why the experiment requires so much time is that many t_1 points are required to acquire an accurate temperature map, and each t_1 point represents the acquisition of an entire image. Ultrafast two-dimensional sequences are one approach to solve this issue [118, 119] and were demonstrated to be feasible for iMQC experiments [113, 120-122]. In all of these cases, the available signal from the entire sample (or from each voxel in an image) is subdivided to acquire multiple t_1 points. However, the most important parameter for a temperature image is a single frequency, which requires far fewer points. As we previously noted [104], it is possible to use multiple pathways to acquire several images (two or more, as shown below) with different effective evolution at the water-fat frequency and with each image containing

the full signal. The acquisition of the two signals with different evolution reduces the number of repetitions (since two t_1 points are acquired from each scan) and allows us to acquire temperature images both in vivo [104] and in vitro in only two minutes. The pulse sequence for two-window HOT is shown in Figure 4-3.

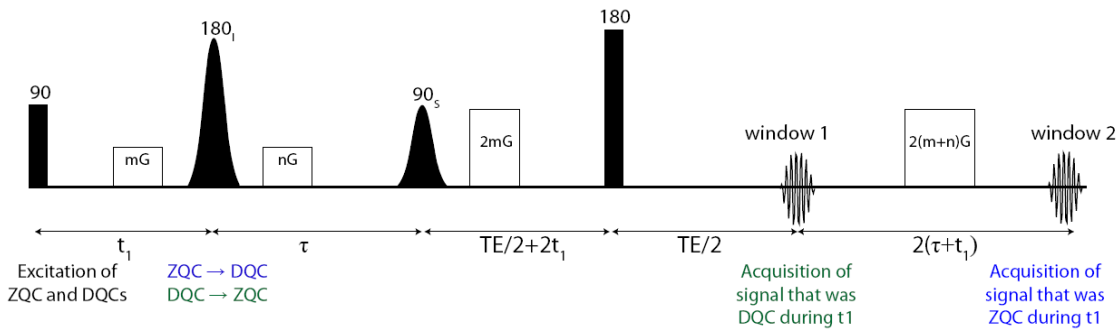

Figure 4-3- Two-window HOT sequence. This sequence acquires two images simultaneously, one which was iDQC during t_1, the other from signal that was iZQC during t_1. The signals in each acquisition window have different amounts of evolution, allowing for a temperature map to be created in a single application of the pulse sequence. In addition, the extra gradients provide a more robust coherence filter, further preventing contamination from unwanted coherence pathways.

To apply this idea to thermometry, the mixed-spin coherences are isolated in a manner very similar to that used for the single acquisition HOT sequence. Two coherence pathways exist, one in which iDQCs are converted to iZQC and the other where iZQCs are converted to iDQCs. In the first pathway (iDQC to iZQC), the signal is refocused in the first acquisition window (see supplemental information for more details). Briefly, the signal starts as iDQC ($\mathbf{I}^+\mathbf{S}^+$). The gradient mGT causes a phase shift of $2mGT$ and the coherence acquires $2t_1$ of evolution. It is converted to an iZQC by the selective inversion pulse, where the subsequent gradient nGT has no effect, and the

coherence evolves at the iZQC (ω_I-ω_S) frequency during τ. The selective mixing pulse then reintroduces the dipolar field, and the signal is refocused by the $2mGT$ gradient and the $2t_1$ evolution time.

The second coherence pathway takes iZQCs and converts them to iDQCs. During the t_1 interval, the signal is iZQC and experiences no gradient and evolves at the iZQC frequency (ω_I-ω_S). The selective inversion pulse converts it to iDQC, where it evolves at the iDQC frequency (ω_I+ω_S) and acquires a phase shift $2nGT$ from the gradient. The coherence is converted to SQC by the mixing pulse, and it acquires an additional phase shift of $2mGT$ (causing a net effect of the gradients to be $2(m+n)GT$) and evolves for an additional $2t_1$. After the refocusing pulse and the first acquisition window, a gradient of $2(m+n)GT$ and $2(\tau+t_1)$ of evolution refocuses the signal, and it is acquired in the second acquisition window.

Since this signal primarily arises from spins that are a correlation distance apart, γ(m+n)GT does not average to zero across the sample, and this signal is refocused. As discussed earlier, if these are replaced with inhomogeneously broadened chemical shifts, the inhomogeneous broadening would be canceled.

Adequate same-spin suppression is crucial for the success of this sequence. While our experimental results have indicated that adequate same-spin suppression can be achieved simply through the extra gradient filters of this sequence, standard phase cycling methods achieve higher SNR more efficiently over multiple scan averages, and a

phase cycle which is compatible with both signals is shown in *Table 3*. For a review of how phase cycling works see section 1.3.

Table 3 – Phase cycling scheme for the 2-window HOT sequence.

Scan #	90	180_I	90_S	Rcvr 1	Rcvr 2
1	**0**	**0**	**0**	**0**	**0**
2	**1**	**2**	**0**	**2**	**0**
3	**2**	**0**	**0**	**0**	**0**
4	**3**	**2**	**0**	**2**	**0**

The phase cycling is designed to select both coherence pathways into separate acquisition windows. The first acquisition collects signal that goes through the coherence pathway starting with a coherence order of +2 (DQC), which is converted to 0 (ZQC) by the 180° pulse, and to a +1 (SQC) coherence by the mixing pulse. The excitation pulse is cycled through the phases 0, 90, 180, 270 (or, as represented in the tables as the modular form, 0, 1, 2, 3). The effect of these phase changes on a +2 coherence is equivalent to a phase shift of 0, 2, 0, 2. The phase cycling of the second pulse has no effect on the desired zero quantum coherences. The resulting phase shift created by the phase cycling is 0, 2, 0, 2, and the receiver is cycled to match that and constructively add

those signals. The second acquisition window collects signal that started as a coherence order of 0, and the cycling of the phases of the excitation pulse have no effect on the phase of the coherence. The 180° mixing pulse is cycled to select +2 coherences, and the phase cycle of 0, 2, 0, 2 causes a net phase shift of the +2 quantum coherences of 0, 0, 0, 0. The receiver phase is set to match the net phase shift of coherences from this pathway by following the phase cycle 0, 0, 0, 0. The details of the phase cycle are given in Table 4.

Table 4- Detailed view of the phase cycling for two-window HOT.

step	90 phase	Δp=0	180 phase	Δp=2	90 phase	Δp=1	total phase
1	0	0	0	0	0	0	0
2	1	0	2	0	0	0	0
3	2	0	0	0	0	0	0
4	3	0	2	0	0	0	0
step	**90 phase**	**Δp=2**	**180 phase**	**Δp=0**	**90 phase**	**Δp=1**	**total phase**
1	0	0	0	0	0	0	0
2	1	2	2	0	0	0	2
3	2	0	0	0	0	0	0
4	3	2	2	0	0	0	2

4.4 Product Operator Description of the HOT sequence

4.4.1. Two Window HOT

The two window HOT sequence is most easily understood with the use of the product operator formalism. The pulse sequence starts with a $\pi/2$ pulse which converts the I_zS_z operators in the initial density matrix into iZQCs and iDQCs. The system evolves for t_1 and experiences a gradient of area mGT. A selective inversion pulse on the I spins converts iDQCs to iZQCs and vice versa.

Window 1 (iDQC ◎ iZQC):

$$\begin{gathered}\mathbf{I}^+\mathbf{S}^+e^{i(\omega_I+\omega_S)t_1+i\gamma 2mGt}+\mathbf{I}^-\mathbf{S}^-e^{-i(\omega_I+\omega_S)t_1-i\gamma 2mGt}\xrightarrow{\pi_I}\\ \mathbf{I}^-\mathbf{S}^+e^{i(\omega_I+\omega_S)t_1+i\gamma 2mGt}+\mathbf{I}^+\mathbf{S}^-e^{-i(\omega_I+\omega_S)t_1-i\gamma 2mGt}\end{gathered} \tag{53}$$

Window 2 (iZQC ◎ iDQC) :

$$\begin{gathered}\mathbf{I}^+\mathbf{S}^-e^{i(\omega_I-\omega_S)t_1}+\mathbf{I}^-\mathbf{S}^+e^{i(-\omega_I+\omega_S)t_1}\xrightarrow{\pi_I}\\ \mathbf{I}^+\mathbf{S}^+e^{i(\omega_I-\omega_S)t_1}+\mathbf{I}^+\mathbf{S}^+e^{i(-\omega_I+\omega_S)t_1}\end{gathered} \tag{54}$$

During the next period, these coherences evolve with chemical shift during τ and also acquire a modulation from the gradient of area nGT. The selective $\pi/2$ mixing pulse on spin S transfers these coherences into single quantum coherences with a transverse I-spin component.

Window 1:

$$-i\mathbf{I}^-\mathbf{S}_ze^{i(\omega_I+\omega_S)t_1+i(-\omega_I+\omega_S)\tau+i\gamma 2mGt}+\mathbf{I}^+\mathbf{S}_ze^{-i(\omega_I+\omega_S)t_1+i(\omega_I-\omega_S)\tau-i\gamma 2mGt} \tag{55}$$

Window 2:

$$-i\mathbf{I}^{-}\mathbf{S}_{z}e^{i(\omega_I-\omega_S)t_1-i(\omega_I+\omega_S)\tau-i\gamma 2nGt}-\mathbf{I}^{+}\mathbf{S}_{z}e^{i(-\omega_I+\omega_S)t_1+i(\omega_I+\omega_S)\tau+i\gamma 2nGt} \tag{56}$$

The gradient of area 2mGT and a $2t_1$ delay refocuses the signal in window 1 and adds an additional phase shift in window 2:

Window 1:

$$-i\mathbf{I}^{-}\mathbf{S}_{z}e^{i(-\omega_I+\omega_S)t_1+i(-\omega_I+\omega_S)\tau}+i\mathbf{I}^{+}\mathbf{S}_{z}e^{i(\omega_I-\omega_S)t_1+i(\omega_I-\omega_S)\tau} \tag{57}$$

Window 2:

$$-i\mathbf{I}^{-}\mathbf{S}_{z}e^{-i(\omega_I+\omega_S)t_1-i(\omega_I+\omega_S)\tau-i\gamma 2(m+n)Gt}-\mathbf{I}^{+}\mathbf{S}_{z}e^{i(\omega_I+\omega_S)t_1+i(\omega_I+\omega_S)\tau+i\gamma 2(m+n)Gt} \tag{58}$$

Since all the evolution that occurs during the TE/2- π -TE/2 portion of the sequence is refocused, the final signal detected in window 1 is:

$$-i\mathbf{I}^{-}e^{i(-\omega_I+\omega_S)t_1+i(-\omega_I+\omega_S)\tau}+i\mathbf{I}^{+}e^{i(\omega_I-\omega_S)t_1+i(\omega_I-\omega_S)\tau} \tag{59}$$

The signal for window 2 evolves for an additional (TE/2)-π-(TE/2+2(τ+t_1)), where the effect of a π pulse is essentially a time reversal for chemical shift. Therefore, this is equivalent to evolving for -2(τ+t_1), followed by the gradient 2(m+n)GT, which gives the following modulation:

$$-i\mathbf{I}^{+}\mathbf{S}_{z}e^{i(\omega_I-\omega_S)t_1-i(\omega_I-\omega_S)\tau}-i\mathbf{I}^{-}\mathbf{S}_{z}e^{-i(\omega_I-\omega_S)t_1-i(\omega_I-\omega_S)\tau} \tag{60}$$

The resulting evolution in both windows is a phase shift $\pm(\omega_I - \omega_S)(t_1+\tau)$

4.4.2. Four window HOT

The four window sequence (figure 4) is an extension of the two window sequence, but with the addition of two more acquisition windows in which standard SQC signal is refocused to provide chemically selective, spin density maps. To understand how the different chemical species are separated into the two windows, we once again need to visit the product operator description of the pulse sequence.

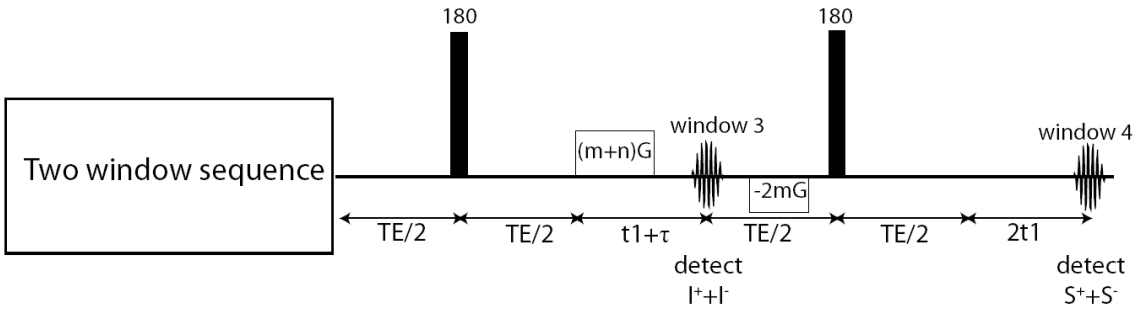

Figure 4-4- Four window HOT sequence. The addition of two 180° pulses after the acquisition of the temperature sensitive iMQC images (acquisition windows 1 and 2) allow for the detection of chemically selective, spin-density images.

The $\pi/2$ degree pulse puts the spins in the xy-plane, and the system evolves for t_1 and acquires a phase shift in the presence of the gradient m. Because the S spins do not see the selective π pulse, we can combine the evolution during τ and t_1, as well as the gradients m and n. The selective π pulse on the I spins changes the sign of the phase shift, and the subsequent τ evolution time, as well as the n gradient, creates the following phase shift:

$$\mathbf{I}_z \xrightarrow{\pi/2} \xrightarrow{t_1, mGt} \mathbf{I}^+ e^{i\omega_I t_1 + i\gamma mGt} + \mathbf{I}^- e^{-i\omega_I t_1 - i\gamma mGt} \xrightarrow{\pi} \mathbf{I}^- e^{i\omega_I t_1 + i\gamma mGt} + \mathbf{I}^+ e^{-i\omega_I t_1 - i\gamma mGt}$$

$$\xrightarrow{\tau, nGt} \mathbf{I}^- e^{i\omega_I (t_1 - \tau) + i\gamma (m-n)Gt} + \mathbf{I}^+ e^{-i\omega_I (t_1 - \tau) - i\gamma (m-n)Gt}$$

(61)

$$\mathbf{S}_z \xrightarrow{\pi/2} \xrightarrow{t_1+\tau, mGt+nGt} \mathbf{S}^+ e^{i\omega_S (t_1+\tau) + i\gamma (m+n)Gt} + \mathbf{I}^- e^{-i\omega_S (t_1+\tau) - i\gamma (m+n)Gt} \tag{62}$$

Since the subsequent π/2 mixing pulse is selective on the S spins, the I spins do not experience it. The spins then evolve for $2t_1$ and see a 2mGT gradient. The TE/2- π - TE/2 module after the mixing pulse changes the sign of the phase shift.

$$\xrightarrow{2t_1, 2mGt} \xrightarrow{\pi} \mathbf{I}^+ e^{i\omega_I (-t_1 - \tau) + i\gamma (-m-n)Gt} + \mathbf{I}^- e^{i\omega_I (t_1 + \tau) + i\gamma (m+n)Gt} \tag{63}$$

$$\xrightarrow{\pi/2} \xrightarrow{2t_1, 2mGt} \xrightarrow{\pi} \mathbf{S}^- e^{i\omega_S (3t_1 + \tau) + i\gamma (3m+n)Gt} + \mathbf{S}^+ e^{i\omega_S (-t_1 + \tau) + i\gamma (-m+n)Gt} +$$
$$\mathbf{S}^- e^{i\omega_S (t_1 - \tau) + i\gamma (m-n)Gt} + \mathbf{S}^+ e^{i\omega_S (-3t_1 - \tau) + i\gamma (-3m-n)Gt} \tag{64}$$

This is the point where the first of the mixed spin iMQC signals is detected. From this calculation, it is clear that the single spin SQCs are not refocused and do not contribute. The SQC coherences evolve for an additional $2t_1$+2τ time and experience a 2(m+n)GT gradient. The $2t_1$ time refocuses the evolution from the previous $2t_1$ time and the signal from the I spins starts to refocus, while the S spins pick up an additional phase shift.

$$\xrightarrow{2t_1 + 2\tau, 2(m+n)Gt} \xrightarrow{\pi} \mathbf{I}^+ e^{i\omega_I (t_1 + \tau) + i\gamma (m+n)Gt} + \mathbf{I}^- e^{i\omega_I (-t_1 - \tau) + i\gamma (-m-n)Gt} \tag{65}$$

$$\xrightarrow{2t_1 + 2\tau, 2(m+n)Gt} \xrightarrow{\pi} \mathbf{S}^- e^{i\omega_S (t_1 - \tau) + i\gamma (m-n)Gt} + \mathbf{S}^+ e^{i\omega_S (t_1 + 3\tau) + i\gamma (m+3n)Gt} +$$
$$\mathbf{S}^- e^{i\omega_S (-t_1 - 3\tau) + i\gamma (-m-3n)Gt} + \mathbf{S}^+ e^{i\omega_S (-t_1 + \tau) + i\gamma (-m+n)Gt} \tag{66}$$

At this point, the second iMQC window is detected. Again, the single spin SQCs are dephased and do not contribute to the signal detected in this window. After the second window, there is a π pulse followed by a $t_1+\tau$ evolution time and an (m+n)GT gradient. This final evolution time, as well as the gradient, refocuses the signal from the I spins.

$$\xrightarrow{\pi} \xrightarrow{t_1+\tau,(m+n)Gt} \mathbf{I}^- e^{i\omega_I(0)+i\gamma(0)Gt} + \mathbf{I}^- e^{i\omega_I(0)+i\gamma(0)Gt} \longrightarrow \frac{1}{2}\mathbf{I}_x \tag{67}$$

$$\begin{aligned}\xrightarrow{\pi} \xrightarrow{t_1+\tau,(m+n)Gt} \mathbf{S}^+ e^{i\omega_S(2t_1)+i\gamma(2m)Gt} + \mathbf{S}^- e^{i\omega_S(2\tau)+i\gamma(2n)Gt} + \\ \mathbf{S}^+ e^{i\omega_S(2\tau)+i\gamma(2n)Gt} + \mathbf{S}^+ e^{i\omega_S(-2t_1)+i\gamma(-2m)Gt}\end{aligned} \tag{68}$$

Thus, the only signal detected in the third window is the signal which was $I^{+/-}$ during t_1, and gives a map of the location of all the I spins in the sample. The S spins in the sample are too dephased to give any signal at this point.

In order to refocus the S signal for the fourth window, a -2mGT refocusing gradient followed by a π refocusing pulse and an additional $2t_1$ evolution time are applied.

$$\begin{aligned}\xrightarrow{-2m} \xrightarrow{\pi} \xrightarrow{2t_1} \mathbf{S}^- e^{i\omega_S(0)} + \mathbf{S}^+ e^{i\omega_S(2\tau+2t_1)+i\gamma(2(n+m))Gt} + \\ \mathbf{S}^- e^{i\omega_S(2\tau-2t_1)+i\gamma(2(n-m))Gt} + \mathbf{S}^+ e^{i\omega_S(0)} \\ \longrightarrow \frac{1}{4}\mathbf{S}_x + \mathbf{S}^+ e^{i\omega_S(2\tau+2t_1)+i\gamma(2(n+m))Gt} + \mathbf{S}^- e^{i\omega_S(2\tau-2t_1)+i\gamma(2(n-m))Gt}\end{aligned} \tag{69}$$

From the product operator description it is clear that the signal collected in acquisition window 3 is the I spin signal only, while the signal collected in window 4 is from the S

spins only. Thus, this simple extension to the two window HOT sequence can provide chemically selective, spin density images.

4.5 Data Processing

4.5.1 One – window HOT

In practice, iMQC temperature imaging takes an approach similar to that of the basic PFS method. In that approach, several complex images are acquired with varying amounts of uncompensated free evolution time. Each pixel in the image contains a complex number that represents the magnetization vector present in that pixel at the time of acquisition. As the t2 evolution time is increased in subsequent images, the magnitude of the vector may shrink with relaxation, but more importantly, the phase of the vector may change due to evolution. If we consider the vector for several such images, when there is only one component, we will see the vector rotate in a circle, and the rate of that rotation will give us the evolution frequency of the magnetization in that vector. In practical terms, iMQC imaging aims to reproduce this method, with two differences in the underlying physics. The vector whose frequency we wish to assess in iMQC thermometry is the magnetization created from water-fat coherences, and we assess that evolution by acquiring images with different t1 evolution times.

4.5.2 Two – window HOT

The processing for the two-window HOT sequence is very similar to that of the one window sequence. First, it is accelerated by only sampling part of the iZQC evolution time. To do this some number of images are taken with different values of τ or t1. For the experiments presented in this paper, τ was varied. An initial series of images are acquired (for example 10 images spanning 10 ms of τ evolution). Once it is verified that the phase of the images is changing at the water – fat iZQC frequency, an initial temperature map is created by fitting the phases of two images separated by several ms of evolution. The further apart the images are in terms of evolution time, the better the line, but this must be balanced against the inevitable signal decay that occurs at long evolution times. In practice we found that using images 2 and 7 worked the best as shown in [123]. All subsequent dynamic thermometry images are created by running the sequence with the τ equivalent to that found in image 2 and image 7. The second difference is that the dual acquisitions have frequencies which shift in opposite directions with temperature, thereby making it double sensitive to temperature. For example, at 7T with the two-window acquisition, there is a 6 Hz/°C shift (or a 0.02 ppm/°C shift). This larger shift is because the two acquisition windows evolve in opposite frequency directions, causing the temperature sensitivity to be twice the frequency as a single window acquisition. These two differences in the two-window

HOT sequence make the two-window (or four-window) HOT sequence much easier and faster for in vivo temperature imaging than the standard one-window HOT sequence.

4.6. Results and Discussion

4.6.1 Spectroscopy Results

The first result necessary to establish the utility of this method was to show that the water-fat iZQC frequency did vary with temperature at the expected rate of 0.01 ppm/°C. This was equivalent to ensuring that the frequency of fat in our phantom did not vary with temperature and could serve as an accurate temperature-independent correction factor. The most direct proof of this was carried out by running (off-resonance) 2D iZQC spectroscopy on a cream sample while its temperature was held constant and repeating the experiment at various temperatures. Those results are presented in Figure 4-5 and verify that the ZQC frequency changes linearly with temperature, shifting by the same 0.01 ppm/°C expected for water.

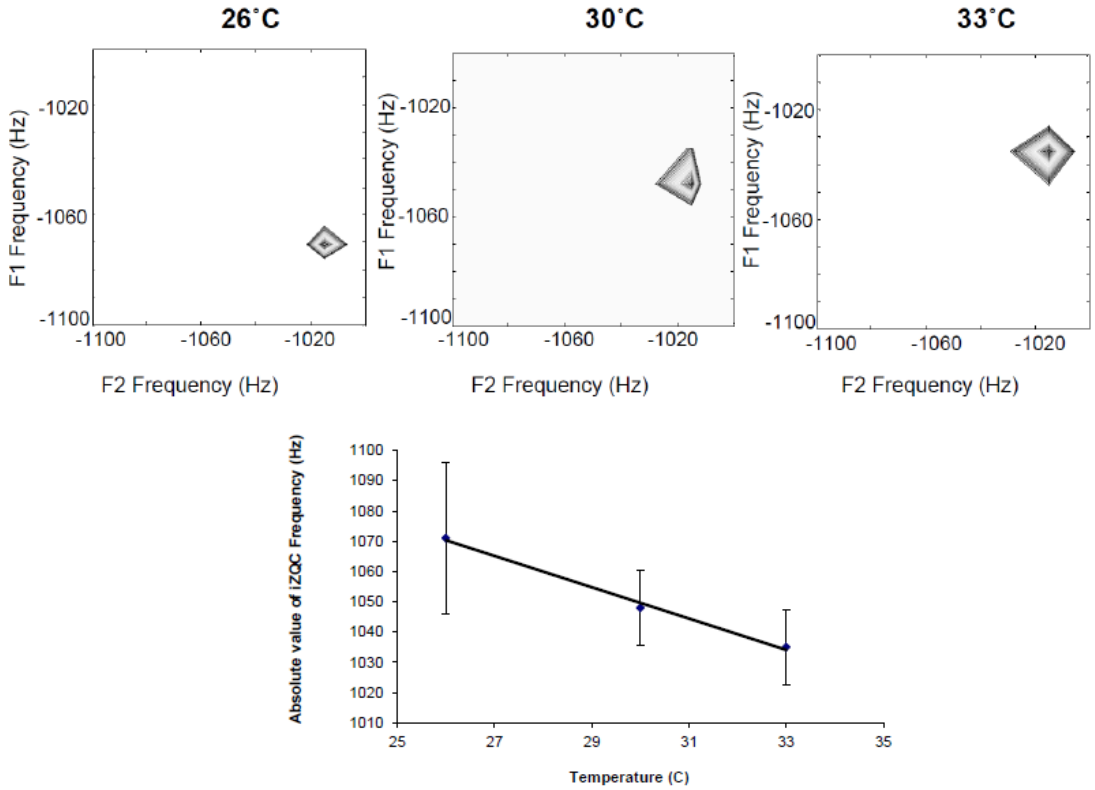

Figure 4-5 - The frequency of the iZQC crosspeak between water and fat shifts linearly with temperature in a water-fat phantom. A graph of the frequencies detected using the HOT sequence is shown in figure 7. The graph below the spectra is a plot of the absolute value of the iZQC frequency versus temperature. The error bars were determined by the resolution in the indirect dimension. All spectra were taken with TE=15 ms, TR=4 s, 8 averages, 512 x 256 matrix, spectral width (direct dimension) = 12626.26 Hz, spectral width (indirect dimension) 3200 Hz, correlation distance = 0.06406 mm.

The advantages of HOT thermography are demonstrated in a 2D experiment which clearly contrasts the characteristics of the iZQC signal along the F1 dimension with those of conventional magnetization along F2. Figure 4-6 presents such data acquired post mortem on an obese mouse (ob/ob, Jackson Laboratories). This spectrum is of the entire mouse abdomen. This clearly demonstrates that this sequence very

efficiently isolates the intended signal in each acquisition window. Furthermore, the iZQC dimension shows its hallmark of improved resolution relative to the directly detected signal. To the left of the 2D spectra, we present traces along F2 (blue), the dimension used to determine temperature in conventional methods, and F1 (black), the iMQC dimension. The iMQC peaks are insensitive to most sources of inhomogeneous broadening, and the observed frequency is almost exclusively a function of chemical shift, which reflects temperature. With the higher resolution of the iMQC spectrum, several component resonances of the fat peak are resolved, but this does not ultimately affect temperature mapping. Once the overall phase shift from these factors is established in a reference image, any changes in the phase of the image only reflect changes in the chemical shift of the water, i.e., changes in temperature.

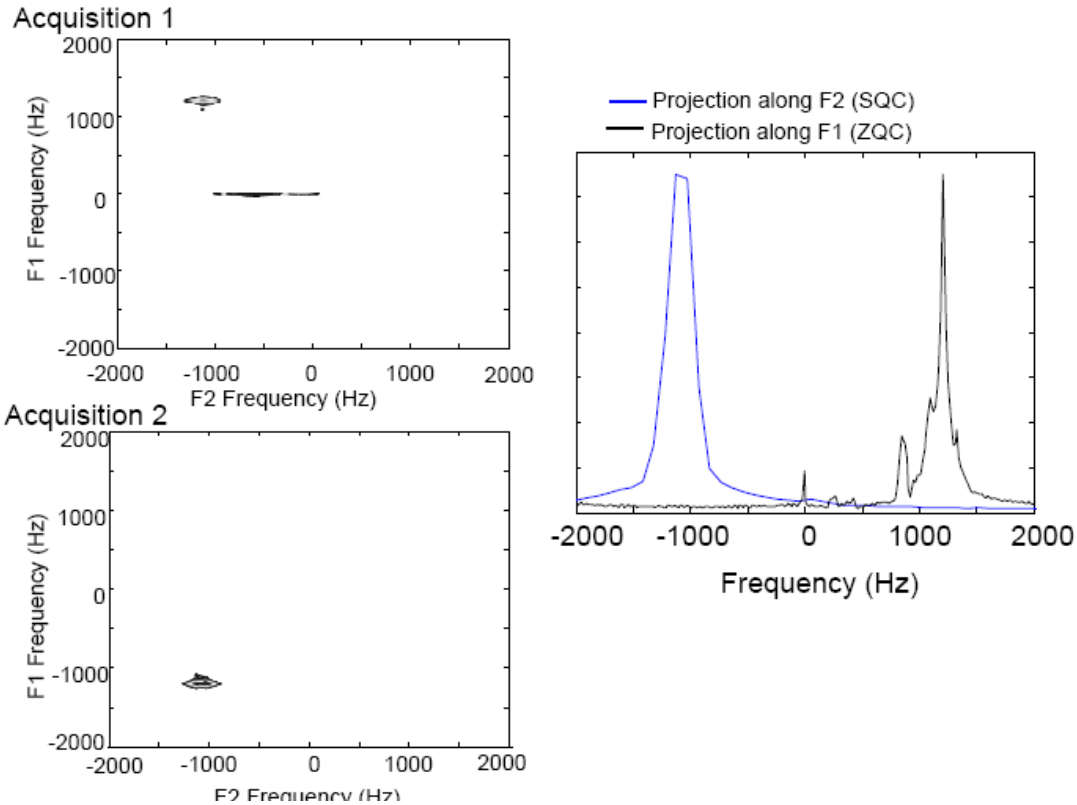

Figure 4-6- Spectra of an obese mouse post mortem demonstrate that the sequence cleanly isolates the water-fat coherence. Spectra on the left are the first (top) and second (bottom) acquisition windows. On the right are traces along F2 (blue) and F1 (black) showing narrower lines in the iZQC dimension. Scan parameters: mGT= 11 G/cm*1ms, nGT=-17 G/cm*1ms, correlation distance = 0.198 mm, TE = 40 ms, t_1 = 2.5 ms, τ = 3 ms, and TR = 4.5 s.

4.6.2 Results from single window HOT imaging experiments

Previous work has demonstrated the accuracy of iZQC imaging in a uniformly heated phantom [104]. In those results, a liquid water/fat phantom (cream) was maintained at a uniform temperature using feedback-controlled airflow and a single thermometer affixed to the outside of the sample. Figure 4-7 illustrates a more realistic

phantom for hyperthermic therapies. For the one-window HOT experiments, a semisolid gel of water and fat was prepared, from heavy cream and agarose, and maintained at a constant temperature gradient. The sample was set up with a continuous flow heat source (water doped with $CuSO_4$) through its center, a cool flow of air along its perimeter, and several fiber optic temperature probes at intermediate points. Using the scale established in the previous liquid state experiments, the agreement between the fiber optic probe temperature readings and the iZQC frequencies are shown in the graph on the bottom right of Figure 4-7.

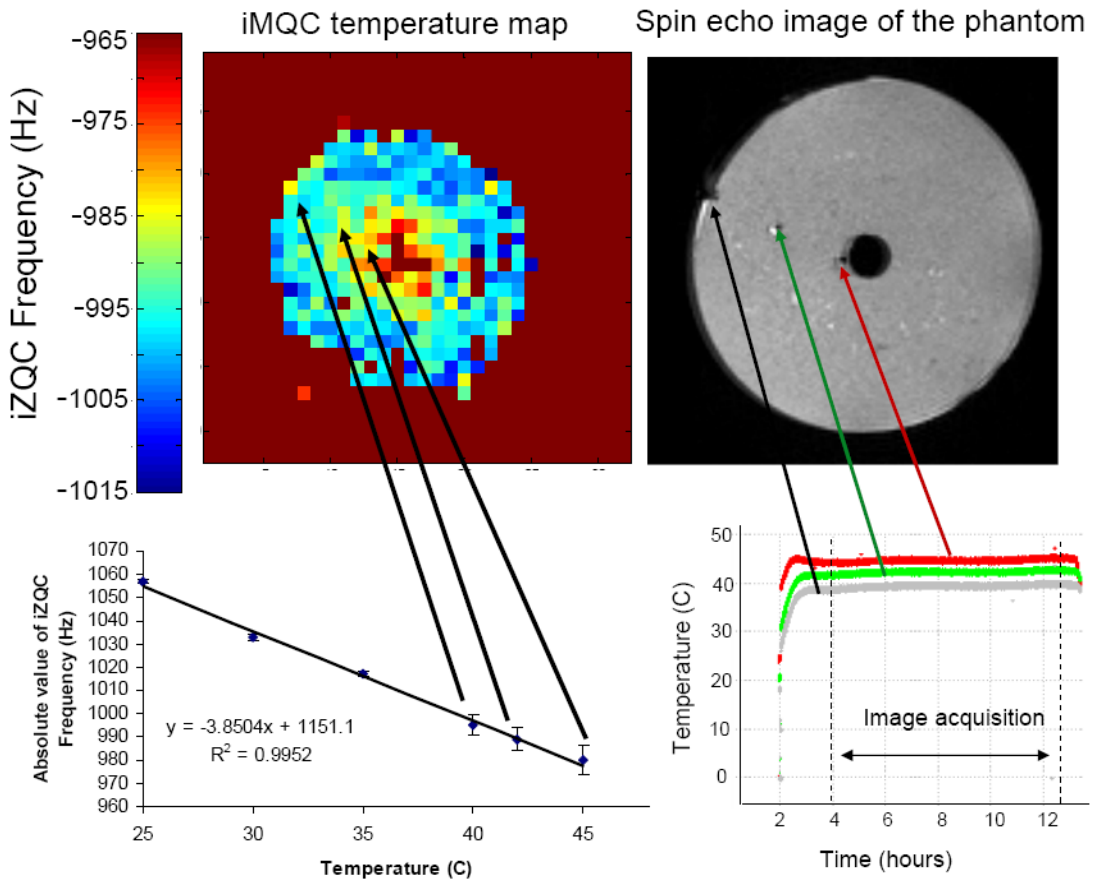

Figure 4-7- Top Right: Spin echo image of cream sample, axial slice. Arrows mark the position of the three fiber optic temperature probes, and the plot below shows the temperature recorded at each point. Top left: Temperature map of the heated sample showing the distribution of iZQC frequencies at the different temperatures. Bottom left: Graph of temperature vs. iZQC frequency. Three data points come from this experiment and the additional three data points come from single temperature measurements reported in [104]. The temperature images were acquired using a RARE acquisition, RARE factor = 4, 28 averages, 76 repetitions, 32 x 32 matrix, TE = 7.54 ms, TR = 1783 ms, t_1 = 1.87 ms, FOV = 4 cm, correlation distance = 0.093474 mm, spectral width of indirect dimension = 5000 Hz.

Note that the three additional data points in that figure come from single temperature imaging experiments described in [104]. The error bars for the plot of iZQC frequency vs. temperature were determined by the standard deviation of the pixels in

the image. For the points coming from the phantom with the temperature gradient, the reported error comes from the standard deviation of surrounding 8 pixels. For the data points from the single temperature phantoms, the error was determined by taking the standard deviation of the entire image. The correspondence between these and the liquid state results further establishes that iZQCs provide a measurement of temperature on an absolute scale.

All the images had a standard deviation below 2 Hz, which means that the accuracy of the method was within 1°C, which is within the acceptable limits for hyperthermia applications. The sensitivity of this experiment is best demonstrated by using it to detect RF heating in a sample. A phantom of heavy cream was imaged using a RARE sequence, and the RARE factor was increased from 1 to 8 to increase the SAR experienced by the sample. The HOT sequence appears to be able to detect this slight temperature increase, as shown in Figure 4-8.

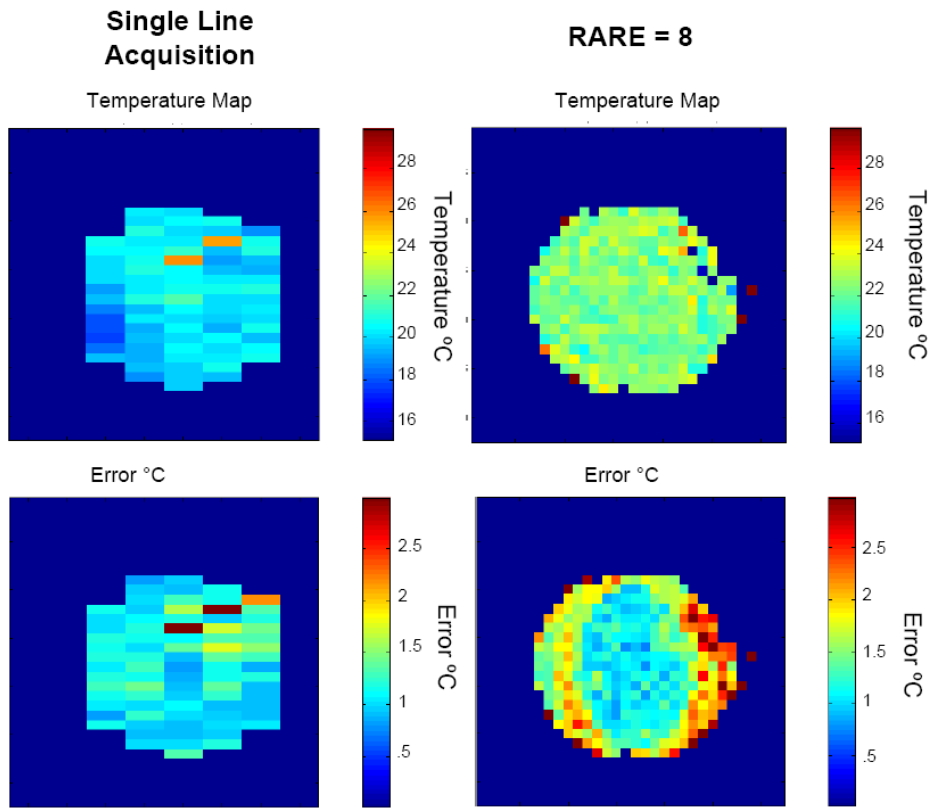

Figure 4-8 - The sensitivity of the iMQC temperature imaging sequence is demonstrated by looking at the heating effects of RF pulses. In the top left image, the temperature map was generated using single line acquisitions. The same experiment was done again, but this time using a RARE acquisition (top right image). The figures on the bottom are confidence intervals for each of the images on the top. The application of 8 additional pulses elevates the sample temperature by about 1 ºC, which is detected by the iMQC temperature map. Scan parameters for the RARE=8 experiment: 16 averages, 50 repetitions, TE = 8 ms, TR = 2 s, t_1 = 1.87 ms, correlation distance = 0.06406 mm, FOV = 4cm, 32 x 32 matrix. For the single line acquisition, the scan parameters were: 16 averages, 40 repetitions, 32 x 8 matrix, TE = 15 ms, TR = 2 s, t_1 = 1.87 ms, correlation distance = 0.06406 mm. Figure courtesy of Dr. R.T. Branca.

4.6.3 Results from two window HOT imaging experiments

The images in the previous section were acquired using the single window HOT sequence over the course of several hours. Figure 4-9 demonstrates the temperature

sensitivity of two window HOT thermography as applied on a sample of porcine adipose tissue. In this experiment, the temperature of the sample was controlled using a tube of heated water running through the center of the tissue. The temperature of the water was gradually increased, and the sample was imaged every two minutes using the two window HOT sequence. The images show both the dynamic heating of the sample throughout the experiment, as well as a temperature gradient between the heated core of the sample and the cooler surface of the sample. Since the frequencies of the two windows shift in opposite directions, the difference image is doubly sensitive to temperature and shifts by 6 Hz/°C.

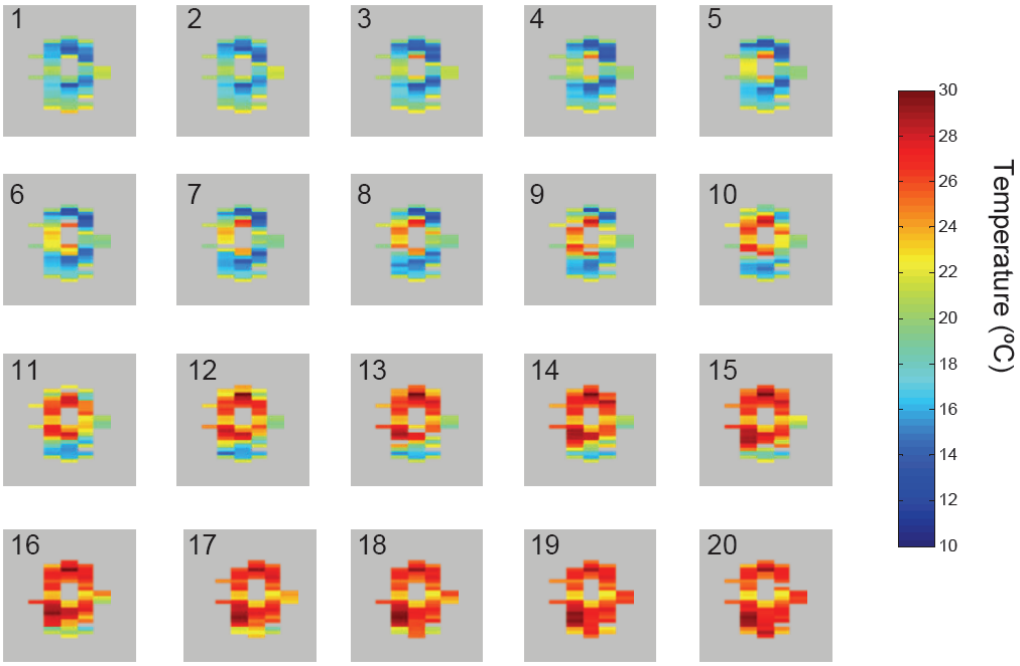

Figure 4-9 - iZQC temperature maps for the heating of porcine adipose tissue acquired every 2 minutes using the two acquisition pulse sequence. Increasingly hot water was pushed through a tube running through the center of the tissue. The sample

was imaged every two minutes using the two window HOT sequence. Each individual image is numbered to indicate the order of the time course of the images. In these experiments, we initially acquired ten images typically spanning 10 ms of τ evolution. Once these scans verified iZQC evolution, the initial temperature map was made by fitting the phases of images 2 and 7 of the series. Subsequent dynamic thermometry was performed by repeatedly running the scan at the τ equivalent to image 7, and phase changes in each window were related to temperature changes. Temperature near the core was seen to increase from 14°C to 36°C as monitored by a temperature probe. FOV = 4 cm TE = 40 ms; TR = 2 s; mGT = 1 ms*8.4 G/cm; nGT = 1 ms*-21 G/cm; correlation distance = 0.0945 mm, t_1 = 3 ms; τ = 10.66 ms. Figure from[124]

4.6.4 Imaging Results from the four window HOT sequence

The four window HOT sequence allows for the imaging of both the iMQC temperature information as well as the acquisition of two additional SQC images. The SQC images separate the sample by chemical shift – one window showing the distribution of the on-resonance spins, and the other window showing the off resonance spins. *Figure 4-10* shows the results from a four window HOT sequence on a water/acetone phantom. The phantom has a 50/50 water and acetone mixture in the larger tube, and just water in the smaller tube (standard spin echo image of the two tubes is Figure 4-10e). In acquisition windows 1 (Figure 4-10a) and 2 (Figure 4-10b) only the larger tube shows up since those sequences only image samples in which there is a mixture of water and acetone (or on and off – resonance spins). In acquisition window 3 (Figure 4-10c), both tubes show up, since that acquisition window detects the on-resonance water spins, which are found in both tubes. Finally, in window 4 (Figure 4-10d) there is only the larger water and acetone tube, since that acquisition only detects the off resonance acetone spins.

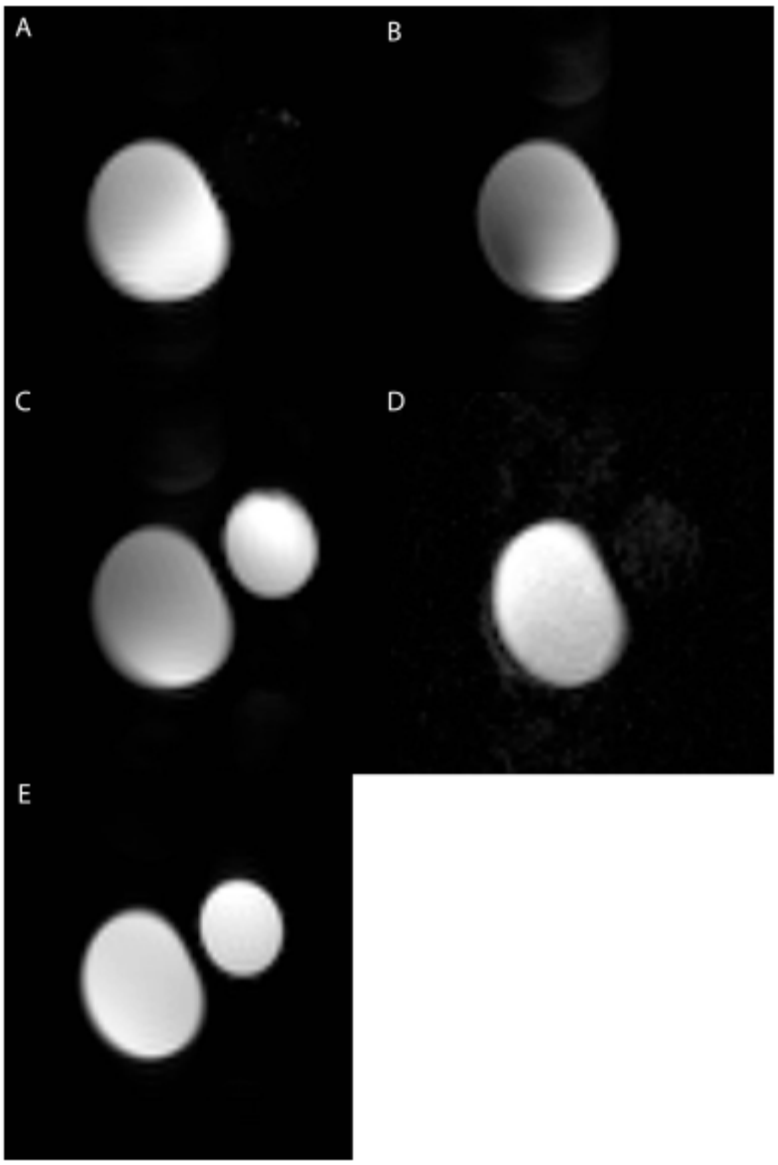

Figure 4-10 - Four window HOT on a tube of water and acetone next to a tube of water. Scan was done at 8.45 T, 64 x 64 matrix size, FOV = 4 cm, 4 averages, TE/2 = 100 ms. Correlation gradient m = 23 G/cm, correlation gradient n = 36.8 G/cm, t_1 = 4.1 ms, correlation distance = 0.0863 mm, τ = 12.5 ms, slice thickness = 2 cm. In figure 10A and B, we detect only the larger tube with a mixture of water and acetone. In C we detect both tubes, since they both contain water. In D, we detect only the larger tube, since it is the only one with acetone. Figure 10E shows a standard spin echo of this sample. All the images are on independent intensity scales. The SNR of A (water + acetone tube) is 488,

B (water + acetone tube) is 251, C (water + acetone tube) is 418 and (water only tube) is 595 and D (water + acetone tube) is 33.

4.6.4. Conclusion

The iMQC based temperature imaging method detects temperature by monitoring the difference in chemical shift between water and fat. This frequency difference is fixed for a tissue type, thus the iMQC frequency detected represents an absolute temperature measurement. We have demonstrated in several phantoms that iMQCs can be used to detect temperature on an absolute scale. With two novel filtering schemes, we can isolate the temperature-sensitive, inhomogeneity-insensitive iMQCs between water and fat spins. We present a thorough analysis of this sequence, and the mechanisms by which it isolates the desired signals. Using a water-fat phantom of heavy whipping cream, we demonstrated that this sequence could be used to acquire temperature maps which are an order of magnitude more accurate than conventional methods. We have also demonstrated that the method is sensitive enough to detect RF heating from standard imaging protocols. Temperature imaging methods using iMQCs are an exciting development in MR imaging of temperature, providing for the first time the ability to use MR to image temperature on an absolute scale. The high level of accuracy of iMQC temperature measurements, combined with the intrinsic insensitivity of the method to motion and susceptibility effects, make iMQC temperature imaging one of the most promising developments in MR temperature imaging. In particular,

iMQC methods have the potential to allow temperature imaging in tissues that were previously inaccessible due to large susceptibility differences and high concentrations of lipids, such as the breast. We believe that the HOT sequence can be adapted to study a wide range of applications relating to temperature.

Chapter 5 **GE Programming**

The conversion of pulse sequences from a research scanner (Bruker) to a clinical scanner (in this case, the console made by GE) is generally a painful procedure. The clinical scanners are designed with many safety safeguards, and the language is not designed to be easily manipulated. The complexity of the language and safeguards means that changes that you think you have made may or may not be executed by the scanner as you expect. The purpose of this chapter is to describe the basics of GE programming, and the necessary changes required to program the two window HOT sequence on a GE scanner.

5.1 Basics of GE programming

EPIC is the name of the language which controls the scanners created by GE. EPIC is based on C, and uses macros to do most of the work in the program. The main file (or source code) that is edited for GE programming is the .e file. All the files necessary to compile need to be located in the same folder named with the pulse sequence name. When starting a new pulse sequence, choose an appropriate starting program (the simplest sequence available is the grass sequence, a very simple gradient echo) and copy that program to a new folder. Open Imakefile, and change the name of the pulse sequence to your pulse sequence name. Rename the .e file to your pulse sequence name. Then prepare the folder by running the command “prep_psd_dir”. All following changes are made to the .e file.

The source code (.e file) is split during compilation by the EPIC preprocessor into two source modules which are found in the .host.c and .ipg.c files. The EPIC preprocessor uses directives (@), expands macros, and links other code. The host is the term used for the scanner console, while IPG (integrated pulse generator) is used to describe the real-time scanner hardware. The host file communicates with the rest of the Signa system through a set of user controlled variables called CVs (control variables). The complete set of CVs and a special set of IPG variables are created which control parameters such as pulse widths, start times and scan features. In the .e file there are 4 places where host routines can begin: cveval, cvinit, cvcheck and predownload. In cvinit the CVs are initialized, in cveval and cvcheck the CVs are evaluated and checked and in predownload the pre-calculations for the IPG are done. The IPG sections of the code are pulsegen, scan, aps and mps. Pulsegen is for waveform generation, scan and prescan are the code that controls the actual scan and prescan, respectively. Calculations done in the host parts of the code create CVs which are passed to the IPG sections of the code and is played out on the scanner. After the data is acquired, it is passed back to the host where the reconstruction occurs.

5.2 Writing the pulse sequence

5.2.1 Inserting gradients

The easiest waveforms to insert into your code are gradients. The standard gradient used is a trapezoid shape, but other shapes are available by using different

shape macros to call them. For a trapezoid shaped gradient, the command is "TRAPEZOID(waveform generator name, pulse name, position reference, pulse area, type, loggrd)". The trapezoid shape has several distinct portions created by the macro. There is the ramp up and ramp down as well as the plateau region. The beginning of the pulse is considered to be the start of the plateau region (figure 1).

Waveform generator name is the channel where the gradient is played. The options are ZGRAD (Z-gradient channel), XGRAD (X-gradient channel), YGRAD (Y gradient channel), RHO (RF channel), THETA (phase channel), OMEGA (phase channel), AUX (auxiliary channel), and SSP (sequence synchronous protocol). Adding a 'b' after the channel name indicated a "bridgeable" pulse. A bridgeable pulse allows two trapezoids to be combined into one which changes amplitude as shown in figure 2.

The pulse name is the name by which this pulse is referenced, and can be chosen by the programmer. It is important to give each pulse a unique name.

The position reference for the pulse determines where, in microseconds, the pulse is to be played. The first pulse (of any type) is usually given a hard coded position reference such as 1ms. All subsequent pulses are usually programmed to occur at some fixed time after the preceding pulse. For example, if you want your pulse (called grad2) to start 1ms after the end of the previous pulse (which we will call grad1), you use the command "pend(&grad1d, "grad1d", 0) + 1m+pw_grad2a". The 'd' at the end of the pulse name in this call refers to the ramp down portion (figure 1). The 'a' at the end of

the pulse name refers to the attack region of the pulse. The start of the shape is considered to be the beginning of the plateau region, so it is important to include the attack and decay portions of each pulse into your position references to prevent waveforms from overlapping. Other position references you can use are pmid (starts at the middle of the waveform), pbeg (starts at the beginning of the waveform).

The pulse area is defined as base*height of the pulse. The height is any 32 bit integer between -32767 and 32767, where the +/- 32767 refers to the maximum output of the gradient channel. The units of the pulse area are gauss*usec/cm. The helix pitch achieved by any gradient waveform depends on the gradient set used. For small animal imaging, the gradients sets are very strong, for the 2T magnet at CIVM the gradient strength is 40 G/cm, for the CIVM 7T, the gradients are 77 G/cm. Human sized scanners have much weaker gradients sets – the one in Radiation Oncology has a 2.5 G/cm gradient set.

Define type is an optional parameter (as indicated by the [] surrounding the name in the definition of TRAPEZOID), which defaults to 1. This parameter calculates the pulse width and amplitude of the plateau region of the pulse, as well as the size and duration of the attack and decay ramps. This parameter is passed to the ampslice function, and it will do nothing if define type is set to 0. Loggrd means logical gradient structure.

An example of a gradient call which will create a gradient that is opposite in sign and half the amplitude of grad1 is: “TRAPEZOID(ZGRAD, grad2, pend(&grad1, “grad1”, 0)+pw_grad2a, (int)*(-.5)*(pw_grad1+pw_grad1a+pw_grad1d), , loggrd);”

5.2.2 Wait times

There are several ways to control the timing of a sequence. The strategy that requires the least programming is to simply calculate the position calls such that there are wait times built in. For example, if you want to keep two gradients, gz1 and gz2 separated by the variable time opte, then simply starting gz2 using the position call pmid(&gz1, “gz1”, 0) + opte - .5*pw_gz2 – pw_gz2a. This position call for the gradient waveform timing will keep the two pulses separated by the CV opte.

An alternative method for programming in wait times is to program in a wait time using the WAIT macro. The wait macro behaves like a gradient and can be placed on any of the channels. The syntax for the WAIT macro is “WAIT(waveform generator name, pulse name, position reference, duration);”. An example of a WAIT call is: “WAIT(ZGRAD, wait1, pend(&rf1, “rf1”, 0), opwait1);” where opwait1 is a user controlled variable for the wait time.

Calculations for the duration of a wait time (or any variable) can be done either in cvinit or cveval. In those sections you can define the duration of the variable that controls the wait time. For example, if you want to define a wait time that keeps rf1 and

rf2 separated by the value t1, then you can calculate the actual wait time on the board, t1, using the following command: opt1=t1-.5*pw_rf1-.5*pw_rf2.

5.2.3 RF pulses

Inserting an RF pulse is slightly more complicated than a gradient pulse or a wait time. Any of the shapes available for the gradients are available for RF pulses. The most common shape is the sinc shape, which is called with the SINC function. The syntax for the SINC macro is: "SINC(waveform generator name, pulse name, position reference, duration, amplitude, resolution, sinc cycles, slice offset, alpha, loggrd);". Sinc cycles refers to the number of zero crossings on either size of the zero point divided by two. The default value is 1. Slice offset is the frequency offset of this pulse, which is an optional parameter that defaults to 0. Alpha is another optional parameter which defaults to .46 (Hamming window), as defined by:

$$(1 - alpha) + (alpha * \cos \frac{2\pi t}{\tau}) \tag{70}$$

Where τ is the number of points in the shape, and t is the total length of the shape. After inserting the appropriate waveform shape macro into the pulsegen section of the source code, additional pieces of code are needed to create an RF wave. First in prescan, the amplitude of the RF pulse needs to be defined. The amplitude of the pulse is written as: "ia_rf1=.5*max_pg_iamp * (*rfpulse[RF1_SLOT].amp);". This code tells the compiler to look at the RF1_SLOT in the associated gradient and RF pulse file (for example, the file is

called grad_rf_grass.h for the grass pulse sequence). In that file are different definitions of the pulse and it is where some of the SAR calculations are done. The above command scales the pulse amplitude relative to the maximum amplitude as defined by the RF1_SLOT. In the scan function, define the amplitude of the pulse using the command "setiamp(ia_rf1, &rf1, 0);". The structure of this call is setiamp(amplitude, pulse name, index). The index allows for repetitive occurrences of the pulse instruction starting with index = 0. The same code is also inserted into the prescan function.

The next step is to define the frequency of the pulse. This is only necessary if you want to define a new frequency for the pulse you are creating (for example, if you want to be able to put this pulse off resonance). If you don't want to have a unique frequency for your pulse, it is only necessary to modify the amplitude commands, not the frequency ones. First, in the @rsp section a pointer to integer is created using the command "int *rf1_freq;". Then, in the scan function, memory is allocated for the frequency with the following code: "rf1_freq=(*int)AllocNode(sizeof(int));". Then the frequency is set in the slice loop with the setfrequency command: "setfrequency(offset, pulsename, 0);". The same commands are placed in the prescan function.

5.2.4 External Waveforms

If you want to use a pulse shape that is not part of the standard library of shapes, you can create a shape and insert it into the code. First the pulse needs to be made in an

external program such as Matlab. You should start with the array of numbers that describe your pulse shape. These numbers should be scaled to be signed 16-bit numbers (i.e. to fall between ± 32767). Each value should be even except for the last number that should be odd. To generate a .rho file you then just have to write these values into a binary file as 16-bit integers in big-endian format. In Matlab or C-code you can do this with an "fwrite( )" call. Note that in Matlab you can open an output file in big-endian mode with a 'b' modifier at the end of the fopen call such as fopen('test.rho','w','b'); and in C/C++ code you should look up what the function ntoh and hton do (I think you want hton - meaning host to network, where big-endian is the network ordering in this situation). Once you have a binary file of 16 bit integers you should run the command "xlatebin" in the terminal on them to make a GE external file format. This command should be in your default EPIC ESE install path and is run using "xlatebin -o outfile.rho infile" where infile is the binary file you made and outfile.rho is the name of the final output external waveform file.

Once the pulse shape is made it can be inspected in the RF Tool which is part of WTools, the simulator package that is in the EPIC environment. Running the rfstat command in the terminal on the pulse will tell you the area, duty cycle and effective width of the pulse needed for power calculations. While this is not necessary to get the code to compile, if you want to use your external waveform on people, it is necessary to

insert the necessary code for SAR calculations. The B_1 of your pulse can be calculated using the following relationship:

$$B_{1,yourpulse} = \frac{area_{sinc} * PW_{sinc} * B_{1,sinc}}{area_{yourpulse} * PW_{your_pulse}} \tag{71}$$

The area of the sinc pulse is .2506, PW of the sinc is 3.2 ms, and the peak B_1 of a 90° pulse is 73mG. The area of your pulse and PW of your pulse are given by the rfstat command. In pulsegen, use the SPACESAVER macro to allocate space. Call addrfbits to generate the appropriate SSP packets. Note that the frequency packet gets sent out 260 microseconds BEFORE the start of the pulse. Call createinstr to generate the necessary IPG instructions. Call AllocNode to allocate local memory for the pulse. Call uextwave to load the pulse into local memory. Call movewaveimm to move the pulse from local memory to IPG memory. Call FreeNode to deallocate the local memory. In the appropriate RSP routine, be sure to properly update the pulse instruction amplitude. The external waveform can be inserted into the source code using the macro EXTWAVE. The syntax for this command is: ”EXTWAVE(waveform generator name, pulse name, position reference, duration, amplitude, resolution, filename, slice offset, loggrd);”. The resolution of the pulse is the number of points and the filename is the name of the location where the pulse is. The default directory is the /usr/g/bin directory. In addition to the EXTWAVE command, the amplitude needs to be defined as is done with a standard RF pulse.

5.2.5 Phase Cycling

Phase cycling is done in the scan section of the pulse sequence. There is no phase cycling in the prescan. To phase cycle the phases of the pulses are defined for each step of the view loop and the storage of the data is controlled by the loaddab routine.

Within the scan function are a series of embedded loops that control the actions during the slice, view and excitation cycles. The outer loop is the slice loop, the inner loop is the view (phase encoding step) loop. The data acquisition occurs in the view loop. The data is stored in the DAB (data acquisition board) and is controlled by the loaddab macro with the syntax "loaddab(pulse, slice, echo, oper, view, acqon_flag, ctrlmask);". The pulse is the same as the pulse names such as echo1 (the name of the acquisition as defined in the pulsegen section). Slice and echo are the slice number and echo number. Oper is the operation field and has four possibilities: DABSTORE, DABADD, DABSUBCNTS, DABSUBXCVR. DABSTORE stores the receiver data, DABADD adds the data, DABSUBCNTS subtracts the contents from the receiver and DABSUBXCVR subtracts the receiver data from the contents. View is the current view number, acqon_flag is the acquisition on/off flag with four possible entries: DABNORM, DABCINE, DABON, DABOFF. The definition of these terms is found in pulsegen.h. Ctrlmask is the DAB activity mask and has eight possible commands: PSD_LOAD_DAB_OFF, PSD_LOAD_DAB_SLICE, PSD_LOAD_DAB_ECHO, PSD_LOAD_DAB_OPER, PSD_LOAD_DAB_VIEW, PSD_LOAD_DAB_ACQON,

PSD_LOAD_DAB_ACQON_RBA,PSD_LOAD_DAB_ALL. This routine will add slice, echo and view numbers to the programmable bits array and then moved to hardware memory.

The phase of the pulses is controlled by the routine "setiphase(phase, pulse, index);". It sets the phase (as defined by the first entry) in integer format. The index allows for repetitive occurrences of the phase bits array for the associated pulse. The default value is 0, and if the value is set to -1 then every phase bit array associated with the pulse will be set.

To phase cycle, the phase of the pulse is changed as a function of the counter for the excitation loop using a modular format. An example of phase cycling where the pulse, rf1 and the acquisition, echo1, cycles between 0° and 180° is given below.

```
for( view = 1; view < (opyres + 1); ++view )
{
      dabop= DABSTORE;  /*first view acqu should be stored*/

   for( excitation = 0; excitation < opnex; ++excitation )
   {
                              if(excitation==0)
                              {
                              dabop = 0;
                              }
                              else
                              {
                              dabop = DABADD;
                              }

                        setiphase(iphase90*(excitation%2), &rf1, 0);
                        setiphase(iphase180*(excitation%2), &echo1, 0);
```

```
                    setiampt( viewtable[view], &gy1, 0 );

                /* loaddab loads SSP packet used by data acquisition */
                loaddab( &echo1, slice, 0, dabop, view, DABON,
PSD_LOAD_DAB_ALL );
                startseq( 0, (short)MAY_PAUSE );
              } /* end-of-excitation loop */
            }  /* end-of-view loop */
```

5.2.6 Adding buttons, changing default values, allowed values and CVs

Once your sequence is on the scanner, the user will want to be able to view and manipulate the available variables. There are several locations where this can happen. When the sequence is in the process of being prescribed, the user CV button can be enabled allowing for user defined variables to be viewed and manipulated. Once the sequence is saved and downloaded, the CVs can be manipulated under the Research CV button.

Enabling the User CV button is done in cvinit. To enable the User CV button, use the call “pititle=1;”. The number of available variables needs to be defined using the call “piuset = (use0 | use1 | use2);”. This tells the scanner that there will be 3 user CVs to manipulate in the User CV window. Then the three CVs have to be defined, including min, max and default values. The syntax for defining these is:

```
cvdesc(opuser1, "tau time");
cvmin(opuser1, 240);
cvmax(opuser1, 8000);
cvdef(opuser1, 480);
```

```
opuser1=480;
optau=opuser1;
```

There are also several variables that always appear when making a prescription such as TE (echo time), TR (repetition time), Freq (frequency encoding size), Phase (phase encoding size) and NEX (number of excitations or averages). Most of these have predefined minimum and maximum values that are defined in the source code. For example the matrix size usually has a minimum allowed resolution of 128 x 128. It is possible to make this number smaller, but it has to be changed in the source code. By changing the code as shown below, the numbers that appear when the box is clicked for the frequency resolution is changed to show frequency encoding sizes of 32, 64, 128 and 256, and the minimum allowed resolution is changed from 128 to 8.

```
cvmin(opxres, 8);
pixresnub = 15;      /* x resolution - bitmask */
pixresval2 = 32;
pixresval3 = 64;
pixresval4 = 128;
pixresval5 = 256;
```

5.3 Compiling

After the source code is written, it is necessary to compile the program to create the necessary code to operate the scanner. In the directory where the source code and

Imakefile are located, run the command “psdqmake clean” to clean the directory, then compile for simulation using “psdqmake sim”. This is not a full compile, it is quicker and is used for debugging. A successful compilation will give the message: /usr/home/ese124/psd12/hot2aq/tgt succeeded.

```
Total makes to do:   3
Succeeded:           3
Failed:              0
Yet to build:        0
Percent complete:    100%
```

After the code is compiled, the simulator, WTools, can simulate the code and check for errors in timing and waveform generation. To run WTools, use the command “WTools.x &”. Once the WTools window opens, check that the name of the psd file displayed is correct in the main command line. Then check the psd under Analysis -> CheckPSD. If everything is correct, the message “check psd successful” will appear. The next step is to define the standard variables for the sequence you are running. The evaluation tool is located under Analysis -> EvalTool. In the evaluation tool, you can type in the names of some of the CVs in the sequence and hit enter. The default values for that variable will appear, and can be edited. After defining a few CVs, you can save the parameters by first setting the eval mode to manual, and then clicking the eval button several times. Only doing it once is not sufficient to calculate all the CV relationships. Then click the save button and save the file. Then you can simulate the real time application of your sequence using the MGD Sim tool located in Analysis ->

MGD Sim. Here, click the load CVs button, then refresh twice. The message "entry completed" will appear if this is successful. Then click the PulseGen button, and refresh twice. The same message will appear if this is successful. To view a graphical output of your sequence, click on the PlotPulse button which will display a graphical representation of the pulse sequence. If at any point the simulator runs into an error, an error message will appear in the main window of WTools.

To compile the code for use on the scanner, first clean the directory (psdqmake clean) and then you can compile for hardware using one of the following commands: psdqmake hw, psdqmake all or hese pulse sequence name. The first two commands output the two files for the scanner to your working directory, and the hese command puts the file into the 2signa folder which is exclusively for transfer to the console. At CIVM, the pulse sequence is transferred to the scanner by ftp. To ftp to the scanners at CIVM, first make sure you are in the correct directory (where your compiled files are located). The type "ftp scanner name". The 2T is onnes and the 7T is kamy. Then you put the file in the /usr/g/bin/psd directory. Once you have put your code on the scanner, you have to change the permissions for the file so that the scanner can read, write and execute the code. To do this, go on the scanner, open the C shell, and move to the /usr/g/bin/psd directory. Then type "chmod 775 *". This makes all the code in that directory read, write and executable.

5.4 Troubleshooting Code

One of the big issues associated with programming on the GE console is that the code you have created does not behave as expected. It is recommended that you always check the execution of the pulse sequence using an oscilloscope to confirm that the sequence is playing out as expected. The oscilloscope can be used to confirm that the scanner is playing out the correct timings and shapes that were programmed into the source code. Often you will encounter errors on the scanner that you did not encounter when you were simulating. If the scanner freezes for several minutes and then releases, there is usually an error message located in the log which is found by clicking on the box at the top left corner of the screen. In addition, sometimes variables can get confused in the scanner after several crashes, so a TPS reset is a good way to confirm that the problem you are having is with your code and not the scanner.

5.5 Analyzing Data

The default for the GE scanners is not to save the raw data file, only the image file. To save the raw data, set the CV autolock to 1. This will save the raw data into the /usr/g/mrraw folder. All the data is stored in "P-files" – files with a name starting with a P followed by some randomly assigned numbers and ending with .7. The P files are 16 bit signed integer files. The first part of the file is a header and the size of that header depends on the version of Signa that you are running. The header size for 12x (CIVM as of 2010) is 66072 and is 144408 for 14x (Radiation Oncology scanner).

5.5.1 Acquiring Incremented Data

While it is possible to program a sequence that will automatically increment a variable by inserting an additional loop into the scan function, the much simpler way to run a series of experiments that vary by a changing parameter is to use one of the ATP scripts. The scanners at CIVM come with the script "multi2D" which will run a series of scans from one prescription in which one variable changes. This script is used to run the temperature imaging experiments as well as the spectroscopy experiments. The script is located in the /usr/g/bin directory. To use it, first load your scan and run through the prescan. Then go into the C shell on the scanner and change directories into the /usr/g/bin directory and type multi2D. A series of prompts will appear to define the variable that is changing from scan to scan, as well as the name of the files to save the data to. The script names the files differently than the standard P file naming routine. The name will start with PT and will not end with the .7. CIVM uses a list of run numbers located in a log book to ensure that the same numbers aren't assigned.

5.5.2 Special Considerations at CIVM

The scanners at CIVM are custom designed scanners, which can result in some unique features and special considerations. First, the consoles controlling the scanners believe the field strength of all the magnets is 1.5T, while in reality the magnets are at 7T, 2T and 9T. This can cause some problems. First, at 7T and 9T you cannot increment the phase of the pulse (i.e. change the echo time) and see the signal phase change in the expected

circular pattern. At 2T, the frequency is close enough to the 1.5T and this is not a problem.

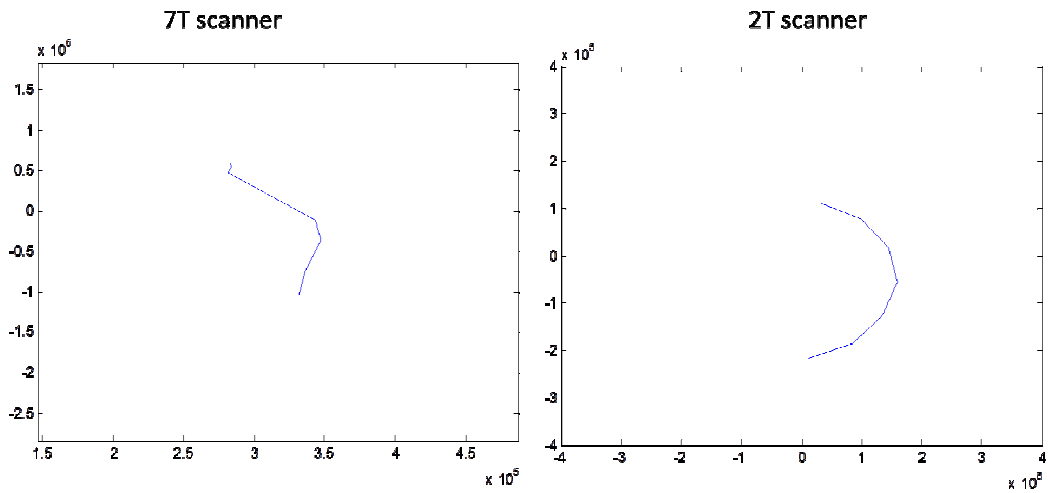

Figure 5-1 - Comparison of signal phase in a spin echo experiment. A sample of cream was imaged on both the 2T and 7T scanner using a spin echo sequence. The echo time was incremented between images, and the phase of two representative pixels is presented above. On the 2T scanner, the phase change between images is exactly as predicted, while the phase change on the 7T is unpredictable and changes greatly between scans. Images were taken with an increment size of 240 us between images.

An additional problem is that the slice profile is not as clean as it is on a clinical system. The scanner uses an envelope feedback system where you describe a waveform and then the scanner computes the frequency response of that pulse, and adjusts it to provide a cleaner slice profile. The envelope feedback system believes the system is at 1.5T, and adjusts the pulse accordingly. Since the scanner is not at 1.5T, this just causes the pulse to be different than expected, and provides a less clean slice profile as shown in Figure 5-2

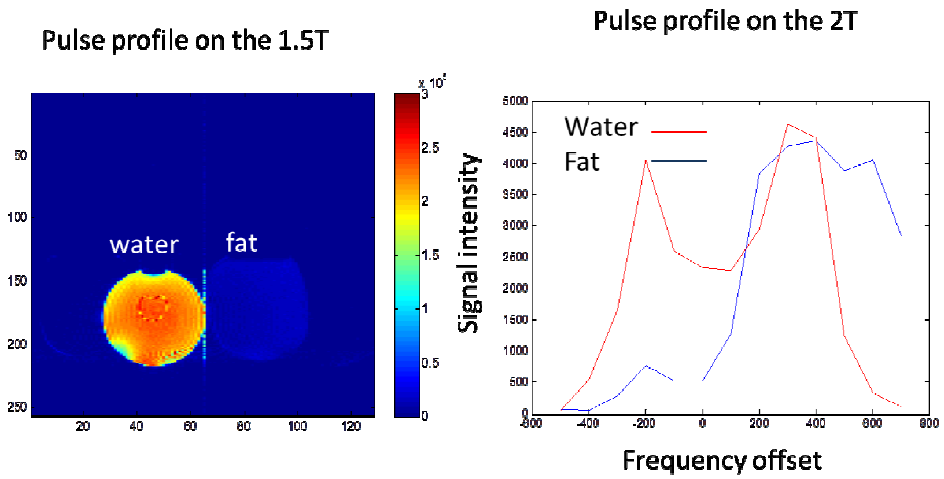

Figure 5-2 - Comparison of the frequency selection of a standard sinc pulse on the 2 T and 1.5 T scanners. The frequency selection of the clinical 1.5 T scanner is much cleaner than that of the 2T scanner, allowing for improved frequency selection.

5.6 Demonstrations of iMQCs on the GE scanner

The first sequence programmed on the scanner was a standard iDQC sequence. To confirm that the sequence was creating iDQCs, images were acquired with the correlation distance along x, y and z in a bottle of water.

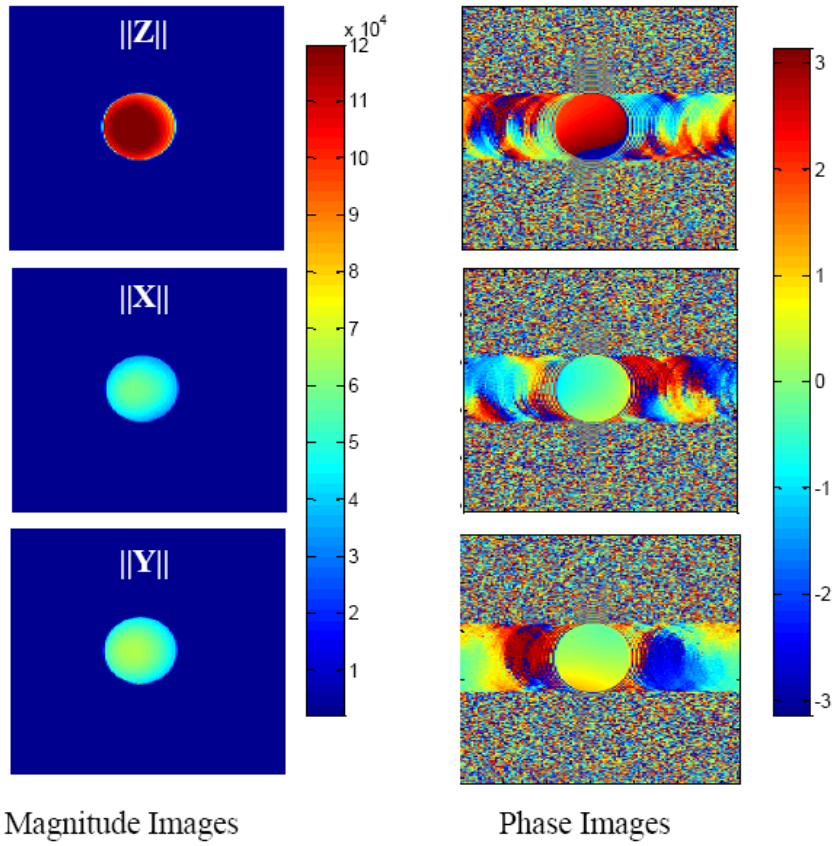

Figure 5-3 - Confirmation of iDQC signal on the GE scanner. Images were of a 50 ml tube of water taken at 7T. TE=60ms, tau = 6.2 ms, correlation distance = 64 μm, 20 mm slice, FOV = 10 cm x 10 cm, matrix = 256 x 128.

This pulse sequence was also applied in vivo and provided the following human brain iDQC image. This image demonstrates that the iDQC sequence works on both the

CIVM research scanner as well as the scanner located in Radiation Oncology.

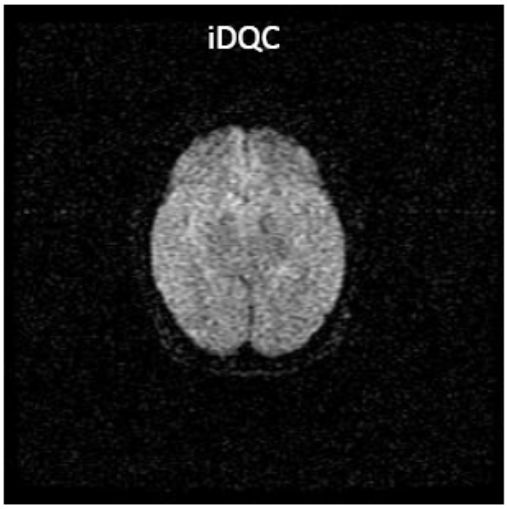

Figure 5-4 - iDQC image of a human brain. TE=20 ms, correlation distance = 140 μm along z, 2 cm slice, tau = 1ms, matrix = 256 x 128.

After confirmation that there is sufficient signal on the clinical scanner to detect iDQC (the basis of the HOT sequence), the next step was to program the HOT sequence on the scanner and use it to detect the mixed spin iMQCs used in temperature imaging using a spectroscopy sequence. It can be challenging to unravel all the different contributions to the signal in an imaging experiment, therefore, it is important to first confirm that the desired signal is being generated by running a 2D spectroscopy experiment.

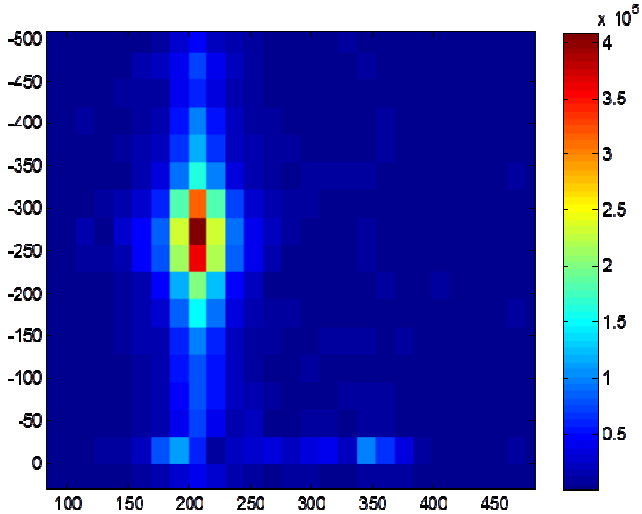

Figure 5-5 - 2D spectrum of cream using the HOT pulse sequence (acquisition of window 1). The 2D spectroscopy experiment on cream confirms that the main signal detected comes from the mixed spin iZQC crosspeak. This experiment was done with 4 averages, TE/2 =30 ms, TR = 1s, offset = 200 Hz, receiver bandwidth = 15.8 kHz, indirect detection bandwidth = 1000 Hz, 32 reps.

The next experiment was a demonstration in a cream phantom that there was sufficient signal to detect a clean temperature map. The first imaging results are presented in Figure 5-6.

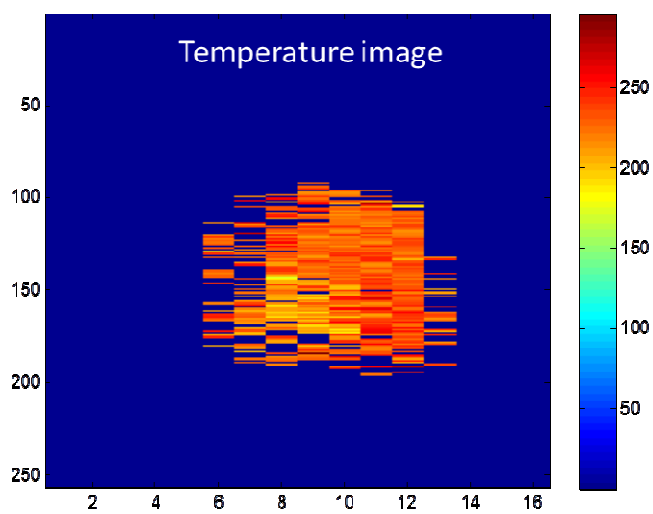

Figure 5-6 Demonstration of the HOT sequence on a cream phantom (milk jug filled with cream) on the clinical 1.5 T scanner. The signal intensity is still fairly low,

limiting the quality of the temperature detection with this method. Matrix = 256 x 16, TE/2=30 ms, TR=1s, FOV= 30 cm^2, no slice selection. Image was taken with the HOT sequence acquiring the first window only.

The above figure shows that temperature detection on the clinical scanner is possible, but more work is needed to improve the signal intensity to allow for in vivo temperature measurements. The future work on this project includes careful calibration of each individual pulse in the sequence, as well as optimization of the timings in order to improve the SNR. Once the SNR has improved enough, this sequence will be tested in vivo on healthy human breast tissue.

Chapter 6 – ^{1}H – ^{13}C Intermolecular Multiple Quantum Coherences

Localized in vivo spectroscopy has been shown to provide useful insights about the metabolic state of tissues. Standard in vivo magnetic resonance spectroscopy (MRS) has been predominantly done by observing the proton signal, due to the larger sensitivity to proton signals than other nuclei. However, there are several confounding issues with proton MRS. First, the large water signal dominates the spectrum, making the detection of less abundant metabolites difficult. Water can be suppressed with water suppression methods, but these methods also suppress any resonances that are near the water line. Second, the range of proton chemical shifts is only about 12 ppm, causing many resonances to overlap. Carbon spectroscopy has the potential to overcome both these obstacles, but it suffers from a much lower signal to noise. The gyromagnetic ratio of carbon is about ¼ that of proton, and the NMR detectable carbon nucleus, ^{13}C, has only 1% natural abundance. Metabolic studies using localized natural abundance ^{13}C have been used to monitor glucose metabolism with some success [125-127], but these require long acquisition times (up to 120 minutes), making routine natural abundance ^{13}C MRS impractical. Alternative approaches using the infusion of ^{13}C glucose have been done [128], improving the SNR of carbon, but this still requires many signal averages.

Hyperpolarization techniques that greatly enhance the SNR of carbon (and other nuclei) have been developed. Dynamic nuclear polarization[62] has recently become one

of the most common methods for carbon polarization, allowing for increases in SNR of greater than 10,000. Using hyperpolarization techniques, many groups have been able to study glucose metabolism with a greater sensitivity than before [25, 38, 39, 42, 43, 45, 47-50, 52, 53, 55, 58]. Unfortunately, most of these studies have low spectral resolution, preventing the discrimination of nominally similar compounds. For applications of hyperpolarized pyruvate, the lack of spectral resolution has not been an issue because there is adequate distance between the detected compounds. For applications other than the glycolysis of pyruvate, this lack of spectral resolution will make the identification of different metabolites difficult. For example, the resonances for the C_2 of glucose, NAA, choline, creatine and glycine are all within 2-3 ppm. In addition, many of the studies in vivo have used "incoherent imaging" (localized spectroscopy after one pulse), which is dominated by magnetic field inhomogeneity that further broadens the lines and makes the identification of these metabolites more challenging.

Intermolecular multiple quantum coherences (iMQCs) have been shown to provide inhomogeneity compensation, even in vivo. Recent studies have demonstrated [129] that proton iMQC spectroscopy techniques can be applied in vivo to provide narrow, high-resolution spectra, even for large voxels and in the presence of magnetic field inhomogeneities. Carbon-carbon iMQCs have been demonstrated using hyperpolarized reagents as demonstrated in the next chapter and in [40], but the signal intensity of iMQCs decays rapidly as the sample becomes more dilute. Observing

iMQCs between different nuclear species allows the properties of the two spin types to be combined. For example, the detection of proton-carbon iMQCs is possible without hyperpolarization[105]. Using proton-carbon iMQCs, it is possible to obtain carbon spectra with inhomogeneity compensation without depending on a high concentration (as is the case for carbon-carbon iMQCs).

6.1 Properties of Proton – Carbon iMQCs

6.1.1 The CRAZED sequence with heteronuclear iMQCs

The physics that generates homonuclear iMQCs is almost identical to that which creates heteronuclear iMQCs, but with some subtle changes. The heteronuclear iMQC signal still comes from the higher order terms of the density matrix, but instead of I and S representing different chemical species, they now represent different nuclear species (both spin ½). The pulse sequence for generating heteronuclear iMQCs is similar to the CRAZED sequence, but with a few changes to accommodate the differences in γ. The standard pulse sequence for heteronuclear iMQCs is given in Figure 6-1.

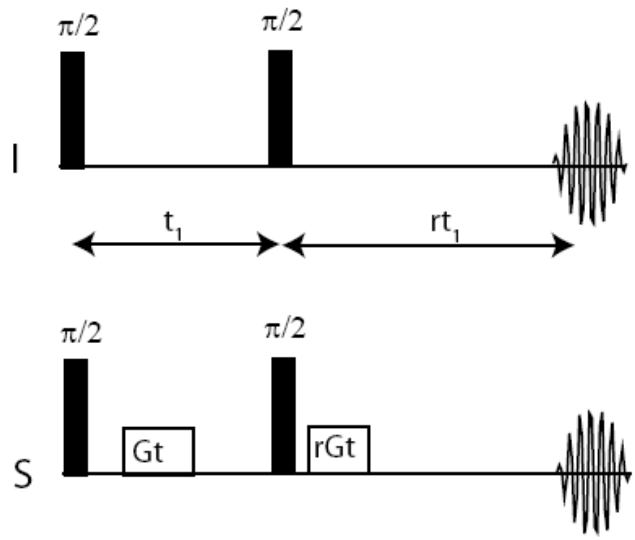

Figure 6-1 - Pulse sequence for the detection of heteronuclear iMQCs. This sequence is very similar to the CRAZED sequence, except for the gradient ratios and timings. Note that the gradients act upon both spin types.

The sequence starts with a π/2 pulse that takes the two-spin $\mathbf{I}_z\mathbf{S}_z$ terms to both DQC and ZQC terms. First, we will describe the timings and gradients for a ZQC experiment. The ZQC term looks like $\mathbf{I}^+\mathbf{S}^-$ and evolves during t_1 at $(\omega_I\text{-}\omega_S)t_1$:

$$\mathbf{I}_z\mathbf{S}_z \xrightarrow{\pi/2,t_1} \mathbf{I}^+\mathbf{S}^- e^{i(\omega_I-\omega_S)t_1} + \mathbf{I}^-\mathbf{S}^+ e^{i(\omega_I-\omega_S)t_1} \tag{72}$$

The first gradient creates dephasing that is different for each spin because they have different γ values.

$$\begin{gathered}\mathbf{I}^+\mathbf{S}^- e^{i(\omega_I-\omega_S)t_1} + \mathbf{I}^-\mathbf{S}^+ e^{i(\omega_I-\omega_S)t_1} \xrightarrow{Gt} \\ \mathbf{I}^+\mathbf{S}^- e^{i(\omega_I-\omega_S)t_1} e^{i(\gamma_I-\gamma_S)Gt} + \mathbf{I}^-\mathbf{S}^+ e^{i(\omega_I-\omega_S)t_1} e^{-i(\gamma_I-\gamma_S)Gt}\end{gathered} \tag{73}$$

The second π/2 pulse converts the two-spin iZQC terms into two-spin SQC terms:

$$\begin{gathered}\xrightarrow{\pi/2} \mathbf{I}^+\mathbf{S}_z e^{i(\omega_I-\omega_S)t_1} e^{i(\gamma_I-\gamma_S)Gt} + \mathbf{I}^-\mathbf{S}_z e^{i(\omega_I-\omega_S)t_1} e^{-i(\gamma_I-\gamma_S)Gt} + \\ \mathbf{I}_z\mathbf{S}^- e^{i(\omega_I-\omega_S)t_1} e^{i(\gamma_I-\gamma_S)Gt} + \mathbf{I}_z\mathbf{S}^+ e^{i(\omega_I-\omega_S)t_1} e^{-i(\gamma_I-\gamma_S)Gt}\end{gathered} \tag{74}$$

At this point dipolar couplings are reintroduced, converting the two-spin SQCs into detectable one-spin SQCs:

$$\begin{aligned}\mathbf{I}^{+}e^{i(\omega_I-\omega_S)t_1}e^{i(\gamma_I-\gamma_S)Gt}+\mathbf{I}^{-}e^{-i(\omega_I-\omega_S)t_1}e^{-i(\gamma_I-\gamma_S)Gt}\\ \mathbf{S}^{-}e^{i(\omega_I-\omega_S)t_1}e^{i(\gamma_I-\gamma_S)Gt}+\mathbf{S}^{+}e^{-i(\omega_I-\omega_S)t_1}e^{-i(\gamma_I-\gamma_S)Gt}\end{aligned} \tag{75}$$

The amplitude of the subsequent gradient needs to be large enough to undo the dephasing of the first gradient, and since $\gamma_I \neq \gamma_S$, the standard size of the second gradient for an iZQC experiment (i.e., 0 gradient) is not correct. Instead the gradient has an amplitude r, such that for the detection of the S spins you need:

$$\begin{aligned}\gamma_I Gt-\gamma_S Gt+\gamma_S rGt=0\\ r=\pm\left(1-\frac{\gamma_I}{\gamma_S}\right)\end{aligned} \tag{76}$$

And for the detection of the I spins the gradient ratio is:

$$\begin{aligned}\gamma_I Gt-\gamma_S Gt+\gamma_I rGt=0\\ r=\pm\left(1-\frac{\gamma_S}{\gamma_I}\right)\end{aligned} \tag{77}$$

Assuming that we want to detect the S spin coherences, we apply a gradient of size r as defined by eq. (76). This results in an overall signal of

$$\begin{aligned}\mathbf{I}^{+}e^{i(\omega_I-\omega_S)t_1}e^{i(\gamma_I-\gamma_S+r\gamma_I)Gt}+\mathbf{I}^{-}e^{-i(\omega_I-\omega_S)t_1}e^{-i(\gamma_I-\gamma_S-r\gamma_I)Gt}\\ \mathbf{S}^{-}e^{i(\omega_I-\omega_S)t_1}e^{i(\gamma_I-\gamma_S-r\gamma_S)Gt}+\mathbf{S}^{+}e^{-i(\omega_I-\omega_S)t_1}e^{-i(\gamma_I-\gamma_S+r\gamma_I)Gt}\end{aligned} \tag{78}$$

Since we have chosen $r=-1+\frac{\gamma_I}{\gamma_S}$, the signal in equation 7 reduces to

$$\begin{aligned}\mathbf{I}^{+}e^{i(\omega_I-\omega_S)t_1}e^{i\left(-\gamma_S-\frac{\gamma_I^2}{\gamma_S}\right)Gt}+\mathbf{I}^{-}e^{-i(\omega_I-\omega_S)t_1}e^{-i(\gamma_S-\frac{\gamma_I^2}{\gamma_S})Gt}\\ \mathbf{S}^{-}e^{i(\omega_I-\omega_S)t_1}e^{i(0)Gt}+\mathbf{S}^{+}e^{-i(\omega_I-\omega_S)t_1}e^{-i(0)Gt}\end{aligned} \tag{79}$$

Thus, the only signals which are refocused by the second gradient are the S terms. The echo will appear at a slightly different timing as well, since ω_I and ω_S are very different. The signal will appear at a time rt_1, which is defined as

$$rt_1 = \left(1 - \frac{\omega_I}{\omega_S}\right) t_1 \tag{80}$$

A similar calculation can be done for the heteronuclear iDQC terms, and these terms require a different gradient ratio and a different timing. The $\pi/2$ excitation pulse, t_1 and gradient Gt create signal of the form

$$\mathbf{I}_z\mathbf{S}_z \xrightarrow{\pi/2, t_1, Gt} \mathbf{I}^+\mathbf{S}^+ e^{i(\omega_I+\omega_S)t_1} e^{i(\gamma_I+\gamma_S)Gt} + \mathbf{I}^-\mathbf{S}^- e^{-i(\omega_I-\omega_S)t_1} e^{-i(\gamma_I+\gamma_S)Gt} \tag{81}$$

The mixing pulse and dipolar couplings convert these coherences into single spin, detectable SQC coherences:

$$\begin{aligned} &\mathbf{S}^+ e^{i(\omega_I+\omega_S)t_1} e^{i(\gamma_I+\gamma_S)Gt} + \mathbf{S}^- e^{-i(\omega_I-\omega_S)t_1} e^{-i(\gamma_I+\gamma_S)Gt} \\ &\mathbf{I}^+ e^{i(\omega_I+\omega_S)t_1} e^{i(\gamma_I+\gamma_S)Gt} + \mathbf{I}^- e^{-i(\omega_I-\omega_S)t_1} e^{-i(\gamma_I+\gamma_S)Gt} \end{aligned} \tag{82}$$

The gradient amplitude that selects the iDQCs has an amplitude which reverses the dephasing caused by the first gradient. To detect the S spins you need the gradient ratio:

$$\begin{aligned} \gamma_I Gt + \gamma_S Gt + r\gamma SGt &= 0 \\ r &= \pm\left(1 + \frac{\gamma_I}{\gamma_S}\right) \end{aligned} \tag{83}$$

For the detection of the I spins the following gradient ratio is needed:

$$\begin{aligned} \gamma_I Gt + \gamma_S Gt + \gamma_I rGt &= 0 \\ r &= \pm\left(1 + \frac{\gamma_S}{\gamma_I}\right) \end{aligned} \tag{84}$$

If we again choose to detect the S^+ coherence, then $r = -\left(1 + \frac{\gamma_S}{\gamma_I}\right)$, causing the signal after the gradient to be

$$\mathbf{S}^+ e^{i(\omega_I+\omega_S)t_1} e^{(0)Gt} + \mathbf{S}^- e^{-i(\omega_I-\omega_S)t_1} e^{(0)Gt}$$
$$\mathbf{I}^+ e^{i(\omega_I+\omega_S)t_1} e^{i\left(\gamma_S+\frac{\gamma_I^2}{\gamma_S}\right)Gt} + \mathbf{I}^- e^{-i(\omega_I-\omega_S)t_1} e^{-i\left(\gamma_S-\frac{\gamma_I^2}{\gamma_S}\right)Gt} \tag{85}$$

The echo from this signal will appear at a different time than the homonuclear case – it will arrive at

$$rt_1 = \left(1 + \frac{\omega_I}{\omega_S}\right) t_1 \tag{86}$$

6.1.2 Characteristics of the Heteronuclear iMQC signal from the CRAZED experiment

The signal from the heteronuclear CRAZED experiment is different from the homonuclear case in several ways. As shown in the previous section, the gradients required to refocus the signal are different and depend on the ratio of the gyromagnetic ratios of the two spin types. The echo also appears at different times than in the standard homonuclear CRAZED experiment. A third difference is that the CRAZED signal is dependent on the concentrations of both spin species. This is not truly a departure from the standard two-component CRAZED signal, but it is an interesting subtlety to the experiment. As shown in the previous chapter, it is possible to detect iMQC signal from two low γ species. This signal scales as M_0^2, meaning that hyperpolarization techniques

are usually required to detect these signals. In the heteronuclear case, the signal also scales as the product of M_0 of each spin type, but if one of the spin types is proton, then this case is not nearly as unfavorable as the low-γ homonuclear case. Indeed, there is enough signal in this situation that proton-carbon iMQCs have been detected for thermal polarizations[105].

The signal from a heteronuclear CRAZED experiment is similar to the signal from a two-component homonuclear CRAZED experiment, except that the equation for the signal explicitly includes the gyromagnetic ratio. The signal for a heteronuclear CRAZED experiment is[105]

$$M^{I^+} = iM_0^I e^{i(\Delta\omega_I t_2)} e^{-i((\Delta\omega_I - \Delta\omega S)t_1)} \frac{\tau_{dI}}{t_2} J_1\left(-\frac{t_2}{\tau_{dI}}\right) J_1\left(-\frac{2\gamma_I t_2}{3\gamma_S \tau_{ds}}\right) \tag{87}$$

where I is the spin being detected, and $\Delta\omega_s$ and $\Delta\omega_I$ are the offsets of and S, respectively. Figure 6-2 compares the relative signals from a hyperpolarized carbon-proton heteronuclear CRAZED experiment, a thermal carbon-proton CRAZED experiment, and a thermal carbon-carbon experiment.

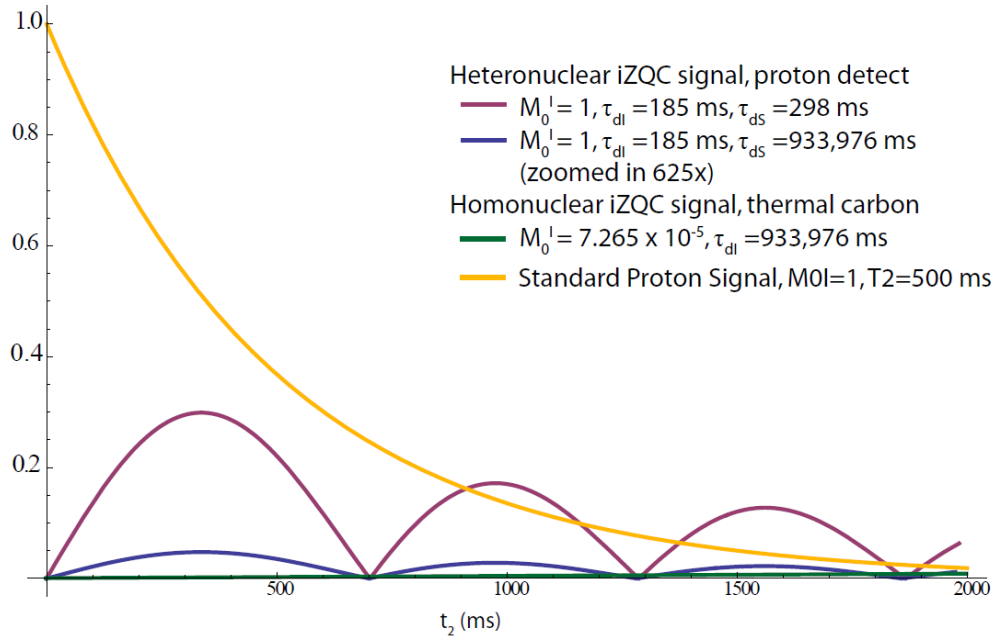

Figure 6-2 - Comparison of the calculated signal for a heteronuclear and homonuclear iMQC experiments. By using heteronuclear iMQCs, significantly more signal is detected than in the case of thermal carbon homonuclear iMQCs. Note that in order to graph all three signals on the same graph, the signal from the thermal proton-carbon experiment was enlarged by 625 and the thermal carbon-carbon signal was enlarged 8,333 times.

From this calculation (which neglects the effects of diffusion, relaxation and radiation dampening), the signals from the thermal carbon experiments are much lower than that of the hyperpolarized experiment. In particular, the extremely low signal of the thermal carbon-carbon experiment indicates that in an experimental situation the signal from those spins would be undetectable.

The behavior of the heteronuclear iMQC signal with concentration depends on the species being detected. If we are detecting spin I, then the concentration of spin S only changes the total amplitude of the signal, but it does not change the zero crossings.

If the concentration of spin I changes, then both the amplitude of the signal and the zero crossings change. Figure 6-3 shows the effect of changing the concentration of the non-detected spin type (S), while holding the concentration of the directly detected spin type (I) constant. Figure 6-4 shows the effect of changing the concentration of the directly detected spin type while maintaining the concentration of the indirectly detected spin.

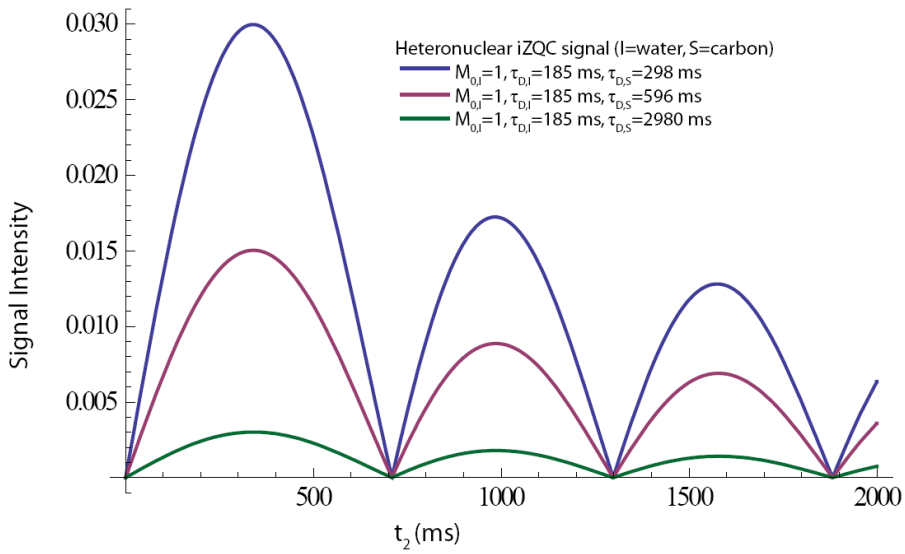

Figure 6-3 - The effect of changing the dipolar demagnetizing time for the indirectly detected spin. Only the signal intensity is affected by this change, not the position of the largest signals.

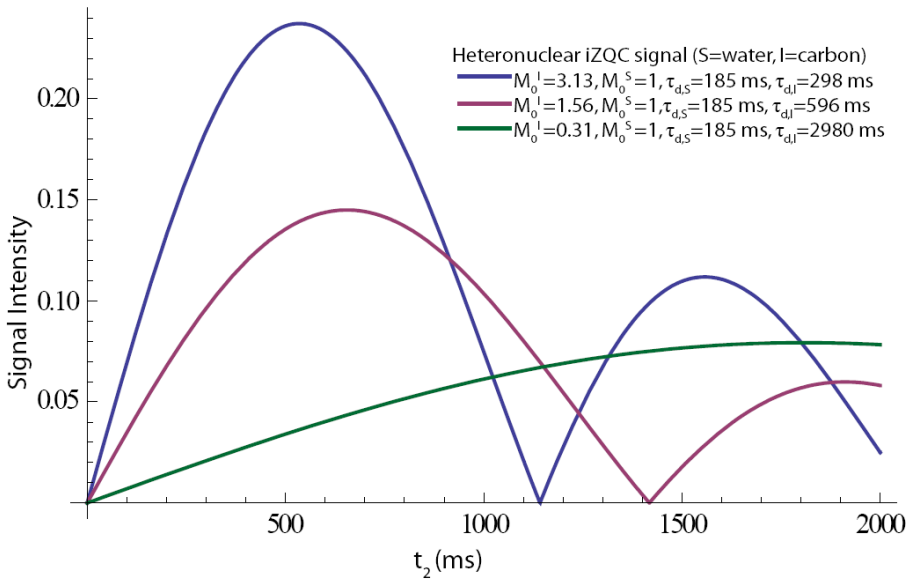

Figure 6-4 - Comparison of the calculated iMQC signal for heteronuclear iMQC experiments as the dipolar demagnetizing time of the directly detected spin is changed. The signal is much more sensitive to changes in the concentration of the directly detected spin than changes in the indirectly detected spin.

From these calculations it is clear that for applications of heteronuclear iMQCs, it is desirable to have one species that has a high concentration and is the directly detected species, while the concentration of the indirectly detected spin can vary over a fairly wide range without causing the signal to become undetectable.

In vivo applications of hyperpolarized iMQC experiments fall exactly into this category. There is a large abundance of bulk water spins, but the concentration of the injected hyperpolarized carbon species can vary depending on the location. Detection of the hyperpolarized carbon-carbon iMQCs would prove challenging as the sample becomes more dilute, but the heteronuclear iMQCs between protons and carbon are

more robust with respect to changes in the concentration of the carbon, allowing for iMQC detection even in dilute samples.

6.2 Reducing Inhomogeneity in the Hyperpolarized Carbon Linewidth using Heteronuclear iMQCs

In chapter 4 we discussed the HOT sequence used for imaging temperature. In that sequence, the timings were arranged so that both iDQCs and iZQCs could be used to provide inhomogeneity compensated signals. The same approach can be applied to heteronuclear iMQCs, and the pulse sequence is shown in Figure 6-5.

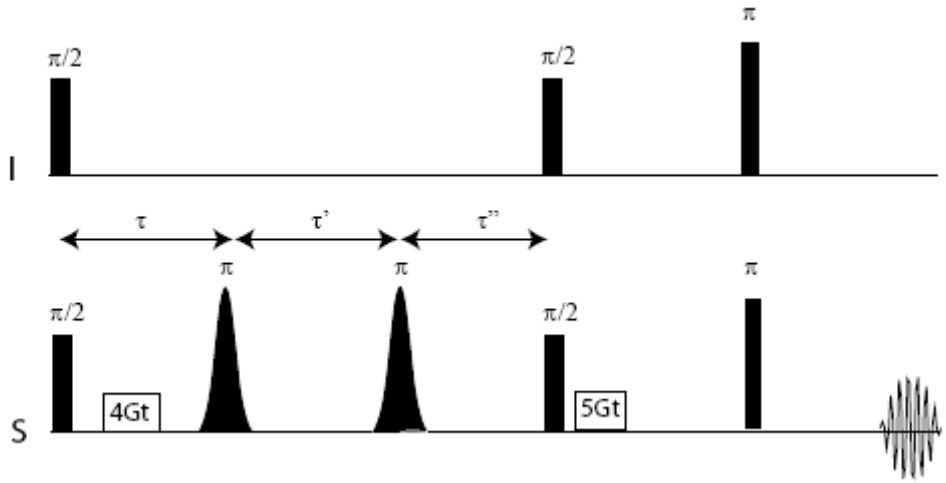

Figure 6-5 – Pulse sequence used to detect heteronuclear iMQCs with minimal contributions from inhomogeneities. The pulse sequence uses the same tricks as the HOT sequence – by converting the coherences from DQCs to ZQCs and carefully choosing the timings, the system can evolve with inhomogeneity compensation.

The sequence starts with a $\pi/2$ pulse on both the S (water) and I (carbon) spins. The system then evolves as a heteronuclear iDQC during the time period τ and a 4Gt gradient is applied.

$$\mathbf{I}_z\mathbf{S}_z \xrightarrow{\pi/2,\tau} \mathbf{I}^+\mathbf{S}^+ e^{i(\omega_I+\omega_S)\tau} e^{i4(\gamma_I+\gamma_S)Gt} \tag{88}$$

Then a hyperbolic secant inversion pulse is applied to the S spins only, converting the coherence from an iDQC to an iZQC and it evolves for time τ′ as an iZQC.

$$\xrightarrow{\pi_S,\tau'} \mathbf{I}^+\mathbf{S}^- e^{i(\omega_I+\omega_S)\tau+i(\omega_I-\omega_S)\tau'} e^{i4(\gamma_I+\gamma_S)Gt} \tag{89}$$

A second hyperbolic secant inversion pulse on the S spins only converts this coherence back to an iDQC where it evolves as an iDQC for an additional time τ″.

$$\xrightarrow{\pi_S,\tau''} \mathbf{I}^+\mathbf{S}^+ e^{i(\omega_I+\omega_S)\tau+i(\omega_I-\omega_S)\tau'+i(\omega_I+\omega_S)\tau''} e^{i4(\gamma_I+\gamma_S)Gt} \tag{90}$$

Then a π/2 pulse is applied to both the I and S spins that re-introduces the dipolar couplings, and a second gradient, 5Gt, is applied to refocus the signal.

$$\begin{aligned}\xrightarrow{\pi/2,5Gt} &\mathbf{I}_z\mathbf{S}^+ e^{i(\omega_I+\omega_S)\tau+i(\omega_I-\omega_S)\tau'+i(\omega_I+\omega_S)\tau''} e^{i4(\gamma_I+\gamma_S)Gt+i5(\gamma_S)Gt}\\ &+\mathbf{I}_z\mathbf{S}^- e^{i(\omega_I+\omega_S)\tau+i(\omega_I-\omega_S)\tau'+i(\omega_I+\omega_S)\tau''} e^{i4(\gamma_I+\gamma_S)Gt-i5(\gamma_S)Gt}\\ &+\mathbf{I}^+\mathbf{S}_z e^{i(\omega_I+\omega_S)\tau+i(\omega_I-\omega_S)\tau'+i(\omega_I+\omega_S)\tau''} e^{i4(\gamma_I+\gamma_S)Gt+i5(\gamma_I)Gt}\\ &+\mathbf{I}^-\mathbf{S}_z e^{i(\omega_I+\omega_S)\tau+i(\omega_I-\omega_S)\tau'+i(\omega_I+\omega_S)\tau''} e^{i4(\gamma_I+\gamma_S)Gt-i5(\gamma_I)Gt}\end{aligned} \tag{91}$$

Since γ_I is ¼γ_S, the signal from the $\mathbf{S}^-$ coherence is the only coherence that is refocused. If we arrange the timings such that τ + τ″ = .6*τ′, then the effect of inhomogeneous broadening is removed, and the coherence evolves with a resonance offset of (ω_I- ¼ω_S)τ′.

$$\begin{aligned}&\mathbf{I}_z\mathbf{S}^- e^{i(\omega_I+\omega_S)\tau+i(\omega_I-\omega_S)\tau'+i(\omega_I+\omega_S)\tau''} e^{-i(0)Gt}\\ &\longrightarrow \mathbf{I}_z\mathbf{S}^- e^{i(\omega_I+\omega_S)(\tau+\tau'')+i(\omega_I-\omega_S)\tau'}\\ &\longrightarrow \mathbf{I}_z\mathbf{S}^- e^{i(\omega_I+\omega_S)(.6\tau')+i(\omega_I-\omega_S)\tau'}\\ &\longrightarrow \mathbf{I}_z\mathbf{S}^- e^{i(\omega_I-\frac{1}{4}\omega_S)(\tau')}\end{aligned} \tag{92}$$

6.2. Demonstration of Inhomogeneity Compensated Heteronuclear iMQCs

The first demonstration of the inhomogeneity compensated heteronuclear iMQC pulse sequence was performed on thermal carbon sample. A sample of ^{13}C enriched urea was dissolved in water. The pulse sequence in figure 4 was applied, producing the spectrum shown in Figure 6-6.

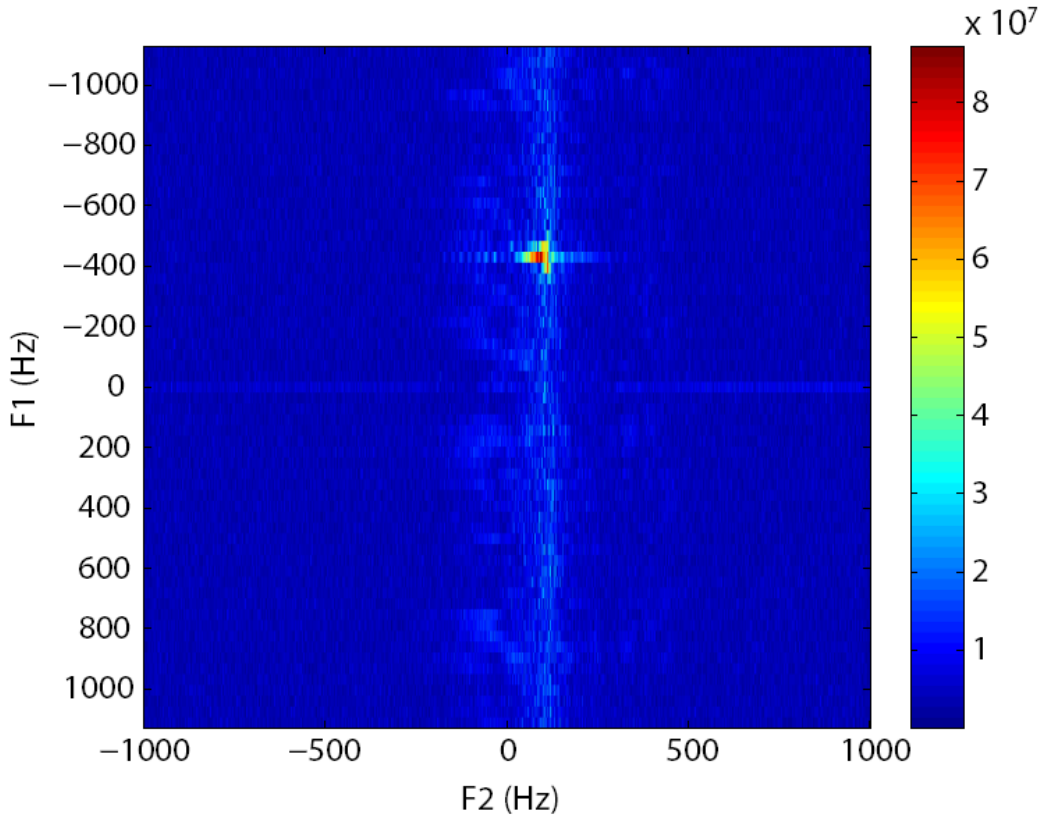

Figure 6-6 - 2D 1H - 13C iMQC spectrum (proton detection) of 13C enriched urea in water. The crosspeak occurs at (100 Hz, -425 Hz), the expected frequency for the inhomogeneity compensated heteronuclear iMQC pulse sequence. NA = 64, NR = 64, water offset = +100 Hz, carbon offset = -400, direct spectral width = 2003.2 Hz, indirect spectral width = 2222.2 Hz.

The crosspeak in the thermal spectrum appears at the expected frequency of ($\Delta\omega_{carbon} - \Delta\omega_{water}/4$). The water offset is +100 Hz, the carbon offset is -400 Hz, and the crosspeak occurs at (100 Hz, -425 Hz).

The inhomogeneity compensation is best shown by overlaying the indirectly detected carbon iMQC spectrum with the directly detected carbon spectrum (the result of a $\pi/2$ – acquire experiment). That result is shown in Figure 6-7.

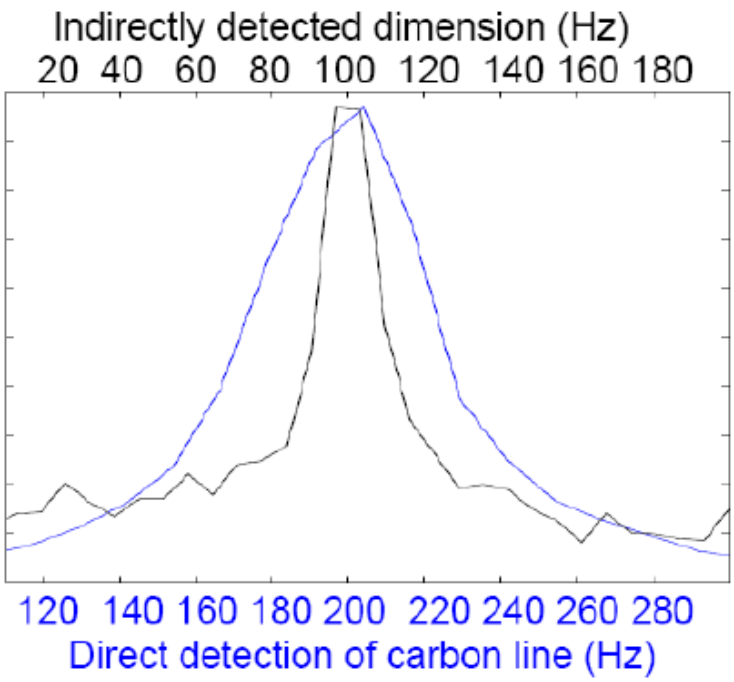

Figure 6-7 - Comparison of the directly detected carbon linewidth with the indirectly detected iMQC carbon linewidth. The iMQC detection allows for narrower lines because of the inhomogeneity compensation.

The indirectly detected carbon line is significantly narrower as a result of the inhomogeneity compensation of the iMQC pulse sequence.

This pulse sequence was also applied to hyperpolarized samples. A comparison of the signal intensity for a hyperpolarized carbon sample with the same sample thermally polarized is shown in Figure 6-8. In this case, a sample of pyruvate was hyperpolarized for 1 hour to approximately 20% polarization and then dissolved in 5 mL of water. The proton-carbon iMQC pulse sequence was applied to produce the signal on the left. The sample was allowed to relax for 5 min (~ 7 x T_1), and then the signal on the right was collected.

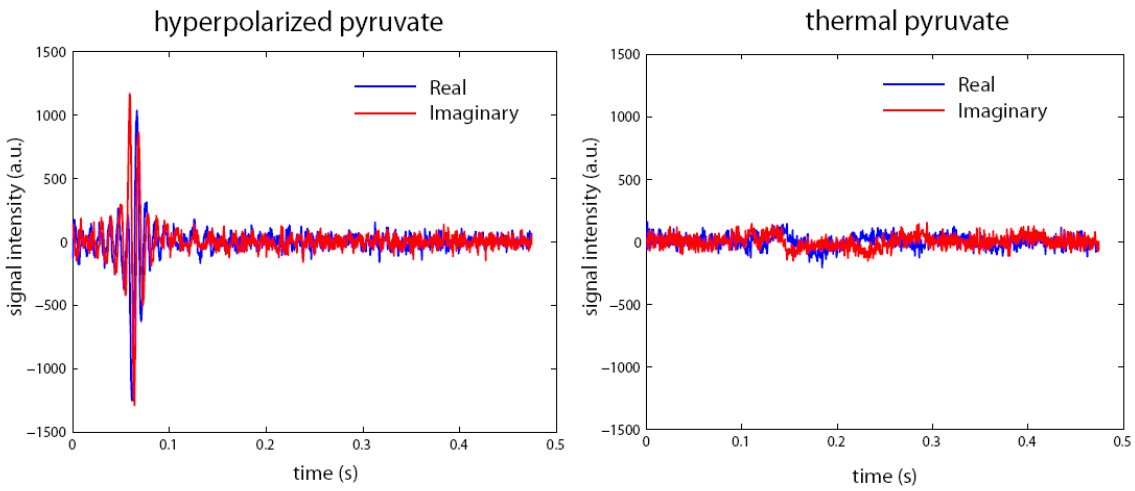

Figure 6-8 - Experimental demonstration of hyperpolarized heteronuclear iMQCs. The signal on the right comes from a hyperpolarized pyruvate sample, while the signal on the right is the same sample, thermally polarized. The hyperpolarization of the sample allows for significantly more heteronuclear iMQC signal, and the iMQC pulse sequence can be used to detect this hyperpolarized signal without broadening from inhomogeneities.

To confirm that the signal from the hyperpolarized experiments is coming from the correct coherence pathway (the iDQC to iZQC to iDQC pathway), an experiment

with and without the inversion pulses on the water was performed. Without the inversion pulses, the signal evolves as iDQC only, and the difference in the echo timing between the iDQC only and the iDQC to iZQC signals should be 37.6 ms, which is what we observed and is shown in Figure 6-9.

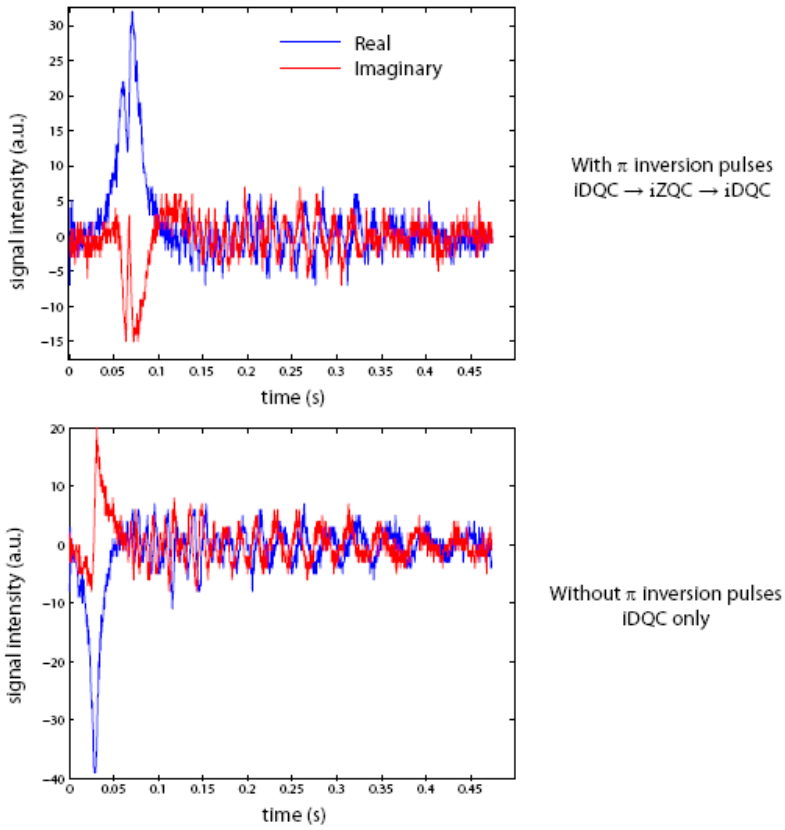

Figure 6-9 - Comparison of the echo timing for the iDQC only sequence (bottom) and the iDQC to iZQC to iDQC pulse sequence (top). For these experiments, $\tau = 28$ ms, $\tau' = 27.6$ ms, and $\tau'' = 10.1$ ms. The difference in echo spacing is 37.6 ms, as predicted.

Conclusions

Heteronuclear iMQCs offer the potential to detect low γ nuclei without inhomogeneities, allowing for improved sensitivity to different molecular species in

vivo. We have demonstrated this technique in thermal samples and shown that it is possible to acquire these signals using hyperpolarized reagents. Further work on this technique is required to allow for the observation of the narrow iMQC lines. To obtain 2D spectra of hyperpolarized carbons, the pulse sequence needs to be further adapted for hyperpolarized applications. First, the application of $\pi/2$ pulses uses up all the hyperpolarized magnetization, and thus the entire spectrum needs to be acquired all at once. Ultrafast spectroscopy with iMQCs has been previously done[120] in which an entire iZQC spectrum was acquired at once. Modifications of the ultrafast iZQC spectroscopy pulse sequence would allow for high resolution hyperpolarized proton-carbon spectroscopy.

Chapter 7 - ^{13}C – ^{13}C iMQCs

During the last decade, dipolar field interactions between different spins in solution have allowed for the detection of new types of magnetic resonance signals, arising from intermolecular multiple quantum coherences (iMQCs). These coherences have unique and fundamentally different properties than conventional signal, in particular an intrinsic sensitivity to sub-voxel structure. This sensitivity makes these signals particularly suitable for a wide range of applications, such as temperature imaging[130], novel contrast in human brain imaging[17], and detection of molecular anisotropy[8].

iMQC experiments in a test tube of water can exhibit strong signals (within a factor of two of the equilibrium magnetization). However, applications to water in more complex samples, such as tissue, are limited by relaxation effects resulting in a smaller signal (typically 10-20% of the conventional signal). For other nuclei the drop is even more dramatic, essentially because the signal scales as the square of the magnetization density. For physiologically reasonable concentrations of molecules with low γ nuclei such as carbon with normal thermal polarization, the low magnetization density makes it nearly impossible to detect iMQC signals. The solution discussed here is to employ hyperpolarization techniques, which provide even more dramatic gains in iMQC experiments than in conventional images. One such technique is dynamic nuclear polarization (DNP) which transfers the large spin polarization present in the electron

spin reservoir to the nuclei. This transfer is routinely done by microwave irradiation at or near the electron Larmor frequency in the presence of a large magnetic field at low temperatures. DNP techniques have been used to see increases in signal to noise of >10,000 [62]. By using hyperpolarization to enhance the initial magnetization of the sample, we were able to acquire the first multi-CRAZED FID of carbon-carbon coherences.

7.1 Generation and Detection of carbon- carbon iMQCs

In the previous chapters, the underlying theory of the CRAZED experiment has been explained both for homonuclear (^{1}H-^{1}H systems) as well as for heteronuclear (^{13}C-^{1}H) systems. The multi-CRAZED experiment, which acquires multiple iMQCs, was first outlined in [131] but it is important to briefly revisit that theory to better understand why iMQCs between low γ nuclei (with thermal polarization) is impractical.

To understand why low γ nuclei give very weak multiple quantum signals, it is important to look at the expression for the signal generated by the multi-CRAZED experiment. The pulse sequence for the multi-CRAZED experiment is shown in Figure 7-1.

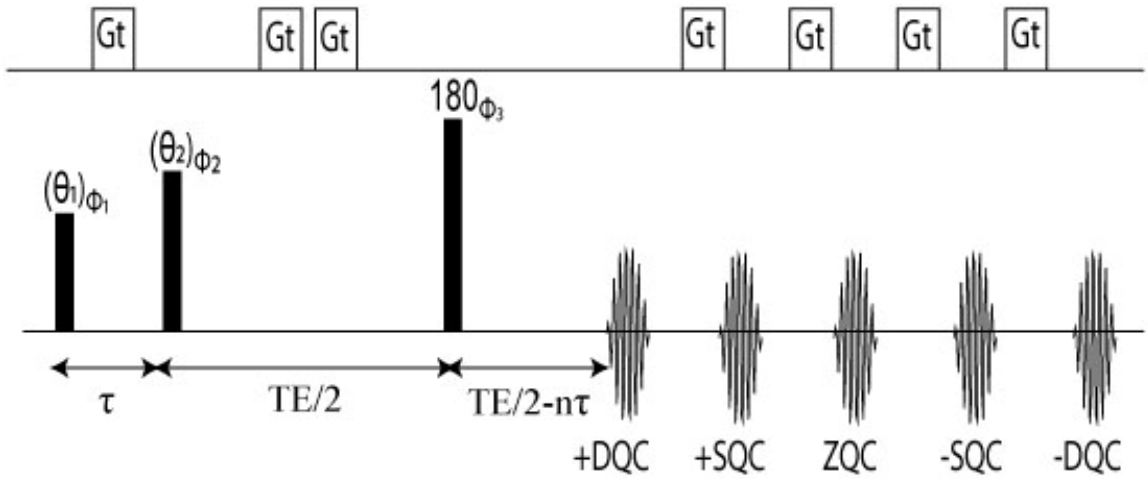

Figure 7-1 - The multi-CRAZED sequence takes advantage of differences in the echo timing to separate the different echoes at full intensity. The +DQC, -DQC and ZQC (+2, -2 and 0 quantum coherences, respectively) have contrast from sub-voxel variations in the magnetization density or resonance frequency. The +SQC and –SQC (+1 and -1 quantum coherences, respectively) signals have conventional contrast.

The standard pulse sequence for acquiring the signal from n-quantum intermolecular coherences is the "CRAZED" sequence 90-[delay τ] – [gradient pulse – area GT] – θ – [gradient pulse area nGT] – [delay TE – 180 – [delay TE – nτ] – acquire. The multi-CRAZED sequence takes advantage of differences in echo timings of the various coherences to acquire multiple echoes [131, 132]. Neglecting diffusion and T_1 relaxation effects, the signal for a multi-CRAZED experiment is[11, 132]:

$$M^{+}(\tau, TE) = i^{n-1} e^{i\Delta\omega TE} e^{TE/T_2} e^{-in\Delta\omega\tau} e^{-in\phi_1} e^{i(n+1)\phi_2} e^{-2i\phi_3} M_0 \sin\theta_1 \left[\frac{n\tau_d}{TE\Delta_s \sin\theta_1 \sin\theta_2} J_n\left(\frac{TE\Delta_s \sin\theta_1 \sin\theta_s}{\tau_d}\right) - \frac{\cos\theta_2}{2} J_{n+1}\left(\frac{TE\Delta_s \sin\theta_1 \sin\theta_2}{\tau_d}\right) + \frac{\cos\theta_2}{2} J_{n-1}\left(\frac{TE\Delta_s \sin\theta_1 \sin\theta_2}{\tau_d}\right) \right. \quad (93)$$

where $\Delta\omega$ is the resonance offset, $\tau_d = (\gamma\mu_0 M_0)^{-1}$ is the dipolar demagnetizing time, $\Delta_s = \frac{3((S\bullet Z)^2-1)}{2}$ where s is the direction of the gradient pulse, θ_1 and θ_2 are the flip

angles of the first two pulses, ϕ_1 is the phase of the first (excitation) pulse, ϕ_2 is the phase of the mixing pulse, and ϕ_3 is the phase of the refocusing pulse.

Note that the argument of the Bessel functions is proportional to TE/τ_d, which can be made large in a test tube of water, but which is limited by the relaxation time T_2 to small values in tissue (Table 5 below). For $x<<1$, $J_n(x)$ is proportional to x^n. This implies that the multiple quantum terms (n=-2, 0, 2) grow in linearly with TE. Table 5 compares these values for water in tissue (the concentration of water in tissue is approximately 80 M) and water in the brain, to thermally polarized 1M ^{13}C urea with at T_2 of 36 ms (measured using a spin echo sequence, with the echo time varied), and the same urea sample hyperpolarized (20% polarization) at 7T. From these values it is clear that for reasonable values of T_2, we expect essentially no iMQC signal from a thermally polarized carbon sample, since by the time the multiple quantum signal has grown in, T_2 has dephased the spins.

Table 5 - Comparison of predicted iMQC signal for protons, thermally polarized carbon and hyperpolarized carbon.

	^1H, 80M water, 7T	^1H water, in the brain (T_2 = 25ms)	^{13}C, 1M, thermally polarized, 7T	^{13}C, 1M, hyperpolarized, 7T
τ_d	**185 ms**	**185 ms**	**933,976 ms**	**298 ms**
T_2/τ_d	**10.81**	**.135**	**.00003854**	**.123**

M_0*T_2/τ_d	**1**	**.0249**	**2.8 x 10^{-9}**	**.3859**

7.2 Experimental Demonstration of ^{13}C-^{13}C iMQCs

Using the Hypersense hyperpolarizer from Oxford Instruments, we polarized a sample of urea (^{13}C labeled, 1M). The sample was polarized for 4 hours at a microwave frequency of 94.105 GHz. The dissolution was done in 3 mL of DI water with a 25 mM EDTA. This sample was inserted in a 7T small animal imager using a Bruker console. The experimental parameters were: TE=7.232ms, θ_1=90, θ_2=135, 45-180 delay = 19.080 ms, 1228 points, SW = 90090.09 Hz.

In Figure 7-2 the carbon-carbon multi-CRAZED fid shows both double quantum (DQC) and zero quantum (ZQC) signal, demonstrating that hyperpolarization techniques can be used to acquire multiple quantum signal between low γ nuclei.

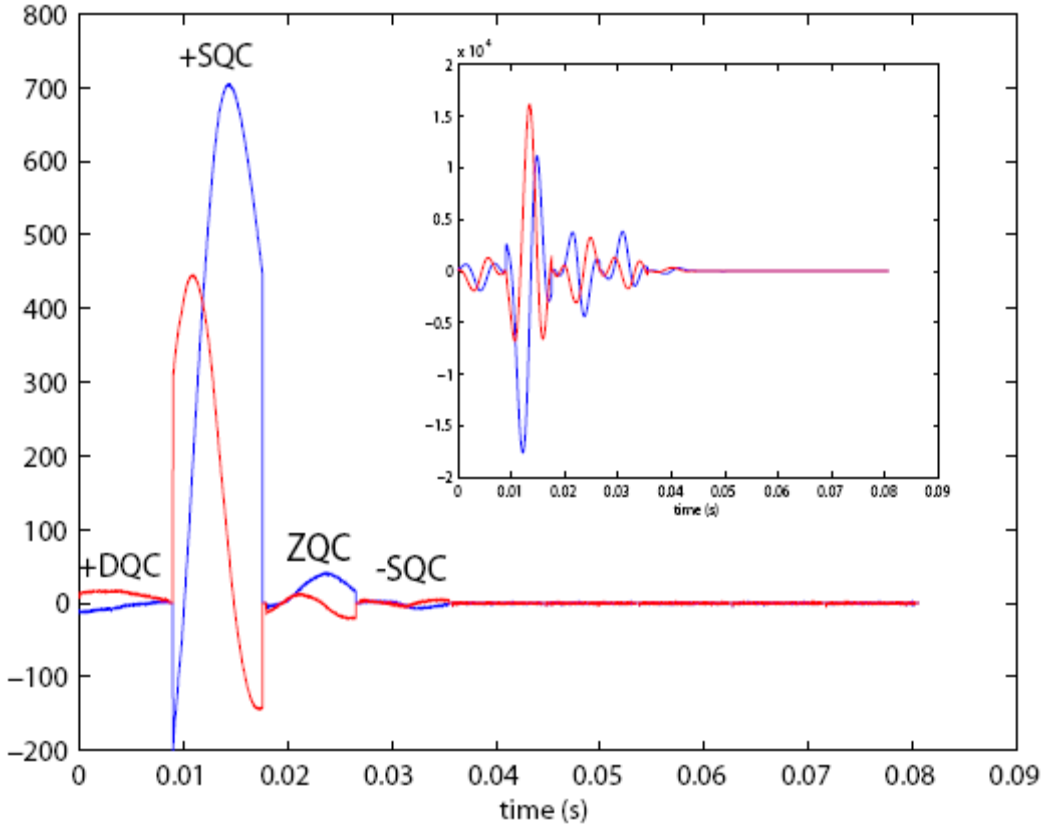

Figure 7-2 - Multi-CRAZED FID of hyperpolarized urea compared to the multi-CRAZED FID of water (top corner). It is important to note that this is not one long FID, but a series of consecutive FIDs separated by a gradient pulse.

For comparison, a multi-CRAZED fid of water is shown in the top corner of the figure, illustrating the standard multi-CRAZED fid. Control experiments were done on a sample of water, with the correlation gradients along the z-axis and along the magic angle. When the correlation gradients are on the magic angle, the distant dipolar field is disabled, and no iMQC signals should appear. The experiments with the correlation gradient along the magic angle show a dramatic decrease in the amount of + iDQC signal (the signal seen in the first acquisition, the +iDQC acquisition period, is .8% of the

signal seen with the gradients just along z). A similar decrease is seen for the –iDQC acquisition window. The drop in iZQC signal is less dramatic, which is also expected because some contamination arises from pulse imperfections.

In the case of hyperpolarized urea, the enhancement of the iMQC signal is hampered by the short T_2 of the sample as illustrated in Figure 7-3.

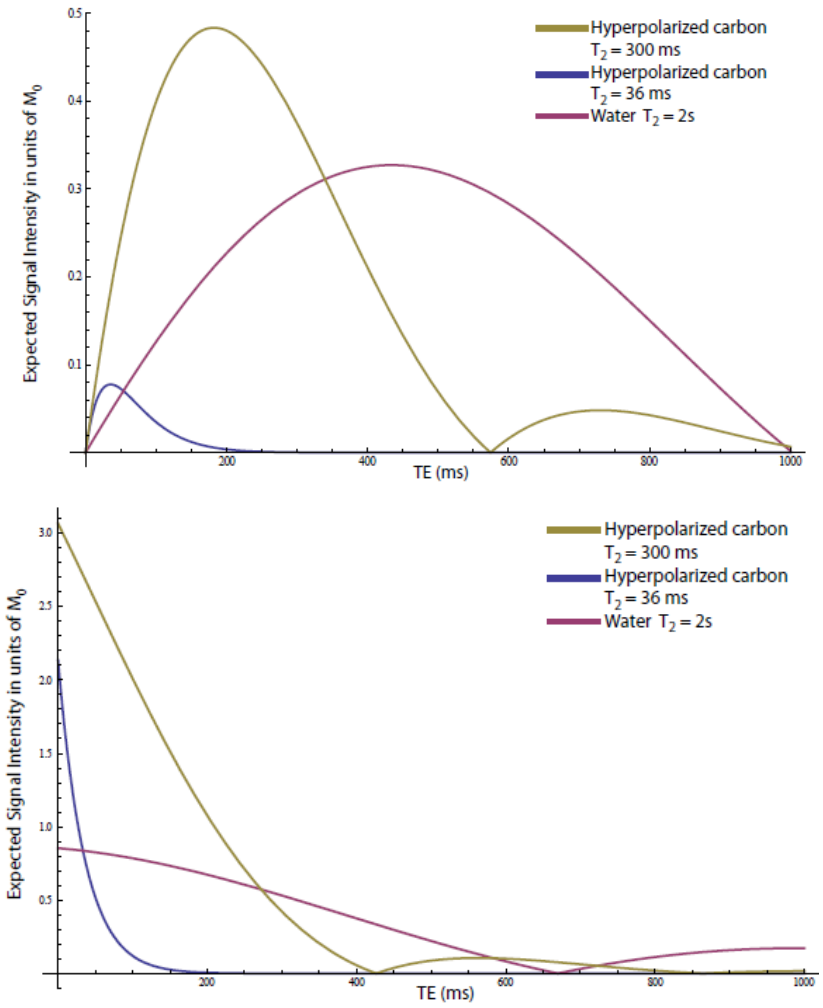

Figure 7-3 - Comparison of the calculated signal (from eq. 1) for a ZQC (top) experiment with an SQC (bottom) experiment for water (T_2 = 2s), and two hyperpolarized carbon samples with T_2s of 300ms and 36 ms with the following

parameters: $\Delta\omega = 0$, τ=7ms, $\phi_1 = \phi_2 = \phi_3 = 0$, M_0 (hyperpolarized carbon) = 2.5, M_0 (water) = 1, $\theta_1 = \pi/2$, $\theta_2 = 3\pi/4$, τ_d=298 ms (hyperpolarized carbon), τ_d=185 ms (water) and Δ_s=1.

It is also clear from Table 5, which compares signal intensities, that the T_2 of the carbon sample is short enough to significantly hamper even the –SQC signal intensity. In the case of water (inset on figure 2) the –SQC signal is 23.6% of the +SQC signal. Figure 7-3 compares the calculated signal intensity (from (93)) for SQC and ZQC signals for water, and two hyperpolarized carbon samples with a short (36ms) T_2 and a long (300ms) T_2. The ZQC signal intensity is hurt much more by the shortening of T_2 than the intensity of the SQC signal. It is clear from the figures that the short T_2 of the carbon nuclei has a profound effect on the amount of iMQC signal that can be obtained. An increase of T_2 from 36 ms to 300 ms results in a seven fold increase in maximum signal intensity. Unfortunately, T_2 for urea and radical is quite short (approximately 36 ms), severely limiting the amount of iMQC signal possible from this molecule. Nonetheless, the demonstration of observable multi-CRAZED signal even under these unfavorable conditions bodes well for imaging applications.

Conclusion

In summary, we have demonstrated that carbon hyperpolarization permits intermolecular multiple quantum signals with intensities comparable to those previously seen in water. In general, hyperpolarized techniques can give useful metabolic information complementary to the anatomical information obtainable

with standard proton MR. One pitfall of these techniques is the inherently short acquisition time, which limits the spatial resolution in MR images and the spectral resolution in NMR spectra. It has been previously demonstrated that iMQC experiments can provide subvoxel resolution and inhomogeneity compensation in MRI and MRS of thermally polarized proton samples. Experiments that are currently done using single quantum coherences, could be done with iMQCs to achieve better spatial and spectral resolution. A particular example of this is that the iMQC signal could be tuned to detect intracellular and extracellular compounds. For low concentration thermally polarized samples of low γ nuclei such as carbon, the exceedingly small magnetization makes iMQC detection nearly impossible; however, for hyperpolarized samples, the demagnetization time becomes reasonably short, and in fact the theoretical signal gain is vastly larger for iMQC sequences than for conventional imaging. The demonstration that carbon – carbon iMQC signal can be observed has been shown in this paper, and opens the door to the possibility of future applications of non-proton iMQC experiments. For example, fast 2D NMR spectroscopy has been demonstrated for iMQCs [10], and for hyperpolarized samples [11], and the combination of these types of experiments would allow for inhomogeneity compensated 2D spectra. In addition, iMQC signals are proportional to M_0^2 instead of M_0, as in standard experiments, and this difference could be used to amplify the concentration variation of different metabolites in vivo. Since this signal is intrinsically different than

the standard MRI signal, we expect this approach will enhance the utility of hyperpolarized experiments.

Chapter 8 – **Long lived singlet states**

A fundamental problem in magnetic resonance is one of sensitivity. The net magnetization of a sample is governed by the Boltzmann distribution (as discussed in chapter 1); for hydrogen atoms in a 7T magnet the net magnetization is ~ 0.001% of the magnetization possible of all the spins were aligned in the same direction. The consequence of this poor sensitivity is that applications of magnetic resonance imaging have been limited to hydrogen (because of its relatively large gyromagnetic ratio) containing molecules in large abundance, such as water or fat (for in vivo applications). Hyperpolarization has emerged as a technology which can artificially enhance the polarization of the system (as discussed in chapter 3), allowing for very low concentrations of hyperpolarized species to be detected. It also allows for the detection of signals coming from low gyromagnetic species such as nitrogen and carbon.

The significant signal enhancements created by hyperpolarization techniques are short lived, decaying back to thermal equilibrium at a rate proportional to T_1. For some applications this lifetime is sufficient, such as the observation of the metabolism (via glycolysis) of 1-^{13}C- pyruvate [25-35, 37-39, 41-45, 47-50, 52-55, 58]. At 3T, the T_1 of the carbon is ~60 s, and many studies have shown this lifetime to be sufficiently long to observe the metabolism of pyruvate into lactate and alanine. Attempts to observe other, slower metabolic processes have proved more challenging. One specific metabolic target is the observation of metabolism via the TCA cycle using hyperpolarized reagents.

Several groups have been able to see the products of TCA in tissues with high metabolic activity such as the heart[47-49] but attempts to observe TCA in tissues with slower metabolic rates have been unsuccessful. The common explanation for this is that in tissues with lower metabolic rates, the hyperpolarized species is not metabolized at a rate faster than T_1 and the hyperpolarization has decayed before a sufficient concentration of the metabolites have accrued.

Another consequence of the short lifetime of hyperpolarized species is that the scope of in vivo hyperpolarized experiments has been forced to limit itself to molecules with relatively long values of T_1. One of the impressive features of dynamic nuclear polarization (DNP, the most common technique for hyperpolarization of carbon and nitrogen compounds) is its great flexibility. In practice, as long as the target molecule for hyperpolarization can be dissolved into a glassy solvent system (which is the case for most metabolically interesting molecules, and a wide range of biologically interesting molecules), the molecule can be hyperpolarized. Unfortunately, this flexibility is for the most part wasted, since the hyperpolarization decays away too quickly to be observed.

In addition, many researchers want to develop DNP into a clinical metabolic imaging technique, competitive with PET (positron emission tomography). The sensitivity of PET is unmatched by MR – PET can detect a single positron decay, while even with hyperpolarization techniques many hundreds to thousands of molecules are needed to detect a signal. The lifetime of PET contrast agents are also significantly

longer, usually around 2 hours (compared with 1-2 minutes for MR). MR does have one significant positive feature – it does not involve the injection of any radioactive substances. In addition, hyperpolarized carbon imaging can access tissues that are not available for PET imaging, brain or inflamed tissue due to the large background signal[57] or in the prostate where there is low uptake in the prostate combined with the proximity of the bladder which has high concentrations of the radiotracer[133]. With hyperpolarized carbon studies the large background from the bladder this would not be a concern (the time after the injection of the contrast agent is not sufficient for it to be processed into the bladder), creating much optimism for applications of hyperpolarized carbon studies for the diagnosis of prostate cancer. In order for MR to evolve into a molecular imaging modality, the application of hyperpolarized reagents needs to become routine and robust, and one key part of that change involves extending the lifetime of the hyperpolarized species.

For the remainder of this chapter, we will present the only (as of the writing on this work) method for extending the lifetime of hyperpolarized species – storage of hyperpolarized populations in a protected eigenstate called a singlet state. To understand how storage of hyperpolarization in the singlet state works, we will discuss the nature of the singlet state: why it extends the lifetime of the polarization and methods for storage and retrieval of populations in the singlet state. Finally, we will

discuss the method for storage and retrieval of hyperpolarized populations via symmetry and chemistry used in our experiments.

8.1 What is a singlet state?

Consider a sample composed of molecules which have two isolated (not coupled to any other spins) spin - 1/2 nuclei which are magnetically equivalent. The energy levels of this system are defined by the Hamiltonian of the system:

$$\mathbf{H} = \omega_1 \mathbf{I}_{z1} + \omega_2 \mathbf{I}_{z2} + 2\pi J_{12} \mathbf{I}_1 \bullet \mathbf{I}_2 \tag{94}$$

Since the spins are magnetically equivalent, $\omega_1 = \omega_2$, this equation collapses down to just:

$$\mathbf{H} = 2\pi J_{12} \mathbf{I}_1 \bullet \mathbf{I}_2 \tag{95}$$

In this situation the energy levels given by $|\alpha\alpha\rangle$, $|\alpha\beta\rangle$, $|\beta\alpha\rangle$ and $|\beta\beta\rangle$ are no longer eigenstates of the system. Instead, the eigenstates can be divided up into so-called singlet and triplet energy levels:

$$\begin{aligned} |S_0\rangle &= \frac{1}{\sqrt{2}} \left(|\alpha\beta\rangle - |\beta\alpha\rangle \right) \\ |T_{+1}\rangle &= |\alpha\alpha\rangle \\ |T_0\rangle &= \frac{1}{\sqrt{2}} \left(|\alpha\beta\rangle + |\beta\alpha\rangle \right) \\ T_{-1}\rangle &= |\beta\beta\rangle \end{aligned} \tag{96}$$

The distribution of the energy levels in a magnetic field is shown in Figure 8-1 1.

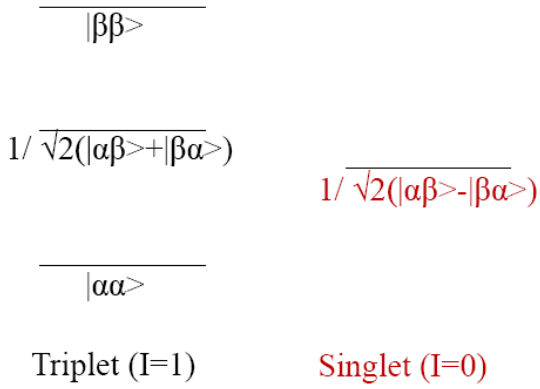

Figure 8-1 - Energy levels for an A_2 system. In this system there are three accessible energy levels (triplet) and one disconnected energy level (singlet). Transitions between the singlet and triplet levels are forbidden, and populations in the singlet state have a much longer relaxation rate than populations in the triplet energy levels**.**

The state $|\alpha\beta>$ has an angular momentum of +1/2 for the first spin and -1/2 for the second spin. The singlet state (S_0) has a total angular momentum of I=0, while the triplet states have a total angular momentum of I=1. They are eigenstates of the total angular momentum operator I ($\mathbf{I}^2 = \mathbf{I}_x^2 + \mathbf{I}_y^2 + \mathbf{I}_z^2$), such that:

$$\begin{aligned} \mathbf{I}^2|S_0\rangle &= 0 \\ \mathbf{I}^2|T_n\rangle &= 2|T_n\rangle, n = \{-1, 0, +1\} \end{aligned} \tag{97}$$

The singlet and triplet states are normalized superpositions of the Zeeman states, but are not eigenstates of the Hamiltonian. This can be seen if one writes the matrix representation of the spin Hamiltonian for two spins:

$$H = \begin{pmatrix} 2\omega_0 + \pi J_{12} & 0 & 0 & 0 \\ 0 & -2\omega_0 + \pi J_{12} & 2\pi J_{12} & 0 \\ 0 & 2\pi J_{12} & -2\omega_0 + \pi J_{12} & 0 \\ 0 & 0 & 0 & 2\omega_0 + \pi J_{12} \end{pmatrix} \tag{98}$$

Since the matrix is not diagonal in this basis, is indicates that these states are not all eigenstates of the Hamiltonian. If we shift to the singlet-triple basis by deriving the elements of the matrix according to the example below, the Hamiltonian becomes diagonal indicating that the singlet-triplet states are eigenstates in this basis.

$$\begin{aligned} \langle S_0|H|T_0\rangle &= \frac{1}{2}\left(\langle\alpha\beta| - \langle\beta\alpha|\right) H \left(|\alpha\beta\rangle + |\beta\alpha\rangle\right) \\ &= \frac{1}{2}\left(\langle\alpha\beta|H|\alpha\beta\rangle - \langle\beta\alpha|H|\beta\alpha\rangle\right) + \left(\langle\alpha\beta|H|\alpha\beta\rangle + \langle\beta\alpha|H|\beta\alpha\rangle\right) \\ &= 0 \end{aligned} \tag{99}$$

The Hamiltonian in this basis is transformed to look like:

$$H = \begin{pmatrix} \omega_0 + \frac{1}{2}\pi J_{12} & 0 & 0 & 0 \\ 0 & \frac{1}{2}\pi J_{12} & 0 & 0 \\ 0 & 0 & -\omega_0 + \frac{1}{2}\pi J_{12} & 0 \\ 0 & 0 & 0 & \frac{3}{2}\pi J_{12} \end{pmatrix} \tag{100}$$

The diagonal elements of this matrix represent the energies of each of the different states. More explicitly, the corresponding eigenequations which give the energy of each level are:

$$\begin{aligned} H|T_{+1}\rangle &= \omega_0 + \frac{1}{2}\pi J_{12}|T_{+1}\rangle \\ H|T_0\rangle &= \frac{1}{2}\pi J_{12}|T_0\rangle \\ H|T_{-1}\rangle &= -\omega_0 + \frac{1}{2}\pi J_{12}|T_{-1}\rangle \\ H|S_0\rangle &= -\frac{3}{2}\pi J_{12}|S_0\rangle \end{aligned} \tag{101}$$

Allowed transitions between states correspond to a single spin flip and can be represented by the operator $\mathbf{I}_{x1} + \mathbf{I}_{x2}$.

$$\begin{aligned}
\mathbf{I}_x|\alpha\rangle &= \frac{1}{2}\hbar|\beta\rangle \\
\mathbf{I}_x|\beta\rangle &= \frac{1}{2}\hbar|\alpha\rangle
\end{aligned} \tag{102}$$

Applying this operator to the singlet states:

$$\begin{aligned}
\mathbf{I}_{x1} + \mathbf{I}_{x2}|S_0\rangle &= \mathbf{I}_{x1} + \mathbf{I}_{x2}|\alpha\beta\rangle - \mathbf{I}_{x1} + \mathbf{I}_{x2}|\beta\alpha\rangle \\
&= \mathbf{I}_{x1}|\alpha\beta\rangle + \mathbf{I}_{x2}|\alpha\beta\rangle - \mathbf{I}_{x1}|\alpha\beta\rangle - \mathbf{I}_{x2}|\beta\alpha\rangle \\
&= \frac{1}{2}\hbar|\beta\beta\rangle + \frac{1}{2}\hbar|\alpha\alpha\rangle - \frac{1}{2}\hbar|\alpha\alpha\rangle - \frac{1}{2}\hbar|\beta\beta\rangle = 0
\end{aligned} \tag{103}$$

There is no dipole moment connecting the singlet and triplet states, thus populations in the singlet state are trapped there and cannot relax. The same treatment can be given to the triplet energy levels:

$$\begin{aligned}
\mathbf{I}_{x1} + \mathbf{I}_{x2}|T_0\rangle &= \mathbf{I}_{x1} + \mathbf{I}_{x2}|\alpha\beta\rangle + \mathbf{I}_{x1} + \mathbf{I}_{x2}|\beta\alpha\rangle \\
&= \mathbf{I}_{x1}|\alpha\beta\rangle + \mathbf{I}_{x2}|\alpha\beta\rangle + \mathbf{I}_{x1}|\alpha\beta\rangle + \mathbf{I}_{x2}|\beta\alpha\rangle \\
&= \frac{1}{2}\hbar|\beta\beta\rangle + \frac{1}{2}\hbar|\alpha\alpha\rangle + \frac{1}{2}\hbar|\alpha\alpha\rangle + \frac{1}{2}\hbar|\beta\beta\rangle \\
&= \hbar|\beta\beta\rangle + \hbar|\alpha\alpha\rangle \\
&= \hbar|T_{-1}\rangle + \hbar|T_{+1}\rangle
\end{aligned} \tag{104}$$

$$\begin{aligned}
\mathbf{I}_{x1} + \mathbf{I}_{x2}|T_{+1}\rangle &= \mathbf{I}_{x1} + \mathbf{I}_{x2}|\alpha\alpha\rangle \\
&= \mathbf{I}_{x1}|\alpha\alpha\rangle + \mathbf{I}_{x2}|\alpha\alpha\rangle \\
&= \frac{1}{2}\hbar|\beta\alpha\rangle + \frac{1}{2}\hbar|\alpha\beta\rangle \\
&= \hbar|T_0\rangle
\end{aligned} \tag{105}$$

$$
\begin{aligned}
\mathbf{I}_{x1} + \mathbf{I}_{x2}|T_{-1}\rangle &= \mathbf{I}_{x1} + \mathbf{I}_{x2}|\beta\beta\rangle \\
&= \mathbf{I}_{x1}|\beta\beta\rangle + \mathbf{I}_{x2}|\beta\beta\rangle \\
&= \frac{1}{2}\hbar|\alpha\beta\rangle + \frac{1}{2}\hbar|\beta\alpha\rangle \\
&= \hbar|T_0\rangle
\end{aligned}
\tag{106}
$$

From this calculation it is clear that there are allowed transitions between the triplet manifold, while there are not allowed transitions between the singlet and triplet states. This isolation of the singlet state prevents relaxation of the population to other energy levels.

8.2 Previous demonstrations of singlet states

The potential for storage of populations in the singlet state was concealed for many years because for two reasons. First, the singlet is antisymmetric with respect to spin exchange and does not give rise to any direct observables. Second, accessing the singlet state requires breaking the symmetry of the molecule. Breaking the symmetry of the molecule causes the singlet state to no longer be an eigenstate of the system and the population stored in that state rapidly interconverts with the populations in the triplet energy levels.

One of the first examples of singlet states is that of *para*-hydrogen (p-H_2). If we consider the wavefunction for the rotational angular momentum (ψ_J) in addition to the total spin angular momentum (ψ_N) waveform, the total angular momentum of p-H_2 is given by $\Phi=\psi_J + \psi_N$. The total angular momentum of the system must be antisymmetric with respect to spin exchange[61] because hydrogen obeys Fermi-Dirac

statistics. The waveforms of the nuclear spins are given by the four states described in (96). The triplet waveforms are symmetric with respect to spin exchange while the singlet waveform is antisymmetric. ψ_J can be either symmetric or antisymmetric, thus the singlet waveform is associated with the symmetric rotational angular momentum wavefunction and the triplet states are associated with the antisymmetric rotational angular momentum wavefunctions. This causes two isomers of H_2: the parahydrogen (named because the nuclear spins are pointed in opposite directions) and orthohydrogen (o=H_2, because the nuclear spins are pointed in the same direction). A sample of H_2 at room temperature contains 25% p-H_2 and 75% o-H_2. Because there are no allowed transitions between the singlet and triplet states, the inter-conversion between the two species is very slow. The long nuclear lifetime of p-H_2 is normally inaccessible to NMR experiments for the same reason. It can only be observed when p-H_2 is added (via hydrogenation reactions) to another non-symmetric molecule, thus breaking the symmetry of p-H_2.

Similar considerations apply to magnetically equivalent spins in molecules such as water. The hydrogens in water are magnetically equivalent, and thus a singlet state exists in this molecule. While reports exist of ortho and para water, the application of para-water remains very difficult. Water continuously undergoes dynamic reactions from H_3O^+ to H_2O to OH^- at a fairly rapid time scale (most estimates are on the milli to nano second timescale, though some reports say that ortho and para water spins states

can last up to an hour[134, 135]). Each time a water molecule converts from one molecular species to another, the nuclear spin order gets shuffled. Imagine a water molecule (H_2O) which does have both the hydrogen spins anti-aligned (para-water). In order for the singlet state of this molecule to survive long enough to observe the effects of the singlet state, the nuclear spin order would have to be preserved. Since the hydrogens on this molecule are rapidly coming and going, it would require that the next hydrogen to associate with the molecule would also have to have the same nuclear spin order. Thus, one can imagine that even a small impurity of ortho water in the sample would rapidly destroy the singlet spin order.

The number of molecular species which contain coupled, magnetically equivalent spins is fairly small. In 2004, Levitt demonstrated[4, 51, 136-144] that it was also possible to store populations in the singlet states of molecules with inequivalent spins. In his systems, he took molecules with two coupled but chemically inequivalent spins and stored population in the singlet state by artificially removing the chemical shift difference by two methods. The first method involves removing the sample from the large magnetic field. The difference in chemical shift is dictated by the strength of the magnetic field, thus, if the magnetic field is removed, the chemical shift difference is also removed[136-138]. The second method involves the rapid application of RF pulses to wipe out the chemical shift[51, 139-142, 145]. The locking of the singlet states with the application of RF pulses involves the competition between the resonant RF field

(symmetric for the two spins) and the chemical shift difference (which is antisymmetric). A sufficiently strong RF field imposes its symmetry on the nuclear spin system and locks the singlet state as long as the RF field is on. Further applications of singlet states (beyond storage of populations) have included extremely low field spectroscopy [139], determination of molecular torsion angles [144], imaging of porous materials [146], measurement of diffusion coefficients and [147].

We present a different and novel approach to the storage of populations in the singlet state. By manipulation of the chemistry of a system (similar to the concept behind the PASADENA experiment with p-H_2) we can control the storage and release of populations in the singlet state. By converting a symmetric molecule (A_2 system) to a non-symmetric molecule (AX system), the stored populations in the singlet state of the A_2 system can be released. The remainder of this document will describe the system used for this method, as well as provide the first demonstration of the storage of hyperpolarized populations in the singlet state. Chapter 9 will provide an in depth theoretical discussion of singlet states, relaxation mechanisms and methods for evaluating molecules for use with the singlet state.

8.3 Molecular system for storage of populations in the singlet state

The molecular requirements for use as a singlet state storage molecule are surprisingly general. For the application of storage of hyperpolarized populations, a non-symmetric molecule (AX system) is needed in which there are two (relatively)

strongly coupled spins. A rapid (faster than T_1) chemical reaction needs to be possible which can take the AX system to a symmetric A_2 system. The A_2 system needs to be fairly stable (little to no reverse reactions back to the AX system), since as long as the molecule stays as an A_2 system the populations in the singlet state will have a much slower relaxation rate. Finally, another reaction which takes the A_2 system to an AX system is needed to release the stored populations.

The initial AX system has four energy levels as shown in Figure 8-2. If we assume this molecule has been hyperpolarized to 20% polarization, then 40% of the spins are in the β state and 60% are in the α state. The population distribution among the energy levels is then 36% $|\alpha\alpha>$, 24% $|\alpha\beta>$, 24% $|\beta\alpha>$ and 16% $|\beta\beta>$. The populations that move into the singlet state are the average of the $|\alpha\beta>$ and the $|\beta\alpha>$ populations, which means that 24% of the populations would be in the singlet state in this case. Thus, despite all the effort of hyperpolarizing the system, we have only deviated from thermal equilibrium (approximately even distribution of populations amongst all energy levels) by 1%. Instead, if we apply a selective inversion pulse to the transition between $|\alpha\alpha>$ and $|\alpha\beta>$ (or $|\beta\alpha>$), then the populations going into the singlet state would be 30%, a much more significant deviation from thermal equilibrium (Figure 8-2).

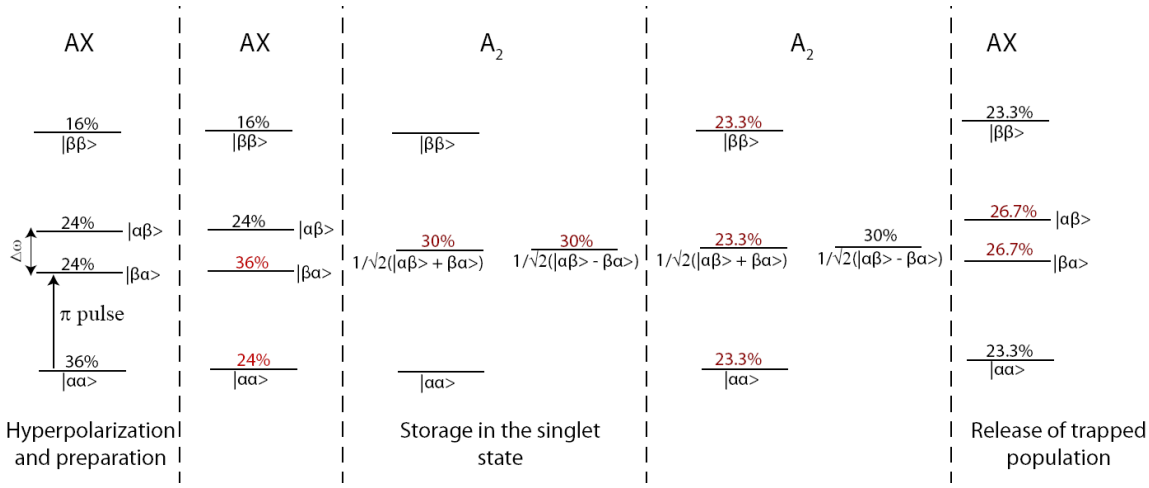

Figure 8-2 – Energy level diagram for the singlet experiment. The sample is hyperpolarized in the AX form, which allows the transfer of hyperpolarized populations into the |αβ> or |βα> energy levels. The sample is converted to an A_2 system where the hyperpolarized population is trapped. The populations in the triple energy levels equilibrate, but the population in the singlet state is trapped. By converting the system back to an AX system, the populations are released, allowing for a resurgence of hyperpolarized signal at a later time.

In some magnets the homogeneity of the magnet is not sufficient to allow for a selective pulse on only one transition. In this situation the pulse sequence in Figure 8-3 is used. This pulse sequence uses the J coupling of the system to overpopulate the |αβ> and the |βα> energy levels by creating terms such as $\mathbf{I}_z\mathbf{S}_z$. The pulse sequence starts with a selective 90° pulse on one component. In the following calculation the two different peaks (the A and X components of the spectrum) are represented as **I** and **S**.

$$\mathbf{I}_z \xrightarrow{90_y} \mathbf{I}_x \tag{107}$$

Then the system evolves under the J coupling between the **I** and **S** spins for a time, τ.

$$\mathbf{I}_x \xrightarrow{2\pi J_{IS}\mathbf{I}_z\mathbf{S}_z} \mathbf{I}_x \cos\left(\pi J_{IS}\tau\right) + 2\mathbf{I}_y\mathbf{S}_z \sin\left(\pi J_{IS}\tau\right) \tag{108}$$

A broadband $180°_y$ pulse is applied which reverses the sign of the coherences:

$$\mathbf{I}_x \cos(\pi J_{IS}\tau) \xrightarrow{180_y} -\mathbf{I}_x \cos(\pi J_{IS}\tau)$$
$$2\mathbf{I}_y\mathbf{S}_z \sin(\pi J_{IS}\tau) \xrightarrow{180_y} -2\mathbf{I}_y\mathbf{S}_z \sin(\pi J_{IS}\tau) \tag{109}$$

The system is again allowed to evolve under J coupling for a time, τ.

$$-\mathbf{I}_x \cos(\pi J_{IS}\tau) \overset{2\pi J_{IS}\mathbf{I}_z\mathbf{S}_z}{\rightarrow} -\mathbf{I}_x \cos(\pi J_{IS}\tau)\cos(\pi J_{IS}\tau) - 2\mathbf{I}_y\mathbf{S}_z \cos(\pi J_{IS}\tau)\sin(\pi J_{IS}\tau)$$
$$-2\mathbf{I}_y\mathbf{S}_z \sin(\pi J_{IS}\tau) \overset{2\pi J_{IS}\mathbf{I}_z\mathbf{S}_z}{\rightarrow} -2\mathbf{I}_y\mathbf{S}_z \sin(\pi J_{IS}\tau)\cos(\pi J_{IS}\tau) + \mathbf{I}_x \sin(\pi J_{IS}\tau)\sin(\pi J_{IS}\tau) \tag{110}$$

This can be simplified to be:

$$-2\mathbf{I}_y\mathbf{S}_z \sin(\pi J_{IS}\tau)\cos(\pi J_{IS}\tau) = -2\mathbf{I}_y\mathbf{S}_z \sin(2\pi J_{IS}\tau)$$
$$-\mathbf{I}_x \cos(\pi J_{IS}\tau)\cos(\pi J_{IS}\tau) + \mathbf{I}_x \sin(\pi J_{IS}\tau)\sin(\pi J_{IS}\tau) = -\mathbf{I}_x\left(\cos^2(\pi J_{IS}\tau) - \sin^2(\pi J_{IS}\tau)\right)$$
$$= \mathbf{I}_x \cos(2\pi J_{IS}\tau) \tag{111}$$

The final selective $90°_x$ pulse converts the two-spin terms into the desired $-\mathbf{I}_z\mathbf{S}_z$ term and does not affect the $\mathbf{I}_z$ term.

$$-2\mathbf{I}_y\mathbf{S}_z \sin(2\pi J_{IS}\tau) \overset{90_x}{\rightarrow} -2\mathbf{I}_z\mathbf{S}_z \sin(2\pi J_{IS}\tau)$$
$$\mathbf{I}_x \cos(2\pi J_{IS}\tau) \overset{90_x}{\rightarrow} \mathbf{I}_x \cos(2\pi J_{IS}\tau) \tag{112}$$

By choosing particular values of τ, we can select either coherence. Since we want the $-\mathbf{I}_z\mathbf{S}_z$term, τ is chosen such that $\sin(2\pi J_{IS}\tau) = 1$, while $\cos(2\pi J_{IS}\tau) = 0$. The overall effect of this pulse sequence is identical to applying a selective inversion pulse on one of the transitions in the AX system.

As long as the system is an AX system, the populations in the singlet and triplet states will be constantly intermixing since the singlet and triplet states are not

eigenstates of this system. In order to convert the $|\alpha\beta>$ and the $|\beta\alpha>$ states into the singlet state, we have to change the configuration of the molecule to make the singlet state an eigenstate. Any rapid (faster than T_1) reaction that converts our AX molecule to an A_2 molecule is acceptable. Once the molecule has been converted to an A_2 molecule, the energy levels are the same as given in eq.3 (96) and shown in Figure 8-1. As long as the molecule stays as an A_2 type system, the singlet population will relax at a much slower rate. Unfortunately, the population in the singlet state is silent to NMR, so in order to access these trapped populations an additional reaction is necessary.

The final step of the singlet experiment is a chemical reaction which converts the A_2 system to an AX system, allowing the populations in the singlet state to be observed. If enough time as passed since the system was converted to an A_2 system, the populations in the triplet manifold will have relaxed and equilibrated populations. With the conversion back to an AX system, the 30% trapped populations will move into the $|\alpha\beta>$ and the $|\beta\alpha>$ states creating an overabundance of population in the middle energy levels. The application of RF pulses can be used to access these populations and a resurgence of signal should be detected.

8.4 Selection and characterization of a molecular system for use with the singlet state.

For our demonstrations of storage of hyperpolarized populations in the singlet state, we selected diacetyl (2,3 butanedione). When diacetyl is placed in water, a hydrate forms where one of the carbonyl groups becomes two –OH groups. Depending on the

temperature and pH of the system the conversion between diacetyl and the hydrate changes. The addition of acetone to the system also changes the exchange rate between the two species; acetone causes the equilibrium of the system to be pushed towards diacetyl and away from the hydrate.

The diacetyl molecule is an A_2 system, where the two carbonyl carbons are chemically (but not magnetically equivalent). When the molecule is in this form, the singlet – triplet basis is almost a perfect basis for this system (see chapter 9 for more details). When diacetyl converts to the hydrate, it converts to an AX system. The rate of exchange between the hydrate and diacetyl system under different conditions (temperature, pH, addition of acetone) can be found by running two experiments. First, the T_1 of the system has to be determined by running a broadband inversion – recovery experiment. In this experiment, a broadband inversion pulse is applied which inverts all the peaks in the spectrum. A delay follows, and then a 90° pulse is applied. As the delay is incremented, the peaks have more time to recover from the inversion pulse. The rate at which the peaks recover is determined by T_1. By fitting the peak intensities to the equation:

$$M = M_0 \left(1 - e^{-\frac{t}{T_1}}\right) \tag{113}$$

The value of T_1 for each peak in a spectrum can be determined.

Once the value of T_1 is known, a second experiment can be done to determine the exchange rate. If a selective pulse is applied to one peak in a spectrum, the rate at which

that peak recovers can provide us with an estimate of the exchange rate T_{ex}. An isolated molecule which is not exchanging with any other molecules in the system would have a T_{ex} which is identical to T_1. If that molecule is exchanging with another, unperturbed species, then T_{ex} would be smaller (faster) than T_1 as given in the following expression:

$$\frac{1}{T_{1,sel}} = \frac{1}{T_{1,bb}} + \frac{1}{T_{ex}} \left(\frac{[Hydrate]}{[Diacetyl]} \right) \tag{114}$$

Using the above methods, we were able to determine the following information about the effect of pH, temperature and acetone concentration on the exchange rate of diacetyl.

Table 6 - Comparison of the hydrate-diacetyl exchange rates. The top row gives the hydration rate (i.e. diacetyl to hydrate), the middle row gives the dehydration rate (hydrate to diacetyl) and the bottom row gives the rate of exchange of the hydrate groups between the two labeled carbon sites on the molecule. Table courtesy of Y. Morris Chen.

	20% Diacetyl 80% Water, 23C
Diacetyl hydration rate	30.6 s
Diacetyl dehydration rate	66.6 s
Diacetyl site exchange rate	270 s

8.5 Demonstration of the existence of singlet states in a thermal sample

The existence of the long lived singlet state can be seen by looking at the FIDs from a thermally polarized sample of doubly ^{13}C labeled diacetyl and water at room

temperature. The $|\alpha\beta>$ and the $|\beta\alpha>$ states were overpopulated by applying a selective inversion pulse on one peak of the hydrate, followed by a delay and a small flip angle pulse to probe the populations. By looking at the FID coming from the hydrate peaks, we can detect signal coming out of the singlet state. Populations that were in the singlet state when the molecule was diacetyl come out into the $|\alpha\beta>$ and the $|\beta\alpha>$ states, causing an overpopulation in these energy levels. The result of this is that instead of destructive interference at 1/2J in the FID, there will be an excess of signal at that time and by watching that point in the FID we can see the signal coming from the singlet state.

In Figure 8-3, we present the results of a thermal experiment. At short delays after the inversion pulse, there is a large amount of signal at 1/2J, which quickly dies off as the delay increases. Some of this decay is due to relaxation, and some is due to that population getting converted to unobservable singlet population. At a delay of 30s, we see a return of signal at 1/2J, indicating the flow of populations out of the singlet state. At later delay times (such as a delay of 50s), we see the FID return to with a null at 1/2J.

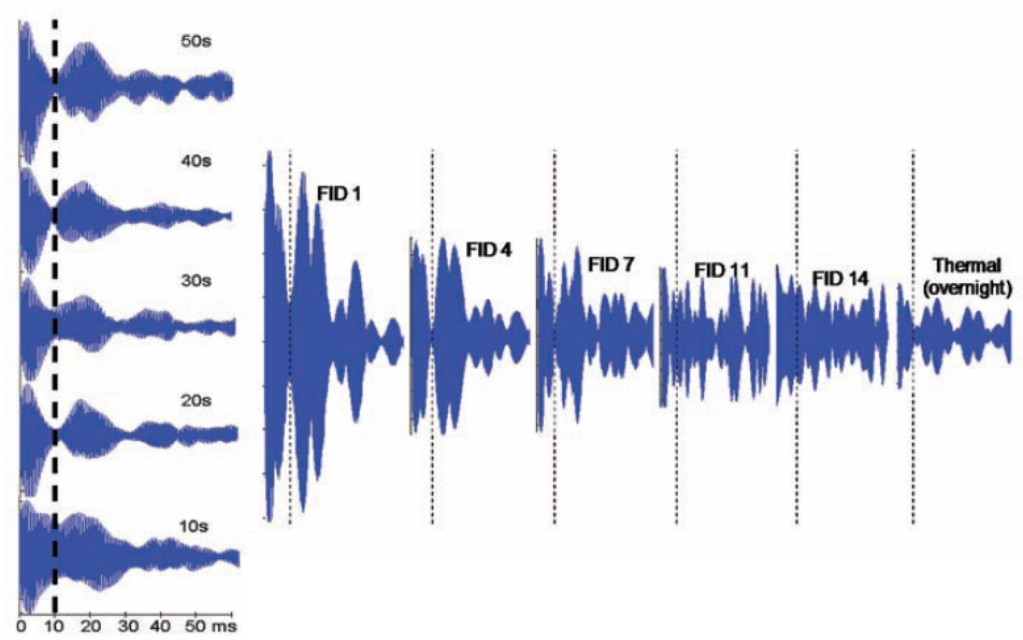

Figure 8-3 – FIDs of the hydrate signal. Left – a single line of the hydrate doublet was inverted, and then some time was allowed to pass, followed by a 45° pulse to probe the magnetization. Right – the magnetization preparation sequence was applied to hyperpolarized samples. The signal at 1/2J is initially present after the preparation of the perturbed state. This signal goes away as the sample converts from the AX hydrate form to the A_2 diacetyl storing the singlet state. At a later time, when the diacetyl has converted back to hydrate the signal reappears.

8.6 Hyperpolarized population storage with the singlet state

The ultimate goal of this work is to extend the lifetime of hyperpolarized species by storing the populations in the singlet state for times longer than T_1. In figure 5 we present the first example of this. A sample of diacetyl with water and DMSO was hyperpolarized. The solution was dissolved in 5 mL of PBS buffer (pH 7.2) and inserted into our 7T small animal magnet using a homebuilt solenoid coil. The hyperpolarization was probed by a small flip angle pulse. The pulse sequence described earlier was used to

prepare the magnetization, interchanging the populations in the $|\alpha\alpha>$ state and the $|\alpha\beta>$ state and maximizing the effect of the hyperpolarization. Acetone was injected after this pulse sequence was run, forcing the equilibrium away from the AX system to the A_2 system and trapping some of the population in the singlet state. A series of 45° pulses were applied, causing the magnetization in the triplet states to equilibrate, but not affecting the singlet populations. Then, warm (~37°C) water was injected, forcing the equilibrium back towards the AX system, and releasing the stored populations. The results of this experiment are shown in Figure 8-4.

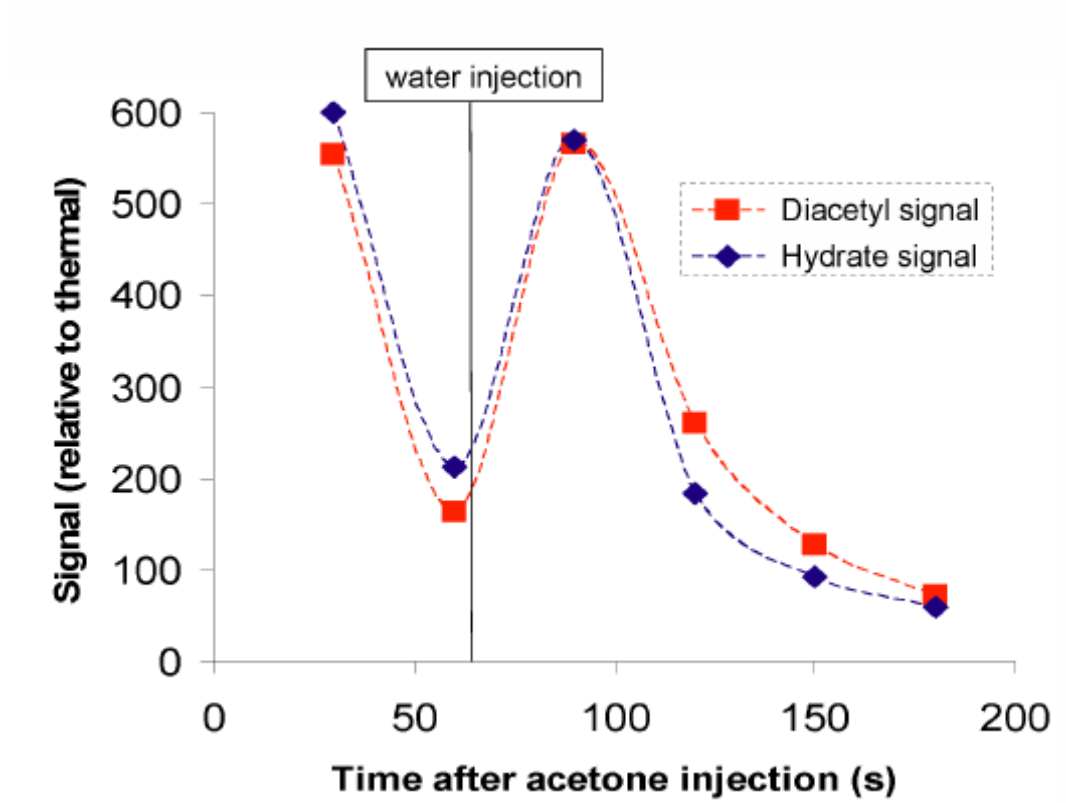

Figure 8-4 - Experimental demonstration of the storage of hyperpolarized species in the singlet state. Hyperpolarized diacetyl was inserted into the magnet and the

magnetization preparation sequence was used to overpopulate the middle energy levels. Acetone was then injected forcing the system away from the AX configuration to the A_2 system (first point on the graph). The signal in the triplet energy levels decays, and then water is injected, causing the system to convert back to an AX system and releasing the stored populations and causing a resurgence of signal at a later time.

This demonstration shows that storage of hyperpolarized populations in the singlet state is possible. The technique appears to be broadly applicable to a wide range of molecules. A description of a molecular screening tool will be given in Chapter 9, which can determine the singlet quality of the energy levels of any molecule. These experiments presented in this chapter represent the first steps towards development of a method which can extend the applicability of DNP to a new range of metabolic processes and lifetimes.

Chapter 9 - **Calculation of Singlet Character and Relaxation**

In the previous chapter we discussed the application of singlet states to the storage of hyperpolarized populations in order to extend the hyperpolarized lifetime. The lifetime extension comes from trapping populations in a disconnected eigenstate (called the singlet state), where no transitions in or out of this state are allowed. In reality, there are only a small number of molecules that have perfect singlet eigenstates-those where the two spins in question are magnetically equivalent, meaning that they have exactly the same resonance frequency and are coupled identically to every other spin in the molecule. $H_2{}^{16}O$ and H_2 are simple examples of molecules which have perfect singlet eigenstates; a slightly more complex example would be $H_2{}^{17}O$ which still has a singlet hydrogen eigenstate because the two ^{17}O-H couplings are identical. The singlet state of H_2 has been widely used (parahydrogen), and is the basis of the hyperpolarization technique called PASADENA. H_2O also has a singlet state, but the hydrogens on water are constantly associating and disassociating, causing the singlet state to have an extremely short lifetime. The experiments in chapter 8 showed that molecules which don't have perfect singlet eigenstates can still be used for the storage of hyperpolarized lifetimes. The focus of this chapter will be on the development of a tool which allows for the calculation of the exact character of the singlet state of any given molecule, and (in the absence of relaxation) what the transition rate in and out of the

singlet state would be. The second focus is on the relaxation mechanisms which affect the singlet state, namely dipole- dipole interactions.

9.1 Calculating the overlap of the singlet state and actual eigenstates of the system

The calculation of the singlet character is a fairly straightforward calculation. In short, all that is needed is to define the Hamiltonian of the system (as given by the magnetic field strength, chemical shifts of all spins and coupling constants), then to watch the evolution of the singlet state under this Hamiltonian with time.

The Hamiltonian of a given spin system is calculated by first defining the number of spins of any nuclear type (i.e. the number of atoms hydrogen, carbon, nitrogen, etc. in a given molecule). By taking a simple 1D NMR spectrum (no decoupling), the coupling constants between all the different spins can be extracted (with the exception of magnetically equivalent spins such as the protons in a methyl group) and included in the calculation, as well as the chemical shifts. Thus, the Hamiltonian can be written:

$$H = \sum_{i=1}^{N} \omega_{0,i} \mathbf{I}_{zi} + \sum_{i=1}^{N} \sum_{j>i}^{N} 2\pi J_{ij} \mathbf{I}_{zi} \mathbf{I}_{zj} \tag{115}$$

$$\omega_{0,i} = \gamma_i \left(1 - \sigma_i\right) B_0 \tag{116}$$

In this expression B_0 is the magnetic field strength, N is the number of spins, σ_i is the chemical shift of the spin i and J_{ij} is the coupling constant between spins i and j. For an N spin system there are 2^N matrix elements in the density matrix. The next step is

to define the singlet density matrix for the N spin system. This is done by taking the Kronecker product between the expression for the 2 – spin singlet state, and the total number of spins in the system:

$$\rho_0 = \left(\frac{\mathbf{E}}{4} - (\mathbf{I}_1 \bullet \mathbf{I}_2)\right) \times \frac{\mathbf{I}_{n-2}}{n^2} \tag{117}$$

Where $\mathbf{I}_n$ is the identity matrix for n spins. For these calculations we always assume that the singlet state exists between spins 1 and 2, and the rest of the spins are of a different nuclear type. This represents the initial state of our system (we are assuming that the system is starting as a perfect singlet state).

To calculate the singlet character of the molecular system, we have to convert ρ_0 to the Hamiltonian eigenbasis. This is done by first finding the eigenstates and eigenvalues of the Hamiltonian. For this tool, we used the Matlab function "eig" which takes in the Hamiltonian and produces two matrices, V and D. D is a diagonal matrix with all the eigenvalues along the diagonal, and V is a matrix where the columns correspond to the eigenstates of the system. Using V as a change of basis matrix, ρ_0 is converted into the Hamiltonian eigenbasis. In order to calculate the overlap between the actual eigenstates of the system and the singlet state, ρ_0 (in the Hamiltonian eigenbasis) is block diagonalized. This matrix is called ρ'. The expectation value of ρ' is calculated by the following:

$$\langle \rho' \rangle = tr\left(\rho_0 * \rho'\right) \tag{118}$$

The percentage of overlap between the actual singlet state of the molecule and the perfect singlet state is calculated by taking:

$$overlap = 100 - \frac{tr\left(\rho_0^2\right) - tr\left(\rho_0 * \rho'\right)}{\frac{1}{2}tr\left(\rho_0^2\right)} * 100 \tag{119}$$

This gives a rough numerical estimate to the quality of the singlet state. For example, the overlap for diacetyl is 96%.

9.2 Calculating the time-dependent behavior of the singlet state

A method for estimating the lifetime enhancement of the storage of populations in the singlet state can be calculated by watching the evolution of the density matrix under the influence of the nuclear spin Hamiltonian with time and then calculating the allowed transitions from that state. The rate of transitions from the singlet state can provide us with an estimation for the lifetime enhancement that we should expect from the nuclear system.

The evolution of the system is described by the equation of motion:

$$\frac{d\rho}{dt} = -\frac{i}{\hbar}\left[\rho, H\right] \tag{120}$$

If we assume that the Hamiltonian is time independent, then an exact solution to this equation is given by:

$$\rho(t) = e^{iHt}\rho(0)e^{-iHt} \tag{121}$$

Allowed transitions are connected by a single spin flip which can be represented by the operator $\mathbf{I}_x$. In the case of allowed transitions out of the singlet state, these

transitions can be written as $\mathbf{I}_{x1} + \mathbf{I}_{x2}$ where the subscripts 1 and 2 indicate the two spins which comprise the singlet state. The intensity (and rate) of a transition is usually calculated using time dependent perturbation theory (Fermi's Golden Rule). The operator $\mathbf{I}_{x1} + \mathbf{I}_{x2}$ is the perturbation that causes transitions in our system, so rate of transitions in our system can be written:

$$W_{f \to i} = \sum_{f} |\langle i|\mathbf{I}_{x1} + \mathbf{I}_{x2}|f\rangle|^2 \tag{122}$$

Where i is the initial state, and f is the final state. This is technically correct, but this equation describes all transitions in the system from every initial state to every final state. We are only concerned with transitions from the singlet state. To calculate the rate of transitions from the singlet state, we first take the commutator of the density matrix (which starts as a perfect singlet state) with the operator that causes the transitions, $\mathbf{I}_{x1} + \mathbf{I}_{x2}$.

$$\dot{\rho}\,(t) = i\,[\rho\,(t)\,, \mathbf{I}_{x1} + \mathbf{I}_{x2}] \tag{123}$$

The expectation value of $\dot{\rho}(t)$ gives us the magnitude of any transitions from the singlet state.

$$\langle\dot{\rho}\rangle = tr\{\dot{\rho}^2\} \tag{124}$$

Using this method, several different molecular systems were evaluated for use as singlet state storage molecules for hyperpolarized populations. The first molecule is diacetyl, our standard test system. Figure 9-1 shows the time dependent transition rate from the singlet state. Note that the average value is 0.033 (a completely

allowed transition would have an average value of 1). This suggests that populations in the singlet state of diacetyl have a lifetime greater than 30 times that of the triplet populations. For comparison, the average transition rate of the hydrate of diacetyl (**Figure 9-2**) is 1, indicating that the singlet state is a poor eigenstate of the system and transitions rapidly move in and out of that state.

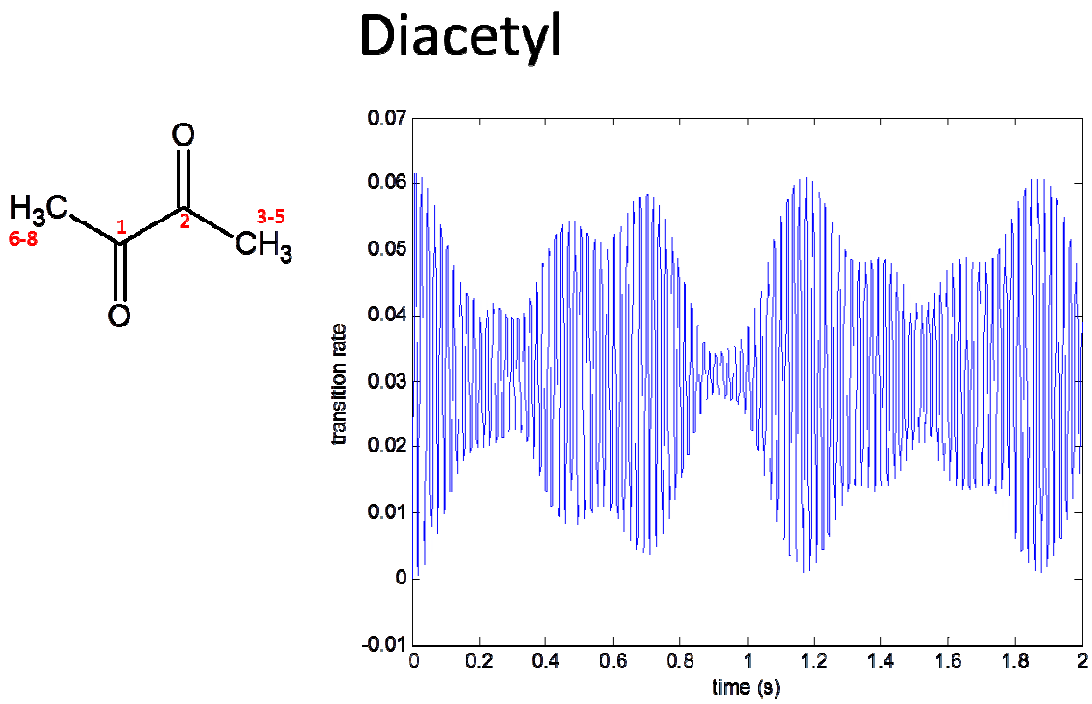

Figure 9-1 - Calculated behavior of diacetyl singlet state. The oscillations of the transition rate are determined by the scalar couplings in the molecule as well as the chemical shift differences between the spins. For this calculation the following parameters were used: Chemical shift (in ppm): spin 1 (C) = 198, spin 2 (C) = 198, spin 3-8 (H) = 2. J couplings (Hz): J12=50, J12=50, J13=6.4, J14=6.4, J15=6.4, J16=-1.1, J17=-1.1, J18=-1.1, J23=-1.1, J24=-1.1, J25=-1.1, J26=6.4, J27=6.4, J28=6.4. Magnetic field is 7T.

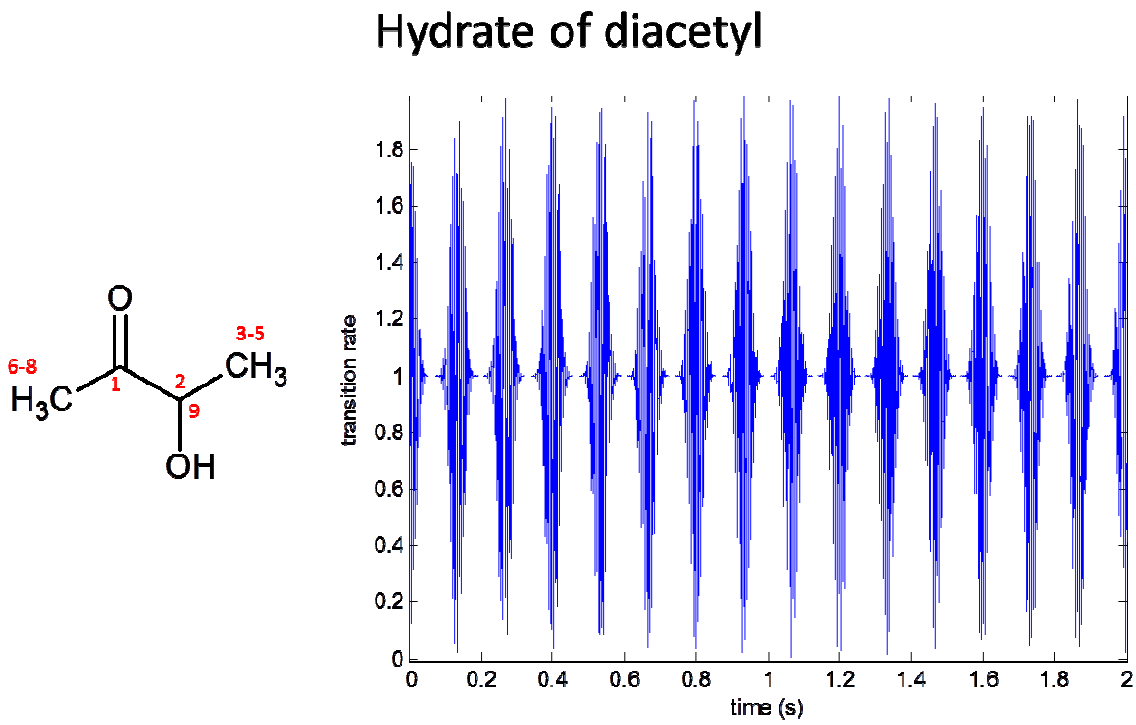

Figure 9-2 Transition rate of the hydrate of diacetyl. The average transition rate for the hydrate is 1 which indicates that the singlet state is not a stationary state in this molecule and populations in the singlet state are free to move to other states. For this calculation the following parameters were used: Chemical shift (in ppm): Spin 1 (C) = 210, spin 2 (C) = 95 ppm, spin 3-5 (H) =4, spin 6-8 (H) = 3. J coupling (Hz): J12=50, J12=50, J13=6.4, J14=6.4, J15=6.4, J16=-1.1, J17=-1.1, J18=-1.1, J23=-1.1, J24=-1.1, J25=-1.1, J26=6.4, J27=6.4, J28=6.4 All other J couplings set to zero. Magnetic field is 7T.

A second example molecule is L-DOPA (**Figure 9-3**). L-DOPA almost fits the requirements for use as a singlet state molecule. It has a non-symmetric precursor, and a metabolic pathway converts L-DOPA into a non-symmetric molecule. The two highlighted carbons in L-DOPA are not perfectly chemically equivalent, their chemical shifts differ by 0.68 ppm. At 7T, the chemical shift is large compared to the J coupling (calculated overlap is 44.5%), and the singlet state is not a good eigenstate. But, at

clinical fields (1.5T) the chemical shift difference is much smaller (overlap is 95.44%) and the average transition rate out of the singlet state for L-DOPA is 0.05.

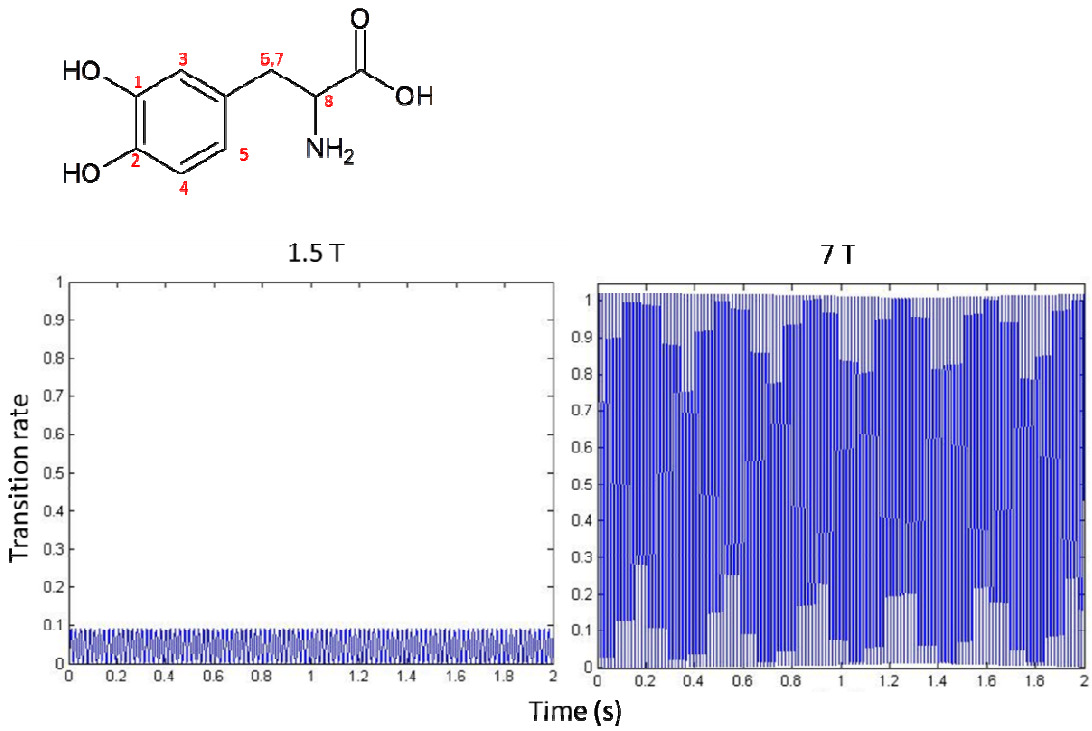

Figure 9-3 - Calculation of the transition rate from the singlet state for L-DOPA at 1.5T and 7T. The parameters for the calculations are: Chemical shift (ppm): spin 1 = 145.08, spin 2 = 144.4, spin 3 = 6.62e-6, spin 4 = 6.49, spin 5= 6.67, spin 6=2.58, spin 7=2.59, and spin 8=3.31. J coupling (Hz): J12=50; J13=0; J14=0; J15=0; J16=0; J17=0; J18=0; J23=0; J24=0; J25=0J26=0;J27=0; J28=0; J34=8; J35=.3; J36=.1; J37=.1;J38=0; J45=1; J46=.5; J47=.5; J48=.1; J56=.5; J57=.5; J58=.1; J67=11; J68=1; J78=1;

The example of L-DOPA demonstrates the effect that Levitt[137] exploited to provide the first demonstration of singlet states. In that work, the sample was removed from the magnet to remove the chemical shift difference between the spins. A perfect singlet state exists when the molecule is an A_2 molecule (e.g. when the chemical shifts

are the same), and then goes to an AB system as the chemical shifts start to get to more dissimilar. At the extreme end, the system becomes an AX system where the chemical shifts are very large compared to the scalar coupling. For an arbitrary AB system (so any coupled two spin molecule) the energy levels of the system can be described by the following:

$$\begin{gathered} |\beta\beta\rangle \\ \cos\theta|\alpha\beta\rangle + \sin\theta|\beta\alpha\rangle \\ -\sin\theta|\alpha\beta\rangle + \cos\theta|\beta\alpha\rangle \\ |\alpha\alpha\rangle \end{gathered} \tag{125}$$

The mixing of the middle energy levels is dictated by the mixing angle, θ, which is determined by comparing the chemical shift difference and the J coupling and is defined as:

$$\begin{gathered} \sin 2\theta = J/D \\ \cos 2\theta = \frac{\omega_1 - \omega)2}{D} \\ D = \left[(\omega_1 - \omega_2)^2 + J^2\right]^{1/2} \end{gathered} \tag{126}$$

The energy levels for an AB system are also dependent on the chemical shift difference relative to the J coupling and are defined as:

$$\begin{gathered} E_{|\beta\beta\rangle} = \frac{1}{2}(\omega_1 + \omega_2) + \frac{1}{4}J \\ E_{\cos\theta|\alpha\beta\rangle + \sin\theta|\beta\alpha\rangle} = \frac{1}{2}D - \frac{1}{4}J \\ E_{-\sin\theta|\alpha\beta\rangle + \cos\theta|\beta\alpha\rangle} = -\frac{1}{2}D - \frac{1}{4}J \\ E_{|\alpha\alpha\rangle} = -\frac{1}{2}(\omega_1 + \omega_2) + \frac{1}{4}J \end{gathered} \tag{127}$$

Using these definitions, an A_2 system is one in which $\omega_1 - \omega_2 = 0$ and thus $\theta = 45^\circ$ causing maximum mixing of the middle energy levels. On the opposite end of the spectrum is an AX system in which $\theta = 0^\circ$, and the energy levels $|\alpha\beta\rangle$ and $|\beta\alpha\rangle$ aren't mixed at all. In the case of L-DOPA, at 7T the chemical shift difference between the two carbons is 112 Hz which is much greater than the J coupling between them of about 50 Hz, putting this system into the AX category. When the field is lowered to 1.5T the chemical shift difference is much smaller, 16 Hz, which is smaller than the J coupling moving it much closer to the A_2 system in which the singlet state is an eigenstate of the system.

Further simulations using WindNMR-Pro help to explain the surprising complexity of the diacetyl spectrum (Figure 9-4). The spectrum of the singly labeled diacetyl (Figure 9-4a) behaves as expected, as a quartet of quartets (first splitting from the nearby protons, second, finer splitting from the protons three bonds away). This spectrum is identical to the simulation in which the carbon coupling is zero, and the scalar couplings to the two different proton groups connect the singlet state to the other states in the system. The more interesting case is when the carbon – carbon coupling is very large. In this case the spectrum behaves as if there was only one, singly labeled carbon in the system (as there is in acetone) and the protons split both the carbons equally. Even more intriguing is that the splitting is an average of the two scalar coupling constants. The reason for this is that the spectrum comes entirely from

transitions in which the carbons are in the $|T_0\rangle$ state, which is delocalized over both the carbons, and is equally coupled to the adjacent protons. In the situation of diacetyl, we are not quite in this limit, but the complexity of the doubly labeled diacetyl spectrum indicates that there is a disconnected eigenstate.

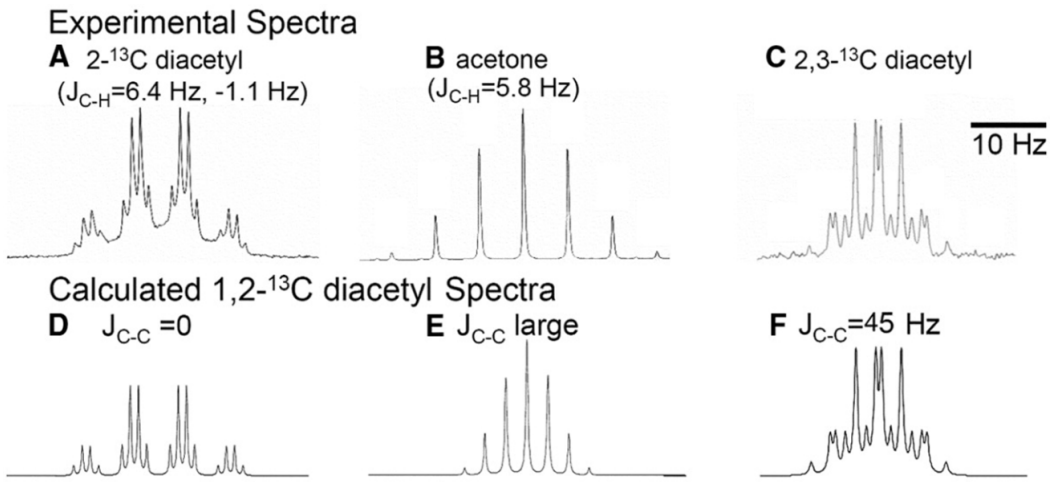

Figure 9-4 - Comparison of the experimental spectra and calculated spectra for acetone and diacetyl. A. Experimental carbon (proton coupled) spectrum of singly labeled diacetyl. B. Proton-coupled carbon spectrum of acetone. C. Proton-coupled spectrum of doubly labeled diacetyl. D. Simulated spectrum of a 8 spin molecule with the C-C coupling set to zero. E. Same simulated spectrum, but with a large C-C coupling. F. Simulation of the diacetyl molecule, doubly labeled.

This straightforward tool allows for the rapid evaluation of molecules for use with the singlet state. By looking at the singlet character with time, we can get an estimation for the expected lifetime enhancement from storing populations in the singlet state. Further work in needed to include the effects of relaxation in this calculation. Singlet states comprised of two chemically equivalent spins is likely longer lived than systems in which the two spins of the singlet state are made equivalent by removing the

magnetic field since many relaxation mechanisms will treat both the spins identically and prevent loss of population from the singlet state. Only events which break the symmetry of the molecule will cause populations to leak from the singlet state.

Chapter 10 - **Improved T2 weighted imaging using unequally spaced pulses**

For much of magnetic resonance imaging, image contrast comes from one (or more) of three parameters: T_1, T_2 and spin density. Manipulation of pulse sequences to enhance contrast based on one of these three parameters constitutes the bulk of the pulse sequences in magnetic resonance. The CPMG (Carr – Purcell – Meiboom – Gill) pulse sequence[148, 149] is one of the most well-known sequences and has been used since the 1950s when it was first designed to create T_2 weighted contrast in MRI. More recent work[150] demonstrated that in tissue the CPMG pulse sequence outperformed standard spin echo pulse sequences, and extended the T_2 of the sample. Even more surprisingly, recent papers from the quantum computing community have demonstrated that for some samples, the CPMG sequence is not the optimum pulse sequence, and an analytically derived sequence using unevenly spaced refocusing pulses can further extend the apparent T_2 [151, 152]. This chapter will focus on the first application of the unevenly spaced pulse sequence derived by Uhrig [152] (the Uhrig Dynamic Decoupling, or UDD, pulse sequence) to magnetic resonance and discuss the mechanisms by which the UDD sequence extends T_2.

The relaxation rate, T_2 refers to the rate at which the transverse magnetization of a system decays (or dephases). The dephasing is caused because different spins experience slightly different magnetic fields causing the Larmor frequencies of the spins

to be slightly different. The differences in magnetic field (which cause the dephasing) are usually caused by other spins, diffusion in and out of different environments (which have different magnetic susceptibilities) and magnetic field inhomogeneities. Some of these changes in the local magnetic field are static with time, such as magnetic field inhomogeneities, while others vary with time such as those caused by diffusion through different environments. Fluctuations in the magnetic field that change with time, and cause irreversible dephasing are characterized with the time constant T_2, while static inhomogeneities which can be refocused with the application of a 180° pulse create a signal decay described by the relaxation time constant T_2^*.

10.1 Refocusing Static Field Inhomogeneities

The explanation of how the static field inhomogeneities (which lead to T_2^* relaxation) are refocused is given by the classic "race track" metaphor. Imagine runners lined up on a race track. The runners start running all at the same time. Each runner has his or her own characteristic speed and after some time the runners are no longer lined up (i.e. dephased). The starter blows a gun and all the runners immediately turn around and run back to the start line at the same speed. At an equal time later all the runners arrive at the start line, all lined up. If we extend this metaphor to magnetic resonance, after an initial 90° pulse which puts the magnetization in the plane, the spins are allowed to precess for some time. During that time, the spins might experience different magnetic fields and precess at different frequencies. After this evolution period, a 180°

pulse causes them to reverse direction and at an equal amount of time later the spins refocus and the signal is recovered, assuming that the spins experience the same local magnetic field before and after the 180° pulse[153] (see Figure 1-1).

This sequence only successfully reverses the dephasing that was the same for each spin throughout the experiment. If there are changes in the magnetic field, or the sample which cause the spins to experience a different magnetic field before the 180° pulse than afterwards, then the spins won't be cleanly refocused and the observed signal will decrease. Returning to the metaphor of the runners, if the runners start running at one speed, but after they turn around they are tired and run back at a different speed, then they won't all reach the start line at exactly the same time.

10.2 Toggling Frame Hamiltonian

To understand how the CPMG and UDD sequences do a better job of refocusing time-varying magnetic field inhomogeneities, we have to change how we think about the pulse sequence. Instead of considering what the spins are doing, we can consider the effect the pulse sequence has on the system, in other words, the modulation imposed upon the system by the pulse sequence. This switch in reference frame is referred to as the "toggling frame Hamiltonian[154]" or the interaction representation. As shown in earlier chapters, the effect of any pulse sequence can be calculated from the equation of motion using the density matrix. If we use this formalism to evaluate the spin echo pulse

sequence ($90°_x$ – TE/2 – $180°_y$ – TE/2), assuming the dephasing is caused by static field inhomogeneities ($H = \Delta\omega \frac{TE}{2} \mathbf{I}_z$) we get:

$$\rho(t) = e^{-i\Delta\omega\frac{TE}{2}\mathbf{I}_z} e^{-i\pi\mathbf{I}_y} e^{-i\Delta\omega\frac{TE}{2}\mathbf{I}_z} e^{-i\frac{\pi}{2}\mathbf{I}_x} \mathbf{I}_z e^{i\frac{\pi}{2}\mathbf{I}_x} e^{i\Delta\omega\frac{TE}{2}\mathbf{I}_z} e^{i\pi\mathbf{I}_y} e^{i\Delta\omega\frac{TE}{2}\mathbf{I}_z} \tag{128}$$

The effect of the first propagator is to covert $\mathbf{I}_z$ to $\mathbf{I}_y$, and by inserting the identity operator ($e^{-i\pi\mathbf{I}_y} e^{i\pi\mathbf{I}_y}$) and ($e^{i\pi\mathbf{I}_y} e^{-i\pi\mathbf{I}_y}$) into the above expression we can get:

$$\rho(t) = e^{-i\Delta\omega\frac{TE}{2}\mathbf{I}_z} e^{-i\pi\mathbf{I}_y} e^{-i\Delta\omega\frac{TE}{2}\mathbf{I}_z} e^{i\pi\mathbf{I}_y} e^{-i\pi\mathbf{I}_y} \mathbf{I}_y e^{-i\pi\mathbf{I}_y} e^{i\pi\mathbf{I}_y} e^{i\Delta\omega\frac{TE}{2}\mathbf{I}_z} e^{i\pi\mathbf{I}_y} e^{i\Delta\omega\frac{TE}{2}\mathbf{I}_z} \tag{129}$$

By re-grouping some of the terms in this equation, we can see that the net effect of the 180° pulses is simply a reversal of the evolution during TE/2.

$$\rho(t) = e^{-i\Delta\omega\frac{TE}{2}\mathbf{I}_z} \left(e^{-i\pi\mathbf{I}_y} e^{-i\Delta\omega\frac{TE}{2}\mathbf{I}_z} e^{i\pi\mathbf{I}_y} \right) e^{-i\pi\mathbf{I}_y} \mathbf{I}_y e^{i\pi\mathbf{I}_y} \left(e^{-i\pi\mathbf{I}_y} e^{i\Delta\omega\frac{TE}{2}\mathbf{I}_z} e^{i\pi\mathbf{I}_y} \right) e^{i\Delta\omega\frac{TE}{2}\mathbf{I}_z} \tag{130}$$

$$\rho(t) = e^{-i\Delta\omega\frac{TE}{2}\mathbf{I}_z} e^{i\Delta\omega\frac{TE}{2}\mathbf{I}_z} \mathbf{I}_y e^{-i\Delta\omega\frac{TE}{2}\mathbf{I}_z} e^{i\Delta\omega\frac{TE}{2}\mathbf{I}_z}$$

$$\rho(t) = \mathbf{I}_y \tag{131}$$

The toggling frame Hamiltonian is a simplified way of describing the effect of the pulse sequence. Instead of considering the 180° degree pulses as rotating the magnetization, instead they can be viewed as rotating the Hamiltonian. With this notation, a pulse sequence with a series of 180° pulses and delays can be described as (see Figure 10-1):

$$\widetilde{H} = \begin{cases} \hbar\Delta\omega(\vec{r})\mathbf{I}_z & t_1, t_3, t_5 ... \\ -\hbar\Delta\omega(\vec{r})\mathbf{I}_z & t_2, t_4, t_6 ... \end{cases} \tag{132}$$

$$\widetilde{H} \equiv \hbar\Delta\omega(\vec{r}) y(t) \mathbf{I}_z \tag{133}$$

$$y(t) = \begin{cases} 1 & t_1, t_3, t_5 ... \\ -1 & t_2, t_4, t_6 ... \end{cases} \tag{134}$$

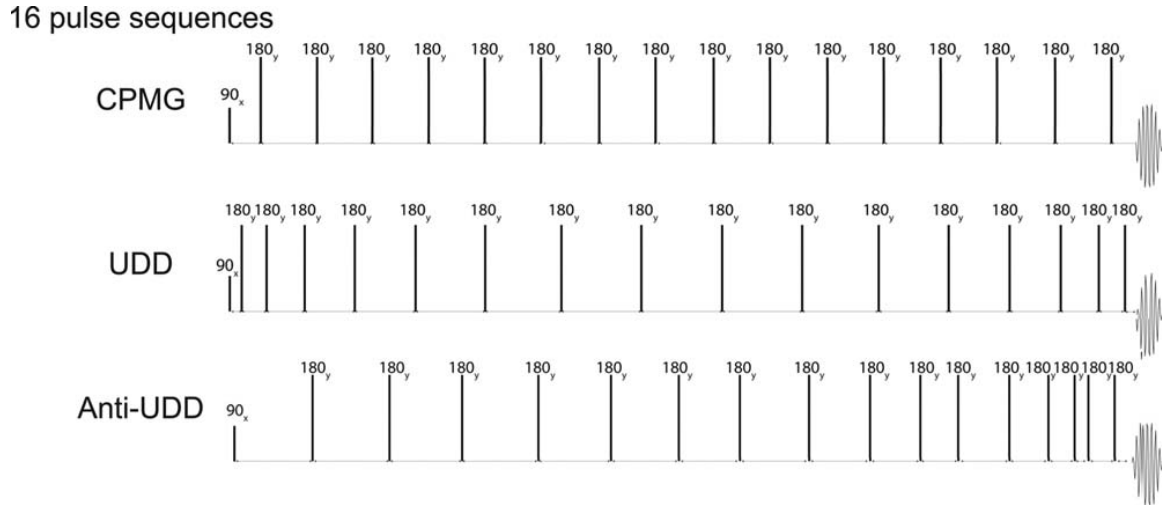

Figure 10-1 - UDD, CPMG and Anti-UDD 16 pulse sequences. The CPMG sequence is characterized by even spacings between the 180° pulses, while the UDD sequence has unequal spacings. The anti-UDD sequence is designed to create a valid echo (the delays add up to create an echo in the absence of time varying fluctuations), and uses the same timings as the UDD sequence, but the timings are not arranged in the same way as prescribed by the UDD formula.

The time intervals t_1, t_2, t_3 … refer to the time intervals after 180° pulses. Since the only spin operators present are $\pm\mathbf{I}_z$, the effect of this pulse sequence is easily calculated. The modulation imposed by the pulse sequence is described as $y(t)$, and as long as the frequency fluctuations are constant then the effect of the Hamiltonian (i.e. the average Hamiltonian, $\bar{H}$) is zero:

$$\bar{H} = \int_0^T \widetilde{H} dt \tag{135}$$

Since the Hamiltonian commutes with itself at different times, the average Hamiltonian needs to be computed. Refocusing of static inhomogeneities requires only that $y(t)$ averages to zero over the experiment. This constraint is loose enough that a large

number of arrangements of pulses and delays can be imagined which satisfy this constraint.

10.2 Refocusing Time Varying Inhomogeneities

If the inhomogeneity is not constant (for example due to diffusion through different microenvironments), then an additional decay is imposed upon the pulse sequence, and the standard spin echo pulse sequence does not refocus all of the signal. A time varying and position dependent resonance offset can also be described as an instantaneous phase shift, $\Phi(T)$ for the time interval, T. This phase shift can be decomposed into its frequency components:

$$\Phi(T_{=} \int_0^T \Delta\omega(\vec{r},t)dt = \int_{t=0}^T \int_{\omega=-\infty}^{\infty} G(\vec{r},\omega)e^{-i\omega t}d\omega dt \tag{136}$$

The spins all accumulate different random phase shifts causing the echo to disappear at long times, T. The intuitive conclusion from this is that long delays should be avoided, thus, the CPMG sequence which has shorter inter-pulse delays is a superior choice to prevent T_2 relaxation.

If we consider a single frequency component in eq. (136), $\hbar G(\omega)e^{-i\omega t}\mathbf{I}_z$, then the toggling frame Hamiltonian becomes[148, 153]:

$$\widetilde{H} = \hbar G(\omega)y(t)e^{-i\omega t}\mathbf{I}_z \tag{137}$$

Which leads to an average Hamiltonian of:

$$\bar{H} = \int \hbar G(\omega) y(t) e^{-i\omega t} \mathbf{I}_z dt = \hbar G(\omega) \widetilde{y}(\omega) \mathbf{I}_z \tag{138}$$

Where $\widetilde{y}(\omega)$ is the Fourier transform of $y(t)$. If we imagine that the fluctuation is simply a sine wave, even if the sine wave itself goes through an integral number of cycles during the pulse sequence, the average Hamiltonian does not equal zero. Thus, multiple echo pulse sequences convert the fluctuations in resonance frequency into an average frequency shift that depends on the phase of the fluctuation. Since we expect $G(\omega)$ to vary across the sample, this creates a position dependent phase shift across the sample which is proportional to:

$$\int_{-\infty}^{\infty} |G(\omega)|^2 |\widetilde{y}(\omega)|^2 d\omega \tag{139}$$

$|G(\omega)|^2$ is the spectral density (identical to the spectral density from chapter 9, $J(\omega)$) and $|\widetilde{y}(\omega)|^2$ is the power spectrum of the modulation created by the pulse sequence. In other words, the quantity $|\widetilde{y}(\omega)|^2$ is a filter function, which contains the information about how the pulse sequence will prevent decoherence caused by $|G(\omega)|^2$. The quality of the suppression of decoherence due to fluctuating magnetic field inhomogeneities can be studied by looking at the range of frequencies suppressed by the pulse sequence (i.e. by looking at $|\widetilde{y}(\omega)|^2$).

10.3 Comparing UDD and CPMG

The CPMG pulse sequence consists of a series of 180° pulses which follow an initial 90° excitation pulse. The 180° pulses are equally spaced and separated by TE/n, and the 90° and the first 180° are separated by TE/2n (Figure 10-1).

The UDD sequence has the same initial excitation pulse and refocusing pulses, but these pulses are not equally spaced. The inter-pulse spacing for the jth pulse (with a total number of pulses, n) and a sequence length of TE is dictated by the equation:

$$\delta_j = TE\left(\sin^2\left(\frac{\pi j}{2n+2}\right)\right) \tag{140}$$

If we compare the power spectrum of the modulations created by the spin echo, CPMG and UDD sequences we can see why the CPMG and UDD sequences show improved refocusing in tissue and other environments in which there are time-dependent fluctuations of the magnetic field.

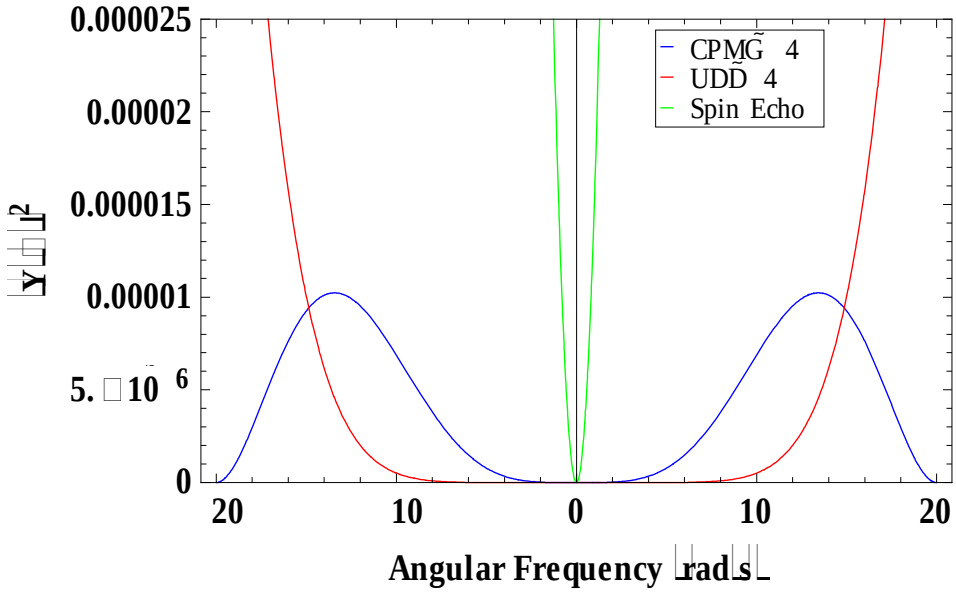

Figure 10-2 - Graph of the power spectrum of UDD, CPMG and Spin echo pulses sequences vs. frequency. Total echo time is 50 ms, CPMG and UDD sequences use 4 pulses. From this plot it is obvious that the UDD and CPMG sequences create a strong filtering function for a wider range of frequencies than the spin echo pulse sequence. Figure courtesy of Yesu Feng.

The CPMG and UDD sequences create a strong filtering function for the low frequency fluctuations, and provide a much wider range of frequencies which are suppressed by these sequences. Additionally, comparing the UDD and CPMG sequences, the two sequences create different suppression profiles – the UDD sequence uniformly suppresses frequencies, while the CPMG sequence suppresses frequencies around +- 5 rad/s and above 20 rad/s, but does a poorer job of suppressing the intermediate frequencies. This simulation suggests that since the UDD and CPMG sequences suppress different ranges of frequencies, it is possible that running both

sequences on the same sample could provide different, unique contrast which reflects the different molecular processes occurring.

10.4 Experimental Demonstration of the UDD sequence

The simulations of the UDD sequence show that for static resonance frequency fluctuations (centered around 0 rad/s) the CPMG, UDD and spin echo sequence all perform the same; in very simple samples such as water in a test tube, the three pulse sequences should perform the same. It is only in samples with greater complexity, such as tissue, that we expect to see a difference between the sequences.

The first experimental demonstration of the UDD sequence was done using a dead, thawed mouse. This mouse had been frozen and thawed, creating some unique tissue characteristics, such as deposits of water where the thawing process had destroyed the cellular structure. The UDD, CPMG and anti-UDD sequences were run on this mouse with different total sequence lengths as well as variations in the number of pulses. By subtracting the images created by each pulse sequence, we are best able to see the situations in which the UDD sequence provides enhanced refocusing over the CPMG sequence.

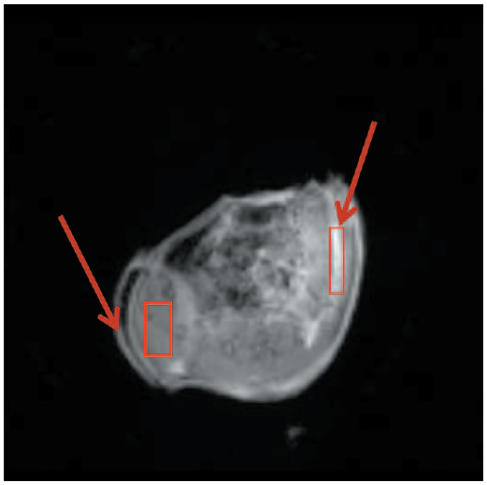

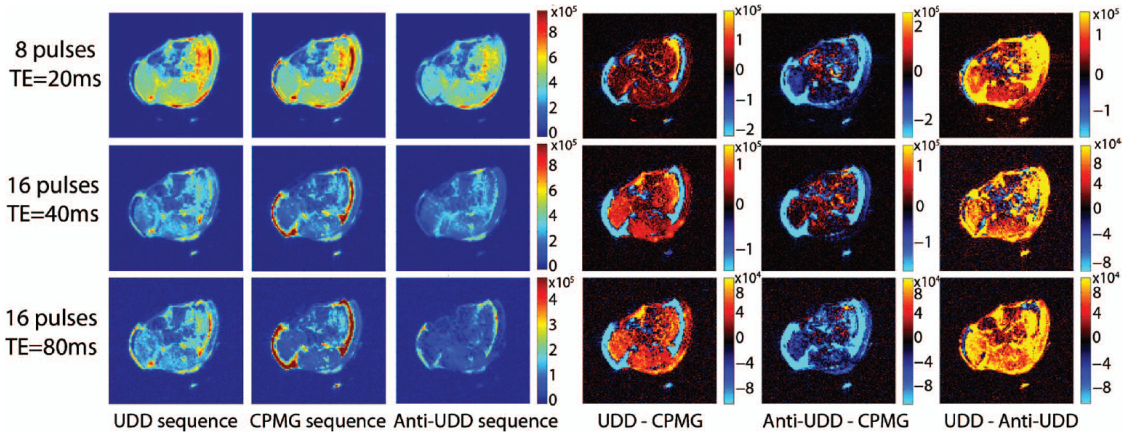

Figure 10-3 – Top: Spin echo image of the slice used for the UDD and CPMG images. The arrows point to the location of free water created by cellular degradation during the freezing/thawing processes. The red box indicated the region used for the comparison of the signal presented in table 1. Bottom: Comparison of the UDD, CPMG and anti-UDD pulse sequences on a thawed mouse. The subtraction images show that the UDD sequence provides enhanced refocusing in the bulk tissue, while the CPMG sequence does a better job of refocusing signal from the water deposits. Pulses were 1.27 ms hermite, 256 x 256 matrix, 8 mm axial slice, 8 cm FOV, crusher gradients flanking the refocusing pulses.

The UDD sequence provides enhanced refocusing in the bulk tissue, while the CPMG sequence refocuses the signal in the water deposits better. Both the CPMG and UDD sequence provide enhanced refocusing compared to the anti-UDD sequence. As

the echo time (TE) increases, as well as the number of pulses, the effect of the UDD sequence becomes more pronounced.

A more quantative analysis of the data from this experiment is given in table 1. In this table, the relative SNR of the UDD, CPMG and anti-UDD sequences are compared for the ROI marked in the top of figure 3. The ratios in table 1 show that in the bulk tissue, the UDD sequence can provide significant increases in SNR, up to a 70% enhancement.

Table 7 - Comparison of the SNR from the UDD, anti-UDD and CPMG sequences. Free water and tissue ROIs were selected as shown in figure 2. Note that at the longer echo times with 16 pulses, the CPMG sequence refocuses the free water very well, while the UDD sequence has significantly improved SNR in the tissue ROI. In addition, the anti-UDD sequence significantly underperforms both the UDD and CPMG sequence in the tissue ROI for the 16 pulse sequence with TE=80ms**.**

	Free water	Tissue
UDD/CPMG, 8 pulse, TE=20 ms	**1 .03**	**1 .41**
Anti-UDD/CPMG, 8 pulse, TE=20 ms	0 .69	1 .35
UDD/Anti-UDD, 8 pulse, TE=20 ms	1 .50	1 .05
UDD/CPMG 16 pulse, TE=40 ms	**0 .40**	**1 .22**
Anti-UDD/CPMG 16 pulse, TE=40 ms	0 .27	0 .93
UDD/Anti-UDD, 16 pulse, TE=40 ms	1 .50	1 .31
UDD/CPMG, 16 pulse, TE=80 ms	**0 .52**	**1 .71**
Anti-UDD/CPMG, 16 pulse, TE=80 ms	0 .32	0 .59
UDD/Anti-UDD,	1	2

16 pulse, TE=80 ms	.65	.88

A T_2 map was run on a different thawed mouse to compare the regions where UDD was optimal with the T_2 values found for those regions. In general, the CPMG sequence performed better in regions with a longer T_2, while the UDD sequence performed better in the moderate T_2 regions.

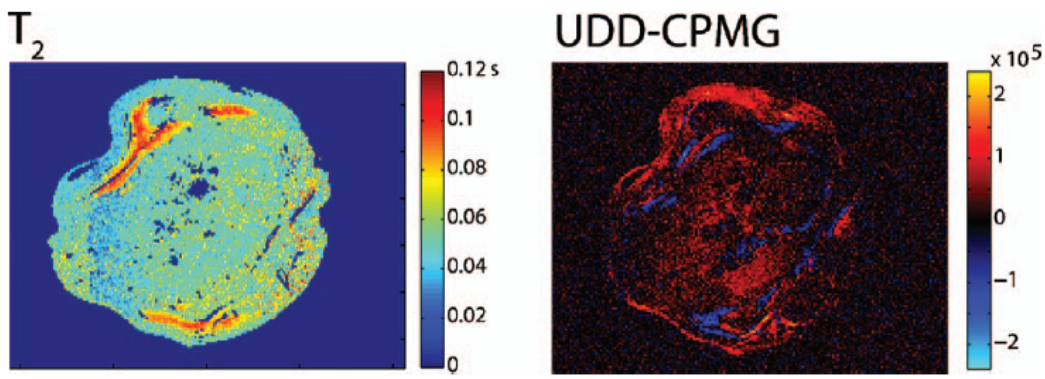

Figure 10-4 - Comparison of T_2 and the effectiveness of UDD and CPMG. The T_2 map was generated by fitting the decay of a series of spin echo images with the TE varying from 10 ms to 160 ms. The difference map on the right was generated by taking the difference between a UDD and CPMG (8 pulse) images with a TE of 80 ms.

The T_2 map demonstrates that there is not a perfect correlation between T_2 and differences in signal from CPMG vs. UDD. This shows that the UDD sequence is providing contrast that is different and unique to that which is produced by T_2 mapping methods.

The most important demonstration of the differences in contrast created by the UDD sequence comes from looking at the types of samples that would benefit the most

from the development of new contrast methods. One example of this is imaging of cancer. In figure 5 we present data from a mouse with a large implanted prostate tumor.

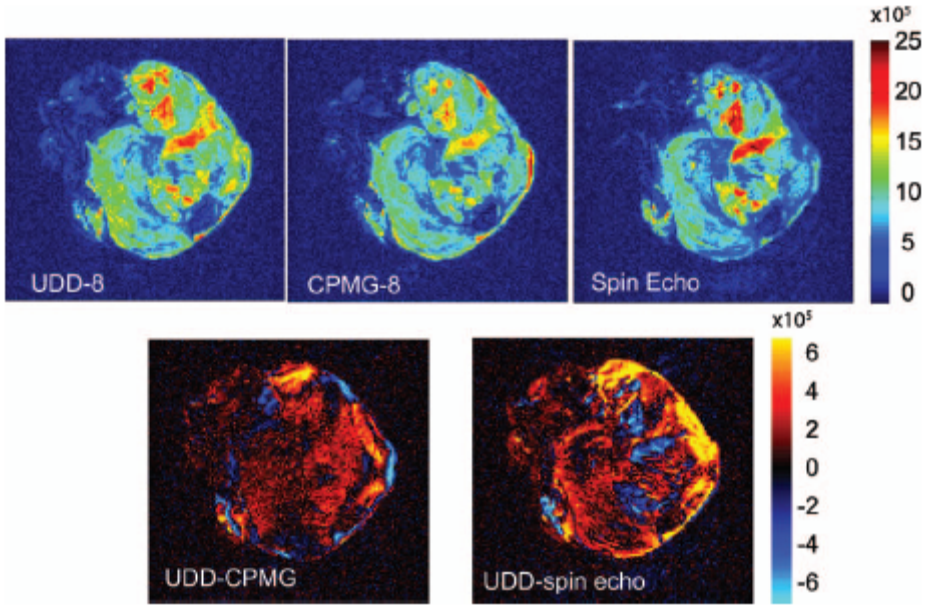

Figure 10-5 - In vivo demonstration of the UDD sequence compared to the CPMG and spin echo pulse sequences. The UDD sequence provides enhanced refocusing in the bulk tissue, while the CPMG and spin echo sequences refocus signal from necrotic areas of the tumor. All of the bright regions in the image are tumor tissue. Slice is a 2 mm, axial slice, .5 ms hermite pulses, 2s TR, 3 cm FOV, 120 ms TE.

The difference maps between the spin echo and the UDD images as well as the difference maps between the CPMG and UDD sequence show that the signal refocused by the UDD sequence provides different contrast than the signal from the CPMG or spin echo methods. The UDD sequence does a better job of refocusing the signal from the bulk tumor tissue, while the CPMG and spin echo sequences seem to highlight the areas of necrosis.

The experiments presented here are the first demonstration of the application of the UDD sequence to magnetic resonance. These preliminary studies indicate that the UDD sequence can provide enhanced refocusing and suppression of T_2 relaxation caused by low frequency fluctuations in the magnetic field. The UDD sequence imposes a unique modulation on the sample which serves as a filtering function, selectively removing contributions to relaxation of a particular frequency range. One can imagine that by choosing other arrangements of sequence timings other ranges of frequencies could be suppressed, allowing for specific and unique contrast to be obtained by manipulating the pulse spacings. In addition, application of T_2 lengthening pulse sequences can be very useful to certain types of signals, such as iMQCs, in which the signal size depends strongly on the length of T_2[19].

Chapter 11 - Future directions for signal enhancement

The projects presented here provide a novel example of methods for signal enhancement resulting from the manipulation of the underlying physics. Many of these projects represent first steps towards the development of clinically useful technologies which promise to help enhance the sensitivity and selectivity of magnetic resonance imaging. The purpose of this chapter is to provide possible future directions for the various projects presented in this thesis with the final goal of developing new clinically useful methods for signal enhancement.

11.1 Temperature Detection with iMQCs in Adipose Tissue

The temperature imaging project presented in chapters 4 and 5 represent the first possible clinical application of iMQCs. In those chapters we showed that temperature detection was possible using iMQCs and the use of iMQCs provided some unique enhancements such as an insensitivity to magnetic field inhomogeneities as well as detection of temperature on an absolute scale. These results laid the groundwork for future clinical applications, but several hurdles remain before this sequence can be used as part of hyperthermia treatments. The main problem that needs to be addressed is the signal to noise of the iMQC temperature measurements are lower than that of conventional methods. As we move to the detection of smaller lesions (and thus smaller slices), the SNR will also drop, and thus methods for enhancing the iMQC signal are needed. Several methods are being developed which address this.

11.1.1 iMQC signal enhancement with ZEBRA

Recent work has demonstrated that a novel method for creating iMQCs, called the ZEBRA sequence[155], which theoretically can produce iMQC signals as large as standard signals. The gradients in a CRAZED sequence create sinusoidally modulated magnetization along the direction of the gradient. In the ZEBRA sequence, the magnetization along the z-axis is modulated into square waves (or "striped"). After the striping, the magnetization is distributed along the z-axis as +z and –z. A mixing pulse, θ_x, is then applied transferring some of the modulation equally between the +y and –y axes, and leaving some remaining portion of the magnetization along the +z and –z axis. The remaining magnetization along the z-axis creates a dipolar field which rotates the transverse magnetization causing it to refocus at a later time. Because of the square modulation of the magnetization, the magnetization that is along –y is refocused only by the magnetization along –z ($\theta < \pi/2$), and the magnetization along +y is only refocused by the magnetization along +z. This method more efficiently uses the dipolar field, causing more of the transverse magnetization to be refocused, leading to higher signals.

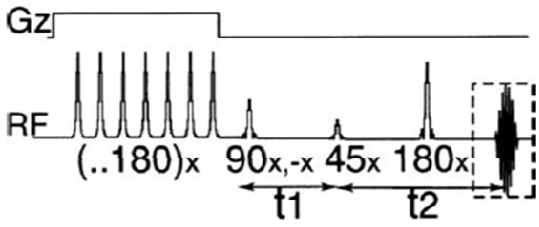

Figure 11-1 - The ZEBRA pulse sequence. The 180 pulses and gradient create a binary modulation of the magnetization, resulting in enhanced iMQC SNR. Figure from [155].

11.1.2 – iMQC signal enhancement with UDD

In chapter 10 we demonstrated that the UDD pulse sequence could prevent T_2 signal decay compared to a spin echo. As we saw in chapters 6 and 7, the iMQC signal intensity is proportional to T_2/τ_D. In order to enhance the iMQC signal we either need to increase T_2 or decrease τ_D. Applying the UDD pulse sequence after the CRAZED sequence can prevent dephasing due to T_2 and thus, increase the signal from iMQCs. A demonstration of this is given in Figure **11-2**.

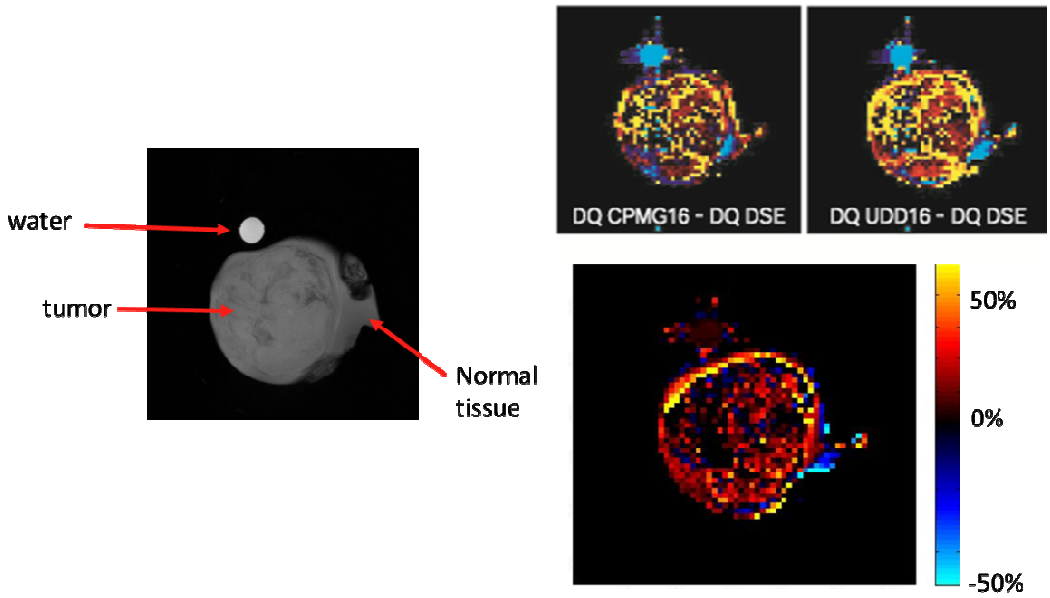

Figure 11-2 - Demonstration of the application of iMQCs with the UDD pulse sequence. Both the UDD and CPMG pulse sequences increase the iMQC signal compared to a spin-echo of the same duration. Figure courtesy of A. Stokes.

11.2 Future work with the singlet state

The work presented here on the singlet state shows that through applications of chemistry we can store hyperpolarized population in the singlet state and recall it at a later time. This represents an exciting first step towards extending the utility of hyperpolarized carbon , since it circumvents the main limitation of that technique – the short lifetime. Future work on the hyperpolarized singlet state could go in several directions. The lifetime extension needs to be characterized and optimized, either through manipulation of the solvent system or through storage of the

hyperpolarized species in carrier vessels such as liposomes. Second, other methods for creating and storing hyperpolarized singlet states are possible.

11.2.1 – Singlet delivery systems

Many different biologically compatible delivery systems exist which could prove to be ideal carriers for hyperpolarized reagents. There are liposomes, micelles and polymeresomes which are designed for drug delivery and only dissipate under certain physiological situations. For example, liposomes[71] have been developed which release chemotherapy drugs when heated to a particular temperature for use with hyperthermia treatments. A similar system could be developed for use with diacetyl or another singlet molecule where the environment inside the vesicle is different than the environment outside the vesicle causing a chemical change in the singlet molecule which releases the stored hyperpolarized signal. In this case, the singlet molecule would work as a reporter agent; creating signal only when there was a mechanism by which the delivery vesicle released the molecule.

11.2.2 – Singlets with para-hydrogen

A recent paper[156] has demonstrated a novel method for hyperpolarization using para-hydrogen. In these experiments a metal intermediate serves to transfer polarization from the para-hydrogen species to the substrate of choice simply by combining them in a tube and shaking. The method that they used was restricted to polarizing AB or AX type systems, in which the substrate molecule has no singlet state,

but one could imagine polarizing an A_2 system, thus transferring the polarization directly to the singlet state of the substrate molecule. This method would circumvent many of the possible problems with the DNP based method presented in chapter 8, since in that method an AX system is hyperpolarized, and there is some time period between the time the sample exits the polarizer and before it is transformed into a singlet in which polarization is lost. This method directly polarizes the singlet state molecule, thus preventing some loss due to relaxation of the AX system.

11.3 – Conclusion

The purpose of this thesis was to describe efforts towards improving the sensitivity of magnetic resonance with the final goal of improving detection of different disease states. The improvements in sensitivity described in this work were all done by manipulating the inherent physics of the system; either by creating new endogenous contrast using multiple echo pulse sequences and iMQCs or by manipulating the physics of hyperpolarized carbon contrast agents. Future work on these projects will focus on applying these techniques in clinical settings to determine if they provide additional information for the diagnosis and treatment of different disease state

Bibliography

1. Bloch, F., *Nuclear Induction.* Physical Review, 1946. **70**(7-8): p. 460-474.
2. Haacke, E.M., R.W. Brown, M.R. Thompson, and R. Venkatesan, *Magnetic Resonance Imaging: Physical Principles and Sequence Design*. 1999: Wiley-Liss.
3. Keeler, J., *Understanding NMR Spectroscopy*. 1 ed. 2005: Wiley.
4. Levitt, M., *Spin Dynamics: Basics of Nuclear Magnetic Resonance*. 2nd ed. 2008: Wiley.
5. Keeler, J., *Understanding NMR Spectroscopy*. 1 ed. 2005: Wiley. 476.
6. Ahn, S. and W.S. Warren, *Effects of intermolecular dipolar couplings in solution NMR in separated time intervals: the competition for coherence transfer pathways.* Chemical Physics Letters, 1998. **291**(1-2): p. 121-129.
7. Ahn, S., W.S. Warren, and S. Lee, *Quantum treatment of intermolecular multiple-quantum coherences with intramolecular J coupling in solution NMR.* Journal of Magnetic Resonance, 1997. **128**(2): p. 114-129.
8. Bouchard, L.S. and W.S. Warren, *Multiple-quantum vector field imaging by magnetic resonance.* Journal of Magnetic Resonance, 2005. **177**(1): p. 9-21.
9. Bowtell, R., *Indirect detection via the dipolar demagnetizing field.* Journal of Magnetic Resonance, 1992. **100**(1): p. 1-17.
10. Branca, R.T., C. Silvia, and M. Bruno, *About the CRAZED sequence.* Concepts in Magnetic Resonance Part A, 2004. **21A**(1): p. 22-36.
11. Cho, J.H., S. Ahn, C. Lee, K.S. Hong, K.C. Chung, S.K. Chang, C. Cheong, and W.S. Warren, *Magnetic resonance microscopic imaging based on high-order intermolecular multiple-quantum coherences.* Magnetic Resonance Imaging, 2007. **25**(5): p. 626-633.
12. He, Q.H., W. Richter, S. Vathyam, and W.S. Warren, *Intermolecular Multiple-Quantum Coherences and Cross Correlations in Solution Nuclear-Magnetic-Resonance.* Journal of Chemical Physics, 1993. **98**(9): p. 6779-6800.
13. Lee, S., W. Richter, S. Vathyam, and W.S. Warren, *Quantum treatment of the effects of dipole-dipole interactions in liquid nuclear magnetic resonance.* Journal of Chemical Physics, 1996. **105**(3): p. 874-900.
14. Lin, Y.Y., S. Ahn, N. Murali, W. Brey, C.R. Bowers, and W.S. Warren, *High-resolution, > 1 GHz NMR in unstable magnetic fields.* Physical Review Letters, 2000. **85**(17): p. 3732-3735.

15. Richter, W. and W.S. Warren, *Intermolecular multiple quantum coherences in liquids.* Concepts in Magnetic Resonance, 2000. **12**(6): p. 396-409.

16. Richter, W.S.L.W., W.S.; Qiuhong He, *Imaging with intermolecular multiple-quantum coherences in solution nuclear magnetic resonance.* Science, 1995. **267**(5198): p. 654-657.

17. Rizi, R.R., S. Ahn, D.C. Alsop, S. Garrett-Roe, M. Mescher, W. Richter, M.D. Schnall, J.S. Leigh, and W.S. Warren, *Intermolecular zero-quantum coherence imaging of the human brain.* Magnetic Resonance in Medicine, 2000. **43**(5): p. 627-632.

18. Vathyam, S., S. Lee, and W.S. Warren, *Homogeneous NMR spectra in inhomogeneous fields.* Science, 1996. **272**(5258): p. 92-96.

19. Warren, W.S., S. Lee, W. Richter, and S. Vathyam, *Correcting the classical dipolar demagnetizing field in solution NMR.* Chemical Physics Letters, 1995. **247**(3): p. 207-214.

20. Warren, W.S., *Rethinking solution NMR.* Science, 1998. **280**(5362): p. 398-399.

21. Warren, W.S., S. Ahn, M. Mescher, M. Garwood, K. Ugurbil, W. Richter, R.R. Rizi, J. Hopkins, and J.S. Leigh, *MR imaging contrast enhancement based on intermolecular zero quantum coherences.* Science, 1998. **281**(5374): p. 247-251.

22. Warren, W.S., W. Richter, A.H. Andreotti, and B.T. Farmer, *Generation of Impossible Cross-Peaks between Bulk Water and Biomolecules in Solution Nmr.* Science, 1993. **262**(5142): p. 2005-2009.

23. Qiuhong He, W.R., Sujatha Vathyam, and Warren S. Warren *Intermolecular multiple-quantum coherences and cross correlations in solution nuclear magnetic resonance.* Journal of Chemical Physics, 1993. **98**(9): p. 6779-6800.

24. Richter, W., S.H. Lee, W.S. Warren, and Q.H. He, *Imaging with Intermolecular Multiple-Quantum Coherences in Solution Nuclear-Magnetic-Resonance.* Science, 1995. **267**(5198): p. 654-657.

25. Albers, M.J., R. Bok, A.P. Chen, C.H. Cunningham, M.L. Zierhut, V.Y. Zhang, S.J. Kohler, J. Tropp, R.E. Hurd, Y.F. Yen, S.J. Nelson, D.B. Vigneron, and J. Kurhanewicz, *Hyperpolarized C-13 Lactate, Pyruvate, and Alanine: Noninvasive Biomarkers for Prostate Cancer Detection and Grading.* Cancer Research, 2008. **68**(20): p. 8607-8615.

26. Bhattacharya, P., E.Y. Chekmenev, W.H. Perman, K.C. Harris, A.P. Lin, V.A. Norton, C.T. Tan, B.D. Ross, and D.P. Weitekamp, *Towards hyperpolarized C-13-succinate imaging of brain cancer.* Journal of Magnetic Resonance, 2007. **186**(1): p. 150-155.

27. Bhattacharya, P., K. Harris, A.P. Lin, M. Mansson, V.A. Norton, W.H. Perman, D.P. Weitekamp, and B.D. Ross, *Ultra-fast three dimensional imaging of hyperpolarized C-13 in vivo.* Magnetic Resonance Materials in Physics Biology and Medicine, 2005. **18**(5): p. 245-256.

28. Chen, A.P., M.J. Albers, C.H. Cunningham, S.J. Kohler, Y.F. Yen, R.E. Hurd, J. Tropp, R. Bok, J.M. Pauly, S.J. Nelson, J. Kurhanewicz, and D.B. Vigneron, *Hyperpolarized c-13 spectroscopic imaging of the TRAMP mouse at 3T - Initial experience.* Magnetic Resonance in Medicine, 2007. **58**(6): p. 1099-1106.

29. Chen, A.P., J. Tropp, R.E. Hurd, M. Van Criekinge, L.G. Carvajal, D. Xu, J. Kurhanewicz, and D.B. Vigneron, *In vivo hyperpolarized C-13 MR spectroscopic imaging with H-1 decoupling.* Journal of Magnetic Resonance, 2009. **197**(1): p. 100-106.

30. Day, S.E., M.I. Kettunen, F.A. Gallagher, D.E. Hu, M. Lerche, J. Wolber, K. Golman, J.H. Ardenkjaer-Larsen, and K.M. Brindle, *Detecting tumor response to treatment using hyperpolarized C-13 magnetic resonance imaging and spectroscopy.* Nature Medicine, 2007. **13**(11): p. 1382-1387.

31. Frydman, L. and D. Blazina, *Ultrafast two-dimensional nuclear magnetic resonance spectroscopy of hyperpolarized solutions.* Nature Physics, 2007. **3**(6): p. 415-419.

32. Gabellieri, C., S. Reynolds, A. Lavie, G.S. Payne, M.O. Leach, and T.R. Eykyn, *Therapeutic target metabolism observed using hyperpolarized N-15 choline.* Journal of the American Chemical Society, 2008. **130**(14): p. 4598-+.

33. Golman, K., R. in't Zandt, M. Lerche, R. Pehrson, and J.H. Ardenkjaer-Larsen, *Metabolic imaging by hyperpolarized C-13 magnetic resonance imaging for in vivo tumor diagnosis.* Cancer Research, 2006. **66**(22): p. 10855-10860.

34. Golman, K., R. in't Zandt, and M. Thaning, *Real-time metabolic imaging.* Proceedings of the National Academy of Sciences of the United States of America, 2006. **103**(30): p. 11270-11275.

35. Golman, K. and J.S. Petersson, *Metabolic Imaging and Other Applications of Hyperpolarized 13C1.* Academic Radiology, 2006. **13**(8): p. 932-942.

36. Golman, K. and J.S. Petersson, *Metabolic imaging and other applications of hyperpolarized C-13.* Academic Radiology, 2006. **13**(8): p. 932-942.

37. Golman, K., J.S. Petersson, P. Magnusson, E. Johansson, P. Akeson, C.M. Chai, G. Hansson, and S. Mansson, *Cardiac metabolism measured noninvasively by hyperpolarized C-13 MRI.* Magnetic Resonance in Medicine, 2008. **59**(5): p. 1005-1013.

38. Hu, S., A.P. Chen, M.L. Zierhut, R. Bok, Y.F. Yen, M.A. Schroeder, R.E. Hurd, S.J. Nelson, J. Kurhanewicz, and D.B. Vigneron, *In Vivo Carbon-13 Dynamic MRS and*

MRSI of Normal and Fasted Rat Liver with Hyperpolarized C-13-Pyruvate. Molecular Imaging and Biology, 2009. **11**(6): p. 399-407.

39. Hurd, R.E., Y.F. Yen, D. Mayer, A. Chen, D. Wilson, S. Kohler, R. Bok, D. Vigneron, J. Kurhanewicz, J. Tropp, D. Spielman, and A. Pfefferbaum, *Metabolic Imaging in the Anesthetized Rat Brain Using Hyperpolarized 1-C-13 Pyruvate and 1-C-13 Ethyl Pyruvate.* Magnetic Resonance in Medicine, 2010. **63**(5): p. 1137-1143.

40. Jenista, E.R., R.T. Branca, and W.S. Warren, *Hyperpolarized carbon-carbon intermolecular multiple quantum coherences.* Journal of Magnetic Resonance, 2009. **196**(1): p. 74-77.

41. Johansson, E., S. Månsson, R. Wirestam, J. Svensson, J.S. Petersson, K. Golman, and F. Ståhlberg, *Cerebral perfusion assessment by bolus tracking using hyperpolarized 13C.* 2004. **51**(3): p. 464-472.

42. Keshari, K.R., J. Kurhanewicz, R.E. Jeffries, D.M. Wilson, B.J. Dewar, M. Van Criekinge, M. Zierhut, D.B. Vigneron, and J.M. Macdonald, *Hyperpolarized C-13 Spectroscopy and an NMR-Compatible Bioreactor System for the Investigation of Real-Time Cellular Metabolism.* Magnetic Resonance in Medicine, 2010. **63**(2): p. 322-329.

43. Kettunen, M.I., D.E. Hu, T.H. Witney, R. McLaughlin, F.A. Gallagher, S.E. Bohndiek, S.E. Day, and K.M. Brindle, *Magnetization Transfer Measurements of Exchange Between Hyperpolarized 1-C-13 Pyruvate and 1-C-13 Lactate in a Murine Lymphoma.* Magnetic Resonance in Medicine, 2010. **63**(4): p. 872-880.

44. Kohler, S.J., Y. Yen, J. Wolber, A.P. Chen, M.J. Albers, R. Bok, V. Zhang, J. Tropp, S. Nelson, D.B. Vigneron, J. Kurhanewicz, and R.E. Hurd, *In vivo 13-carbon metabolic imaging at 3T with hyperpolarized13C-1-pyruvate.* Magnetic Resonance in Medicine, 2007. **58**(1): p. 65-69.

45. Kohler, S.J., Y. Yen, J. Wolber, A.P. Chen, M.J. Albers, R. Bok, V. Zhang, J. Tropp, S. Nelson, D.B. Vigneron, J. Kurhanewicz, and R.E. Hurd, *In vivo (13)carbon metabolic imaging at 3T with hyperpolarized C-13-1-pyruvate.* Magnetic Resonance in Medicine, 2007. **58**(1): p. 65-69.

46. Mayer, D., Y.S. Levin, R.E. Hurd, G.H. Glover, and D.M. Spielman, *Fast metabolic imaging of systems with sparse spectra: Application for hyperpolarized C-13 imaging.* Magnetic Resonance in Medicine, 2006. **56**(4): p. 932-937.

47. Merritt, M.E., C. Harrison, C. Storey, F.M. Jeffrey, A.D. Sherry, and C.R. Malloy, *Hyperpolarized C-13 allows a direct measure of flux through a single enzyme-catalyzed step by NMR.* Proceedings of the National Academy of Sciences of the United States of America, 2007. **104**(50): p. 19773-19777.

48. Merritt, M.E., C. Harrison, C. Storey, A.D. Sherry, and C.R. Malloy, *Inhibition of Carbohydrate Oxidation During the First Minute of Reperfusion After Brief Ischemia:*

NMR Detection of Hyperpolarized (CO2)-C-13 and (HCO3-)-C-13. Magnetic Resonance in Medicine, 2008. **60**(5): p. 1029-1036.

49. Moreno, K.X., S.M. Sabelhaus, M.E. Merritt, A.D. Sherry, and C.R. Malloy, *Competition of pyruvate with physiological substrates for oxidation by the heart: implications for studies with hyperpolarized 1-C-13 pyruvate.* American Journal of Physiology-Heart and Circulatory Physiology, 2010. **298**(5): p. H1556-H1563.

50. Park, I., P.E.Z. Larson, M.L. Zierhut, S. Hu, R. Bok, T. Ozawa, J. Kurhanewicz, D.B. Vigneron, S.R. VandenBerg, C.D. James, and S.J. Nelson, *Hyperpolarized C-13 magnetic resonance metabolic imaging: application to brain tumors.* Neuro-Oncology, 2010. **12**(2): p. 133-144.

51. Pileio, G., M. Carravetta, E. Hughes, and M.H. Levitt, *The long-lived nuclear singlet state of N-15-nitrous oxide in solution.* Journal of the American Chemical Society, 2008. **130**(38): p. 12582-+.

52. Schroeder, M.A., L.E. Cochlin, L.C. Heather, K. Clarke, G.K. Radda, D.J. Tyler, and R.G. Shulman, *In vivo assessment of pyruvate dehydrogenase flux in the heart using hyperpolarized carbon-13 magnetic resonance.* Proceedings of the National Academy of Sciences of the United States of America, 2008. **105**(33): p. 12051-12056.

53. Schroeder, M.A., P. Swietach, H.J. Atherton, F.A. Gallagher, P. Lee, G.K. Radda, K. Clarke, and D.J. Tyler, *Measuring intracellular pH in the heart using hyperpolarized carbon dioxide and bicarbonate: a C-13 and P-31 magnetic resonance spectroscopy study.* Cardiovascular Research, 2010. **86**(1): p. 82-91.

54. Svensson, J., S. Mansson, E. Johansson, J.S. Petersson, and L.E. Olsson, *Hyperpolarized C-13 MR angiography using TrueFISP.* Magnetic Resonance in Medicine, 2003. **50**(2): p. 256-262.

55. Tyler, D.J., M.A. Schroeder, L.E. Cochlin, K. Clarke, and G.K. Radda, *Application of hyperpolarized magnetic resonance in the study of cardiac metabolism.* Applied Magnetic Resonance, 2008. **34**(3-4): p. 523-531.

56. Warren, W.S., E. Jenista, R.T. Branca, and X. Chen, *Increasing Hyperpolarized Spin Lifetimes Through True Singlet Eigenstates.* Science, 2009. **323**(5922): p. 1711-1714.

57. Witney, T.H., M.I. Kettunen, S.E. Day, D.E. Hu, A.A. Neves, F.A. Gallagher, S.M. Fulton, and K.M. Brindle, *A Comparison between Radiolabeled Fluorodeoxyglucose Uptake and Hyperpolarized C-13-Labeled Pyruvate Utilization as Methods for Detecting Tumor Response to Treatment.* Neoplasia, 2009. **11**(6): p. 574-U88.

58. Yen, Y.F., P. Le Roux, D. Mayer, R. King, D. Spielman, J. Tropp, K.B. Pauly, A. Pfefferbaum, S. Vasanawala, and R. Hurd, *T-2 relaxation times of C-13 metabolites*

in a rat hepatocellular carcinoma model measured in vivo using C-13-MRS of hyperpolarized 1-C-13 pyruvate. Nmr in Biomedicine, 2010. **23**(4): p. 414-423.

59. Goodson, B.M., *Nuclear Magnetic Resonance of Laser-Polarized Noble Gases in Molecules, Materials, and Organisms.* Journal of Magnetic Resonance, 2002. **155**(2): p. 157-216.

60. Mugler, J.P., B. Driehuys, J.R. Brookeman, G.D. Cates, S.S. Berr, R.G. Bryant, T.M. Daniel, E.E. deLange, J.H. Downs, C.J. Erickson, W. Happer, D.P. Hinton, N.F. Kassel, T. Maier, C.D. Phillips, B.T. Saam, K.L. Sauer, and M.E. Wagshul, *MR imaging and spectroscopy using hyperpolarized Xe-129 gas: Preliminary human results.* Magnetic Resonance in Medicine, 1997. **37**(6): p. 809-815.

61. Bowers, C.R. and D.P. Weitekamp, *Para-hydrogen and synthesis allow dramatically enhanced nuclear alignment.* Journal of the American Chemical Society, 1987. **109**(18): p. 5541-5542.

62. Ardenkjaer-Larsen, J.H., B. Fridlund, A. Gram, G. Hansson, L. Hansson, M.H. Lerche, R. Servin, M. Thaning, and K. Golman, *Increase in signal-to-noise ratio of > 10,000 times in liquid-state NMR.* Proceedings of the National Academy of Sciences of the United States of America, 2003. **100**(18): p. 10158-10163.

63. Abragam, A. and M. Goldman, *Principles of dynamic nuclear-polarization.* Reports on Progress in Physics, 1978. **41**(3): p. 395-467.

64. Goldman, M., *Overview of spin temperature, thermal mixing and dynamic nuclear polarization.* Applied Magnetic Resonance, 2008. **34**(3-4): p. 219-226.

65. Wust, P., B. Hildebrandt, G. Sreenivasa, B. Rau, J. Gellermann, H. Riess, R. Felix, and P.M. Schlag, *Hyperthermia in combined treatment of cancer.* Lancet Oncology, 2002. **3**(8): p. 487-497.

66. Falk, M.H. and R.D. Issels, *Hyperthermia in oncology.* International Journal of Hyperthermia, 2001. **17**(1): p. 1-18.

67. Furusawa, H., K. Namba, S. Thomsen, F. Akiyama, A. Bendet, C. Tanaka, Y. Yasuda, and H. Nakahara, *Magnetic resonance-guided focused ultrasound surgery of breast cancer: Reliability and effectiveness.* Journal of the American College of Surgeons, 2006. **203**(1): p. 54-63.

68. van der Zee, J., D. González, G.C. van Rhoon, J.D.P. van Dijk, W.L.J. van Putten, and A.A.M. Hart, *Comparison of radiotherapy alone with radiotherapy plus hyperthermia in locally advanced pelvic tumours: a prospective, randomised, multicentre trial.* The Lancet, 2000. **355**(9210): p. 1119-1125.

69. Rau, B., P. Wust, W. Tilly, J. Gellermann, C. Harder, H. Riess, V. Budach, R. Felix, and P.M. Schlag, *Preoperative radiochemotherapy in locally advanced or recurrent rectal cancer: regional radiofrequency hyperthermia correlates with clinical parameters.*

International Journal of Radiation Oncology*Biology*Physics, 2000. **48**(2): p. 381-391.

70. Lohr, F., K. Hu, Q. Huang, L. Zhang, T.V. Samulski, M.W. Dewhirst, and C.-Y. Li, *Enhancement of radiotherapy by hyperthermia-regulated gene therapy.* International Journal of Radiation Oncology*Biology*Physics, 2000. **48**(5): p. 1513-1518.

71. Needham, D., G. Anyarambhatla, G. Kong, and M.W. Dewhirst, *A New Temperature-sensitive Liposome for Use with Mild Hyperthermia: Characterization and Testing in a Human Tumor Xenograft Model.* Cancer Research, 2000. **60**(5): p. 1197-1201.

72. Kim, J.H. and E.W. Hahn, *Clinical and biological studies of localized hyperthermia.* Cancer Research, 1979. **39**(6): p. 2258-2261.

73. Mark Dewhirst, Z.V., Ellen Jones, Donald Thrall, *Re-setting the biologic rationale for thermal therapy.* International Journal of Hyperthermia, 2005. **21**(8): p. 779-790.

74. Jones, E., D. Thrall, M.W. Dewhirst, and Z. Vujaskovic, *Prospective thermal dosimetry: The key to hyperthermia's future.* International Journal of Hyperthermia, 2006. **22**(3): p. 247-253.

75. Jones, E.L., J.R. Oleson, L.R. Prosnitz, T.V. Samulski, Z. Vujaskovic, D.H. Yu, L.L. Sanders, and M.W. Dewhirst, *Randomized trial of hyperthermia and radiation for superficial tumors.* Journal of Clinical Oncology, 2005. **23**(13): p. 3079-3085.

76. Hand, J.W., D. Machin, C.C. Vernon, and J.B. Whaley, *Analysis of thermal parameters obtained during Phase III trials of hyperthermia as an adjunct to radiotherapy in the treatment of breast carcinoma.* International Journal of Hyperthermia, 1997. **13**(4): p. 343-364.

77. Kapp, D.S. and R.S. Cox, *Thermal - treatment parameters are most predictive of outcome in patients with single tumor nodules per treatment field in recurrent adenocarcinoma of the breast.* International Journal of Radiation Oncology Biology Physics, 1995. **33**(4): p. 887-899.

78. Oleson, J.R., T.V. Samulski, K.A. Leopold, S.T. Clegg, M.W. Dewhirst, R.K. Dodge, and S.L. George, *Sensitivity of hyperthermia trial outcomes to temperature and time - implications for thermal goals of treatment.* International Journal of Radiation Oncology Biology Physics, 1993. **25**(2): p. 289-297.

79. Seegenschmiedt, M.H., P. Martus, R. Fietkau, H. Iro, L.W. Brady, and R. Sauer, *Multivariate - analysis of prognostic parameters using interstitial thermoradiotherapy (IHT-IRT) - tumor and treatment variables predict outcome.* International Journal of Radiation Oncology Biology Physics, 1994. **29**(5): p. 1049-1063.

80. Sherar, M., F.F. Liu, M. Pintilie, W. Levin, J. Hunt, R. Hill, J. Hand, C. Vernon, G. vanRhoon, J. vanderZee, D.G. Gonzalez, J. vanDijk, J. Whaley, and D. Machin,

Relationship between thermal dose and outcome in thermoradiotherapy treatments for superficial recurrences of breast cancer: Data from a phase III trial. International Journal of Radiation Oncology Biology Physics, 1997. **39**(2): p. 371-380.

81. Depoorter, J., C. Dewagter, Y. Dedeene, C. Thomsen, F. Stahlberg, and E. Achten, *Noninvasive MRT Thermometry with the proton-resonance frequency (PRF) method - In -vivo results in human muscle.* Magnetic Resonance in Medicine, 1995. **33**(1): p. 74-81.

82. Depoorter, J.,*Noninvasice MRI Thermometry with the proton-resonance frequency method - study of susceptibility effects.* Magnetic Resonance in Medicine, 1995. **34**(3): p. 359-367.

83. Ishihara, Y., A. Calderon, H. Watanabe, K. Okamoto, Y. Suzuki, K. Kuroda, and Y. Suzuki, *Precise and fast temperature mapping using water proton chemical-shift.* Magnetic Resonance in Medicine, 1995. **34**(6): p. 814-823.

84. Carter, D.L., J.R. MacFall, S.T. Clegg, X. Wan, D.M. Prescott, H.C. Charles, and T.V. Samulski, *Magnetic resonance thermometry during hyperthermia for human high-grade sarcoma.* International Journal of Radiation Oncology Biology Physics, 1998. **40**(4): p. 815-822.

85. Clegg, S.T., S.K. Das, Y. Zhang, J. Macfall, E. Fullar, and T.V. Samulski, *Verification of a hyperthermia model method using MR thermometry.* International Journal of Hyperthermia, 1995. **11**(3): p. 409-424.

86. MacFall, J.R., D.M. Prescott, H.C. Charles, and T.V. Samulski, *H-1 MRI phase thermometry in vivo in canine brain, muscle, and tumor tissue.* Medical Physics, 1996. **23**(10): p. 1775-1782.

87. Gellermann, J.W., W.; Feussner, A.; Fähling, H.; Nadobny, J.; Hildebrandt, B.; Felix, R.; Wust, P., *Methods and potentials of magnetic resonance imaging for monitoring radiofrequency hyperthermia in a hybrid system.* International Journal of Hyperthermia, 2005. **21**(6).

88. Rieke, V. and K.B. Pauly, *MR thermometry.* Journal of Magnetic Resonance Imaging, 2008. **27**(2): p. 376-390.

89. Samulski, T.V., S.T. Clegg, S. Das, J. Macfall, and D.M. Prescott, *Application of a new technology in clinical hyperthermia.* International Journal of Hyperthermia, 1994. **10**(3): p. 389-394.

90. Craciunescua, O.I., P.R. Stauffer, B.J. Soher, C.R. Wyatt, O. Arabe, P. Maccarini, S.K. Das, K.S. Cheng, T.Z. Wong, E.L. Jones, M.W. Dewhirst, Z. Vujaskovic, and J.R. MacFall, *Accuracy of real time noninvasive temperature measurements using magnetic resonance thermal imaging in patients treated for high grade extremity soft tissue sarcomas.* Medical Physics, 2009. **36**(11): p. 4848-4858.

91. Abragam, A., *Principles of Nuclear Magnetism*. 1961, Oxford: Oxford University Press.

92. Hindman, J.C., *Proton Resonance Shift of Water in the Gas and Liquid States.* The Journal of Chemical Physics, 1966. **44**(12): p. 4582-4592.

93. McDannold, N., *Quantitative MRI-based temperature mapping based on the proton resonant frequency shift: Review of validation studies.* International Journal of Hyperthermia, 2005. **21**(6): p. 533-546.

94. Schenck, J.F., *The role of magnetic susceptibility in magnetic resonance imaging: MRI magnetic compatibility of the first and second kinds.* Medical Physics, 1996. **23**(6): p. 815-850.

95. Dickinson, W.C., *The time average magnetic field at the nucleus in nuclear magnetic resonance experiments.* Physical Review, 1951. **81**(5): p. 717-731.

96. Chu, S.C.K., Y. Xu, J.A. Balschi, and C.S. Springer, *Bulk magnetic - susceptibility shifts in NMR - studies of compartmentalized samples - use of paramegnetic reagents.* Magnetic Resonance in Medicine, 1990. **13**(2): p. 239-262.

97. Sprinkhuizen, S., M. Konings, C. Bakker, and L. Bartels. *Heating of fat leads to significant temperature errors in PRFS based MR thermometry*. in *Proceedings 17th Scientific Meeting, International Society for Magnetic Resonance in Medicine*. 2009. Honolulu.

98. Depoorter, J., *Noninvasive MRI thermometry with the proton - resonance frequency method - study of susceptibility effects.* Magnetic Resonance in Medicine, 1995. **34**(3): p. 359-367.

99. Stollberger, R., P.W. Ascher, D. Huber, W. Renhart, H. Radner, and F. Ebner, *Temperature monitoring of interstitial thermal tissue coagulation using MR phase images.* Jmri-Journal of Magnetic Resonance Imaging, 1998. **8**(1): p. 188-196.

100. Wyatt, C., B. Soher, P. Maccarini, H.C. Charles, P. Stauffer, and J. Macfall, *Hyperthermia MRI temperature measurement: Evaluation of measurement stabilisation strategies for extremity and breast tumours.* International Journal of Hyperthermia, 2009. **25**(6): p. 422-433.

101. El-Sharkawy, A.M., M. Schar, P.A. Bottomley, and E. Atalar, *Monitoring and correcting spatio-temporal variations of the MR scanner's static magnetic field.* Magnetic Resonance Materials in Physics Biology and Medicine, 2006. **19**(5): p. 223-236.

102. Gellermann, J., B. Hildebrandt, R. Issels, H. Ganter, W. Wlodarczyk, V. Budach, R. Felix, P.U. Tunn, P. Reichardt, and P. Wust, *Noninvasive magnetic resonance thermography of soft tissue sarcomas during regional hyperthermia - Correlation with response and direct thermometry.* Cancer, 2006. **107**(6): p. 1373-1382.

103. Gellermann, J., W. Wlodarczyk, H. Ganter, J. Nadobny, H. Fahling, M. Seebass, R. Felix, and P. Wust, *A practical approach to thermography in a hyperthermia/magnetic resonance hybrid system: Validation in a heterogeneous phantom.* International Journal of Radiation Oncology Biology Physics, 2005. **61**(1): p. 267-277.

104. Galiana, G., R.T. Branca, E.R. Jenista, and W.S. Warren, *Accurate temperature imaging based on intermolecular coherences in magnetic resonance.* Science, 2008. **322**(5900): p. 421-424.

105. Bachiller, P.R., S. Ahn, and W.S. Warren, *Detection of intermolecular heteronuclear multiple-quantum coherences in solution NMR.* Journal of Magnetic Resonance Series A, 1996. **122**(1): p. 94-99.

106. Ahn, S., N. Lisitza, and W.S. Warren, *Intermolecular zero-quantum coherences of multi-component spin systems in solution NMR.* Journal of Magnetic Resonance, 1998. **133**(2): p. 266-272.

107. Ahn, S., S. Lee, and W.S. Warren, *The competition between intramolecular J couplings, radiation damping, and intermolecular dipolar couplings in two-dimensional solution nuclear magnetic resonance.* Molecular Physics, 1998. **95**(5): p. 769-785.

108. Chen, Z. and J.H. Zhong, *Unconventional diffusion behaviors of intermolecular multiple-quantum coherences in nuclear magnetic resonance.* Journal of Chemical Physics, 2001. **114**(13): p. 5642-5653.

109. Qiuhong, H., S. Pavel, J.H. Regina, R.L. Donald, C.W. Jeffrey, and B. Veerle Ilse Julie, *In vivo MR spectroscopic imaging of polyunsaturated fatty acids (PUFA) in healthy and cancerous breast tissues by selective multiple-quantum coherence transfer (Sel-MQC): A preliminary study.* Magnetic Resonance in Medicine, 2007. **58**(6): p. 1079-1085.

110. Chen, X., M.J. Lin, Z. Chen, S.H. Cai, and J.H. Zhong, *High-resolution intermolecular zero-quantum coherence spectroscopy under inhomogeneous fields with effective solvent suppression.* Physical Chemistry Chemical Physics, 2007. **9**(47): p. 6231-6240.

111. Balla, D. and C. Faber, *Solvent suppression in liquid state NMR with selective intermolecular zero-quantum coherences.* Chemical Physics Letters, 2004. **393**(4-6): p. 464-469.

112. Chen, Z., Z.W. Chen, and J.H. Zhong, *High-resolution NMR spectra in inhomogeneous fields via IDEAL (intermolecular dipolar-interaction enhanced all lines) method.* Journal of the American Chemical Society, 2004. **126**(2): p. 446-447.

113. Chen, Z., S.H. Cai, Z.W. Chen, and J.H. Zhong, *Fast acquisition of high-resolution NMR spectra in inhomogeneous fields via intermolecular double-quantum coherences.* Journal of Chemical Physics, 2009. **130**(8): p. 11.

114. Jianhui, Z., K. Edmund, and C. Zhong, *fMRI of auditory stimulation with intermolecular double-quantum coherences (iDQCs) at 1.5T.* Magnetic Resonance in Medicine, 2001. **45**(3): p. 356-364.

115. Andreas, S., H.J. Thies, and E.M. Harald, *Functional magnetic resonance imaging with intermolecular double-quantum coherences at 3 T.* Magnetic Resonance in Medicine, 2005. **53**(6): p. 1402-1408.

116. Hennig, J., A. Nauerth, and H. Friedburg, *RARE imaging - a fast imaging method for clinical MR.* Magnetic Resonance in Medicine, 1986. **3**(6): p. 823-833.

117. Schneider, J.T. and C. Faber, *BOLD imaging in the mouse brain using a TurboCRAZED sequence at high magnetic fields.* Magnetic Resonance in Medicine, 2008. **60**(4): p. 850-859.

118. Frydman, L., T. Scherf, and A. Lupulescu, *The acquisition of multidimensional NMR spectra within a single scan.* Proceedings of the National Academy of Sciences of the United States of America, 2002. **99**(25): p. 15858-15862.

119. Frydman, L., A. Lupulescu, and T. Scherf, *Principles and features of single-scan two-dimensional NMR spectroscopy.* Journal of the American Chemical Society, 2003. **125**(30): p. 9204-9217.

120. Galiana, G., R.T. Branca, and W.S. Warren, *Ultrafast intermolecular zero quantum spectroscopy.* Journal of the American Chemical Society, 2005. **127**(50): p. 17574-17575.

121. Chen, X., M.J. Lin, Z. Chen, and J.H. Zhong, *Fast Acquisition Scheme for Achieving High-Resolution MRS With J-Scaling Under Inhomogeneous Fields.* Magnetic Resonance in Medicine, 2009. **61**(4): p. 775-784.

122. Balla, D.Z., G. Melkus, and C. Faber, *Spatially localized intermolecular zero-quantum coherence spectroscopy for in vivo applications.* Magnetic Resonance in Medicine, 2006. **56**(4): p. 745-753.

123. Galiana, G., *Biomedical applications of intermolecular multiple quantum coherences*, in *Chemistry*. 2008, Princeton University: Princeton. p. 173.

124. Jenista, E.R., G. Galiana, R.T. Branca, P.S. Yarmolenko, A.M. Stokes, M.W. Dewhirst, and W.S. Warren, *Application of mixed spin iMQCs for temperature and chemical-selective imaging.* Journal of Magnetic Resonance, 2010. **204**(2): p. 208-218.

125. De Feyter, H., K. Petersen, G. Mason, G. Sanacora, J. Krystal, B. Gulanski, R. Sherwin, K. Behar, R. de Graaf, F. Boumezbeur, G. Shulman, and D. Rothman.

13C MRS during [3-13C]lactate infusion under hyperinsulinemic-hypoglycemic conditions reveals compartmentalized lactate metabolism in human brain. in *Proceedings 17th Scientific Meeting, International Society for Magnetic Resonance in Medicine*. 2009. Honolulu.

126. Heins, J., W. Jiang, S. Gottschalk, D. Leibfritz, R. Butterworth, and C. Zwingmann. *Improvement of ammonia removal by glutamine synthesis is associated with attenuation of encephalopathy in acute liver failure: protective effects of the NMDA receptor antagonist memantine*. in *Proceedings 17th Scientific Meeting, International Society for Magnetic Resonance in Medicine*. 2009. Honolulu.

127. Sailasuta, N., K. Harris, O. Abulseoud, and B. Ross. *Cerebral Glutamate Metabolism via [2-13C] glucose in Normal Brain*. in *Proceedings 17th Scientific Meeting, International Society for Magnetic Resonance in Medicine*. 2009. Honolulu.

128. Pfeuffer, J., I. Tkac, I.Y. Choi, H. Merkle, K. Ugurbil, M. Garwood, and R. Gruetter, *Localized in vivo H-1 NMR detection of neurotransmitter labeling in rat brain during infusion of 1-C-13 D-glucose.* Magnetic Resonance in Medicine, 1999. **41**(6): p. 1077-1083.

129. Yanqin, L., G. Tianliang, C. Zhong, K. Scott, J. Mathews, and Z. Jianhui, *High-resolution MRS in the presence of field inhomogeneity via intermolecular double-quantum coherences on a 3-T whole-body scanner.* Magnetic Resonance in Medicine, 2010. **63**(2): p. 303-311.

130. Galiana, G., Branca, R.T., Jenista, E.R., and W.S. Warren, *Accurate Temperature Imaging using Intermolecular Coherences.* Proc. Int. Soc. Mag. Res. Med., 2007. **8**(3370).

131. Tang, X.P., H. Ong, K. Shannon, and W.S. Warren, *Simultaneous acquisition of multiple orders of intermolecular multiple-quantum coherence images.* Magnetic Resonance Imaging, 2003. **21**(10): p. 1141-1149.

132. Shannon, K.L., R.T. Branca, G. Galiana, S. Cenzano, L.S. Bouchard, W. Soboyejo, and W.S. Warren, *Simultaneous acquisition of multiple orders of intermolecular multiple-quantum coherence images in vivo.* Magnetic Resonance Imaging, 2004. **22**(10): p. 1407-1412.

133. Takahashi, N., T. Inoue, J. Lee, T. Yamaguchi, and K. Shizukuishi, *The roles of PET and PET/CT in the diagnosis and management of prostate cancer.* Oncology, 2007. **72**(3-4): p. 226-233.

134. Konyukhov, V.K., *Spin state of ortho-parawater molecules in liquid.* Bulletin of the Lebedev Physics Institute, 2009. **36**(4): p. 123-125.

135. Tikhonov, V.I. and A.A. Volkov, *Separation of Water into Its Ortho and Para Isomers.* Science, 2002. **296**(5577): p. 2363-.

136. Carravetta, M., O.G. Johannessen, and M.H. Levitt, *Beyond the T-1 limit: Singlet nuclear spin states in low magnetic fields.* Physical Review Letters, 2004. **92**(15).

137. Carravetta, M. and M.H. Levitt, *Long-lived nuclear spin states in high-field solution NMR.* Journal of the American Chemical Society, 2004. **126**(20): p. 6228-6229.

138. Carravetta, M. and M.H. Levitt, *Theory of long-lived nuclear spin states in solution nuclear magnetic resonance. I. Singlet states in low magnetic field.* Journal of Chemical Physics, 2005. **122**(21).

139. Pileio, G., M. Carravetta, and M.H. Levitt, *Extremely Low-Frequency Spectroscopy in Low-Field Nuclear Magnetic Resonance.* Physical Review Letters, 2009. **103**(8).

140. Pileio, G. and M.H. Levitt, *J-Stabilization of singlet states in the solution NMR of multiple-spin systems.* Journal of Magnetic Resonance, 2007. **187**(1): p. 141-145.

141. Pileio, G. and M.H. Levitt, *Isotropic filtering using polyhedral phase cycles: Application to singlet state NMR.* Journal of Magnetic Resonance, 2008. **191**(1): p. 148-155.

142. Pileio, G. and M.H. Levitt, *Theory of long-lived nuclear spin states in solution nuclear magnetic resonance. II. Singlet spin locking.* Journal of Chemical Physics, 2009. **130**(21).

143. Pilelo, G., M. Concistre, M. Carravetta, and M.H. Levitt, *Long-lived nuclear spin states in the solution NMR of four-spin systems.* Journal of Magnetic Resonance, 2006. **182**(2): p. 353-357.

144. Tayler, M.C.D., S. Marie, A. Ganesan, and M.H. Levitt, *Determination of Molecular Torsion Angles Using Nuclear Singlet Relaxation.* Journal of the American Chemical Society, 2010. **132**(24): p. 8225-8227.

145. Pileio, G., *Relaxation theory of nuclear singlet states in two spin-1/2 systems.* Progress in Nuclear Magnetic Resonance Spectroscopy, 2010. **56**(3): p. 217-231.

146. Yadav, N.N., A.M. Torres, and W.S. Price, *NMR q-space imaging of macroscopic pores using singlet spin states.* Journal of Magnetic Resonance, 2010. **204**(2): p. 346-348.

147. Cavadini, S., J. Dittmer, S. Antonijevic, and G. Bodenhausen, *Slow diffusion by singlet state NMR spectroscopy.* Journal of the American Chemical Society, 2005. **127**(45): p. 15744-15748.

148. Carr, H.Y. and E.M. Purcell, *Effects of diffusion on free precession in nuclear magnetic resonance experiments.* Physical Review, 1954. **94**(3): p. 630-638.

149. Meiboom, S. and D. Gill, *Modified Spin-Echo Method for Measuring Nuclear Relaxation Times.* Review of Scientific Instruments, 1958. **29**(8): p. 688-691.

150. Michaeli, S., H. Gröhn, O. Gröhn, D.J. Sorce, R. Kauppinen, C.S.S. Jr., K. U, gbreve, urbil, and M. Garwood, *Exchange-influenced T2rho contrast in human brain images measured with adiabatic radio frequency pulses.* Magnetic Resonance in Medicine, 2005. **53**(4): p. 823-829.

151. Jenista, E.R., A.M. Stokes, R.T. Branca, and W.S. Warren, *Optimized, unequal pulse spacing in multiple echo sequences improves refocusing in magnetic resonance.* Journal of Chemical Physics, 2009. **131**(20): p. 7.

152. Uhrig, G.S., *Keeping a Quantum Bit Alive by Optimized pi -Pulse Sequences.* Physical Review Letters, 2007. **98**(10): p. 100504.

153. Hahn, E.L., *Spin Echoes.* Physical Review, 1950. **80**(4): p. 580-594.

154. Haeberlen, U., *High Resolution NMR in Solids: Selective Averaging*. 1976, New York: Academic.

155. Branca, R.T., G. Galiana, and W.S. Warren, *Enhanced nonlinear magnetic resonance signals via square wave dipolar fields.* Journal of Chemical Physics, 2008. **129**(5).

156. Adams, R.W., J.A. Aguilar, K.D. Atkinson, M.J. Cowley, P.I.P. Elliott, S.B. Duckett, G.G.R. Green, I.G. Khazal, J. Lopez-Serrano, and D.C. Williamson, *Reversible Interactions with para-Hydrogen Enhance NMR Sensitivity by Polarization Transfer.* Science, 2009. **323**(5922): p. 1708-1711.

Biography

Elizabeth Jenista was born in Berkeley, CA on October 8th, 1983. She attended college at the University of Notre Dame located in Notre Dame, IN, where she received a bachelor's of science in chemistry in May 2005. During the course of her graduate work at Duke University in Durham, NC she received the following honors and awards: 2010 ENC Ritchey Travel Award, she was invited to attend the 2009 Lindau Nobel Laureate Meeting in Lindau, Germany, 2010 Krigbaum Memorial Fellowship, 2009 Hobbs Endowment Fellowship, 2009 C.R. Hauser Fellowship, and the 2009 Paul M. Gross Research Fellowship. Published works during graduate school include: Temperature Imaging using iMQCs, E.R. Jenista, R.T. Branca, W.S. Warren, *accepted, invited review, International Journal of Hyperthermia,* Application of Mixed Spin iMQCs for Temperature and Chemical-Selective Imaging, E.R. Jenista, G. Galiana, R.T Branca, A.M. Stokes, P. Yarmolenko, M. Dewhirst, W. S. Warren, *accepted, Journal of Magnetic Resonance , September 2009,* UDD Multiple Echo Sequences Improve Refocusing in T_2-weighted Imaging Applications, E.R. Jenista, A.M. Stokes, R.T. Branca, W.S. Warren, *Journal of Chemical Physics, 131, 204510 November, 2009,* Hyperpolarized Magnetic Resonance Using True Singlet Eigenstates, W.S. Warren, E.R. Jenista, R.T. Branca, X. Chen, *Science, 2009, 323(5922), 1711-1714.* (This work was highlighted in as part of the cover story in Chemical and Engineering News, October 2008 and in Nature Chemistry, June 2009), iDQC anisotropy map imaging for tumor tissue characterization in vivo, R. T. Branca,

Y.M. Chen, V. Mouraviev, G. Galiana, E. R. Jenista, C. S. S. R. Kumar, C. Leuschner, and W. S. Warren, *Magnetic Resonance in Medicine, 2009, 61(4), 973-943*, Hyperpolarized Carbon-Carbon Intermolecular Multiple Quantum Coherences, E. R. Jenista, R.T. Branca, W. S. Warren, *Journal of Magnetic Resonance, 2009, 198(1), 74-77,* Accurate Temperature Imaging Based on Intermolecular Coherences in Magnetic Resonance, G Galiana, R. T. Branca, E. R. Jenista, and W. S. Warren, *Science, 2008, Vol. 322. no. 5900, pp. 421 - 424* (This work was highlighted in Science Daily, October 21, 2008)